The Dissertation Committee for Megha Madhukar Surve
certifies that this is the approved version of the following dissertation:

Interactions, Phase Behavior and Rheological Properties of Polymer-Nanoparticle Mixtures

Committee:

Venkat Ganesan, Supervisor

Keith Johnston

Peter Rossky

Isaac Sanchez

Thomas Truskett

Interactions, Phase Behavior and Rheological Properties of Polymer-Nanoparticle Mixtures

by

Megha Madhukar Surve, B.E.; M. Tech.

DISSERTATION
Presented to the Faculty of the Graduate School of
The University of Texas at Austin
in Partial Fulfillment
of the Requirements
for the Degree of

DOCTOR OF PHILOSOPHY

THE UNIVERSITY OF TEXAS AT AUSTIN
December 2006

Dedicated to my parents, Madhuri and Madhukar Surve.

Acknowledgments

This thesis represents culmination of a long journey through graduate school and I am indebted to many people for helping me reach this point.

First of all, I would like to thank my advisor, Prof. Venkat Ganesan. It has been an exciting experience to work under his able guidance. Without his continuous encouragement and enduring patience, this thesis would not have been possible.

I would also like to extend my sincere thanks to Dr. Victor Prymitsyn. It was a real pleasure to work with him and numerous discussions with him have helped steer the development of this research.

I am also grateful to all the dedicated teachers and professors I had along the way from primary school, high school, college to here at UT, who have contributed greatly in shaping my career.

I could not leave Austin without mentioning Rhutesh, Bharad, Shobha, Shalini, Shweta, Namrata, Smita & Rohan. Thanks for making the last four years more enjoyable. Thanks to Rani, Revati, Sorabh, Rashmi and Adil for their healthy interest in ‘How many years more?’ which served as an inspiration to finish the graduate school faster!

I am especially thankful to Ravindra for his support and encouragement. He always had the right words to motivate me through the ups and downs of the graduate school. Thanks for being there for me.

Finally, I would like to thank my family for their encouragement over the years and their patience with me during this journey through graduate school. I owe you much - for all your love and support.

Interactions, Phase Behavior and Rheological Properties of Polymer-Nanoparticle Mixtures

Publication No. ______________

Megha Madhukar Surve, Ph.D.
The University of Texas at Austin, 2006

Supervisor: Venkat Ganesan

This research focuses on the interactions, phase behavior, structural characteristics and rheological properties of multicomponent polymer-particle mixtures. The systems considered in this study include spherical and rodlike particles in presence of non-adsorbing, adsorbing and grafted polymers. A hybrid multiscale approach is presented which implements polymer self consistent field theory in combination with the McMillan-Mayer framework to deduce the polymer-mediated interactions between the particles. The conformational characteristics of the polymers in the vicinity of particles are extracted within the mean field framework. A novel off-lattice simulation scheme is presented which combines the equilibrium interactions between the particles with the structural characteristics of polymers and allows for simultaneous identification of thermodynamic phase behavior, structure and rheological properties of polymer-particle mixtures. An accurate numerical solution of field theoretic equations is employed to discern the role of particle curvature in governing the equilibrium phase behavior, gelation transitions and rheological characteristics of such mixtures, with particular emphasis on the nanoparticle regime.

For the case of non-adsorbing polymer, our results demonstrate significant multibody effects with profound consequences for the phase behavior of the particles. We have also analyzed the effect of surface saturation and particle curvature on the polymer adsorption characteristics to highlight differences in the structure of adsorbed polymer layers on nanoparticles from that on larger particles. These structural characteristics are utilized in particle-based simulations to quantify the phase behavior, percolation thresholds and elastic properties of polymer-nanoparticle systems and successfully rationalize experimental observations in context of polymer-nanoparticle mixtures. We also present a systematic study on the adsorption characteristics, the effective pair-interaction potentials and the resulting phase behavior, percolation transitions of nanorods dispersed in solutions of adsorbing polymers and discuss the efficacy of polymers in preventing van der Waals induced bundling of nanotubes. Finally, we study adsorption of model proteins on the surfaces carrying grafted polymer layers and delimit the physical parameters that control the resistance of surface grafted polymers to protein adsorption.

Table of Contents

List of Figures

Chapter 1

Introduction

The research work detailed in this dissertation focuses on interactions, phase behavior and rheological properties of nano-sized particles in presence of polymer solutions under different physical conditions. The objective of this research is to develop a predictive understanding of the influence of microscopic interactions in the binary polymer-particle system on the thermodynamical phase behavior and structural properties of the macroscopic mixtures. The systems that are studied in the course of this research include mixtures of (i) non-adsorbing, (ii) adsorbing and (iii) grafted polymers with (i) spherical and (ii) cylindrical nanoparticles. To examine the thermodynamics and structural features of such systems, we followed the steps summarized below:

1. Developed a multiscale framework to map the binary polymer-particle system onto an effective one component system.
2. Proposed a generic self consistent field theory for the inhomogeneous polymeric component, which accounts for a variety of interactions between the polymer segments and surface of the particles.
3. Extended the above developed field theory to quantify conformational characteristics of adsorbed polymer layers on the surface of particles.

4. Developed an efficient numerical scheme to effect solutions of the above field theories to obtain interparticle interactions and conformational statistics for a wide range of polymer to particle size ratios

5. Employed simple analytical models to translate the information about pair interactions into thermodynamic phase behavior of polymer-particle systems.

6. Proposed a hybrid off-lattice Monte Carlo simulation scheme to combine the thermodynamics of the system with the polymer structural features to predict the clustering behavior and percolation transitions for nanoparticles in adsorbing polymers.

7. Extended the Flory theory for anisotropic interactions to delineate the isotropic-nematic transitions and percolation behavior for nanorods in polymeric solutions.

1.1 Overview and Motivation

Adding polymer components to colloidal suspensions has emerged as a versatile approach to control their interactions, phase behavior, and rheological properties. Such systems exhibit a complex interplay of different interactions depending upon the nature of the polymer, the particle surface and the solvent which govern the phase behavior and rheology of the resultant mixtures. For instance, for the case of a polymer with no preferential interactions (non-adsorbing) with the particles, an effective attraction of purely entropic origin is induced between the particles [1–3]. The latter typically results in demixing and phase separation of the colloid-polymer mixture. For the case of polymers which can adsorb onto the particles, the effective interparticle interactions range from being strong attractions at low polymer concentrations to purely repulsive at high polymer concentrations [4, 5]. These characteristics can lead to a rich phase behavior of the colloid-polymer mixture such as phase separation, reentrant miscibility etc [6, 7]. Finally, when the polymer is grafted onto the particles, the excluded volume repulsions between tethered chains result in a net repulsion between the polymer coated particles, which stabilizes colloidal dispersions [8]. This ability of the polymer to induce and to control the interactions among the suspended particles has been a topic of active scientific research and has been used successfully in a number of technological applications. Some of the industrial applications where such polymer-particle mixtures and their phase behavior play an important role include colloidal stabilization, protein crystallization, food preservation applications, separations of surfactant micellar solutions [9–11], and polymer nanocomposites [12, 13].

Conventional applications where polymers are used as colloidal stabilizers, flocculants or rheology modifiers are characterized by particle sizes larger than the radius of gyration R_g. Typically, the colloidal radii (R) are in the range of $10-100$ nm whereas R_g ranges between $5-40$ nm resulting in particle-to-polymer size ratios $R/R_\mathrm{g} \geq 1$. This size limit is usually referred to as the 'colloid limit' and has been studied extensively. However, more recent advances have shifted the focus from the regime of colloidal suspensions to the regime of nanoparticle suspensions, where the typical size of the particle is comparable to or smaller than the size of the polymer additives. For instance, in the case of polymer nanocomposites, filler particles of different shapes with sizes in the range 5 - 50 nm (comparable to R_g) are routinely dispersed in polymeric matrices to enhance their properties [14, 15]. The nanoparticle limit is also relevant to the understanding of the phase behavior in applications wherein the polymers are mixed with surfactant micelles [16]. Furthermore, in many situations polymers such as PEG are added to globular proteins to aid in their precipitation and crystallization [17–19]. There again, the size of the proteins is $\sim O(5-40)$ nm while the polymer size is $\sim O(10-50)$ nm placing such applications in the nanoparticle regime.

The transition from ‘colloid’ to ‘nanoparticle’ limit has brought forth new challenges in the field of colloidal science. The curvature of particle becomes an important factor in determining the equilibrium behavior and interactions in polymer-particle mixtures. The physics of polymer-particle suspensions is expected to be quite different in the nanoparticle limit. In the case of depletion interactions (when the polymers do not interact with the particles), many theoretical and experimental studies have clearly shown that the curvature of the particle can have profound qualitative and quantitative effects on both the interactions and the stability characteristics of the mixture [20–24]. Recent experimental observations in the context of polymer-nanoparticle systems have indicated that similar richness in phase behavior and structural characteristics also prevails in the context of adsorbing polymers. For instance, in many cases even extremely low particle loadings (around a volume fraction 2 %) have been shown to lead to significant changes in the rheological properties of the mixture [25], which in turn suggest nontrivial structural characteristics for the mixture. Further, observations in the context of polymer-clay composites, laponite-PEO, silica-PEO etc. suggest a variety of phase behavioral characteristics ranging from macroscopic flocculation, phase separation, stable 1-phase gels etc [26–29].

The presence of particles can also significantly alter conformational characteristics of the polymer chains in contact with the surface. Adsorbed polymer layers form a variety of structures such as loops, dangling tails and bridges (segments connecting two or more surfaces) [30]. In addition to governing the interactions, these conformational characteristics influence the rheological and mechanical properties of polymer-particle complexes significantly. For instance, many experiments on the rheology of nanoparticle-polymer suspensions have reported dramatic enhancements in the low frequency elasticity (storage modulus) at very low loadings of the particles [25, 27, 31]. Polymer-bridging induced gelation of particles is speculated to be responsible for the enhancements in the elastic moduli of the composite. Several experimental results supporting this mechanism are available. For instance, in many experiments, the effects on the mechanical properties manifest at particle loadings far below that expected/required for particle gelation. For instance, for systems of PEO containing silica nanoparticles, Zhang and Archer have observed a transition to solid-like viscoelastic response at silica loadings as low as 2 % [25].

More pertinently, they observed that systems involving bare silica particles where the polymer-particle interactions are strongest induce the strongest reinforcement. Similar results were also observed by Macosko *et al* in the context of Silica particles mixed with PDMS matrix [32].

So far, many of the above observations have only been rationalized qualitatively by invoking the influence of polymer-mediated interactions and the resulting polymer conformational characteristics. For instance, the formation of gels and flocs has been speculated to arise as a result of a large number of interparticle bridges in the nanoparticle limit [27, 28]. The occurrence/lack thereof of phase separation has again been attributed to the magnitude and the range of the interaction potentials. Existing theoretical results for adsorbing polymers are mainly at a scaling level and relate only to the adsorption characteristics on a single nanoparticle [30, 33, 34]. Very little is known quantitatively about features such as effective interactions, stability and structural characteristics of the mixture and the differences, if any, with the colloid limit for the case involving *depletion and adsorbing* polymers.

At a fundamental level, the challenge in the polymer-particle mixtures is the apparent complexity of these systems. These mixtures are characterized by a number of competing length scales. Typical length scales that characterize the colloidal particles (such as radius of particles and length for the case of anisotropic particles) are in the range of a few nm to about a micrometer. On the other hand, the polymeric component is characterized by the monomeric length scale, which is typically at least an order of magnitude smaller than the particle size. These highly asymmetric length scales make fully atomistic/molecular level treatment of these systems computationally cumbersome and is, in most cases, out of reach of the available computational resources. A computationally more viable alternative to fully atomistic models is *to group the atoms/molecules into larger 'particles'*, the efficiency and accuracy of such an approach are sensitively dependent on the degree of coarse graining. For example, the monomeric units on the polymers can be lumped into a larger unit or bead such that each bead represents force center of a collection of a small number of backbone monomers. However, incorporating essential molecular level interactions (especially, the short ranged interactions) in the coarse-grained particle-based methods becomes intractable and the accurate parameterization of such beads/particles is often difficult. Moreover, for heterogeneous systems involving phase transitions and for highly dense polymeric systems such a coarse grained particle approach remains computationally expensive. This necessitates development of hybrid theoretical approaches which will enable one to study the macroscopic features of inhomogeneous polymer-particle mixtures without sacrificing important molecular level information.

In this work we take advantage of the apparent complexity of polymeric systems which actually contributes to simplification of the physics of the system on the coarse grained level and to a large extent, results in averaging out of the microscopic details. This study is motivated by the basic idea that a few characteristic attributes of the system – which absorb the microscopic details of the polymers and account only for the main properties of the polymer and their interactions with surfaces – can be successfully used to determine the macroscopic behavior of the system. Such 'mean field' approaches have been widely used to describe inhomogeneous polymeric systems. In this work, we utilize one of the most powerful mean field tools in the context of polymeric systems, *the self consistent field theory*, to describe the equilibrium properties of polymer-particle mixtures. In a nutshell, the idea behind the self consistent theory is to describe the distribution of the polymer in terms of a fluctuating position dependent potential field which self consistently depends on the distribution of the polymer. We develop numerical self consistent field theories to model the configurational distributions of polymeric components. Such theories when used in conjunction with the McMillan-Mayer framework result in accurate determination of 'polymer mediated' interactions between the particles. The latter are combined with the structural characteristics of polymers in a hybrid particle-based computer simulation scheme as well as in a number of theoretical models to examine the macroscopic structure, gelation transition and rheological properties of polymer-particle mixtures.

1.2 Outline of Dissertation

In this section, we present a brief outline of this dissertation. In Chapter 2, we detail a generalized version of polymer self consistent field theory and elaborate on the McMillan-Mayer framework used in this work to deduce the polymer mediated interactions between the particles and polymer conformational characteristics in presence of particles. The specific applications of the above frameworks to the case of nanoparticles in presence of depleting, adsorbing and grafted polymers, the resulting interaction potentials and phase behaviors are presented in subsequent Chapters.

1.2.1 Theoretical Formalism (Chapter 2)

In this chapter, we discuss the statistical mechanical framework to deduce the interaction potentials between particles suspended in polymeric solutions and present steps involved in the self consistent field theoretic formulation for inhomogeneous polymeric systems. The appropriate adaptations of the SCFT framework for specific polymeric systems are discussed in the subsequent chapters. We also elaborate on the extension of the field theory to extract the structural characteristics of polymer layers in the vicinity of particles.

1.2.2 Interactions and Phase Behavior of Nanoparticles in Non-adsorbing Polymer Solutions (Chapter 3)

We present a detailed analysis of the polymer depletion induced interactions between the nanoparticles and the resultant phase behavioral characteristics using a McMillan-Mayer like approach in combination with the polymer field theory. In the nanoparticle limit, the volume of the polymer depletion layers is observed to exceed the size of the nanoparticles themselves, leading to effective polymer concentrations typically in the semidilute and concentrated regimes even when the average polymer concentrations are in the dilute regimes. The multibody depletion overlaps are accounted through an approximate approach. We address the depletion characteristics in the nanoparticle regime by effecting an accurate numerical solution of polymer mean field-theory in bispherical coordinate system. The depletion interactions are observed to be characterized by both the importance of polymer interactions as well as the curvature of the nanoparticles relative to the correlation length of polymers. The depletion characteristics of the nanoparticle-polymer mixture are observed to be quite different when viewed in this framework, and have profound consequences for the phase behavior of the nanoparticles.

1.2.3 Interactions and Phase Behavior in Mixtures of Adsorbing Polymer and Nanoparticles (Chapter 4)

In this chapter, we analyze the polymer adsorption characteristics, pair-interaction potentials, phase and percolation behavior in nanoparticle-polymer mixtures. A “saturable” adsorption model is proposed to capture the effect of the finite surface saturation capacity for adsorption. A polymer self-consistent field theory is implemented in combination with a McMillan-Mayer framework to compute the pair interaction potentials. The results demonstrate novel size effects that distinguish the adsorption characteristics of nanoparticles from that of larger particles. Specifically, the nanoparticle regime is observed to be characterized by a significant adsorbance of polymers, albeit distributed predominantly in the form of tails. An interplay between the surface saturation, polymer-to-particle size ratios and the polymer concentrations is predicted to govern the overall effective interactions between nanoparticles in presence of adsorbing polymer. Simple, mean-field models are used to relate these characteristics to the phase and percolation behavior in such systems. The percolation threshold for smaller particles are shown to be significantly smaller (and overall correspond only to a few volume percent) compared to that of the larger particles.

1.2.4 Structure and Elasticity of Polymer Bridged Gels of Nanoparticles (Chapter 5)

A combination of field theory and off-lattice Monte Carlo simulations is used to study the gelation phenomena observed in mixtures of nanoparticles and adsorbing polymers. By combining the polymer bridging statistics and polymer mediated interparticle interactions into the simulation framework, we analyze effect of particle size and polymer concentration on the polymer bridging induced gelation of particles. Further we complement the Monte Carlo simulations with graph theory to predict the structural characteristics and elastic properties of such polymer-bridged gels of the particles. Our results indicate that such gels exhibit a universal fractal structure and the elastic modulus of the gels follows a universal scaling law with volume fraction of particles.

1.2.5 Dispersions and Phase Transitions in Mixtures of Adsorbing Polymer and Nanorods (Chapter 6)

Next, we study the adsorption characteristics, the effective pair-interaction potentials and the resulting phase behavior, percolation transitions of nanorods dispersed in solutions of adsorbing polymers. A polymer self-consistent field theory is used in conjunction with a Derjaguin approximation to compute the polymer-mediated orientation-dependent pair interaction potentials between cylindrical nanorods. A modified Flory theory and a simple analytical model is then implemented to delineate the different equilibrium phases and the onset of percolation for nanorods in polymer solutions. We present results for the influence of polymer-surface affinity, the polymer concentrations, the radius of rods, and the aspect ratio of rods, on the topology of equilibrium phases and percolation regimes. As a model mimicking nanotube-polymer mixtures, we consider the influence of strong rod-rod van der Waals interactions on the above equilibrium characteristics.

1.2.6 Adsorption of Model Proteins on Polymer Grafted Surfaces (Chapter 7)

Polymer grafting on particle surfaces has been actively utilized to reduce or prevent adsorption of proteins on foreign materials in many biomedical applications. We extend our field theoretic framework to examine the structure of grafted polymer layers on nanosized particles and highlight the differences between structure of grafted polymer on nanosized particles and on planar surfaces. We idealize the protein molecule as a rigid spherical particle and analyze the effect of different parameters such as grafting density, size of protein and polymer molecular weight on the effectiveness of polymer grafting in preventing protein adsorption.

1.3 Summary

Binary polymer-particle systems are characterized by a rich phase behavior and percolation characteristics which are sensitively dependent on the nature of molecular interactions between the constituents of the system. A large body of research work has been devoted to understanding the role of polymer in governing the interactions and phase behavior of colloidal particles and in general, successfully describes the equilibrium characteristics of such polymer-particle mixtures in the colloidal particle size range. However, the recent developments in the field of nanotechnology and biological applications have shifted the focus from 'colloidal' regime to 'nanoparticle' regime where the conventional asymptotic approaches are found to be inadequate to characterize the physics of such mixtures. In this work, we explore the thermodynamics and structural characteristics of polymer-particle mixtures in the 'nanoparticle' regime by developing multiscale modeling approaches. To achieve this, we combine ideas from statistical mechanics, equilibrium thermodynamics and polymer physics and effect numerical modeling and computer simulations of binary polymer-particle systems. This dissertation presents a hybrid multiscale approach developed by us to address the issues in the polymer-particle mixtures and summarizes our contribution to the field of equilibrium thermodynamics and rheological characteristics of binary polymer-particle mixtures.

Chapter 2

Theoretical Framework

In this research, we present a coarse-grained multiscale approach which allows for simultaneous quantification of the phase behavior, percolation and gelation transitions and also the structural and rheological characteristics of resultant gels in polymer-particle systems. Our idea is to use the polymer field theory (i) to deduce the polymer induced 'effective' pair interactions between the particles and (ii) to quantify the structural characteristics of polymer in the vicinity of particles. Subsequently, we implement a number of analytical models and computer simulations (with the particles interacting through the effective interaction potentials) to deduce the phase and percolation behavior of polymer-particle systems. Second aspect of this research focuses on the polymer-induced clustering of particles, the consequent gelation of particles and structural characteristics of such particulate gels. In order to make progress on these issues, we utilize the structural statistics of polymer chains to deduce the probability of formation of polymeric bridges between the particles. The latter is utilized into a hybrid particle based simulation framework to map the connectivity between the particles and to predict the gelation transitions and the elastic properties of resultant gels in such systems. In this chapter, we first illustrate a multiscale statistical mechanical framework which allows us to decouple the binary polymer-particle systems into an effective one component particle system by 'averaging out' the polymer degrees of freedom. We subsequently implement the polymer self consistent field theory to treat the polymer component and present an adaptation of field theory to quantify the structural features of the polymer chains.

The rest of the chapter is arranged in the following manner. Section 2.1 details the McMillan-Mayer framework used in this work to map the two component polymer-particle system onto an 'effective' one component particle system. In section 2.2 we discuss a generalized self consistent field theory used by us to model the polymer component. The specific applications of the field theory to non-adsorbing, adsorbing and grafted polymers are detailed later in the subsequent chapters. In section 2.3, we discuss extension of the self consistent field theory to characterize the structural conformations of the polymer in the vicinity of particles.

2.1 McMillan Mayer Framework

Binary hard sphere systems serve as model system for studying the equilibrium phase behavior and rheological properties of polymer-particle mixtures encountered in many technological applications. We consider a model system comprising of colloidal particles immersed in polymers in an organic solvent. As the differences in the length scales (as well as time scales) for solvent (S) molecules and for polymers (P) and colloidal particles (C) are significant, the solvent degrees of freedom can be ignored safely. We treat the solvent as an inert continuum and assume that the particles and polymers are interacting by effective, solvent-averaged interaction potentials. In this description, we denote the bare particle-particle interactions by $U_{\mathrm{cc}}(r)$, the monomer-monomer interactions by $U_{\mathrm{pp}}(r)$ and the polymer particle interactions by $U_{\mathrm{cp}}(r)$. For a system consisting of N_{c} particles in presence of N_{p} polymer chains, the interaction energy $H = H_{\mathrm{cc}} + H_{\mathrm{cp}} + H_{\mathrm{pp}}$ and can be written in terms of pair interaction potentials $U_{\mathrm{cc}}, U_{\mathrm{cp}}$ and U_{pp} as,

$$\begin{aligned} H_{\mathrm{cc}}(\mathbf{R}) &= \sum_{i<j}^{N_{\mathrm{c}}} U_{\mathrm{cc}}(|\mathbf{R}_{\mathrm{i}} - \mathbf{R}_{\mathrm{j}}|) \\ H_{\mathrm{cp}}(\mathbf{R};\mathbf{r}) &= \sum_{i=1}^{N_{\mathrm{c}}} \sum_{j=1}^{N_{\mathrm{p}}} U_{\mathrm{cp}}(|\mathbf{R}_{\mathrm{i}} - \mathbf{r}_{\mathrm{j}}|) \\ H_{\mathrm{pp}}(\mathbf{r}) &= \sum_{i<j}^{N_{\mathrm{p}}} U_{\mathrm{pp}}(|\mathbf{r}_{\mathrm{i}} - \mathbf{r}_{\mathrm{j}}|) \end{aligned} \tag{2.1}$$

where $\mathbf{R}$ and $\mathbf{r}$ represent the coordinates of the particles and the polymers respectively.

Such binary polymer-particle mixtures have been studied using a number of different theoretical approaches, which differ in the specific assumptions that are made to arrive at quantitative predictions for the equilibrium as well as non-equilibrium behavior of such systems. In this study we take advantage of the large size asymmetry between the monomeric units and the particle components to achieve an effective, coarse grained one component representation of the original two component (polymer and colloid) system. We follow an approach described by Dijkstra *et al.* [35] and map the two component polymer-particle system onto an effective one component particle system, by integrating out the polymer degrees of freedom.

For this purpose, we consider a system in semigrand canonical ensemble $(N_\mathrm{c}, z_\mathrm{p}, V, T)$, where along with volume (V) and temperature $(\beta = 1/k_\mathrm{B}T)$ of the system, the number of particles N_c and activity of polymeric component $z_p = \exp[\beta\mu_p]$ (where μ_p is the chemical potential of the polymer component) are fixed. Thus our model system considers the particle component in a canonical ensemble (N_c, V, T) where as the polymer component is modeled in the grand canonical framework (z_p, V, T). The thermodynamic potential βF associated with this ensemble can be expressed as,

$$\begin{aligned}\exp[-\beta F] &= \sum_{N_\mathrm{p}=0}^{\infty} \frac{z_\mathrm{p}^{N_\mathrm{p}}}{N_\mathrm{c}! N_\mathrm{p}!} \int_V d\mathbf{R} \int_V d\mathbf{r} \exp[-\beta(U_\mathrm{cc} + U_\mathrm{cp} + U_\mathrm{pp} - \mu_\mathrm{p} N_\mathrm{p})] \\ &= \frac{1}{N_\mathrm{c}!} \int_V d\mathbf{R} \exp[-\beta(U_\mathrm{cc} + \Omega)], \qquad (2.2)\end{aligned}$$

where Ω is defined as,

$$\exp[-\beta\Omega] = \sum_{N_\mathrm{p}=0}^{\infty} \frac{z_\mathrm{p}^{N_\mathrm{p}}}{N_\mathrm{p}!} \int_V d\mathbf{r} \exp[-\beta(U_\mathrm{cp} + U_\mathrm{pp})]. \qquad (2.3)$$

Ω depends not only on the fugacity of polymer (z_p) but also on the coordinates $\mathbf{R}_i$ of the particles $i = 1, 2, \cdots$ which are treated in canonical framework. Thus Ω can be interpreted as the grand partition sum for the polymeric component in the external field of a fixed configuration of particles. The effective interaction potential for the system then can be written as,

$$U_\mathrm{eff} = U_\mathrm{cc} + \Omega. \qquad (2.4)$$

Once Ω, and thus U_{eff} are known for different z_{p} values, the phase behavior of the system can be determined. For this purpose, we expand Ω in terms of Mayer functions, $f_{ij} = f(\mathbf{R}_i, \mathbf{r}_j) = \exp[-\beta U_{\text{cp}}(\mathbf{R}_i - \mathbf{r}_j)] - 1$ and $g_{jk} = f(\mathbf{r}_j, \mathbf{r}_k) = \exp[-\beta U_{\text{pp}}(\mathbf{r}_j - \mathbf{r}_k)] - 1$ as:

$$\exp[-\beta\Omega] = \sum_{N_{\text{p}}=0}^{\infty} \frac{z_{\text{p}}^{N_{\text{p}}}}{N_{\text{p}}!} \int_V d\mathbf{r} \prod_{i=1}^{N_{\text{c}}} \prod_{j=1}^{N_{\text{p}}} (1 + f_{ij}) \prod_{k<l}^{N_{\text{p}}} (1 + g_{kl}). \tag{2.5}$$

Using the diagrammatic techniques, the above expression can be rewritten in terms of diagrams:

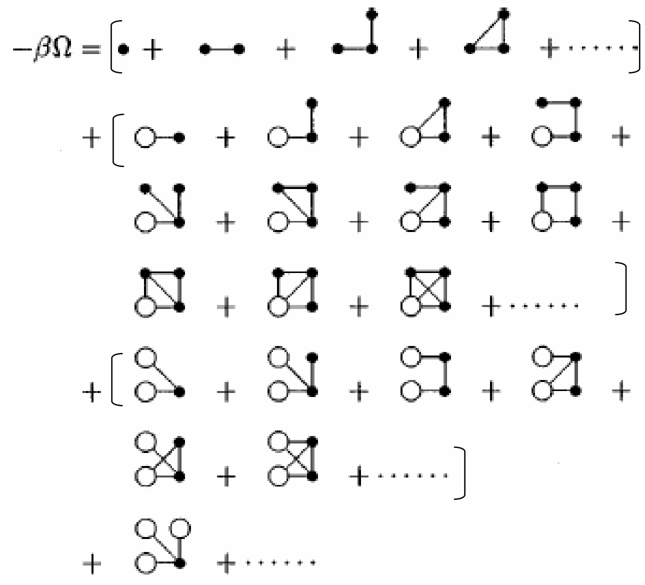

(2.6)

where (i) each black circle represents a factor z_{p} and an integral of $\mathbf{R}_i$ over the volume V, (ii) each line between two black circles represents a g bond, and

(iii) each open big circle connected with a black circle represents an f bond and a summation over all different particles at positions $\mathbf{R}_i$ for $i = 1, ..., N_\mathrm{c}$. The grand potential Ω can then be classified according to the number $n = 0, 1, 2, \cdots, N_\mathrm{c}$ of particles which interact simultaneously with the polymer at constant z_p as:

$$\beta\Omega = \sum_{n=0}^{N_\mathrm{c}} \beta\Omega_n. \tag{2.7}$$

This procedure can also be used to explicitly express Ω_n in terms of polymer partition function Ξ_n. Here we give explicit expressions for Ω_n for $n = 0, 1$ and 2. The first bracketed term in eq. 2.6 can be reexponentiated to obtain,

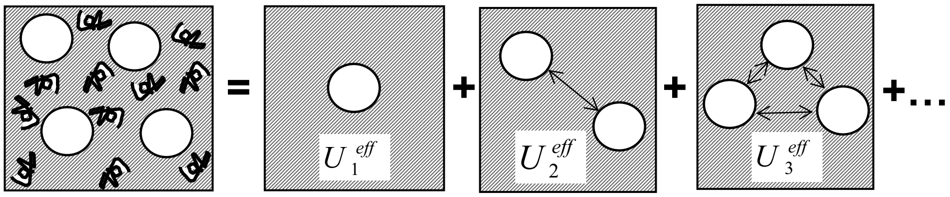

Figure 2.1: Schematic illustration of McMillan-Mayer framework for effective interactions. The N_c-body binary polymer-particle system at polymer fugacity z_p is expressed in terms of n-body ($n = 0, 1..N_c$) one-component systems with polymer-mediated effective interactions between the particles.

$$\exp[-\beta\Omega_0] \equiv \Xi_0(z_p, V) = \sum_{N_\mathrm{p}=0}^{\infty} \frac{z_\mathrm{p}^{N_\mathrm{p}}}{N_\mathrm{p}!} \int_V d\mathbf{r} \exp[-\beta H_{pp}] \tag{2.8}$$

where $\Xi_0(z_p, V)$ characterizes the partition function of a pure polymer at fugacity z_p. The diagrams involving only one open big circle, represent $-\beta\Omega_1$

and can be recovered as:

$$-\beta\Omega_1 \equiv N_{\mathrm{c}} \left[\ln[\Xi_1(\mathbf{R}_i, z_p, V)] - \ln[\Xi_0(z_p, V)]\right] \tag{2.9}$$

where $\Xi_1(\mathbf{R}_i, z_p, V)$ is the partition function for a polymeric system consisting of a single particle:

$$\Xi_1(\mathbf{R}_i, z_p, V) = \sum_{N_{\mathrm{p}}=0}^{\infty} \frac{z_{\mathrm{p}}^{N_{\mathrm{p}}}}{N_{\mathrm{p}}!} \int_V d\mathbf{r} \exp[-\beta H_{pc}^{(1)}] \exp[-\beta H_{pp}] \tag{2.10}$$

Note that the term in brackets in eq. 2.9 represents the grand partition difference between a pure polymer at z_{p} with and without a single particle and thus, gives the insertion free energy βF_C^1 for a particle in a polymeric bath:

$$-\beta F_C^1 \equiv \ln \Xi_1(\mathbf{R}_i, z_p, V) - \ln \Xi_0(z_p, V). \tag{2.11}$$

Similarly, it can be shown that the sum of connected diagrams involving two open big circles is given by:

$$\exp[-\beta\Omega_2] \equiv \prod_{i<j}^{N_c} \frac{\Xi_2(\mathbf{R}_i, \mathbf{R}_j, z_p, V)/\Xi_0(z_p, V)}{\Xi_1^2(\mathbf{R}_i, z_p, V)/\Xi_0^2(z_p, V)} \tag{2.12}$$

where $\Xi_2(\mathbf{R}_i, \mathbf{R}_j; z_p, V)$ represents the grand partition sum of a polymeric system containing two particles at position $\mathbf{R}_i$ and $\mathbf{R}_j$ and is given as,

$$\Xi_2(z_p, V) = \sum_{N_{\mathrm{p}}=0}^{\infty} \frac{z_{\mathrm{p}}^{N_{\mathrm{p}}}}{N_{\mathrm{p}}!} \int_V d\mathbf{r} \exp[-\beta H_{pc}^{(2)}] \exp[-\beta H_{pp}]. \tag{2.13}$$

It follows directly from eq. 2.12 that

$$\beta\Omega_2 \equiv \sum_{i<j}^{N_c} U_2^{\mathrm{eff}}(\mathbf{R}_i, \mathbf{R}_j, z_p, V) \tag{2.14}$$

where $U_2^{\text{eff}}(\mathbf{R}_i, \mathbf{R}_j, z_p, V)$ represents the effective pair potential between the particles and is defined by:

$$\exp[-\beta U_2^{\text{eff}}] = \frac{\Xi_2(\mathbf{R}_i, \mathbf{R}_j, z_p, V)/\Xi_0(z_p, V)}{\Xi_1^2(\mathbf{R}_i, z_p, V)/\Xi_0^2(z_p, V)} \tag{2.15}$$

Note that by spatial homogeneity of the polymer solution, $\Xi_1(\mathbf{R}_i; z_p, V)$ is independent of $\mathbf{R}_i$ and $\Xi_2(\mathbf{R}_i, \mathbf{R}_j; z_p, V) \equiv \Xi_2(|\mathbf{R}_i - \mathbf{R}_j|; z_p, V)$. Thus, we have decoupled the binary polymer-particle system onto an effective one component system consisting of only particles which interact through polymer mediated effective interactions. The latter are expressed in terms of n body partition functions for the polymeric systems. To obtain $\Xi_n(\mathbf{R}_i, \mathbf{R}_j, \ldots, \mathbf{R}_n; z_p)$, we implement a mean-field theoretic approach described below.

2.2 Polymer Self Consistent Field Theory

An essential starting point for theoretical studies of polymeric systems is a microscopic model to describe the conformations of polymer chains. In this research, we concern ourselves with *flexible* polymer chains which are characterized by relatively unhindered rotations of monomeric bonds along the polymer backbone. We represent such flexible polymer chains using a 'Gaussian thread model'. A Gaussian chain is usually represented by a mechanical model termed as bead-spring model where the polymer is assumed to be made up of $N+1$ beads connected through N harmonic springs of length b. If we assume no correlations between the bonds, the distribution of the vector

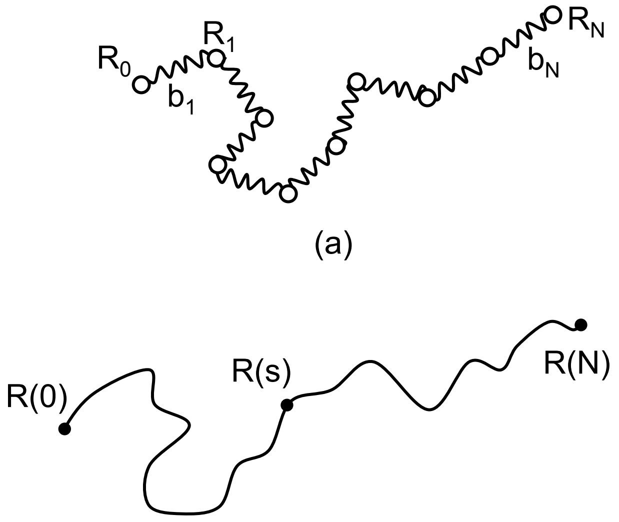

(a)

(b)

Figure 2.2: Schematic representations of a Gaussian chain. (a) A discrete bead-spring model with N+1 beads connected through N springs. The bead positions are denoted by $R_0, \cdots R_N$ and the springs are represented by bond vectors by $b_1, \cdots, bN$. (b) Continuous representation of the Gaussian chain. $R(s)$ represents the continuous space curve with $s \in [0, N]$ as a contour variable that describes the location of a segment along the backbone of the chain.

$\mathbf{R}_n - \mathbf{R}_m$ between any two units n and m can be expressed as,

$$P(\mathbf{R}_n - \mathbf{R}_m; n - m) = \left(\frac{3}{2\pi|n-m|b^2}\right)^{3/2} \exp\left[-\frac{3(\mathbf{R}_n - \mathbf{R}_m)^2}{2|n-m|b^2}\right] \qquad (2.16)$$

In the continuum limit of this model, the polymer chains are represented by continuous space curves $\mathbf{R}(\bar{s})$ and $\mathbf{R}_n - \mathbf{R}_{n-1}$ can be replaced by $d\mathbf{R}(\bar{s})/d\bar{s}$ where $\bar{s}$ denotes the arc length variable running from 0 to N. For an ensemble of m polymer chains, the bonded interactions in the Gaussian thread model then can be quantified by an elastic interaction potential U_{elastic} of the form:

$$\beta U_{\text{elastic}}(\{\mathbf{R}_\alpha(s)\}) = \frac{1}{4R_{\text{g}}^2}\sum_{\alpha=1}^{m}\int_0^1 \left|\frac{d\mathbf{R}_\alpha(s)}{ds}\right|^2 ds, \tag{2.17}$$

where $R_{\text{g}} = \sqrt{Nb^2/6}$ represents the unperturbed radius of gyration of the polymer. Here, b represents the bond length and is generally referred to as 'Kuhn segment length' or 'statistical segment length' in polymer literature. In the above, the arc length variable has been nondimensionalized as $s = \bar{s}/N$. The subscript α in eq. 2.17 indexes the different polymer chains. Besides the bonded elastic interactions, the polymer segments also interact through non-bonded interactions (such as steric effects, van der Waals attractions and other solvent mediated interactions) if they come close to each other. Such interactions between the polymer segments are generally represented in terms of an excluded volume effect. The latter arises from the fact that the segments have finite volume and no two segments can occupy same volume. Thus the interaction between two polymer segments n and m can be represented as, $vk_BT\delta(\mathbf{R}_n - \mathbf{R}_m)$ where v denotes excluded volume parameter and $\delta(\cdots)$ represents the delta function enforcing locally the exclusion of overlaps of monomers. The excluded volume parameter v symbolizes the solvent quality and is positive for the case of good solvent indicating swelling of a polymer chain. On the other hand, negative v corresponds to poor solvent where the chain size is smaller than the ideal chain (polymer chain with no excluded volume interactions). The total excluded volume interactions between monomers

$U_{\mathrm{ex}}(\{\mathbf{R}_\alpha(s)\})$ then can be expressed as [36, 37],

$$\beta U_{\mathrm{ex}}(\{\mathbf{R}_\alpha(s)\}) = \frac{v}{2}\sum_{i=0}^{\infty}\sum_{j=0}^{\infty}\int_0^1 ds \int_0^1 ds' \delta[\mathbf{R}_i(s) - \mathbf{R}_j(s')], \tag{2.18}$$

If we define microscopic monomer density $\hat{\rho}(\mathbf{r})$ as,

$$\hat{\rho}(\mathbf{r}) = \sum_{\alpha=0}^{\infty}\int_0^1 ds \delta(\mathbf{r} - \mathbf{R}_\alpha(s)), \tag{2.19}$$

then βU_{ex} can be equivalently expressed as,

$$\beta U_{\mathrm{ex}}(\{\hat{\rho}(\mathbf{r})\}) = \frac{v}{2}\hat{\rho}^2(\mathbf{r}), \tag{2.20}$$

In the grand canonical framework, the partition function of the polymer solution can be expressed as:

$$\Xi(z_p, V, T) = \sum_{m=0}^{\infty}\frac{z_p^m}{m!}\int\prod_{\alpha=1}^{m} d\mathbf{R}_\alpha(s)\exp[-U_{\mathrm{elastic}}(\{\mathbf{R}_\alpha(s)\}) - U_{\mathrm{ex}}(\{\hat{\rho}(\mathbf{r})\})]. \tag{2.21}$$

In order to proceed we introduce functional integrals over delta functions,

$$1 = \int D\{\rho\}\delta(\rho - \hat{\rho}) = \int D\{\rho\}\int_{-i\infty}^{+i\infty} D\{w\}\exp[w(\mathbf{r})(\rho(\mathbf{r}) - \hat{\rho}(\mathbf{r}))] \tag{2.22}$$

where $w(\mathbf{r})$ denotes an imaginary auxiliary field. The partition function given by Eq. 2.21 can then be rewritten as,

$$\Xi(z_p, V, T) = \int D\{\rho\}\int_{-i\infty}^{+i\infty} D\{w\}\exp[-\beta F\{\rho(\mathbf{r}), w(\mathbf{r})\}]. \tag{2.23}$$

where,

$$\beta F\{\rho(\mathbf{r}), w(\mathbf{r})\} = \int d\mathbf{r}(\frac{v}{2}\rho^2(\mathbf{r}) - w(\mathbf{r})\rho(\mathbf{r})) - z_p Q\{w\}. \tag{2.24}$$

$Q\{w\}$ represents the partition function of a single chain moving in the field $w(\mathbf{r})$,

$$Q\{w\} = \frac{\int D\mathbf{R}\exp[-U_0 - \int_0^1 ds w(\mathbf{R}(s))]}{\int D\mathbf{R}\exp[-U_0]} \tag{2.25}$$

and is given by a Feynman-Kac formula as:

$$Q = \frac{1}{V}\int q(\mathbf{r}, s = 1)\, d\mathbf{r}, \tag{2.26}$$

where the field $q(\mathbf{r}, s)$ satisfies the diffusion equation [38, 39]:

$$\frac{\partial q(\mathbf{r}, s)}{\partial s} = \frac{Nb^2}{6}\nabla^2 q(\mathbf{r}, s) - w(\mathbf{r})q(\mathbf{r}, s); \qquad q(\mathbf{r}, s = 0) = 1. \tag{2.27}$$

The monomer density field $\rho(\mathbf{r})$ is then obtained from $q(\mathbf{r}, s)$ as

$$\rho(\mathbf{r}) = z_p \int_0^1 q(\mathbf{r}, s)q(\mathbf{r}, 1 - s)\, ds. \tag{2.28}$$

Similar field theories have been developed in many different contexts such as polymer solutions, block copolymers, and polymer blends. A number of analytical techniques such as perturbation expansions, renormalization-group theories, and field-theoretic simulations have been used to approximate the resulting integrals. In the present work, we use the mean-field approximation, commonly referred to in this context as self-consistent field theory (SCFT). Polymer self-consistent field theory corresponds to a saddle point approximation of the above field theory [38, 39]. First we perform a saddle point integration for Eq. 2.23 with respect to w. In this approximation the path integral over the potential field $w(\mathbf{r})$ is replaced by the value of the exponent evaluated at its saddle point:

$$\left.\frac{\partial F}{\partial w}\right|_{w^*} = 0 \tag{2.29}$$

which leads to,

$$\rho(\mathbf{r}) = -z_p \frac{\delta Q\{w\}}{\delta w} = \langle \hat{\rho}(\mathbf{r}) \rangle_{GC}. \tag{2.30}$$

The brackets $\langle \cdots \rangle_{GC}$ denote the statistical average taken in a grand canonical ensemble at fixed polymer activity z_p. The above saddle point approximation thus amounts to replacing the exact constraint $\rho(\mathbf{r}) = \hat{\rho}(\mathbf{r})$ by a more relaxed requirement $\rho(\mathbf{r}) = \langle \hat{\rho}(\mathbf{r}) \rangle_{GC}$ and the functions $w(\mathbf{r})$ can be interpreted as Lagrange parameters which enforce this condition. The partition function then reduces to,

$$\Xi(z_p, V, T) = \int D\{\rho\} \exp[-\beta F\{\rho(\mathbf{r}), w\{\rho(\mathbf{r})\}\}]. \tag{2.31}$$

Now we perform a second saddle point integration of Eq. 2.31 with respect to $\rho(\mathbf{r})$ to approximate the free energy as,

$$\beta F(z_p, V, T) = -\ln \Xi \approx F^{SCF} = \min\, F\{\rho^*(\mathbf{r}), w\{(\rho^*(\mathbf{r}))\}\}. \tag{2.32}$$

with the minimization equations given by,

$$\left. \frac{\partial F}{\partial \rho} \right|_{\rho^*} = 0 \tag{2.33}$$

which results in the self-consistency condition,

$$w(\mathbf{r}) = v\rho(\mathbf{r}). \tag{2.34}$$

On substituting Eq. 2.34 in Eq. 2.24 we obtain the free energy of the system as,

$$F[w(\mathbf{r})] = -\frac{1}{2v} \int d\mathbf{r}\, w^2(\mathbf{r}) + ZQ(w). \tag{2.35}$$

If we deduct a constant α from $w(\mathbf{r})$ ($w(\mathbf{r}) \to w(\mathbf{r}) + \alpha$) so as to subtract out the free energy corresponding to a homogeneous polymer solution, the above expression can be transformed as:

$$F[w(\mathbf{r})] = -\frac{1}{2B} \int d\mathbf{r}\, w^2 + \frac{\alpha}{B} \int d\mathbf{r} w + Z e^{-\alpha} Q(w) \tag{2.36}$$

where all length scales have been nondimensionalized by the R_g. The constants $B \equiv vN^2/R_\mathrm{g}^d$ and $Z \equiv z_p R_\mathrm{g}^d$ represent the nondimensional excluded volume parameter and the activity coefficient of the polymer solution. The constant α satisfies $\alpha = B\exp(-\alpha)$. The nondimensional homogeneous polymer solution density $C = \rho_p R_\mathrm{g}^d/N$ can be obtained in terms of Z as: $C = Z\exp(-\alpha)$.

The above formalism provides a mean-field approach to compute the grand canonical partition function Ξ as a function of the polymer chemical potential Z and the excluded volume parameter B. The above approach can be extended to compute $\Xi_1(Z, B)$ and $\Xi_2(\mathbf{R}_i, \mathbf{R}_j; Z, B)$. In the latter cases, the presence of the particles is accounted by imposing the potential $U_{cp}(r)$ in the single chain partition function $Q(w)$. This external potential can be transformed as a boundary condition imposed on the surface of the particles [40–42]. Computation of $\Xi_1(Z, B)$ and $\Xi_2(\mathbf{R}_i, \mathbf{R}_j; Z, B)$ then requires the solution of the self-consistent equations (2.27), (2.28) and (2.34) with the appropriate boundary conditions on the surface of the particles.

Similar SCFT based approaches have been used earlier as a fruitful approach to analyze the properties of interacting polymer solutions and melts [38, 40, 41, 43]. While SCFT is only a mean-field approach, nevertheless the qualitative, and in many cases, the quantitative features of semi-dilute polymer solutions can also be predicted by using such an approach. Most earlier applications have restricted this approach by either using it in conjunction with the ground-state dominance assumption (valid for $N \to \infty$) and/or by considering only the case of flat geometries [41]. However, even within the ground state dominance approach, the diffusion equation (2.27) does not admit an analytical solution for the case of a single sphere in a polymer solution and requires either further approximations [44] or a numerical solution [45]. In order to examine the pair interactions for a range of sizes, especially for regimes where the curvature of the particles proves crucial in determining the physics, we solve the diffusion equation (2.27) numerically [46]. This procedure is effected in spherical coordinates during the computation of $\Xi_1(Z, B)$ and in bispherical coordinates during the computation of $\Xi_2(\mathbf{R}_i, \mathbf{R}_j; Z, B)$.

The use of bispherical coordinate system for the case of pair interaction potentials is particularly advantageous as this coordinate system allows one to access a wide range of particle sizes without encountering any artifacts arising from geometrical discretization errors. The bispherical coordinates (η, θ, ϕ) can be obtained from applying the following coordinate transformation to the Cartesian coordinates (x, y, z):

$$x = \frac{a \sin\theta \cos\phi}{\cosh\eta - \cos\theta};\ y = \frac{a \sin\theta \sin\phi}{\cosh\eta - \cos\theta};\ z = \frac{a \sinh\eta}{\cosh\eta - \cos\theta} \tag{2.37}$$

where a is the distance from the origin, defined by $\eta = 0$ and $\theta = \pi$. The "infinity" in Cartesian coordinates is given in bispherical coordinates as

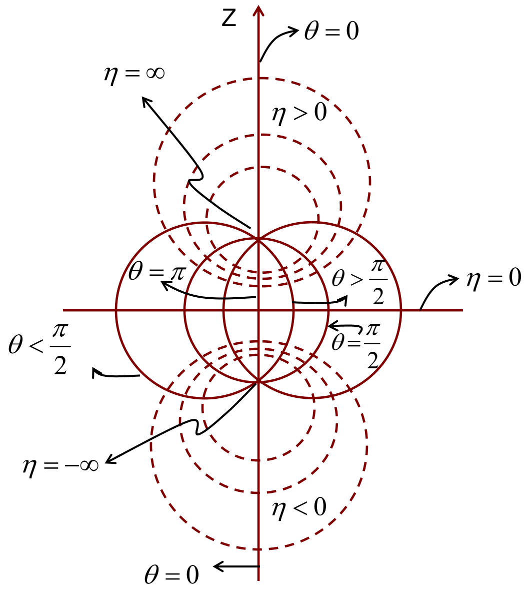

Figure 2.3: Schematic illustration for the bispherical coordinate system. The solid curves correspond to surfaces with constant θ where as broken curves represent surfaces with constant η. The line between the two poles,$\eta = \pm\infty$, has $\theta = \pi$. The z axis of the corresponding Cartesian coordinate system is given by $\theta = 0$ and $\theta = \pi$ in the bispherical coordinate system.

$\eta = 0$ and $\theta = 0$, while the $\eta = \pm\infty$ in bispherical coordinates is given in Cartesian coordinates as $z = a$. For the case of two spheres, specification of the radii of the two spheres R_1 and R_2 and the center-to-center distance between them uniquely defines the coordinate system. The Laplacian operator in the bispherical coordinates is given as,

$$\nabla^2 = \frac{1}{h_\eta^2}\left[\partial_\eta^2 - \frac{h_\eta}{a}(\sinh\eta)\partial_\eta - \partial_\theta^2 + \frac{h_\eta}{a}\frac{\cosh\eta\cos\theta - 1}{\sin\theta}\partial_\theta + \frac{1}{\sin_\theta^2\partial_\phi^2}\right] \tag{2.38}$$

where the scale factors are given as,

$$h_\eta = h_\theta = \frac{h_\phi}{\sin\theta} = \frac{a}{\cosh\eta - \cos\theta}. \tag{2.39}$$

Note that for the case of two spheres, the system is characterized by rotational symmetry and hence is ϕ independent. To solve the diffusion equation in bispherical coordinates [42], we employ a non-uniform $\eta - \theta$ grid generated using Fornberg's algorithm. We solve the resulting finite difference equations using an unconditionally stable alternating direction implicit (ADI) method [42].

2.3 Structural Conformations of Polymer Chains

Adsorbed polymer layers form a variety of interesting structures such as loops, dangling tails and interparticle bridges (as shown schematically in Fig 5.1). The conformations of these structures result from the competition between monomer-monomer interactions and elastic forces - the structures stretch away from the surface to exploit the relatively low density, this elongation is counterbalanced by elastic restoring forces of entropic origin [30, 47].

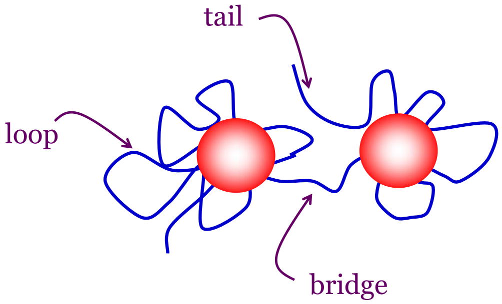

Figure 2.4: Structures of polymer on the particle surface. A loop is defined as the chain segments between two consecutive surface contacts, while a tail represents the segments of the polymer chain between the first/last surface contact and the chain ends. Polymer segments between consecutive surface contacts on two different particle surfaces constitute a polymer bridge.

Distribution of number and lengths of the polymer structures formed between the particles has attracted tremendous interest because of their effect on the rheology and mechanical properties of the polymer-particle mixtures. In this section, we extend the self consistent field approach to quantify the number and size distributions of bridges, loops and tails for reversibly adsorbed polymer. This information will be later utilized in Chapters 4 and 5 to predict clustering behavior and elastic properties of the polymer-particle mixtures.

For the case of adsorbing polymer, the polymers can be classified into being either adsorbed onto the particles or free in solution [48–50]. The former includes chains which have one or more contacts with the surfaces, while the latter incorporates the remainder. In this section, we propose a framework for quantification of loops, tails and bridges from the one point and two point propagators for a polymer chain. By restricting the chain propagators to appropriate positions in space, we obtain chain propagators for tails, loops and bridges between the surfaces. For instance, for the loop propagator, both the starting and end point of a chain propagator are restricted on the surface of same particle. From these propagators, we extract the density of the monomers in loops, tails and bridges and subsequently compute the number and size distributions of these structures.

We begin with the chain propagator $q(\mathbf{r}, s)$ defined in equation 2.27. The one point propagator $q(\mathbf{r}, s)$ gives the statistical weight for a polymer chain segment s to be at position $\mathbf{r}$ in space. For the case of adsorbing polymer, the specific interactions between the polymer segments and the particle surface are usually modeled through a short range attraction and the resultant boundary condition for this case becomes,

$$n.\nabla q(\mathbf{r}, s)|_{surface} = -w(\mathbf{r}) q(\mathbf{r}, s). \tag{2.40}$$

As our purpose here is only to present a general framework for characterization of adsorbed polymer layers in terms of the structural distribution, we defer the details of the polymer self consistent field theory for adsorbing polymer till Chapter 4. However, it should be noted that the boundary condition specified by Eq. 2.40 does not distinguish between different chain conformations and applies to both the adsorbed as well as free chains. Thus, $q(\mathbf{r}, s)$ represents the statistical weight for the "s" segment of a polymer chain to be at position $\mathbf{r}$ regardless of whether it touches the particle surface or not. The conformations of the *free chains* are then obtained by considering the statistical weight

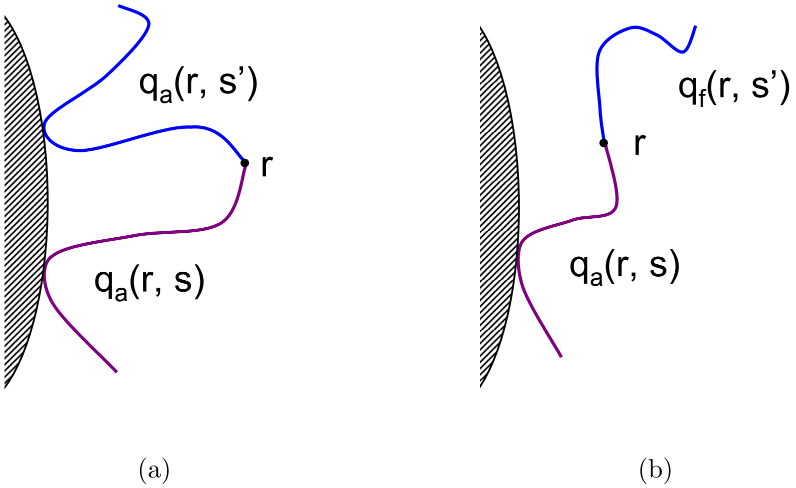

(a) (b)

Figure 2.5: Schematic showing different propagators (a) Loop, (b) Tail.

$q_{\mathrm{f}}(\mathbf{r}, s)$ of the polymer chains in the self-consistent potential field $w(r)$, where $q_{\mathrm{f}}(\mathbf{r}, s)$ satisfies the boundary condition: $q_{\mathrm{f}}(\mathbf{r}, s)|_R = 0$. Implementation of this 'zero' boundary condition excludes all the polymer conformations that touch the particle surface. The statistical weights of the *adsorbed polymer* conformations can be obtained as: $q_{\mathrm{a}}(\mathbf{r}, s) = q(\mathbf{r}, s) - q_{\mathrm{f}}(\mathbf{r}, s)$. This is equivalent to solving Eq. 2.27 for $q_{\mathrm{a}}(\mathbf{r}, s)$ with the 'initial' condition, $q_{\mathrm{a}}(\mathbf{r}, s = 0) = 0$, and the boundary condition, $q_{\mathrm{a}}(\mathbf{r}, s)|_R = q(\mathbf{r}, s)|_R$, where R represent the radius of particle. The volume fraction profile of the segments in adsorbed chains are then obtained by counting all the chains having at least one adsorbed segment [49]:

$$\phi_{\mathrm{ads}}(\mathbf{r}) \propto \int_0^1 q_{\mathrm{a}}(\mathbf{r}, s) q(\mathbf{r}, 1 - s)\, ds. \qquad (2.41)$$

For the case of adsorption on a single particle, an adsorbed polymer chain can be found in loop or tail conformations. A loop is defined as the chain segments between two consecutive surface contacts, while a tail represents the segments of the polymer chain between the first/last surface contact and the chain ends [48]. Using the statistical weights of the free and adsorbed chain conformations, the volume fraction of the segments belonging to tails and loops can be obtained as,

$$\begin{aligned} \phi_{\text{loop}}(\mathbf{r}) &= \int_0^1 q_{\text{a}}(\mathbf{r}, s) q_{\text{a}}(\mathbf{r}, 1-s)\, ds; \\ \phi_{\text{tail}}(\mathbf{r}) &= \int_0^1 q_{\text{a}}(\mathbf{r}, s) q_{\text{f}}(\mathbf{r}, 1-s)\, ds. \end{aligned} \tag{2.42}$$

In the above, the product $q_{\text{a}}(\mathbf{r}, s) q_{\text{a}}(\mathbf{r}, s')$ gives the statistical weight of a polymer segment s at a position $\mathbf{r}$ such that at least one of the first s segments is in contact with the surface and at least one of the last s' segments to be in contact with the surface. Similarly, $q_{\text{a}}(\mathbf{r}, s) q_{\text{f}}(\mathbf{r}, s')$ gives the statistical weight of an adsorbed chain section of length s to be connected with a free chain section of length s' at position $\mathbf{r}$ thus forming a tail.

In the case of two particles, the adsorbed chains can also form interparticle bridges [4]. A polymer bridge is defined as a chain segment whose consecutive surface contacts occur on different particles [50, 51]. To extract the volume fractions of monomers belonging to bridging conformations, we need the statistical weights of chains which are adsorbed on the surface of only one particle. We denote the chain propagator that gives the statistical weight of a chain adsorbed on only particle I as q_{a}^I. The $q_{\text{a}}^I(\mathbf{r}, s)$ is obtained by

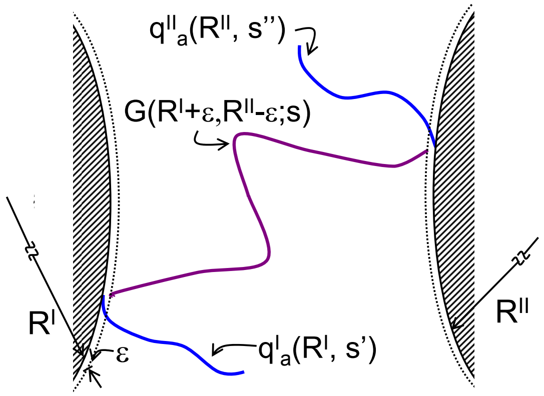

Figure 2.6: Schematic showing a bridging chain in terms of different chain propagators

solving Eq. 2.27 with the initial condition, $q^I_{\mathrm{a}}(\mathbf{r}, s=0) = 0$, and the boundary conditions, $q^I_{\mathrm{a}}(\mathbf{r}, s)\big|_{R_I} = q(\mathbf{r}, s)|_{R_I}$ and $q^I_{\mathrm{a}}(\mathbf{r}, s)\big|_{R_{II}} = 0$. Then, the bridging segment volume fraction can be expressed as,

$$\phi_{\mathrm{br}}(\mathbf{r}) = \int_0^1 q^I_{\mathrm{a}}(\mathbf{r}, s) q^{II}_{\mathrm{a}}(\mathbf{r}, 1-s)\, ds. \tag{2.43}$$

Equivalently, the bridging segment volume fractions $\phi_{\mathrm{br}}(\mathbf{r})$ can be expressed in terms of adsorbed, loop and tail volume fractions as: $\phi_{\mathrm{br}}(\mathbf{r}) = \phi_{\mathrm{ads}}(\mathbf{r}) - \phi_{\mathrm{loop}}(\mathbf{r}) - \phi_{\mathrm{tail}}(\mathbf{r})$.

Quantification of statistics of bridges in terms of average size and number distribution of bridges, requires computation of two point propagator. A two point propagator $G(\mathbf{r}, \mathbf{r}', s)$ embodies the statistical weight of a s segment polymer chain whose first and last segments are located at $\mathbf{r}$ and $\mathbf{r}'$, and satisfies the following equation and boundary conditions,

$$\frac{\partial G(\mathbf{r},\mathbf{r}^{'},s)}{\partial s} = \nabla^2 G(\mathbf{r},\mathbf{r}^{'},s) - w(\mathbf{r})G(\mathbf{r},\mathbf{r}^{'},s);\; G(\mathbf{r},\mathbf{r}^{'},0) = \delta(\mathbf{r}-\mathbf{r}^{'});$$
$$\text{and}\;\; G(\mathbf{r},\mathbf{r}^{'},s)\Big|_{\mathbf{r}=R^I,R^{II}} = 0. \quad (2.44)$$

The zero boundary condition in the above equation restricts $G(\mathbf{r},\mathbf{r}^{'},s)$ to only those chain configurations which do not touch the surfaces. In terms of the one and two point propagators, the statistical weight of a polymer chain to form a bridge of length s can be expressed as,

$$q_{\text{br}}(s) = \int d\mathbf{r} \int d\mathbf{r}^{'} \delta[\mathbf{r} - (R^I + \epsilon)]\delta[\mathbf{r}^{'} - (R^{II} - \epsilon)]\; G(\mathbf{r},\mathbf{r}^{'},s)$$
$$\times \int_0^{1-s} q^I(R^I,s^{'})q^{II}(R^{II},1-s-s^{'})\,ds^{'} \qquad (2.45)$$

where q^I and q^{II} are the statistical weights of polymer chains to be in contact with surfaces I and II respectively. In Eq. 2.45, the first integrals account for all the chain segments of length 's' which extend from surface I ($\mathbf{r} = R^I + \epsilon$) to the surface II ($\mathbf{r} = R^{II} - \epsilon$). Counting only those chain configurations which are within an infinitesimally small distance ϵ (*without actually touching the surfaces*) from both the surfaces I and II ensures that the loops and trains associated with the bridge are not counted in $q_{\text{br}}(s)$. The last integral in Eq. 2.45 is proportional to the probability that the remaining polymer chain of $(1-s)$ segments is in contact with surfaces I and II. Using q_{br}, the number of polymer segments in a bridge N_{br} can be obtained as,

$$N_{\text{br}}/N = \int_0^1 s\; \frac{q_{\text{br}}(s)}{\int_0^1 q_{\text{br}}(s')ds'} ds \qquad (2.46)$$

where N denotes the length of a polymer chain in terms of the total number of statistical segments. The average number of bridging chains can then be expressed in terms of the total number of monomers in the bridges ($\int_0^\infty \phi_{\mathrm{br}}(\mathbf{r})d\mathbf{r}$, where $\phi_{\mathrm{br}}(\mathbf{r})$ is the density of monomers in bridges (Eq. 2.43)) and the average size of the bridges N_{br} as,

$$M_{\mathrm{br}} = \frac{N}{N_{\mathrm{br}}} \int_0^\infty \phi_{\mathrm{br}}(\mathbf{r})d\mathbf{r}. \tag{2.47}$$

In Chapters 4 and 5, we use above derived number distribution of bridges to deduce the probability of formation of polymeric bridges between the particles and in turn, to gain insights into the clustering and structural characteristics, percolation transitions and elastic properties of polymer particle mixtures.

2.4 Summary

In summary, we have developed a generic multiscale approach to study the effect of polymer on the interparticle interactions, resultant phase behavior and structural features of polymer-particle mixtures. The size and length scale asymmetries encountered in such mixtures are addressed by coarse graining the polymeric component and by mapping the two component system in terms of an effective one component system consisting of just particles. The resultant one component system is characterized by *polymer mediated effective interactions*. To extract the latter, we have developed a mean field approach and implement a numerical version of polymer self consistent field theory in bispherical coordinates. The latter allows us to access a wide range of polymer and particle sizes, while simultaneously eliminating the artifacts arising from geometrical discretizations. Further we have extended the mean field theory to gain more insights into the configurational structure of adsorbed polymer layers in the vicinity of the particles. In the subsequent chapters, we adapt the above developed framework : (i) to examine the phase behavior and percolation characteristics for nano-sized particles in presence of nonadsorbing, adsorbing and grafted polymers (ii) to probe the polymer bridging induced gelation phenomena and (iii) to predict the structure and elastic properties of particulate gels.

Chapter 3

Nanoparticles in Presence of Non-adsorbing Polymers

Polymer induced depletion attraction between colloidal particles has been studied extensively for last three decades. Addition of particles to a solution of non-adsorbing polymers excludes the polymer centers from the vicinity of the particles. This reduction in the free volume available for the polymer results in a conformational entropy loss for the polymer. The resulting osmotic pressure imbalance for the polymer pushes the colloidal particles together (cf. Fig. 3.1), giving rise to an effective attraction between the two particles termed as 'depletion attraction.'

Asakura and Oosawa (AO) [1] and independently Vrij [2] were the first to quantify the depletion interaction and showed that this polymer mediated effective attraction between the particles is characterized by a range R_g (the radius of gyration of the polymers) and a strength proportional to the concentration of the polymers. The AO model is known to be adequate only for the case of *dilute and noninteracting* polymer solutions and only when R_{g} is much smaller than the size R of the particle, i.e. $R/R_{\mathrm{g}} \gg 1$ (this regime of sizes, $R/R_{\mathrm{g}} > 1$, is also commonly termed as the "colloid" limit) [12, 52–54].

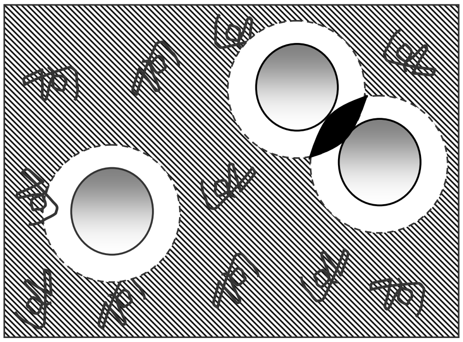

Figure 3.1: Schematic illustration of polymer depletion around a particle and free volume. Each particle is surrounded by a 'depletion zone', (shown in white) which is inaccessible to centers of polymer coils. The hatched area is the free volume V_{free} available for the polymer. Overlap of depletion zones (black) leads to increase in free volume for polymer resulting an 'effective' attraction between the particles.

Subsequent studies have examined the depletion characteristics in nanoparticle-polymer mixtures for situations where such conditions are not valid. For instance, Meijer and Frenkel [55] used a lattice simulation approach to analyze the case of dilute, ideal polymer solutions with smaller R/R_{g} values, and showed that multibody interactions between the particles can lead to significant corrections to the phase behavior predicted by the AO theory. Realizing the breakdown of AO theory for the regime $R/R_{\mathrm{g}} \leq O(1)$, Schweizer and coworkers [20, 53, 56, 57] have developed sophisticated integral equation approaches which incorporate the interactions between the polymers and can treat a wide range of polymer and particle sizes. Louis, Bolhuis and coworkers have used coarse-graining techniques to treat the case of interacting polymers for sizes R/R_{g} upto $O(1)$ [54, 58]. Both Schweizer and Louis's researches established the importance of interpolymer interactions, and also delineated the resulting phase behavior for a variety of parametric conditions. Lekkerkerker [21], Tuinier and coworkers [12, 22] have pioneered the Gibbs adsorption and free volume theories to develop the phase diagrams for mixtures of colloids of different geometrical shapes in both ideal and interacting polymer solutions.

The above-mentioned theoretical approaches in conjunction with systematic experimental studies of Zukoski, Pusey and coworkers [11, 59, 60] have led to a solid understanding of the physics behind the colloid ($R/R_{\mathrm{g}} \geq 1$) limit. However the other limit, $R/R_{\mathrm{g}} > 1$ (commonly termed as the "protein/nanoparticle" limit) is also of significant interest. Such situations arise in relation to protein crystallization applications [19, 61], separation of proteins using polymers [62, 63], and in experimental studies of protein aggregation, stability using inert polymers such as PEG and Dextran [64]. In such contexts, experiments have shown that depletion effects can be used to rationally control the physicochemical properties of the protein solutions. For instance, tuning the strengths and the ranges of polymer-induced effective interactions between proteins has been suggested as an approach to control the rates of crystal-nucleation in protein solutions [19, 65]. Moreover, many *in-vitro* experiments have demonstrated that the same characteristics of inter-protein interactions can be used as a means to control the aggregation rates of proteins [64]. In other contexts, the size dependence of the solvation free energies has been used to control the solubility and the stability of the proteins [66–68].

Some previous theoretical studies have also examined the depletion characteristics of protein-polymer mixtures. For such systems in semidilute and concentrated polymer solutions (the case of interest in this study), the radius of gyration of the polymer is expected to be irrelevant in determining the interaction characteristics. Rather, a new length scale ξ corresponding to the polymer correlation length emerges. One of the widely studied issues in the protein limit (i.e. $R_{\mathrm{g}}/R < 1$) is the macroscopic phase behavior of the protein-polymer mixture. Early scaling arguments by deGennes [69] and more quantitative calculations of Eisenriegler [70] showed that the insertion free energy βF_s of a nonadsorbing sphere of size R into an athermal semi-dilute polymer solution scales as

$$\beta F_s \sim (R/\xi)^{3-1/\nu}, \tag{3.1}$$

where ν denotes the Flory exponent of the polymer (= 0.59 in three dimensions [40]). This suggests that $\beta F_s \ll 1$ for $R \ll \xi$, leading deGennes [69], and later Odijk [71], to conclude that the polymer depletion induced inter-protein interactions are weak and that protein-polymer mixtures tend to be miscible. On the other hand, it is well known from many experiments that polymer-protein solutions tend to demix and phase separate. To explain these observations, Odijk [71] (and Sear [72]) used simple theories to suggest that a poor solvent for the polymer may facilitate phase separation. Schweizer and coworkers [53, 73] have proposed that subtle effects on polymer-polymer interactions can rationalize the phase behavior of such systems. Bolhuis *et al.* used a lattice simulation approach and implicated multibody interaction effects as responsible for the phase behavior of proteins in nondilute polymer solutions [23]. Also, alternative approaches invoking perturbation theories [74], cell models [24] and free volume concepts [22] have all been used to predict that protein-polymer mixtures can indeed show a liquid-gas like phase separation.

This chapter examines the single and two-body depletion characteristics of protein-polymer mixtures. Some of the interesting questions in this context are: "Why would dilute proteins aggregate or precipitate out from concentrated polymer solutions ?," "Does one need to invoke multibody interactions to explain the phase behavior of protein-polymer mixtures ?," "Is solvent quality necessary to explain the phase behavior ?," "Are specific interactions between proteins and polymers a necessity to account for the observations ?"

The rest of this chapter is arranged in the following manner: Section 3.1 outlines the statistical mechanical model for polymers and proteins and the formalism whereby the depletion characteristics can be computed. In section 3.2, we explain our hypothesis regarding free volume and propose a model for incorporating the effect of multibody interactions. We examine the depletion thickness, free volumes and the effective concentrations to demonstrate that the effective concentrations fall in the semidilute and concentrated regimes. Section 3.3 concerns with the concentration dependence of the solvation free energies. In section 3.4, we present the qualitative and quantitative features of the pair interactions and their implications for the thermodynamics of the protein-polymer mixture. The chapter concludes with a summary of the results and an outlook on future applications of the formalism used.

3.1 Theoretical Formalism

The physical details of the model for the protein-polymer mixture are similar to that expounded in Chapter 2. In the following, we discuss the changes in the generalized polymer field theory pertinent to the non-adsorbing polymers and depletion interactions. Our approach is based on the hypothesis that the thermodynamical characteristics of the system are independent of the ensemble used to study it. Whence, the depletion characteristics of proteins in a polymer solution at an overall concentration ϕ_p^B with a concentration η_c of proteins can be mapped onto the *infinite* dilution depletion and interaction characteristics in a polymer solution whose fugacity is fixed at the value z_p corresponding to the fugacity of the polymer in the polymer-protein mixture. For non-adsorbing polymer, the exclusion of polymer near the particle surface is expressed through 'depletion' boundary condition for the diffusion equation (cf. Eq. 2.27),

$$q(\mathbf{r}, s)|_{surface} = 0. \tag{3.2}$$

Following the procedure detailed in the Chapter 2, the saddle point approximation results the self consistency condition:

$$w(\mathbf{r}) = \alpha[\phi(\mathbf{r}) - 1], \tag{3.3}$$

where the volume fraction field $\phi(\mathbf{r})$ is obtained using Eq. 2.28. In this approximation, the Grand canonical partition function can be written as:

$$\ln \Xi - \ln \Xi_0(Z, V, T) = -\frac{1}{2B} \int dr\, (w)^2 + \frac{\alpha}{B} \int drw + Ze^{-\alpha} Q(w). \tag{3.4}$$

where $\ln \Xi_0(Z, V, T)$ represents the mean-field free energy of a homogeneous polymer solution. The nondimensional homogeneous polymer solution density $C = \rho_p R_{g0}^d / N$ can be obtained in terms of Z as: $C = Z \exp(-\alpha)$. Computation of $\Xi_1(Z, B)$ and $\Xi_2(\mathbf{r}_i, \mathbf{r}_j; Z, B)$ is achieved by solving the self-consistent equations (2.27) – (2.28) numerically: in spherical coordinates during the computation of $\Xi_1(Z, B)$ and in bispherical coordinates during the computation of $\Xi_2(\mathbf{r}_i, \mathbf{r}_j; Z, B)$. To solve the diffusion equation in bispherical coordinates [42], a nonuniform $\eta - \theta$ grid is employed with Δs of 0.001, $N_\eta^+ = N_\eta^- = 100$ and $N_\theta = 100$. The tolerance on maximum difference in mean field potential $w(r)$ was 0.0001. About 500-700 iterations were required to satisfy this convergence criterion, giving an accuracy of $\sim$ 0.00001 in free energy values.

3.1.1 Model Parameters and Relationship to Experimental Variables

The polymer solution model used corresponds to the classical two-parameter model used widely in polymer physics literature. The mean field approximation detailed in the previous chapter neglects the contributions other than those arising from the saddle point of the integral in eq. (2.23). Physically, this approximation is known to be qualitatively accurate, but manifests as quantitatively incorrect scaling exponents and concentration dependencies of the polymer solution properties when compared with the experiments [40]. Consequently, it is expected that the formulation expounded in the preceding section can predict the qualitative trends, one cannot use it to predict the quantitative behavior of the depletion characteristics, interparticle interactions, virial coefficients etc. To overcome this limitation, a physically motivated approach is used which deduces the parameters in the mean-field model based on the appropriate physical properties of the polymer solution for which the depletion characteristics are desired.

The polymer model explained in Chapter 2 is characterized by two nondimensional parameters, B and Z. The former quantifies the solvent quality while the latter in turn determines the nondimensional polymer density C. *To make predictions and enable a comparison with experimentally realizable systems, the parameters B and Z are chosen such that the mean-field correlation lengths and the osmotic pressures match the respective values for a semidilute solution at a density ρ_p.* The latter rescalings also rescale the solvation free energies and the pair potentials deduced from our field-theoretic approach. This approach is similar in spirit to the scaling approach proposed by deGennes to modify the mean-field expressions for the free energy of a polymer solution [41]. To implement this idea, the published expressions for the correlation length (ξ) and the osmotic pressure (Π) of a semidilute solution are used to determine B and Z corresponding to a given ρ_p [75]. These expressions relate the correlation length and the osmotic pressure to polymer concentration, ϕ_p:

$$\frac{3}{4\pi}\frac{\delta(\beta\Pi_{\mathrm{s}})}{\delta\phi_{\mathrm{p,s}}} = 1 + 2.63\phi_{\mathrm{p,s}}\left(\frac{1+3.25\phi_{\mathrm{p,s}}+4.15\phi_{\mathrm{p,s}}^2}{1+1.48\phi_{\mathrm{p,s}}}\right)^{0.309} \quad ; \quad \text{and} \quad \xi_{\mathrm{s}} \propto \phi_{\mathrm{p,s}}^{-3/4} \tag{3.5}$$

where $\phi_{\mathrm{p,s}} = 4\pi R_{\mathrm{g}}^3 C_{\mathrm{p,s}}/3$ and subscript s indicates semidilute regime. In the present formalism, the mean field osmotic pressure can be obtained from the grand partition function (see Eq. 2.35) as

$$\beta\Pi_{\mathrm{m}} = \ln \Xi = \frac{BC^2}{2} \quad \text{with } C = \frac{4\pi R_{\mathrm{g}}^3 \phi_{\mathrm{p,m}}}{3} \tag{3.6}$$

The mean field correlation length ξ_{m} is related to the non-dimensional excluded volume parameter B and polymer concentration C as,

$$\xi_{\mathrm{m}}^2 = \frac{3}{2BC} \tag{3.7}$$

Comparing Eqs. 3.5, 3.6 and 3.7 to the leading order we obtain scaling relations between the mean field parameters B and C and semidilute concentration C_{s} as,

$$C \propto C_{\mathrm{s}}^{0.809} \text{ and } B \propto C_{\mathrm{s}}^{0.691} \tag{3.8}$$

The above scaling approach will still not yield the correct exponents characterizing the renormalized field theory (which requires a local scaling approach, rather than the global scaling used). Moreover, by fixing both the B and Z parameters at finite values, in reality only the “good” but not “athermal” solvent regime of the polymer solution is accessed (see section 3.4.3 for a further discussion of this point). However, despite these limitations, this scaling approach can be expected to yield semi-quantitatively accurate results for the depletion thicknesses and the interaction potentials when compared with more rigorous implementations of the field theory. In principle, by using this approach one can also address the effect of solvent quality on the depletion characteristics. However, the majority of this chapter (except in section 3.4.3) focuses only on the results for athermal solutions. In the following, we present the results obtained by this scaled mean-field theory as a function of $\phi_p = \rho_p/\rho_p^*$.

3.2 Depletion Profiles and Thickness

The polymer fugacity z_p depends on both the overall polymer density ϕ_p^B and the concentration of proteins η_c. Whence, to discuss the depletion characteristics at a fixed ϕ_p^B and η_c, one needs a framework to obtain the z_p corresponding to those conditions. Here the density of a homogeneous polymer solution (in the absence of proteins) with the fugacity coefficient at a value z_p is denoted as ϕ_p. In essence, ϕ_p is viewed as the effective or local polymer concentration determining the depletion characteristics, and corresponds to the density of a pure polymer solution in a reservoir in equilibrium with the protein-polymer mixture. The basis underlying this work is that, in the protein limit, that the depletion thickness Δ is much larger than the size of the proteins. Consequently, even for conditions corresponding to dilute or semidilute polymer concentrations ϕ_p^B, the effective concentrations ϕ (corresponding to the number of polymers in the free volume) and fugacities z_p that determine the depletion and interaction characteristics correspond to the semidilute or concentrated solutions of the polymer. The first issue addressed in this section pertains to the magnitude of the depletion thickness Δ in the protein limit.

Current theories do not all agree on the behavior of the depletion thickness Δ for proteins in semidilute and concentrated polymer solutions. In the limit when $R/\xi \gg 1$ (which is termed here as the Protein-Colloid (PC) limit in analogy to the colloidal suspensions), almost all theories acknowledge that the depletion thickness should be proportional to ξ [52, 53]. However, there have been conflicting predictions about the depletion thickness in the limit $R/\xi \ll 1$

(which we term as the Protein-Protein (PP) limit in relation to the physics of protein suspensions). Using approximate analytical methods, deGennes [69] and Odijk [71] suggest that in the extreme PP limit ($R/\xi \ll 1$), the relevant length scale for the polymer depletion is the radius of the particle R itself. On the other hand, Schweizer and Fuchs used an integral equation approach to suggest that the polymer density profiles exhibit two length scales, one of which is a long ranged depletion at the length scale of ξ itself [53]. More recently, Fleer *et al.* [45] proposed an analytical approximation that predicts a depletion thickness that is intermediate between these values and scales as $\xi^{2/3}R^{1/3}$.

Fig. 3.2 displays the volume fraction profiles $\phi(r)$ around a single protein sphere plotted as a function of the distance r from the surface (normalized as r/ξ). The volume fractions, $\phi(r)$ were obtained from the numerical solution of polymer SCFT around a single protein sphere. The bulk polymer density was maintained at $\phi_p = 2.6$, and the radii of the proteins were chosen to span the R/ξ values corresponding to the PP and PC limits. As is evident from the results, all the volume fraction profiles vanish at the surface of the sphere and asymptote to their bulk values within a distance of about 3ξ. Also plotted in Fig. 2.1 are the results corresponding to the polymer density profile near a flat plate (denoted as $R/\xi = \infty$). It can be seen that for asymptotic values in the PC limit ($R/\xi \gg 1$), the polymer density profiles quantitatively match with the results corresponding to the flat plate.

Interestingly, it can be seen from Fig. 3.2 that the polymer depletion

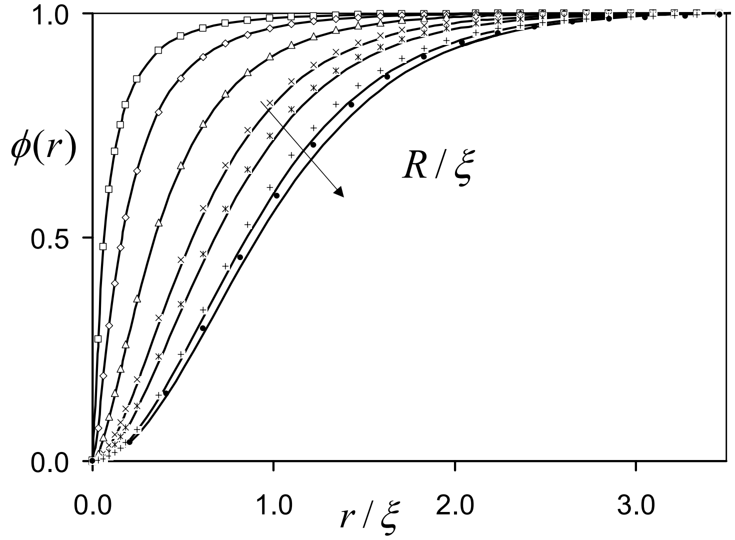

Figure 3.2: Polymer depletion profiles around a sphere. $\phi(r)$ denotes the volume fraction and r represents the distance from the surface of the sphere. Depletion profiles for different R/ξ plotted as a function of r/ξ. In the direction of increasing R/ξ, the different results correspond to $R/\xi = 0.03, 0.1, 0.33, 1, 2, 10$ and ∞. The solid curves correspond to an extrapolation formula proposed in Ref. [76] which displays an extremely good fit to our data.

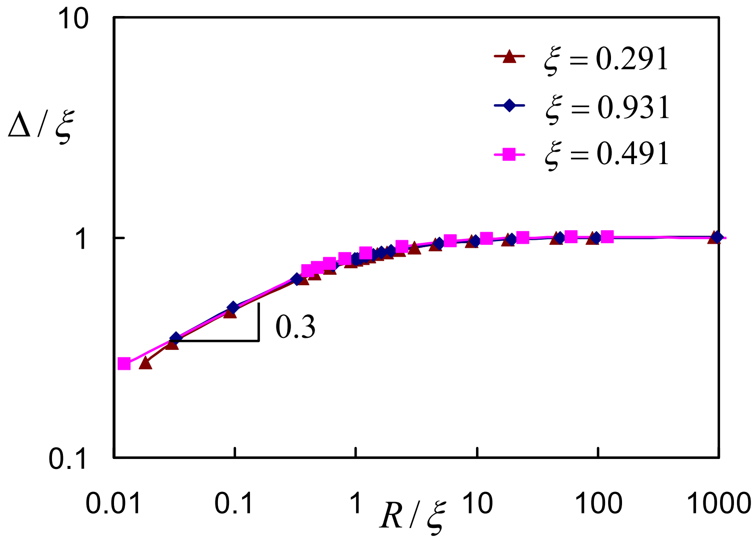

Figure 3.3: Depletion thickness Δ (normalized by ξ) plotted as a function of R/ξ

profiles in the PP regime do show that with a decrease in the ratio R/ξ, the density profiles move closer to the particle surface, followed by a longer range decay. The latter qualitatively resembles the predictions of integral equation approaches [53], and is indicative of possibly a new length scale governing the polymer depletion profiles. The length scale corresponding to the polymer depletion is quantified in terms of an overall depletion thickness Δ defined as the equivalent radius of a shell over which a step function profile for the polymer density would be depleted [22, 45]. In other words,

$$\frac{4\pi}{3}[(R+\Delta)^3 - R^3] = 4\pi \int_R^\infty dr\, r^2[\phi(r) - 1]. \tag{3.9}$$

Shown in Fig. 3.3 is a plot of Δ/ξ computed from the volume fraction profiles displayed as a function of R/ξ. It can be seen that in the PC limit ($R/\xi > 1$), Δ/ξ remains at the value unity, thereby confirming that the depletion thickness is indeed the correlation length of the polymer solution. On the other hand, in the PP limit Δ/ξ monotonically decreases with R/ξ, suggesting the emergence of a new length scale other than ξ. To extract this length scale and the depletion thickness, the asymptotic values in the PP limit are fitted to a power law fit. The latter yields a slope of 0.3, suggesting that in PP limit $\Delta/\xi \simeq (R/\xi)^{0.3}$ or $\Delta \sim R^{0.3}\xi^{0.7}$. The latter result is in remarkable agreement with the recent analytical predictions of Fleer*et al.* [45] but is much larger than the asymptotic approaches [71].

The above results indicate that in the PP limit, the overall depletion thickness Δ is much larger than the size of the proteins, i. e. $\Delta/R \gg 1$.

Whence, at a finite concentration of proteins, the overall depleted volume is expected to be significant, and the effective concentrations ϕ_p will be much larger than the actual concentrations ϕ_p^B. Further, in combination with the McMillan-Mayer framework, the above reasoning suggests that a key to understanding the thermodynamical characteristics of the protein-polymer mixtures is to understand the depletion and interaction characteristics at these effective concentrations ϕ_p. To make progress in this idea, first the difference between the "actual" and the "effective" concentrations is defined through,

$$\phi_p = \frac{\phi_p^B}{\alpha}, \tag{3.10}$$

where α represents the *fractional free volume available to the polymers* [12, 21]. Here, α is a function of both ϕ_p^B and η_c, and represents the reduction in the volume available for the polymers due to the depletion around the proteins. In the next section a model for $\alpha(\phi_p^B, \eta_c)$ in eq. (3.10) is postulated which allows estimation of the "effective concentrations" ϕ_p corresponding to a given bulk concentration ϕ_p^B and η_c. A more rigorous approach, accurate to the level at which the depletion and interaction characteristics are described, would be to determine $\alpha(\phi_p^B, \eta_c)$ from the one and two body depletion results presented in the following sections. However, since $\Delta/R \gg 1$, multibody overlaps of depletion layers, which become important for packing fractions $\eta_c \Delta^3/R^3 \simeq 1$, occur at relatively low concentrations of the proteins. Whence, a simpler approach is adopted wherein a model for $\alpha(\phi_p^B, \eta_c)$ is devised which will not match with the one- and two-body level approximation, but approximately accounts for the multibody interactions and overlaps between the different proteins.

3.2.1 Model For Free Volume

As shown later in this section, for a wide range of protein sizes and average polymer concentrations ϕ_p^B, the effective concentrations ϕ_p which determine the depletion characteristics fall in the semidilute and concentrated regimes. In these regimes, the radius of the gyration of the polymers $R_{\rm g}$ is irrelevant, but the interactions and the overlap between the polymers play an important role in determining the depletion characteristics. To model the free volume available for the polymer, an approach similar to that used earlier by Lekkerkerker, Tuinier and coworkers [12] is adopted. In this model, the polymers are visualized as spheres of radius equal to the depletion thickness Δ, and then the free volume α is approximated as the volume available for inserting a sphere of radius Δ in the protein solvent. Scaled-particle theory [21, 77] provides an approximate expression for the free volume available for the insertion of a sphere of radius Δ in the hard sphere (protein) solvent of size R at a packing fraction η_c:

$$\alpha(\phi_p^B, \eta_c) \approx (1 - \eta_c) \exp[-\hat{A}\gamma - \hat{B}\gamma^2 - \hat{C}\gamma^3]. \tag{3.11}$$

In the above equation, $\gamma = \eta_c/(1 - \eta_c), \hat{A} = 3\beta + 3\beta^2 + \beta^3, \hat{B} = 9\beta^2/2 + 3\beta^3, \hat{C} = 3\beta^3$, with $\beta = \Delta/R$. It should be noted that for a given average polymer and protein concentrations ϕ_p^B and η_c, Δ itself depends on the effective concentration ϕ_p and hence also upon the free volume α. Whence, the above equation for the free volume α needs self-consistent solution for the value of α corresponding to a given ϕ_p^B and η_c.

Equations (3.10) and (3.11) provide a complete set of equations to map the depletion characteristics of a protein-polymer mixture at a specified overall concentration ϕ_p^B and η_c onto the *infinite dilution* depletion and interaction characteristics of the proteins in a polymer solution maintained at an activity coefficient z_p. In the subsequent sections, ϕ_p is termed as the "effective concentration" determining the depletion and interaction characteristics of the proteins. A key aspect of the present model is the self-consistent manner by which ϕ_p is determined for a given ϕ_p^B and η_c. It should be noted that the above provides just a specific model, and alternative models for the free volume α can also be combined with the results of the subsequent sections to study the polymer depletion and the thermodynamic characteristics of protein-polymer mixtures. Despite the inherent approximations, the above model has some attractive features preserving the physics of the problem. By viewing the polymers as spheres of radius equal to the depletion thickness, the above model accounts for both the interactions between the polymers as well as the nonzero concentration of the polymers. On the other hand, for real hard sphere solutes, the depletion thickness near a hard sphere solvent matches exactly with the correlation length of the solutes [35, 78]. As shown in the next section, for a range of polymer concentrations ϕ_p^B of interest in this study, the depletion thickness Δ is of the same order of magnitude as the correlation length ξ of the polymer solution. The latter suggests *a posteriorly* the consistency of viewing the polymer solution as spheres of size Δ. Also, the above approach provides an attractive way to study the real "multibody" effects arising from simultaneous interactions of all the protein spheres. Alternative methods such as studying the three-body interactions reveal only a part of this effect.

3.2.2 Effective Concentrations

The above model for free volume results in two important outcomes. The first aspect pertains to the magnitudes and the regimes of the effective concentrations ϕ_p corresponding to different bulk concentrations ϕ_p^B. Fig. 3.4a displays the ϕ_p for a protein of size ratio $q = 10$ (where q is defined as $q = R_{\rm g} = R$) for different conditions of bulk polymer and protein concentrations ϕ_p^B and η_c. To maintain a close connection with the experimental results, only conditions at the border between dilute and semidilute concentrations of bulk polymer solution (i. e. $\phi_p^B \simeq O(1)$) are considered. It can be observed that over the entire range of bulk concentrations in the dilute regime, the effective concentrations fall in the semidilute and concentrated regimes (i. e. $\phi_p > 1$). For instance, for conditions corresponding to $\phi_p^B = 0.1$ and $\eta_c = 0.05$, corresponding to a dilute suspension of proteins in a dilute polymer solution, the effective concentrations that determine the depletion characteristics correspond to a concentrated polymer solution of $\phi_p \simeq 5$. Furthermore, it is also evident that significant changes in ϕ_p can result from changes in the protein and polymer concentration. The depletion characteristics in semidilute polymer solutions can be quite different

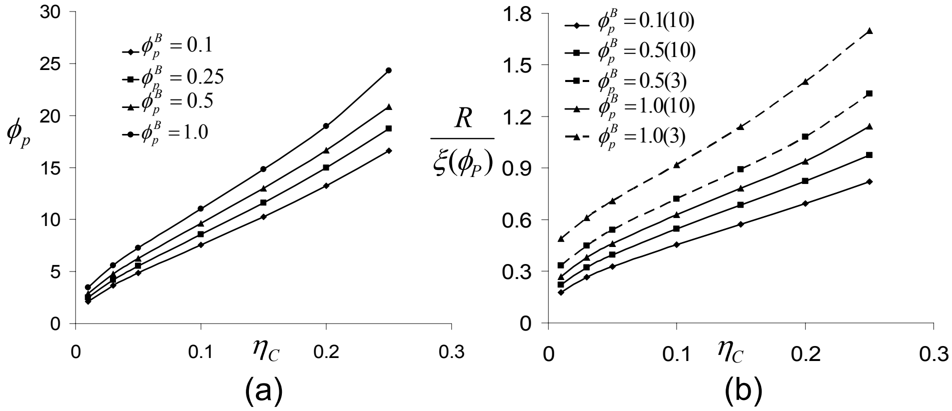

Figure 3.4: (a) The effective polymer concentrations ϕ_p as a function of the protein volume fraction η_c. ϕ_p^B's are the bulk polymer concentrations. The nondimensionalized protein size was fixed $q = R_\mathrm{g}/R = 10$; (b) The ratio $R/\xi(\phi_p)$ for different bulk concentrations ϕ_p^B. The solid lines represent the results for $q = 10$ while the dashed lines represent the results for $q = 3.0$ (also indicated in the brackets of the legend).

from those expected in the context of dilute polymer solutions. As will be shown in the next section, due to the interplay between the protein size and the polymer concentrations, one can have qualitatively distinct regimes even within the semidilute concentrations. This fact, in combination with the dependencies of ϕ_p upon ϕ_p^B and η_c will be shown to be crucial in rationalizing the thermodynamical characteristics of protein-polymer mixtures.

The second aspect pertains to the fact that previous theoretical studies in semidilute polymer solutions have mainly addressed the depletion characteristics in the asymptotic limits $R/\xi \ll 1$ and $R/\xi \gg 1$, where ξ denotes the correlation length of the polymer solution. Fig. 3.4b displays the values of R/ξ

for different concentrations of the protein and polymers and for protein sizes corresponding to $q = R_{\rm g}/R = 3.0$ and $q = 10$, where ξ denotes the correlation length corresponding to the effective concentration ϕ_p. It can be seen that over a wide range of protein and polymer concentrations chosen in the present study, the effective concentrations which determine the depletion characteristics actually correspond to $R/\xi \simeq O(1)$. Another interesting aspect is that changes in both ϕ_p^B and η_c concentration can lead to changes in the regime of R/ξ controlling the depletion characteristics. In the subsequent sections it will be demonstrated that the depletion characteristics resulting from the crossover effects in these nonasymptotic regimes can prove important for the thermodynamics of protein-polymer mixture.

To summarize, our results suggest that in the protein limit, even at dilute bulk concentrations ϕ_p^B of the polymer, the effective concentrations ϕ_p determining the depletion characteristics are much larger and are in the semidilute and/concentrated regimes. Furthermore, the magnitude of the ratio of the protein size to the correlation length corresponding to the effective concentration falls in the regime $R/\xi \simeq O(1)$. Asymptotic theories corresponding to $R/\xi \ll 1$, can be expected to hold only for protein sizes $R/R_{\rm g} \ll 1$. While the above conclusions were based on a specific model for the free volume effects, we believe that the qualitative features are generic to the protein limit. In the following sections, the depletion and interaction characteristics of proteins are examined while specifically focusing on the regime $R/\xi \simeq O(1)$ and it is shown that nontrivial crossover characteristics can manifest and have important implications for the phase behavior of protein polymer mixtures. It should also be noted that the scaling result for Δ in the PP limit taken together with the fact that interest of this study lies in the regime $R/\xi \simeq O(1)$, suggests that the disparities between the depletion thickness Δ and ξ are not significant. The latter thereby provides consistency to the present framework for the free volume which views the polymer solution as hard spheres of size Δ.

3.3 Insertion Free Energies

In this section, we discussed the results for the insertion free energies F_C^1 of proteins into semidilute and concentrated polymer solutions. The objective is to analyze the dependence of F_C^1 on the ratio R/ξ, and the qualitative features resulting from the crossover from $R/\xi < 1$ to $R/\xi > 1$. The focus is on the case of dilute protein solutions ($\eta_c \rightarrow 0$), and by considering the polymer concentration dependence of F_C^1, it is demonstrated below that qualitatively and quantitatively distinct regimes can occur even within the semidilute concentrations of the polymer. These features indicate the new effects that can result from changes in the effective concentration ϕ_p due to changes in ϕ_p^B and η_c. We further show that this results from the crossover behavior between the regimes $R/\xi < 1$ and $R/\xi > 1$. The concept of insertion free energies and their size dependencies are commonly invoked to explain the effect macromolecular solutes have upon the stability, denaturation and solubility of proteins [66, 79]. The results presented below incorporate both the polymer concentrations and their interactions in a rigorous manner and could

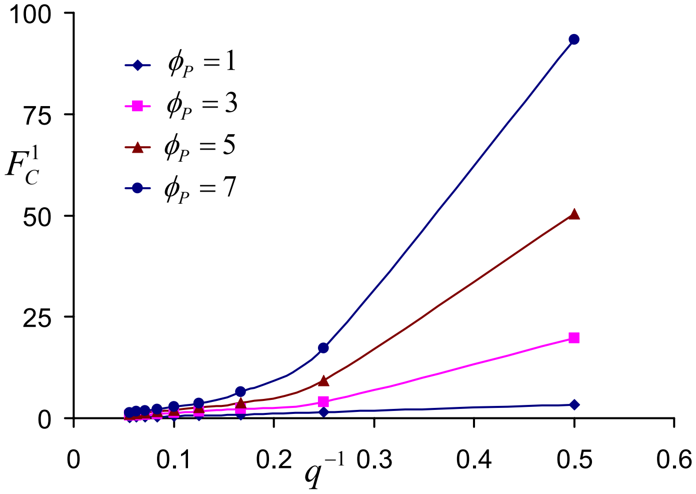

Figure 3.5: Insertion free energies F_C^1 as a function of nondimensionalized protein sizes q^{-1} for different polymer concentrations ϕ_p.

have important ramifications for macromolecular crowding experiments in the limit considered in this section (i.e. concentrated polymers + dilute proteins).

In Fig. 3.5 we display the insertion free energies F_C^1 computed using eq. (2.9) for a range of nondimensionalized sizes of the protein and for four different polymer concentrations within the semidilute regime. It can be seen that the magnitudes of the insertion free energies are relatively small for small proteins and/or for concentrations close to overlap concentration ($\phi = 1$). The latter is consistent with the scaling predictions embodied in (3.1) which suggests $F_c^1 \lesssim O(k_B T)$ in this regime. With an increase in the polymer concentrations ϕ_p, the magnitudes of F_c^1 for smaller proteins are observed to be unaffected, while those corresponding to the larger proteins grow to signif-

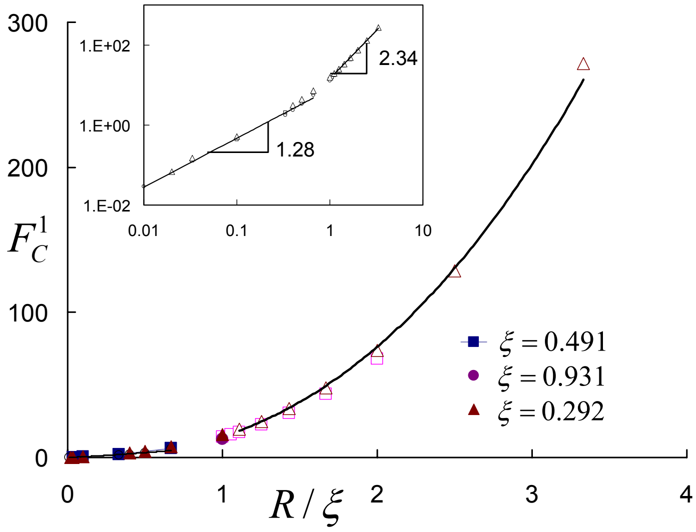

Figure 3.6: Insertion free energies F_C^1 as a function of R/ξ. Inset depicts the same results in a log-log scale.

icantly larger values compared to k_BT. Moreover, with increasing polymer concentrations, the transition from $F_c^1 \sim O(k_BT)$ to $F_c^1 \gg O(k_BT)$ continuously moves towards the smaller sized proteins.

Since the only effect of increasing the polymer concentration is to decrease its correlation length ξ (which in turn affects the osmotic pressure etc.), it is interesting to first probe if indeed the above results can all be collapsed onto a universal function of the ratio R/ξ. In Fig. 3.6 we display the insertion free energies for a range of polymer concentrations within the semidilute regime. It is evident that the insertion free energies do collapse onto a single universal function, with the transition between the small ($F_C^1 \sim O(k_BT)$) and large protein ($F_c^1 \gg O(k_BT)$) limits occurring at sizes such that $R/\xi \simeq 0.5 - 0.6$. In this framework, the concentration dependencies can be explained by reasoning that for small proteins and/or for small polymer concentrations, the protein radii are such that $R \leq \xi$. In this limit, eq. (3.1) should be applicable, and hence $F_C^1 \sim O(k_B T)$. However, larger proteins and/or for higher concentrations fall in the regime for which $R \geq \xi$. In this regime, the insertion free energy is expected to be dominated by the work of evacuating the protein volume within the polymer solution. At these high concentrations of the polymer, the osmotic pressure against which this work is done, is also extremely large, leading to the result that $F_c^1 \gg O(k_B T)$. These expectations are confirmed in the inset to Fig. 3.6, where the variation of F_C^1 with the ratio R/ξ is displayed on a log-log format. As can be seen, in the limit $R < \xi$, the solvation free energies $F_c^1 \sim (R/\xi)^{1.28}$, which is close to the theoretical prediction [69, 70] of $F_c^1 \sim (R/\xi)^{1.33}$. In the limit $R/\xi > 1$, $F_c^1 \sim (R/\xi)^{2.4}$, which reflects the cross-over to the asymptotic regime where F_c^1 scales as R^3, the volume of the protein [41].

The above results have interesting consequences for the context of macromolecular crowding experiments. The concentration dependencies of the insertion costs suggest that an increase in the concentration of the polymer leads to a decrease in the solubility and eventual precipitation of the proteins. Also it is seen from Fig. 3.5 that the solubility limit of a protein depends sensitively on its size, and that smaller proteins precipitate out of polymer solutions at higher concentrations of the polymer solutions. Some such effects have been seen in some selected experiments using PEG as a crowding agent [80].

The above results also provide a first indication of the nontrivial effects that can arise from an increase in the concentration of the polymers. As evident from Fig. 3.4, the effective concentrations ϕ_p corresponding to a range of bulk concentrations ϕ_p^B fall around the regimes studied in this section. Whence, upon an increase in the concentration ϕ_p^B or of the proteins, one can expect to move from the regime $R/\xi < 1$ to the limit $R/\xi > 1$. This will lead to concomitant increases in the insertion free energy of the protein and its eventual precipitation. In the next section, we explore the consequences of these transitions upon the macroscopic thermodynamics of the protein-polymer mixture.

3.4 Pair Interactions and Phase Behavior

In this section, we analyze the qualitative and quantitative features of the pair interaction potentials obtained using the grand canonical framework discussed in section 3.1. The pair interaction potentials are obtained using eq. (2.15) by effecting numerical solution of polymer SCFT in bispherical coordinates. Consequently, the numerical results are expected to be quite accurate for the entire range of protein sizes including when they are comparable to the correlation length of the polymer. At the outset, the focus is on the qualitatively new features of the pair interactions arising as a result of the free volume effects at finite concentration of the proteins. We discuss these potentials in the framework of changes in the polymer and protein concentrations. Subsequently, these features and their dependencies upon the ratio R/ξ are examined to rationalize the observations. Our objective here is to discern

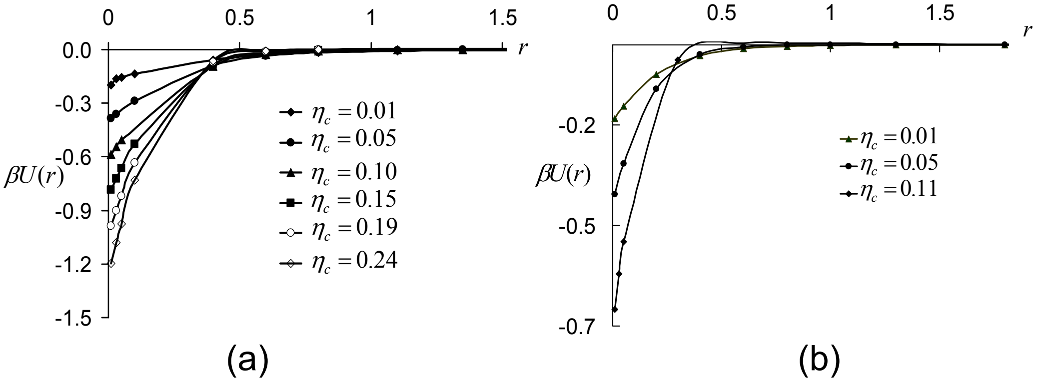

Figure 3.7: Depletion-induced pair interaction potentials $\beta U(r)$ as a function of the surface to surface distance between the two proteins: (a) For protein size $q = 5$; (b) For protein size $q = 10$. The bulk concentration is fixed at $\phi_p^B = 0.2$ and the numbers in the brackets denote the effective concentrations ϕ_p

the depletion characteristics in the non-asymptotic regime ($R/\xi \simeq 0.2 - 2$) and its differences from the predictions made for the asymptotic regimes.

3.4.1 Qualitative Features of the Pair-Potential

In Fig.s 3.7a and b we display a selection of inter-protein pair potentials determined for proteins of sizes $q = 5$ and 10. In both cases, the bulk concentration of the polymer was maintained at a value $\phi_p^B = 0.2$, and the plots display the changes resulting in the pair interactions due to changes in the volume fraction of the protein η_c. Previous studies of the depletion-induced pair interactions have demonstrated that the strength of the pair interactions correlates monotonically with the concentration, while the range of the interaction correlates with the correlation length of the polymer solution [41, 58]. It can be seen that the $u(r)$ displayed in Fig. 3.7 qualitatively exhibits characteristics similar to that expected at the infinite dilution limits. Indeed, an increase in the concentration of the proteins results in an increase in the effective concentrations determining these potentials (see Fig. 3.4). The latter leads to a corresponding increase in the strength of the pair-interactions. Concomitantly, the effective correlation length of the polymer solution decreases, and leading to a decrease in the range of the pair-interactions. On the other hand, from a quantitative framework, the potentials represented in Figs. 3.7a and b display differences from what one may naively expect for the protein limit in a polymer solution maintained at a concentration ϕ_p^B. The magnitudes of the contact value of the potentials for both $q = 5$ and 10 are of the order of k_BT. In contrast, if the magnitudes of the contact potentials are assumed to be of the same order of magnitude as the insertion free energies F_c^1, and if the renormalization group (RG) expression [70, 81] $F_c^1 = 4.39\phi_p^B q^{-1.3}$ is used, then one obtains $F_c^1 \sim 0.1k_BT$ for $q = 5$. and $\sim 0.04k_BT$ for $q = 10$, which are an order of magnitude smaller than the contact values.

An interesting question pertains to the comparison of the pair potentials (at infinite dilution of particles) determined by the polymer SCFT approach to the predictions from other approaches. Figs. 3.8a–d display the pair potentials determined for the size ratios $q = 7.78, 1.09$ and 0.67 for different reservoir/effective concentrations ϕ_p alongside the pair potentials published in Louis, Bolhuis *et al.* [23, 58] and Tuinier *et al.* [22]. Note that $q = 0.67$ does not

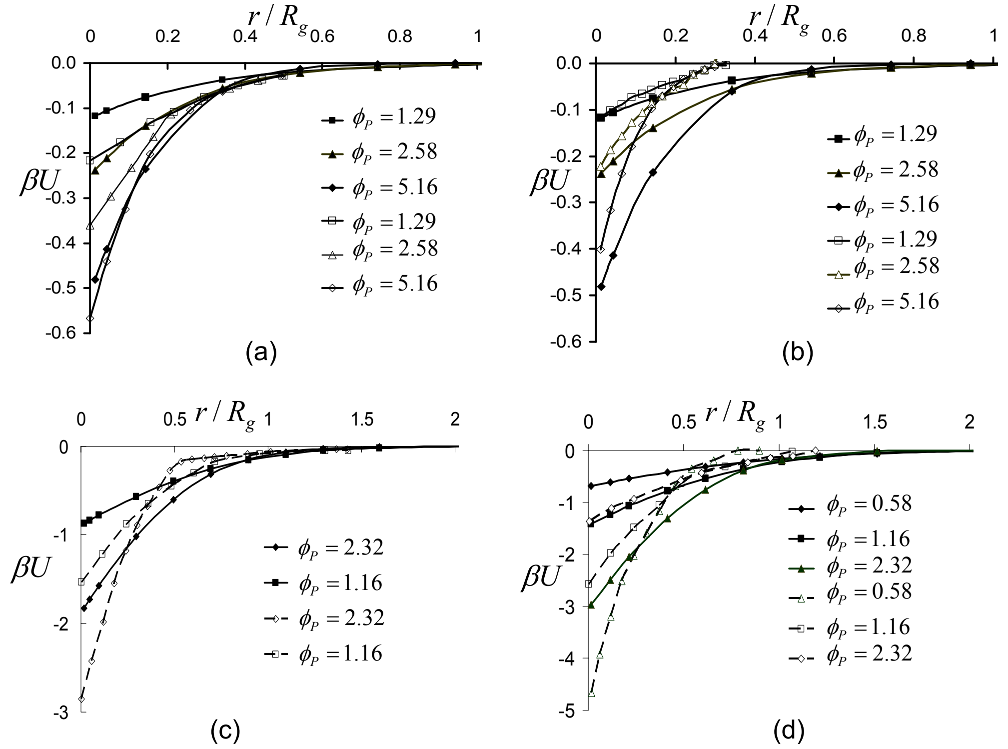

Figure 3.8: Comparison of pair-potentials at different polymer concentrations ϕ_p: (a) Compares the results of the present work (solid symbols) with that of Tuinier *et al.* [22] (open symbols) ($q = 7.78$); (b) Compares the results of the present work (solid symbols) with that of Bolhuis *et al.* [23] (open symbols) ($q = 7.78$). (c) ($q = 1.09$) and (d) ($q = 0.67$) Compares the results of the present study (solid symbols) with that of Louis *et al.* [58] (open symbols).

correspond to the protein limit considered in this study. Nevertheless, since the present approach is expected to work equally well for the colloid limit, the latter are displayed for comparison. As can be seen, the range of the potential as determined from SCFT matches extremely well with the corresponding results of the Tuinier *et al.*, while the contact values of the interaction potentials (in the protein limit) match much more closely with the results of Louis, Bolhuis *et al.* These discrepancies could arise from a number of sources, including the scaled mean-field approach, the inherently approximate one-body framework of Tuinier *et al.*, the lattice effects in the simulations of Bolhuis *et al.* Despite these discrepancies arising from the different models employed, a semiquantitative agreement between the different potentials is evident, suggesting the validity of the SCFT approach used in this study.

The next issue addressed here is the manner in which the different features of the pair-interactions correlate with the ratio R/ξ, where ξ denotes the correlation length corresponding to the effective concentration? First the dependence of the contact value of the potentials $u(r = 0)$ upon the ratio R/ξ is examined. In Fig. 3.9a we show the contact potentials determined for a number of different protein sizes, while fixing the bulk concentrations in the range $\phi_p^B = 0.1 - 1.25$. It is evident that the magnitudes of the contact strengths increase with an increase in the ratio R/ξ, and for $R/\xi \simeq 1$ (the regime of interest in this work), acquire values of the $O(k_BT)$. These features manifested in Fig. 3.7 as both the magnitudes and the changes in the strength of interactions upon increasing the concentration of the proteins. Previous

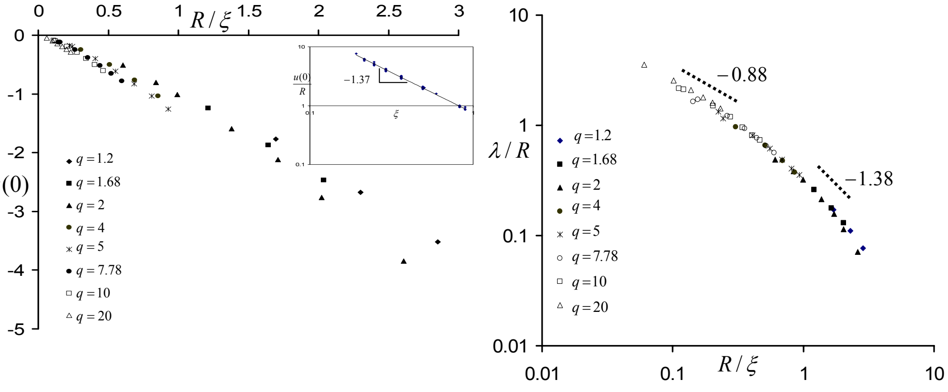

(a)

(b)

Figure 3.9: (a) Contact potentials $u(0)$ as a function of R/ξ. Inset shows the same results plotted as the ratio $u(0)/R$ as a function ξ. (b) Range of the potential λ (nondimensionalized by the radius of the protein R) plotted as a function of the ratio R/ξ

theoretical predictions have suggested that the contact potentials are expected to scale as $(R_{\mathrm{g}}\xi/R)^{-4/3}$ in the protein regime [40, 70, 71] ($R \ll \xi$) and as $\Pi\xi^2$ in the colloid regime [40, 41, 58, 76] where $\Pi \sim \xi^{-3}$ represents the osmotic pressure of the solution. From the inset in Fig. 3.9a we note that all the values for $u(0)$ can actually be collapsed onto a single curve of the form $q^{-1}\xi^{-1.37}$. In the scaled *mean-field* approach employed, the present results are not expected to match exactly with the scaling expressions [82]. On the other hand, the scaling exhibited by the contact potentials obtained using SCFT is strongly representative of the behavior expected from the asymptotic predictions in the protein regime, suggesting that this behavior also persists through the crossover regimes of R/ξ.

How does the range of the interaction potentials depend on the ratio R/ξ ? At a practical level, tuning the ranges of the polymer-induced effective interactions between proteins has been demonstrated as an approach to control the rates of crystal-nucleation in protein solutions [19, 65]. At a fundamental level, knowledge of the range of the potential is important for quantifying the role of multibody interactions. However, previous theoretical researches have come to somewhat contradictory conclusions regarding the range of the interaction potentials in the protein limit. Both Eisenriegler [70] and Odijk [71] have independently suggested that the range of the potential is of the order of the protein size for $R \ll \xi$. However, Schweizer and Fuchs [53] have predicted that the range of the potential has a much larger range of the order ξ itself. For the regime $R/\xi \gg 1$, the range is expected to be similar to the colloid regime and of the order the polymer correlation length ξ [41, 58].

We use an idea suggested by Noro and Frenkel [83] to extract the range from the interaction potentials and define the range of the potential as the width of the square-well potential which has an identical (normalized) second virial coefficient, B_2^* as the given potential. The nondimensionalized second virial coefficient citeNoroF00:

$$B_2^* = 1 - \frac{3}{8R^3} \int_R^\infty dr\, r^2 \left[\exp(-\beta u(r)) - 1\right], \tag{3.12}$$

is extracted from the potential by using numerical integration procedure. In the above $B_2^* = B_2/B_2^{\mathrm{HS}}$, with $B_2^{\mathrm{HS}} = 16\pi R^3/3$ representing the virial coefficient of hard spheres of radius R. The range λ is then extracted using the

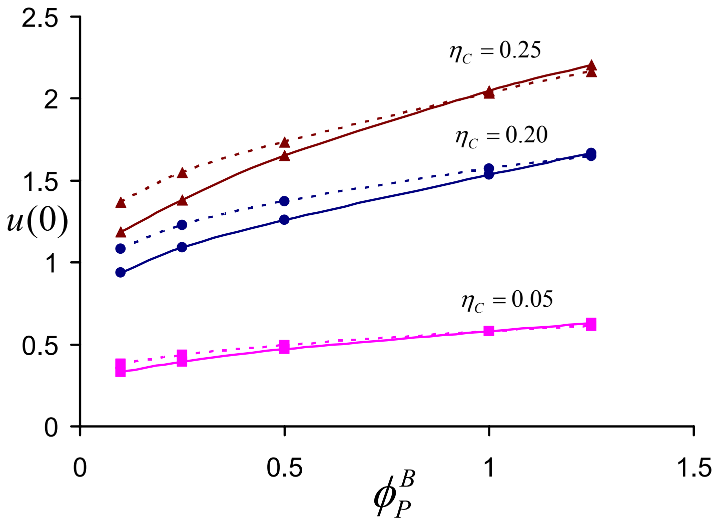

Figure 3.10: Magnitudes of the depletion induced contact potentials as a function of the bulk polymer concentration ϕ_p^B for different concentrations of the proteins η_c. The solid lines represent the results for $q = 5$ and the dashed lines for $q = 10$.

expression [83]:

$$\frac{\lambda}{R} = \sqrt[3]{1 + \frac{1 - B_2^*}{e^{u(0)} - 1}} - 1. \tag{3.13}$$

In Fig. 3.9b we display the nondimensionalized ranges λ as a function of the ratios R/ξ. It is evident that for the $R/\xi \ll 1$, the range of the potential λ is actually much larger compared to the radius of the proteins themselves, and scales approximately as $(R/\xi)^{-0.88}$. The latter is close to the predictions of Schweizer and Fuchs [53], and suggests that for protein sizes and (effective) polymer concentrations such that $R/\xi \lesssim 0.6$, the depletion interactions of small proteins are of much larger range compared to their sizes. On the other hand, for the regime $R/\xi \geq 1$, the range λ shows a different behavior, scaling approximately $(R/\xi)^{-1.38}$. This behavior indicates an eventual crossover to the regime $\lambda \simeq \xi$. As expected in the latter regime, the range of the potential is smaller than the size of the proteins [41, 58].

While the different features of the pair potentials can be rationalized based on the effective correlation length ξ, the interplay between the depleted volumes for different sized proteins and the resulting effective concentrations, can lead to nonintuitive results for pair interactions. It is evident even from Fig. 3.7 that at around the same concentrations of the proteins η_c, the strength of the contact value of the pair interactions (i.e. $u(r = 0)$) for protein sizes $q = 5$ and $q = 10$ are approximately the same magnitude. This effect is illustrated more clearly in Fig. 3.10, where we display the contact values $u(0)$ for protein sizes $q = 5$ and $q = 10$ for a range of polymer and protein concentrations ϕ_p^B's and η_c. As is evident from Fig. 3.10, for a given bulk polymer and protein concentration, the values of the contact potentials are to a good approximation independent of the size of the proteins. This feature differs from the predictions of the existing theories for the infinite dilution limit, which have suggested that the interaction potentials become weaker upon decreasing the size of the proteins (see eq. (3.1)). What is evident from the present results are subtle effects arising from an increase in the total depleted volume at smaller sizes. The latter leads to concomitant increases in the effective concentrations determining the strength of the potential. These two effects (approximately) cancel the decrease in the interaction strengths expected due to the smaller protein sizes.

3.4.2 Second Virial Coefficients

The interaction pair potentials play an important role in the discussion of the miscibility characteristics of the protein-polymer mixtures. The above results suggest that the magnitude of their strengths can be enhanced compared to the values expected for the given bulk concentration. Moreover, it is also shown that nontrivial effects may arise in comparing different sized proteins. The nondimensionalized second virial coefficient provides a unified approach to quantify these interaction features while also providing a framework to discuss the miscibility characteristics. Previous researches have indicated that B_2^* is a sensitive measure of both the strength and the range of the depletion interactions [58, 83]. Moreover, for many simple systems with a repulsive and an attractive component in their interaction potentials, the location of liquid-gas critical points [84], and the stability of the liquid-gas transitions [83] etc. have all been correlated with B_2^*.

An earlier study by Louis *et al.* [58] examined B_2^* for a range of protein sizes in *dilute polymer solutions*. They showed that for protein sizes q upto 20 and for polymer concentrations in the dilute regimes, the B_2^* values are extremely close to zero (cf. Fig. 14 of Ref. [58]). To compare with these results, in Figures 3.11a and b we display the corresponding B_2^* values as determined from the pair interaction potentials discussed in the previous section. The protein sizes are fixed at $q = 5.0$ and $q = 10.$, and the interaction potentials and B_2^* were determined as a function of both the concentration of the proteins and the polymers (some of the displayed values were determined by a smooth

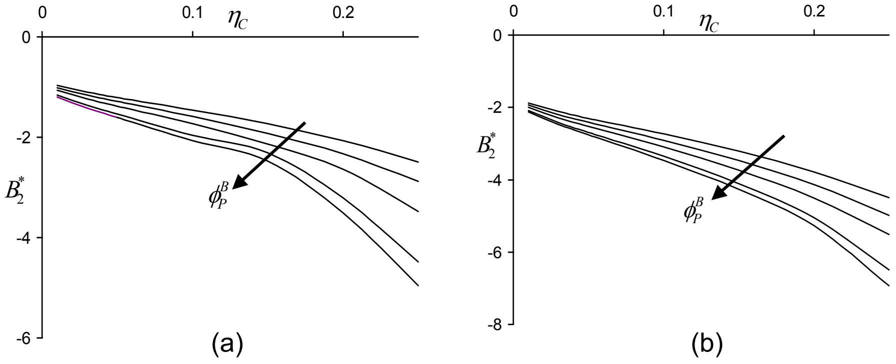

Figure 3.11: Normalized second virial coefficients B_2^* as a function of protein concentration η_c for protein sizes (a) $q = 5.0$; (b)$q = 10$. ϕ_p^B denotes the bulk polymer concentration and the different plots in the increasing direction of the arrow corresponds to $\phi_p^B = 0.1, 0.25, 0.5, 1.0, 1.25$.

extrapolation between the B_2^* values determined at different protein concentrations). The bulk polymer concentration ϕ_p^B was maintained at conditions below and around semidilute polymer concentrations.

Qualitatively, some of the features exhibited by the B_2^* determined from the potentials obtained using SCFT match with the results predicted by earlier researches. For instance, Louis *et al.* [58] showed that an increase in the polymer concentration within the dilute regime leads to a decrease in the B_2^* values. Further, they also predicted that the magnitudes of B_2^* are somewhat larger for smaller proteins. It can be seen from the present results that indeed proteins of smaller sizes in general have a more negative B_2^* values and that an increase in the polymer concentrations does lead to a decrease in the B_2^*. On the other hand, as observed in Fig. 3.11a, at low concentrations of proteins, while the B_2^* values are almost independent of the concentration of the polymers and proteins, these values are neither small in magnitude nor positive. The latter contrasts with the quantitative values predicted by Louis *et al.* and indicates that incorporating the free volume effects proves critical to determining the quantitative characteristics of the pair interactions. It can also be seen that upon increasing the concentration of the proteins, the B_2^* values become more negative and fall rapidly beyond a certain concentration of the proteins. The latter fall-off is a manifestation of the strongly attractive forces that arise as a consequence of the large effective concentrations experienced by the protein (cf. Fig. 3.4) at finite protein concentrations.

Conjectures regarding the miscibility of proteins are based on both the magnitude and the size dependence of their interactions in a polymer solution at the specified concentration. In Fig. 3.12, we display the B_2^* values as a function of the ratio R/ξ, where ξ corresponds to the correlation length at the effective concentration. The displayed results are obtained for a number of different protein sizes for which the bulk concentrations were maintained in the dilute-semidilute range corresponding to $\phi_p^B = 0.1 - 1.25$. Based on earlier mean-field studies [56], it is determined empirically that the B_2^* values can be collapsed onto a single universal curve by rescaling them as $B_2^* q^{-1}$ (rationalizing the fact that smaller proteins show larger magnitudes of B_2^*). At small R/ξ values, it can be seen that the $B_2^* q^{-1}$ tends to a constant value around -0.15. The latter manifested as the asymptotically constant value (albeit size dependent) attained for small protein concentrations η_c. Indeed, in these

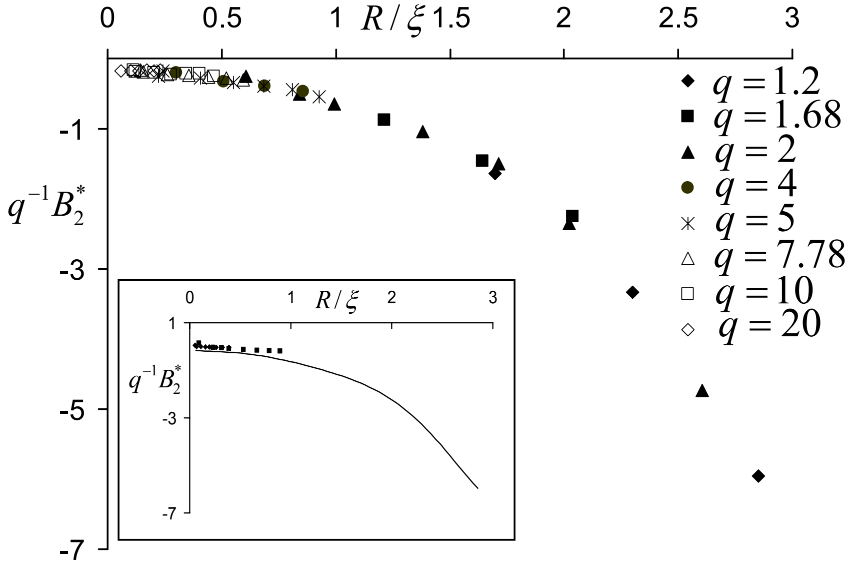

Figure 3.12: Normalized second virial coefficients B_2^* (rescaled as $q^{-1}B_2^*$) as a function of the ratio of the radius of the proteins R to the correlation length ξ at the effective concentration. The inset presents a check of our empirical scaling suggestion by comparing our B_2^* values (represented as a best fit line) with the numerical results of Bolhuis *et al.* [23] for $q = 3.8$ and 7.78 (represented as points).

regimes, the free volume effects are sufficiently strong to push the effective polymer concentrations into the semidilute regimes, but, the R/ξ values are still relatively small for a range of protein sizes. A further increase in the R/ξ values can be seen to lead to a rapid decrease in the corresponding B_2^* values. The latter manifested as the decrease in B_2^* values seen upon increasing either the protein or polymer concentrations, which was argued as resulting from an increase in the effective concentrations. Eisenriegler and coworkers used RG theories [70, 81] and predicted that as a function of the polymer concentration, B_2^* exhibits a minimum at $\phi \simeq 1$ followed by an increase (i.e. becomes less negative) to an asymptotically constant value with increasing polymer concentrations. The polymer concentration dependencies predicted by Eisenriegler were applicable for $R/\xi \ll 1$ and occur as a slow variation with increasing polymer concentration. Schweizer and Fuchs predict a qualitatively similar behavior [57], but do note that there could be interesting effects arising when $R \approx \xi$. The above results show differences from these theoretical predictions. At small R/ξ values, the present results do asymptote to a constant value. The latter is believed to correspond to the predictions of Eisenriegler for the regime $R/\xi \ll 1$. On the other hand, upon entering the regime $R/\xi \simeq 0.3$, we see from our results that B_2^* grows exponentially with the ratio R/ξ and acquires significantly negative values. From the earlier discussion, the quantitative values of B_2^* in this regime can be rationalized as resulting significantly higher contact strengths $u(0)$ manifesting from the crossover to a colloid-like regime ($R/\xi > 1$) not captured in the earlier theories.

The above differences between the asymptotic predictions and the crossover effects can be expected to have important implications for the phase behavior of the protein-polymer mixture. As pointed out in previous sections, for a wide range of bulk polymer concentrations ϕ_p^B and protein sizes q, the effective R/ξ values determining the depletion characteristics are in the range $0.2-2$ for the protein limit. Moreover, an increase in the bulk protein and/or polymer concentrations leads to an increase in the effective R/ξ values, thereby pushing the system into either the crossover or the colloid-like regimes. In this regime B_2^* values are strongly negative, suggestive of strong cohesive interactions between the proteins. The latter can rationalize the aggregation and the phase separation behavior of proteins in polymer solutions. In the next section we consider a simple model to quantify these effects.

3.4.3 Implications for the Phase Behavior

In this section, the B_2^* values discussed in the previous section are used in conjunction with an approximate equation of state to examine the miscibility characteristics of the protein-polymer mixtures. The main objective is to study how the qualitative and quantitative characteristics of the pair potentials discussed in the previous section translate in terms of phase behavior in the $\phi_p^B-\eta_c$ plane. However, the consideration of solid phases is eschewed and only the occurrence of fluid-fluid transitions is examined. Before embarking on this exercise, it should be emphasized that the protein density dependence of the potentials *does not lead* to the thermodynamical inconsistencies occurring in typical density dependent potentials [85]. The potentials derived in this study for the state point (ϕ_p^b, η_c) were in reality determined in the grand canonical ensemble with z_p fixed at the value corresponding to the state point (A lucid discussion of the same idea can be found in Ref. [85]). Whence, using this potential does generate the correct density distribution functions for the proteins, and furthermore the virial expression without additional density derivatives does yield the correct equation of state for the mixture [85].

In the semi-grand canonical formalism used in this study, the proteins are at a fixed concentration η_c and the polymers are at a fixed fugacity z_p. Thus, the equilibrium of the polymer component between the different phases is automatically ensured. Consequently, phase equilibria calculations need to ensure only the equality of the chemical potential and the osmotic pressure of the protein phase. To enable this, the following approximate virial expansion based equation of state for the protein phase is proposed:

$$\beta A_{ex} = \frac{\eta_c(4 - 3\eta_c)}{(1 - \eta_c)^2} + 4[B_2^*(z_p) - 1]\eta_c^2 \tag{3.14}$$

where A_{ex} denotes the excess Helmholtz free energy of the protein phase. The first term in the above expression represents the Carnahan-Starling (CS) expression for the hard sphere free energy [86]. The polymer contribution to the Helmholtz free energy is captured at a second virial coefficient level through the second term in the above equation. Note that B_2^* as defined in eq. (3.12) includes the hard-sphere contribution. In view of the fact that the CS expression already incorporates the hard-sphere contribution, the latter is subtracted from the second term. Since the objective here is to discern the coexisting compositions of the protein component, the free energy contributions arising from the polymer solution are not included. Further, the contribution from the solvation free energy has also been ignored since it contributes only to a uniform shift in the chemical potential of proteins.

The above approximation differs from the classical van der Waals theory in that the virial coefficient B_2^* is used in place of the a parameter of the van der Waals approximation [87]. In this manner, this approximation is expected to accurate for dilute concentrations of proteins without any restriction on the range of the potential. As a further support for the above model, it is noted that the critical point of the above model occurs at around $B_2^* = -1.65$, which is close to the empirically observed value $B_2^* = -1.5$ for many systems with a repulsive and an attractive component in their interaction potentials [84]. However, the above model can be considered at best as an easily implementable *approximation.* For instance, the critical point of the above model always occurs at $\eta_c = 0.13$, whereas in real experiments, the values are closer to $\eta_c = 0.2 - 0.28$ [88]. Moreover, Louis [89] has pointed out that even slight modifications to the above model can lead to significant changes in the binodals. With this understanding of the limitations, to discern the phase coexistence compositions using the above model, we obtained $B_2^*(z_p)$ for a fixed z_p. Subsequently, a common tangent construction is performed on A_{ex} to determine the protein compositions in the coexisting phases η_c^1 and η_c^2. From η_c^1, η_c^2 and z_p the values of the coexisting bulk polymer compositions

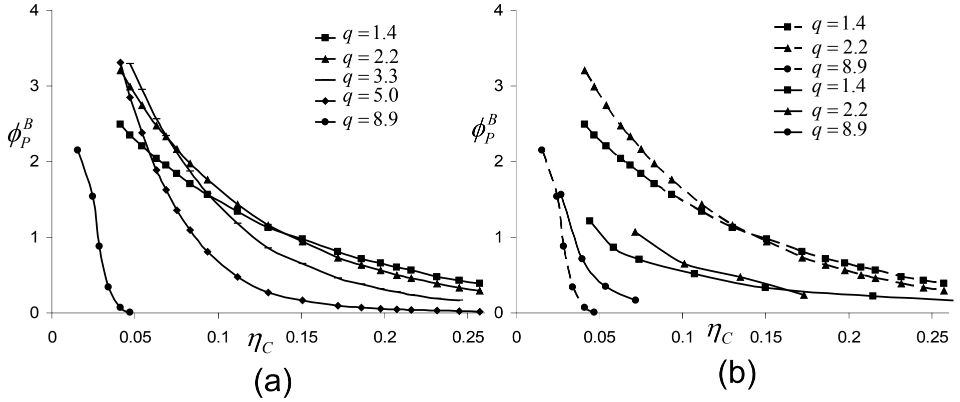

Figure 3.13: Fluid-fluid coexistence curves: (a) Based on the numerical formalism of this work; (b) Comparison to experimental data of Lynch *et al.* [90] (reproduced from the figure 11(a) in their article). The solid lines represent the experimental data and the dashed lines represent the numerical results displayed in (a).

$\phi_p^{B(1)}$ and $\phi_p^{B(2)}$ are determined using the formalism outlined in section 3.2.

Figure 3.13a displays the coexistence curves for different protein sizes in the plane of ϕ_p^B and η_c. To eschew clutter, the tie lines corresponding to the binodals are not displayed. The protein-polymer mixtures indeed show a large region of immiscibility over a wide range of protein sizes from $q = 2.0$ to $q = 8.9$. It is also evident that for smaller proteins, a decrease in the size of the protein shifts the binodals monotonically towards lower concentrations of proteins. The latter is indicative of more extensive immiscibility for smaller proteins, and provides strong evidence of the significance of the free volume effects incorporated in our model. Indeed, at a given polymer concentration and for the infinite dilution concentrations of the protein, quantities such as the contact potentials, insertion free energy etc. decrease monotonically with the size of the proteins. On the other hand, at a given bulk polymer and protein concentrations ϕ_p^B and η_c, the reduction in free volume is much more significant for smaller proteins (cf. Fig. 3.4b), and hence the effective concentrations are much larger. This interplay between the depletion volumes and the interaction effects at the effective concentrations leads to the observed variations in the binodal with the changes in the size of the proteins.

From Fig. 3.13a, we observe that for smaller proteins (notably, $q =$ 5 and 8.9), the binodals are indicative of the coexistence of an extremely concentrated polymer solution (and dilute protein phase) in equilibrium with a concentrated protein phase (in an extremely dilute polymer phase). This behavior is strongly suggestive of the phase separation behavior of a polymer in poor solvents [40]. Indeed, in a protein solvent of small enough size, the repulsions between the polymer and proteins manifest as an attractive interaction between the polymer segments. The latter feature is similar to the interactions experienced by the polymer in poor solvents, thereby rationalizing our observations.

While a direct comparison of our numerical results with the experiments is precluded due to the approximations involved in the above model, in Fig. 3.13b, the numerical results are compared with the experimental results of Lynch *et al.* [90] It can be seen that while the results are in qualitative agreement for larger protein sizes $q = 1.4$ and $q = 2.2$, the results for $q = 8.9$ match semiquantitatively with the experimental results. Indeed, experimental results also display a nonmonotonic trend for larger proteins, followed by a monotonic shift towards lower polymer and protein concentrations for smaller proteins. Moreover, the phase separation for smaller proteins is similar to the phases seen for polymer solutions in a poor solvent, again in qualitative agreement with our predictions.

It is noted that the above results for the phase diagram differ significantly from the PRISM based predictions of Schweizer *et al.* [59, 60] and the simulations of Bolhuis *et al.* [23] The most striking difference is in the miscibility trends observed upon increasing the size ratio q. PRISM and other approaches have considered the extreme limits of ideal and athermal solvents, and have suggested that in ideal solvents, miscibility should exhibit a nonmonotonic behavior with q and should decrease with increasing q for large size ratios q. In contrast, for athermal solvents, the miscibility has been predicted to increase with increasing q. In this respect, the above results seem more akin to the results for an ideal solvent. On the other hand, the comparison of pair potentials presented in section 3.4 suggested quantitative agreement with comparable theories for the athermal solvent limit. The quantitative discrepancies evident in the phase diagram could be a result of a combination of factors, including the approximate models used in this study for the free energies, the scaled-particle theory expression for free volume, and the neglect of real multibody interactions. Another possible resolution of this discrepancy could be from the subtle effects by which solvent quality manifests in the present computations. Indeed, even though the parameters B and C are

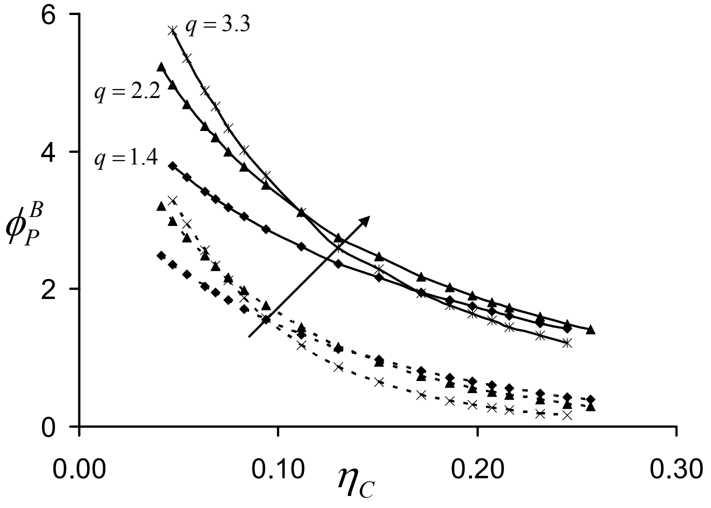

Figure 3.14: The phase behavior of protein-polymer mixtures at two different solvent qualities. The results on the dotted line corresponds to those displayed in Fig. 3.13. The solvent quality increases in the direction of the indicated arrow.

chosen such that the osmotic pressure and correlation lengths are the same as an athermal solution, the latter suffices only approximately to mimic the solvent quality. Indeed, the B parameter relates to the classical excluded volume parameter which should scale as $N^{1/2}$ for an athermal solvent. On the other hand, the actual values chosen for the excluded volume parameter B in this study were closer to $O(1)$, suggesting that these parameters represented a good (and possibly closer to ideal), but not an athermal solvent.

To further probe the above issue relating to solvent quality effects, displayed in Fig. 3.14 are the phase diagrams for the size ratios $q = 1.4, 2.2$ and 3.3 determined by the above model for conditions corresponding to better solvent quality where the excluded volume parameter B was fixed at twice the value used to determine Fig. 3.13a. As is evident, an increase in the solvent quality leads to an increase in the region of miscibility of the protein-polymer mixture. This is a direct result of the influence of the enhanced repulsive interactions between the polymers which arises in better solvent conditions. More strikingly, it is evident that the miscibility regions tend to become more monotonic with the size ratio q. The latter behavior matches with the predictions of Schweizer *et al.* [53, 59, 60] which predict that in the extreme limit of athermal solvent the region of miscibility would increase monotonically with the size ratio q.

3.5 Discussion and Outlook

In conclusion, this chapter highlights several important aspects of depletion in protein-polymer mixtures which had not been addressed in earlier studies. The main hypothesis in the present study was that the depletion characteristics at an one- and two-body level would suffice to address the phase behavior of such mixtures. However, this idea is used within a McMillan-Mayer like framework which ensures that the depletion characteristics are computed at the effective concentration or the concentration of the reservoir. It is pointed out that an important aspect of protein-polymer mixtures arises from the size of the depletion volumes relative to the protein sizes themselves. This suggested that the effective concentrations were in the semidilute or concentrated polymer solution regime even when the average concentration itself was in the dilute regimes. Moreover, the results suggested that the asymptotic results derived for the protein limit are applicable only for extremely small proteins, and that crossover effects, especially into the colloid-like regime can play an important role.

As an intermediate component in this analysis, an approximate model for the free volume that incorporates multibody overlaps of the depletion layers is used. As mentioned earlier, the main role played by the model was to relate the chemical potential of the polymer to the experimentally measurable polymer concentrations. Use of alternative models would lead to changes in the phase diagrams in the $\phi_p^B - \eta_c$ plane, but not to the physical features leading to the phase separation. The free volume model addressed the effects of nonzero concentrations and the interactions of polymers by the changes in the depletion thickness Δ. While this assumption implements the intuitive viewpoint that the polymers are depleted upto a distance Δ near the proteins and that the latter should determine the effective free volume, further checks of this assumption through more rigorous simulations are necessary.

Together, all the above effects led to prediction of the phase diagram displayed in Fig. 3.13. The latter suggested that purely depletion effects can lead to phase separation in protein polymer mixtures. Furthermore, all the calculations also highlighted the importance of solvent conditions in influencing the quantitative characteristics of the phase behavior. Finally, multibody interactions are believed to play an important role in determining the actual locations of the phase boundaries. To verify the latter conclusion, a different model for α is probed:

$$\alpha_{\mathrm{SB}} = 1 - \eta_c \left(1 + \frac{\Delta}{R}\right)^3, \tag{3.15}$$

which ascribes a nonoverlapping radius of $R + \Delta$ to each protein. While the above model also predicted phase separation and immiscibility of protein-polymer mixtures, the phase coexistence curves were much shifted from those displayed in Fig. 3.13.

One of the main outcomes of this work, was the use of a two-body formalism to compute the quantitative characteristics of the solvation free energies and pair interactions potentials for the protein limit in semidilute and concentrated solutions. These results arose from a rigorous numerical solution of the two-body problem using appropriate numerical techniques and hence are expected to be accurate for a wide range of protein curvatures not captured in earlier studies. Moreover, by using a field theoretic framework, many of the important physical features that arise from polymer overlaps and interactions at semidilute and concentrated polymer solutions are incorporated . The formalism outlined in this chapter can be easily extended to address the interaction characteristics for cases where the rigidity of the polymers are important [91], polymers can adsorb onto the particles and/or for polyelectrolyte solutions.

The following summarizes the main advances and results arising from the present framework:

(i) A McMillan-Mayer like approach [92] (see Dijkstra *et al.* [35, 78] for recent applications of this framework) is used to study the depletion characteristics of protein-polymer mixtures. This framework suggests that depletion in protein-polymer mixtures should be studied not at the bulk/average polymer concentration, but rather at an effective concentration which is a function of both the average polymer concentration and the protein concentrations. This effective concentration arises from the difference between the system volume and the actual "free" volume accessible for the polymers.[21] While this fact was pointed out first by Lekkerkerker *et al.* [21], the novel feature is that in the protein limit ($R/R_\mathrm{g} < 1$) the volume of the polymer depletion layers far exceeds the size of the proteins, leading to effective polymer concentrations which are much higher (and typically in the semidilute and concentrated regimes) than the average system concentrations (which can be in the dilute regimes). It is shown that the depletion characteristics of the protein-polymer mixture can be substantially different at these effective concentrations, and this can have profound consequences for the phase behavior of the mixture.

(ii) An approximate approach is proposed to incorporate the effects arising from the multibody overlaps of the depletion layers. Intuitively, one would expect that in the limit $q > 1$, significant overlap of the depletion layers can occur even at relatively low volume fraction of proteins, leading to nontrivial multibody interactions [23, 23, 55, 93]. The latter would render all depletion characteristics such as depletion thickness, solvation free energies, interprotein potentials etc. to be strongly dependent on the volume fraction of the particles — an effect not accounted for in many of the simplistic models.

In this work, an approach similar to earlier applications of free volume theory is used and the multibody depletion characteristics are mapped onto the one- and two-particle level depletion characteristics in a polymer solution at an effective concentration determined accounting for multibody effects. This approach provides a tractable *approximation* to study the effects arising from the multibody overlap of depletion layers.

(iii) The depletion characteristics are examined in the nonasymptotic regimes of the ratio R/ξ. Earlier theoretical researches have mainly examined the depletion characteristics in the asymptotic regimes $R/\xi \ll 1$ and $R/\xi \gg 1$ [41, 69, 70, 81]. The free volume and multibody interactions based analysis used in the present study suggest that a key to understanding the phase behavior of protein-polymer mixtures (even for the case of dilute polymer solutions), is to study the depletion effects over a range of concentrations spanning the transition between $R/\xi < 1$ and $R/\xi > 1$. These results have ramifications for interpreting some of the macromolecular crowding experiments [64, 66]. In such contexts, the polymer sizes are of the order of 10-100 nm while the globular proteins, micelles and nanoparticles are of the order of 2-30 nm. Moreover, the polymer concentrations are typically such that $\phi_p \sim 1-5$ (where $\phi_p = \rho_p/\rho_p^*$, where ρ_p^* denotes the overlap concentration of the polymers). These conditions correspond to $R/R_{\mathrm{g}} < 1$, but with $R/\xi \sim O(0.1-5)$.

(iv) To address the above issues, a numerical solution of polymer mean field-theory [40, 41] (also referred to as the self-consistent field theory, SCFT) is effected which incorporates the effects arising from polymer overlaps and interactions, while also being accurate over a wide regime of protein sizes characterized by the importance of their curvature relative to the correlation length of polymers. In the subsequent chapters, we extend the numerical SCFT developed in this chapter to the case of adsorbing polymers and grafted polymers to address the interaction characteristics, phase behavior and rheological properties in presence of spherical and rodlike nanoparticles.

Chapter 4

Nanoparticles in Presence of Adsorbing Polymer

Most polymer-particle mixtures involve situations where the polymers exhibit weak to strong preferential interactions with the particles [94]. In such cases, the effective interactions between the particles exhibit rich characteristics, ranging from strong attractions to non-monotonic interactions and strong repulsions, the regimes of manifestations of which depend on the polymer concentrations, polymer molecular weights and the adsorption strengths [4, 5, 95–97]. These interaction characteristics have been extensively exploited in applications such as coatings, lubricating oils and personal care products as a means to control their stability and/or the rheological properties [98].

The potential applications have also prompted many theoretical investigations of the physical characteristics of adsorption of polymer on solid surfaces. On the one hand, the scaling theories have been constructed based on the self similar structure of adsorbed layers [5, 95, 96, 99]. These approaches have served to provide a good description of the global properties of adsorbed polymer layers such as the polymer concentration profiles, the layer thickness and the interactions between adsorbed polymer layers. On the other hand, mean field models have also been developed and provide a more detailed description of the structure of adsorbed layers in terms of the distributions of the loop and tail conformations of the adsorbed layer [48, 97, 100, 101]. Additionally, various molecular modeling techniques such as the density functional theories [102, 103], integral equation theories [104, 105] have been successfully applied to extract the detailed structural descriptions and thermodynamic properties of polymer in presence of flat surfaces. Overall, the above-mentioned approaches have led to a very good understanding of the polymer conformations [30, 33, 34] and the effective interactions resulting in the context of flat surfaces and for large colloidal particles [4, 49, 51, 97].

As mentioned earlier, the recent advances in the nanotechnolgy have shifted the focus from ‘colloid’ size range to ‘nanoparticle’ regime. For instance, in the polymer-nanocomposite applications, the filler particles added for enhancement in the material properties are characterized by particle sizes which are either comparable to or in most cases, smaller than the average size of polymers. As highlighted in the previous chapter, the physics of polymer-particle suspensions is observed to be quite different in the nanoparticle limit. In the nanoparticle regime, the curvature of the particle is shown to have profound qualitative and quantitative effects on both the depletion interactions and the resultant stability characteristics of the mixture [20–24]. Recent experimental observations in the context of polymer-nanoparticle systems have indicated that similar richness in phase behavior and structural characteristics also prevails in the context of adsorbing polymers. For instance, in many cases even extremely low particle loadings (around a volume fraction 2 %) have been shown to lead to significant changes in the rheological properties of the mixture [25], which in turn suggest nontrivial structural characteristics for the mixture. Further, observations in the context of polymer-clay composites, laponite-PEO, silica-PEO etc. suggest a variety of phase behavioral characteristics ranging from macroscopic flocculation, phase separation, stable 1-phase gels etc [26–29].

So far, many of the above observations have only been rationalized qualitatively by invoking the influence of polymer-mediated interactions and the resulting polymer conformational characteristics. For instance, the formation of gels and flocs has been speculated to arise as a results of a large number of interparticle bridges in the nanoparticle limit [27, 28]. The occurrence/lack thereof of phase separation has again been attributed to the magnitude and the range of the interaction potentials. In contrast to the depletion situation, existing theoretical results for adsorbing polymers are mainly at a scaling level and relate only to the adsorption characteristics on a single nanoparticle [47, 106, 107]. Very little is known quantitatively about features such as effective interactions, stability and structural characteristics of the mixture and the differences, if any, with the colloid limit for the case involving *adsorbing* polymers.

Motivated by the above experimental observations, in this chapter we study the polymer-nanoparticle mixtures in which the polymers can adsorb onto the particles. Specifically, the following issues are addressed: (i) How does the structure of adsorbed polymer layer change with increase in curvature of particle ? (ii) What is the effect of the polymer concentrations on the structure of adsorbed polymer layers ? (iii) How does the particle-to-polymer size ratio influence the interparticle interactions and polymer bridging characteristics ? (iv) What is the role of the preceding features in determining the structure and the phase behavior of nanoparticle mixtures ?

To address the above mentioned issues, we examine the adsorption behavior of polymers on spherical particles using a numerical solution of polymer self consistent field theory (SCFT) [39, 108]. Here we extend the SCFT framework discussed in the previous chapter to characterize the adsorption properties of polymers in terms of both the adsorbance and the loop, tail segment conformations for a range of polymer-to-particle size ratios and for concentrations in the semi-dilute regime. Secondly, we quantify the effect of different physical parameters on the effective pair-interaction potentials and the conformational characteristics (such as bridging) in the presence of two particles. Finally, we characterize the phase behavior and the percolation phenomena in such mixtures using simple theoretical models.

The rest of this chapter is arranged as follows: In Section 4.1, we motivate and outline a new model for polymer adsorption which accounts for the surface saturation effects. The details of the framework used for determining pair interactions, and the numerical aspects of the approach are similar to that discussed in Chapter 2. Section 4.2 discusses the case of adsorption on single particle with specific focus on the surface saturation and the relative sizes of the polymer and the particle. In section 4.3, we discuss the pair interaction potentials and the conformational characteristics for the case of two particles. Section 4.4 examines the stability characteristics and percolation thresholds for the mixture followed by a discussion of the presented results.

4.1 Saturable Adsorption Model

Early studies on polymer adsorption phenomena have suggested that the overall adsorption and interaction characteristics are determined by an interplay between two competing factors: (a) The reduction in entropy arising from the confinement of polymers between the surfaces; and (b) The energetic gain due to the adsorption of polymers. The former results in a repulsive contribution to the interactions whereas the latter leads to a favorable component to the interaction free energy. Pioneering studies by de Gennes [95], Fleer and Scheutjens [4] have demonstrated that *reversibility* of adsorption plays a critical role in governing the interplay between these features and the resulting interactions. In the case termed "reversible adsorption," the polymer layer is assumed to be in strict thermodynamic equilibrium with the surrounding polymer solution. When the interacting surfaces are brought closer, the overall polymer concentration in the gap between the surfaces then decreases to maintain the chemical equilibrium with the bulk solution. The polymer remaining in the gap then reduces its energy by forming bridges between the particles. In such a situation, the enthalpic gain resulting from adsorption dominates the loss of entropy, and the interactions between the surfaces *remain always* *attractive* independent of the interparticle distances or the parametric conditions [4, 96].

deGennes [96] also suggested an alternate scenario, where the polymer can be "irreversibly adsorbed," corresponding to situations where the polymer is strongly adsorbed to the surfaces such that the energy barriers and the time scales associated with the desorption become macroscopic. Early models [96] postulated to mimic this effect were termed as "restricted equilibrium" adsorption. In this model, the total amount of polymer confined between the surfaces was kept at a constant value during the approach of the particles. Since the adsorbed polymer is now unable to leave the gap between the surfaces, decreasing surface separation leads to increasing confinement-induced entropy losses, and the resulting interactions can either be attractive or repulsive depending on whether further adsorption is possible. In the approach of "starved" surfaces, the total amount of confined polymer is kept at a value lower than that corresponding to the equilibrium adsorption on individual plates. In such instances, mean field and scaling theories predict an adsorption-induced attraction at large interplate separations followed by entropic-loss induced repulsion at closer intersurface separations [5]. In contrast, for "saturated" surfaces, the amount of confined polymer equals to or is greater than the equilibrium adsorption, for which case restricted equilibrium model predicts repulsive interactions at all distances [95, 109].

The above ideas were mainly designed to model the experiments of surface force apparatus [110, 111], for which the predictions of the restricted equilibrium model were found to be in excellent agreement with the experimental results. However, it is neither straightforward to extend the idea nor the formulation of the restricted equilibrium model to analyze the interactions the interactions between spherical particles, especially in the nanoparticle regime. Physically, since the polymers are not restricted from redistributing on the surface, during approach of the particles, the polymers are no longer "kinetically trapped" in the gap between the particles [96]. On the other hand, mathematically it is also not straightforward to directly constrain the amount of polymer in the gap while also maintaining a specified value for the bulk polymer concentration [112].

In this work, a revised version of the reversible adsorption model, termed the "saturable" adsorption model is proposed which more faithfully accounts for the surface saturation effects while also allowing a straightforward generalization to the case of spherical particles. The main physical feature of this model is that the polymer adsorption is assumed to always be in equilibrium with the surrounding solution, but the surfaces of the particles are ascribed a fixed maximum capacity (per unit area) for adsorption. The latter situation accords closely with experimental situations which commonly report a maximum saturation limit for adsorption on particles [28, 113, 114]. This model accommodates this feature by restricting the maximum surface concentration of the adsorbed polymer. It should be noted that this model differs from both the reversible and the restricted equilibrium adsorption models. In reversible adsorption, there is no restriction on the adsorption capacity of the surface, and the surface polymer concentration is determined solely by the bulk polymer concentration and the adsorption strength, and in principle, can increase unboundedly. The present model also differs from the 'restricted equilibrium' model in that no restriction is placed on the total amount adsorbed between the surfaces. Rather, as explained below, the constraint on the surface saturation is incorporated automatically into the model as an additional entropic penalty which becomes relevant when the surface concentration approaches maximum surface saturation ϕ_{m}. In this manner, the model also allows one to study the polymer-particle interactions for particles with different surface properties such as saturation.

In this chapter, the polymer mean field theory is used to study the effects of the surface saturation, the polymer-to-particle size ratio and the polymer concentration on the interplay between energetic and entropic interactions of the polymer-particle system using the saturable adsorption model. The polymer is modeled using the Gaussian thread model, with the effects of the solvent accounted by effective excluded volume interactions between the monomers [36]. The case of good solvents is considered, where the excluded volume parameter v is positive [36]. The specific interactions between the polymer segments and the surface of particles are expressed in terms of an inverse adsorption length $\lambda^{'}$, which can be mapped onto a square well interaction potential between the polymer and the particle [115]. Explicitly, if the range of the square well potential is denoted as δ and its depth as u_0 then,

$$\lambda^{'} = \pi^2 (u_0 - u_{\mathrm{c}})/8 u_{\mathrm{c}} \delta, \tag{4.1}$$

where u_0 represents the change in the free energy of the system (all energies are expressed in $k_{\mathrm{B}}T$ units) when a polymer segment adsorbs on the surface of particle, replacing solvent molecules and can be experimentally measured by chromatographic method [116]. u_{c} is termed as the critical interaction strength, and is related to the polymer segment length b as $u_{\mathrm{c}} = \pi^2 b^2/24\delta^2$. Physically, u_{c} represents the interaction strength characterizing the transition between a "depleting" to an "adsorbing" polymer [95]. Explicitly, a positive $\lambda^{'}$ ($u_0 > u_{\mathrm{c}}$) represents the case of adsorbing polymer where there is an enhanced polymer density at the surface of the particle, whereas a negative $\lambda^{'}$ ($u_0 < u_{\mathrm{c}}$) corresponds to the case of polymer depletion where there is a reduced density at the surface. In experimental systems, λ' can be characterized through neutron scattering measurements [117]. In this chapter, the case of a fixed adsorption potential corresponding to intermediate adsorption strength where $u_0 \simeq -kT$ [95] is considered. The constraint of the finite surface saturation is mimicked as an entropic contribution, ΔS, in terms of volume fraction of unoccupied sites as,

$$\Delta S = [\phi_{\mathrm{m}} - \phi_{\mathrm{s}}(\mathbf{r})] \left[\ln[\frac{\phi_{\mathrm{m}} - \phi_{\mathrm{s}}(\mathbf{r})}{\phi_{\mathrm{m}}}] - 1 \right] \tag{4.2}$$

where ϕ_{m} represents the maximum allowed polymer concentration at the surface (i.e. the surface saturation) and $\phi_{\mathrm{s}}(\mathbf{r})$ represents the density of the polymer segments at the surface (cf. Eq. 2.46). Note that for large values of ϕ_{m}, the influence of ΔS is weak and the above formalism corresponds to the model of reversible adsorption [96]. In case where ΔS is relevant, the free energy of the polymer-particle mixture is determined by an interplay of three components:

(1) The gain in free energy due to polymer segment-surface contacts, U_{ads} (2) The entropic loss arising from the excluded volume repulsions between the monomers, U_{ex} (3) The entropic loss due to the constraint on the surface saturation, ΔS. The enthalpic gain arising from the segment-surface interactions can be represented as,

$$\beta U_{ads}(\{\mathbf{R}_\alpha(s)\}) = \frac{\lambda' N}{R_g} \sum_{\alpha=1}^{m} \int_0^1 ds \; \delta[\mathbf{R}_\alpha(s) - \mathbf{r}_{surface}]. \tag{4.3}$$

The effect of excluded volume interactions between the monomers is accounted in the same manner as discussed in Chapter 2(see Eq. 2.18). The entropic contribution arising from the surface saturation constraint is incorporated in the total free energy as,

$$\beta H(\{\mathbf{R}_\alpha(s)\}) = \beta U_{ex}(\{\mathbf{R}_\alpha(s)\}) + \beta U_{ads}(\{\mathbf{R}_\alpha(s)\}) - S(\{\mathbf{R}_\alpha(s)\})]. \tag{4.4}$$

where,

$$S(\{\mathbf{R}_\alpha(s)\}) = \frac{bN}{R_g} \sum_{\alpha=1}^{m} \int_0^1 ds \delta[\mathbf{R}_\alpha(s) - \mathbf{r}_{surface}](\phi_{\mathrm{m}} - \phi(\mathbf{r})) \left[\ln \left(\frac{\phi_{\mathrm{m}} - \phi(\mathbf{r})}{\phi_{\mathrm{m}}} \right) - 1 \right]. \tag{4.5}$$

ϕ_{m} in the above equation denotes the surface saturation and represents the maximum allowed polymer concentration at the surface and b is the statistical segment length for the polymer. In the grand canonical ensemble, the partition function for polymer solution can be written as [118],

$$\Xi(z_p, V, T) \propto \sum_{m=0}^{\infty} \frac{z_p^m}{m!} \int \prod_{\alpha=1}^{m} d\mathbf{R}_\alpha(s) \; \exp(-\beta[H(\{\mathbf{R}_\alpha(s)\})]) \tag{4.6}$$

Using functional integral methods [119], the above partition function can be expressed in terms of a fluctuating potential field $w(r)$ as,

$$\Xi = \int_{-i\infty}^{i\infty} Dw \exp(-\beta H[w(\mathbf{r})]), \tag{4.7}$$

where

$$-\beta H[w(\mathbf{r})] = \frac{1}{2B}\int d\mathbf{r}[\, w^2(\mathbf{r}) + 2\alpha w(\mathbf{r})] + Z\exp(-\alpha)Q(w) - \int_s dr\, w(\mathbf{r})\phi(\mathbf{r}) \\ +\lambda \int_s dr\,\phi(\mathbf{r}) - \frac{\lambda}{\mu}\int_s dr\,[\phi_m - \phi(\mathbf{r})]\left[\ln\left(\frac{\phi_m - \phi(\mathbf{r})}{\phi_m}\right) - 1\right] \tag{4.8}$$

where $\mu = u_0/b$ and $\int_s$ represents integrals evaluated over the particle surface. The presence of particles is accounted as an external potential that is included in the single-chain partition function Q(w(r)) by imposing an adsorption boundary condition at the particle surface. In this formalism, the adsorption boundary condition for the Eq. 2.27 becomes,

$$n.\nabla q(\mathbf{r},s)|_{surface} = -w(\mathbf{r})q(\mathbf{r},s). \tag{4.9}$$

By following the procedures outlined in Chapter 2, the self consistency condition for 'saturable' adsorption is expressed as,

$$w(\mathbf{r}) = \begin{cases} \lambda/2 + \lambda/2\mu \ln[(\phi_{\mathrm{m}} - \phi(\mathbf{r}))/\phi_{\mathrm{m}}], & \mathbf{r} = R \\ \alpha(\phi(\mathbf{r}) - 1.0), & \mathbf{r} > R \end{cases} \tag{4.10}$$

Together, Equations 2.27, 4.8, 4.9 and 4.10 constitute a complete set of self consistent equations. As discussed in Chapter 2, numerical solution of these SCFT equations allows us to compute the partition function Ξ_n for a system containing n particles immersed in a polymer bath at constant chemical potential Z. To deduce the pair interactions from one body and two body partition functions ($\Xi_1,\ \Xi_2$), we use the McMillan-Mayer approach [92] detailed in Chapter 2.

The present model is characterized by three parameters in addition to the surface saturation concentration ϕ_{m} and the particle to polymer size ratio R/R_{g}. These are the excluded volume parameter v, the chemical potential Z and the polymer segment-surface interaction parameter u_0. The first two parameters quantify the solvent quality and the polymer densities, whereas u_0 determines the strength of attraction between the polymer segments and the particle surface. In this work, the adsorption characteristics are studied for the case of good solvent conditions ($v > 0$) and the non-dimensional excluded volume parameter $B = vN^2/Rg^d$ is chosen to be 10.0. The parameter Z represents the activity coefficient for the polymer solution and determines the polymer concentration as $\rho_p = -1/VdH/d\ln Z$ where H is the Hamiltonian of the system given by Eq. 4.8. In the following, all polymer concentrations are normalized by the semi-dilute crossover concentration [40], ρ_p^* with $\phi_p = \rho_p/\rho_p^* > 1$ indicating the semidilute concentration regime. The values of parameter Z are chosen such that the bulk polymer concentrations correspond to the semi-dilute regime ($\phi_p > 1.0$), where the mean-field approach is expected to be at least qualitatively accurate. The nondimensional segment surface parameter $\lambda = \lambda' N/R_g$ is fixed to 10.0 corresponding to an adsorption length of $d = 1/\lambda \simeq 0.1$ which represents an intermediate adsorption strength. In section 4.5 the effects resulting from other choices for these parameters are discussed qualitatively.

4.2 Adsorption Characteristics On a Single Nanoparticle

First, we consider the adsorption characteristics on a single particle and present the results highlighting the influences of particle curvatures, the surface saturation and the bulk polymer concentrations upon: (i) The total amount of polymer adsorbed; and (ii) The conformational characteristics of adsorbed polymer, viz., the distribution of adsorbed polymer between loops and tails. In the following sections, we will make extensive use of these adsorption characteristics to rationalize the pair interaction characteristics in such systems.

We start by presenting a pair of intuitively contradictory results which serve to illustrate the profound differences between the adsorption characteristics in the nanoparticle and large particle limits. The first of these relates to the polymer adsorbance, defined as the number of polymer segments (per unit surface area of the particle) which belong to the adsorbed polymer chains. As discussed in the Section 2.3(cf. Eq. 2.46), a polymer chain is classified as adsorbed if one or more of its segments contact the particle. The adsorbance Γ is then defined as:

$$\Gamma = \frac{1}{4\pi R^2} \int_R^\infty \phi_{\mathrm{ads}}(\mathbf{r})\, d\mathbf{r}. \tag{4.11}$$

where R represents the radius of the particle and $\phi_{\mathrm{ads}}(\mathbf{r})$ denotes the segment density profile of adsorbed polymers (Eq. 2.46). The adsorbance Γ quantifies

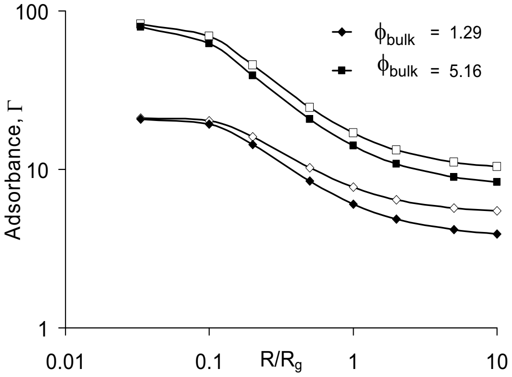

Figure 4.1: Adsorbance as a function of particle size, R/R_g for saturable adsorption (filled symbols) and for reversible adsorption (open symbols). The bulk polymer concentrations (expressed as a ratio of the actual concentration to the overlap concentration, ρ_p^*) are $\phi_{\mathrm{bulk}} = 1.29$ and 5.16 and the surface saturation concentration is $\phi_{\mathrm{m}} = 20.0$.

the amount of polymers stuck to a particle, and will later be seen to play also an important role in determining the polymer compositions of coexisting phases.

Figure 4.1 presents the results for the adsorbance Γ as a function of the polymer-particle size ratio R/R_g for a set of bulk concentrations ϕ_{bulk} for both the "saturable" (closed symbols) and the "reversible" ($\phi_{\mathrm{m}} \to \infty$, open symbols) models. The most important characteristic noted from the results is the effect of the particle sizes. It is seen that for the case of large particles ($R > R_g$), the adsorbance asymptotically approaches a constant value, becoming independent of the particle size itself. This is intuitive considering that in the latter limit, the adsorption should resemble that on flat surfaces and become independent of the curvature of the particles. However, we observe that when the particle size R becomes smaller than the size of the polymer (the nanoparticle limit), a decrease in the size leads to significant enhancement in the adsorbance, suggesting that the smaller particles “soak” more polymers.

A second interesting effect observed from Fig. 4.1 is the role of the surface saturation. By comparing the reversible and saturable adsorption results we observe that for small particles the surface saturation constraint plays little or no role in modulating the total adsorbance. In contrast, for larger particles it is evident that the saturation limit of the surface reduces the overall adsorbance of the polymer. Finally, it is seen that bulk polymer concentration ϕ_{bulk} also impacts the adsorbance, albeit in a more intuitively understandable manner. It is seen that an increase in the ϕ_{bulk} leads to an increase in the number of adsorbed polymers, an effect ascribable to the increase in the osmotic pressure of the bulk solution.

Why does the saturation limit only weakly affect small particles ? In Fig. 4.2 we consider the ϕ_{bulk} dependence of the actual surface concentrations ϕ_{s} for the case of particles of different sizes but with the same fixed surface saturation. Overall, we observe that the surface concentrations for all particle sizes increase with an increase in the bulk concentrations (reflecting the increased adsorption of polymers) and asymptote at higher concentrations to the limit constrained by the surface saturation value. However, for a fixed bulk polymer concentration, a decrease in the size of the particle leads to a corresponding decrease in the surface concentration. Further, this effect is observed

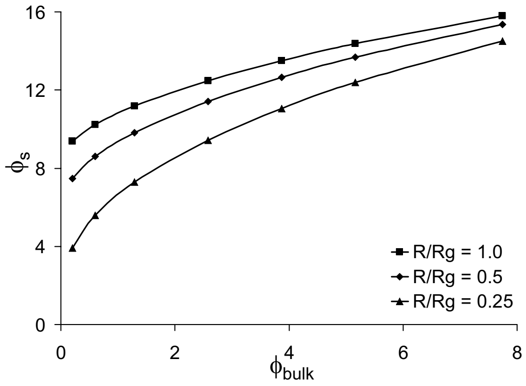

Figure 4.2: Surface concentrations (ϕ_s) as a function of the bulk polymer concentration for saturable adsorption. The surface saturation is fixed at $\phi_\mathrm{m} = 20.0$. The polymer-to-particle size ratios are $R/R_\mathrm{g} = 1.0, 0.5, 0.25$.

to become more pronounced as the particle size R becomes smaller than R_g. The latter suggests that for larger particles, the surface concentration ϕ_s approaches the surface saturation value ϕ_m at lower bulk polymer concentrations compared to the smaller particles (i.e. larger particles saturate earlier).

The above results for the adsorbance Γ and the surface concentration ϕ_s appear consistent with each other, albeit only partially. On the one hand, the observation that the adsorption on larger particles saturates earlier rationalizes the more pronounced impact of the saturation constraint upon the adsorbance Γ for such systems. On the other hand, the observation that the surface concentrations are substantially lower for smaller particles is some what contradictory to the earlier result that the adsorbance on such particles is significantly higher. A resolution of these contradictory effects comes from examining the size-dependent differences in the structure of the adsorbed layers themselves.

Figs. 4.3a and b display the volume fraction profiles of the monomers belonging to the loop and tail conformations for a given bulk polymer concentration and for different polymer-particle size ratios R/R_{g}. Qualitatively, for all cases the volume fraction profiles for the loops display a maximum at the surface of the particle and decrease monotonically away from the surface. In contrast, the volume fraction profiles of the tail monomers (Fig. 4.3b) increase with increasing distance from the surface and are characterized by a maximum in the distribution at some intermediate distance. These observations accord with the intuitive picture of adsorbed layers [97] that near the surface of the particle, the adsorbed layer is primarily made of loops, whereas contribution of tail monomers becomes more important away from the surface, with a maximum in the tail segment distribution arising from the finite extension of the polymer chains.

How does the size of the particle affect the above conformational characteristics ? We observe that increasing the curvature of the particle leads to an overall decrease in the volume fraction of the loop monomers, and a corresponding increase in the volume fraction of the tail monomers. Moreover, the maximum in the distribution of tail monomers moves closer towards the particle surface. These two features are more clearly evident in the inset to Fig. 4.3b which shows the cross-over between loops and tail volume fraction profiles for $R/R_g = 1.0$ and 0.25. It is seen that a decrease in the size of the

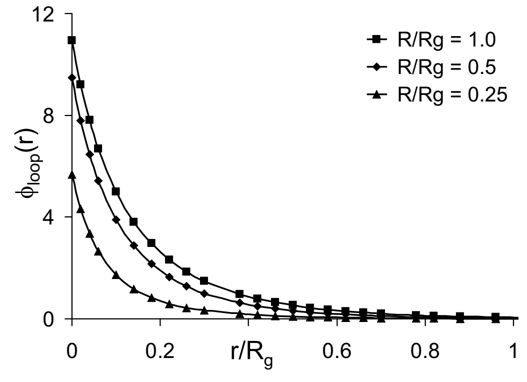

(a)

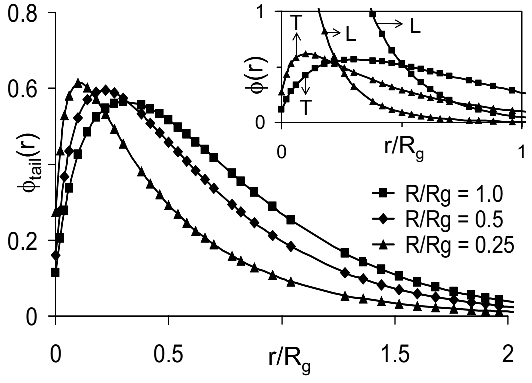

(b)

Figure 4.3: (a) Segment volume fraction of loops, ϕ_{loop}, as a function of distance r from the surface (normalized by R_{g}) for saturable adsorption for $R/R_{\mathrm{g}} = 1, 0.5, 0.25$ for bulk polymer concentration $\phi_{\mathrm{bulk}} = 2.58$. The surface saturation is $\phi_{\mathrm{m}} = 20$. (b) Segment volume fraction profiles for tails, ϕ_{tail}, for the same parameters as in (a). Inset shows the cross-over between loops (denoted as 'L') and tails (denoted as 'T') volume fractions for $R/R_{\mathrm{g}} = 1$ and 0.25.

particle is accompanied by a corresponding movement towards the surface of the crossover between the volume fraction of the loop and tail monomers.

The above results rationalize the particle size effects observed in Figs. 4.1 and 4.2. Indeed, for smaller particles, the enhancement in the adsorbance vs lower surface concentrations can be reconciled by noting that the adsorption occurs predominantly in the form of tails, which count towards the adsorbance but not towards the surface concentration. In contrast, for larger particles, a significant fraction of the adsorbed polymer is present in the form of loops. In turn, the effects observed for smaller particles can be justified by noting that an increase in the particle curvature increases the accessible solution volume for an adsorbed polymer chain. For small particles, the latter renders the chain conformations with large portions of the chain dangling in the solution entropically more favorable than smaller loops with multiple surface contacts.

It is of interest to probe if the surface saturation and/or the bulk concentrations affect the above conformational characteristics. Figures 4.4a and b display these effect on the loop and tail density profiles for both reversible and saturable adsorption. Increasing the bulk polymer concentration is observed to lead to a significant increase in the tail monomer density profiles while leading to only a weak change in the loop monomer density profiles. In other words, at lower bulk polymer concentrations, the majority of the adsorbed monomers are present in the form of loops. However, at higher ϕ_{bulk} the adsorption proceeds mainly in the form of tails. The surface saturation is

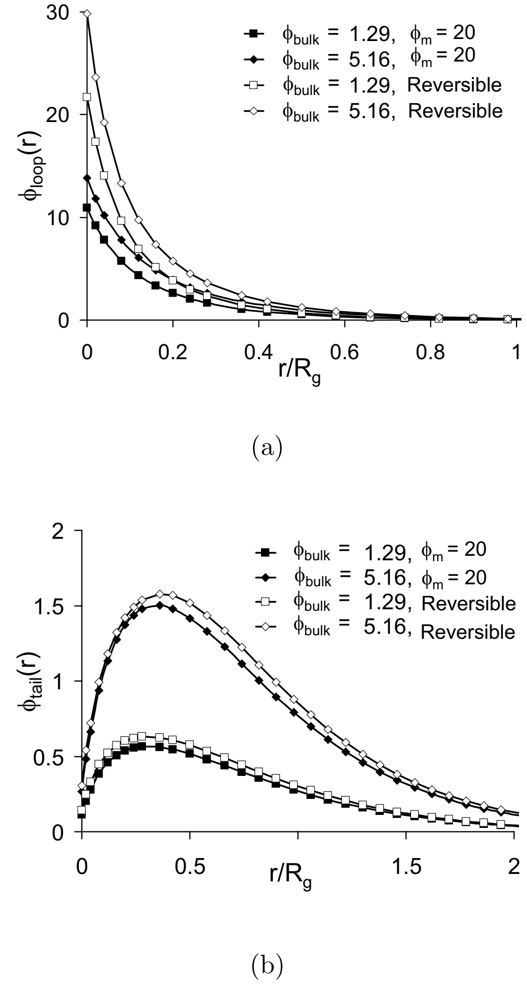

Figure 4.4: (a) Segment volume fraction profiles for loops, ϕ_{loop}, as a function of distance r from the surface (normalized by R_{g}) for reversible and saturable adsorption for bulk polymer concentrations $\phi_{\mathrm{bulk}} = 1.29$ and 5.16. The particle size ratio is $R/R_{\mathrm{g}} = 1.0$. The surface saturation for saturable adsorption is $\phi_{\mathrm{m}} = 20.0$. (b) Segment volume fraction profiles for tails, ϕ_{tail}, for the same parameters as in (a).

seen to accentuate this effect, whereby, for a fixed particle size and bulk concentrations, decreasing the surface saturation leads to a substantial decrease in the loop densities while resulting in only a weak change in the magnitudes of tail density profiles.

Interestingly, it can be noted from Fig. 4.3 that the curvature of particle by itself does not affect the extension of tails. For instance, even for a particle radius as small as $0.25R_g$ tails extend to a distance of $\sim 2R_g$. The latter could have important implications for both the flow behavior and hydrodynamic radii of smaller particles [120], since the latter features are sensitively dependent on the extension and the number of the tails. Furthermore, the presence of long tails would increase the propensity and the range of interparticle bridging, and in turn, affect the phase behavior and gelation characteristics of the mixture. In the following sections, the latter features are analyzed for nanoparticle suspensions.

To summarize, the adsorption characteristics on a single isolated particle by themselves suggest important differences between the nanoparticle and colloid regimes. An increase in the particle curvature in the nanoparticle regime is observed to lead to a significant enhancement in the adsorbance. More importantly, the conformations of the adsorbed polymers exhibit markedly different features in the colloid and nanoparticle limits. Indeed, with a decrease in the particle radius, the adsorbed layer on smaller particles primarily consists of large number of tails whereas adsorption on larger particles is dominated by presence of large number of loops.

It should be noted that the above features are consistent with the predictions of related studies. For instance, scaling predictions of Aubouy and Raphael [47] predicted a significant increase in adsorbance with a decrease in the size. A similar behavior was also reported by Marla and Meredith [121] for the case of polymers modeled through a Lennard Jones bead-spring model. Their Monte Carlo simulations predict both an enhancement in the adsorbance with increase in the particle curvature and an eventual saturation of the adsorbance as the particle size approaches the flat surface limit. Above differences in the adsorption characteristics in the infinite dilution limit for nanoparticle and colloid limit are expected to result in marked differences in the interactions and phase behavior of polymer-particle mixtures at finite particle volume fraction. In the following, the characteristics of pair interaction potentials are discussed and are used to analyze the phase and percolation behavior of the polymer-particle mixtures in the subsequent sections.

4.3 Interaction Potentials

In this section, we consider mainly the case of particle of a fixed surface saturation value and examine the influence of the bulk polymer concentration and the size of the particles upon the pair interactions is examined. It should be emphasized here that the pair interactions deduced using the present model are applicable only for a completely equilibrium situation. Whence, when two particles carrying adsorbed polymer layers are brought closer, the polymers are completely free to adjust their structure. The polymer may leave the gap

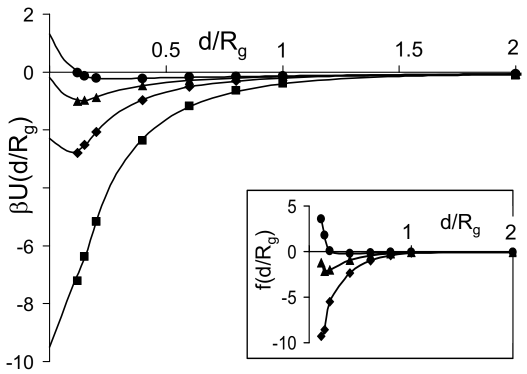

Figure 4.5: Pair interaction potentials as a function of interparticle distance d (normalized by polymer radius of gyration, R_{g}) for different bulk concentrations, ϕ_{b} Particle size, $R/R_{\mathrm{g}} = 1.0$ and surface saturation $\phi_{\mathrm{m}} = 20.0$. The bulk polymer concentrations are $\phi_{\mathrm{bulk}} = 1.29\,$(squares)$, 2.58\,$(diamonds)$, 3.87\,$(triangles)$, 5.16\,$(circles). The inset shows corresponding interparticle forces as a function of interparticle distance d/R_{g} for $\phi_{\mathrm{bulk}} = 1.29, 2.58, 3.87$. The interaction potentials at small d/R_{g} and the contact potentials are obtained by integrating the best fits for the force curves.

to maintain chemical equilibrium, or transform from loops or tails to bridges (and vice versa) to decrease the free energy. The latter feature would allow the polymers to form interparticle bridges (by transforming their loops) even in the event that the particles are initially saturated. In the latter respect, the restricted equilibrium model also has a similar feature and does not capture the nonequilibrium effects such as arising from incomplete/non-rearranging polymer layers [122].

First we consider a fixed size of the particle and identify the role of bulk polymer concentration in controlling the pair interaction potentials. Fig. 4.5

presents the pair interaction potentials (with best fit lines to guide the eye) for a particle size ratio $R/R_g = 1.0$ for a range of bulk polymer concentrations. We observe that for dilute bulk polymer concentrations ϕ_{bulk}, the interaction potentials are monotonically attractive as a function of interparticle distance, with the strength of attraction of the order of many kT. However, upon increasing the ambient polymer concentration, the interactions develop a non-monotonic character, displaying attraction at large interparticle separations followed by a repulsive behavior at smaller interparticle distances. At even higher bulk concentrations, it is seen that the interactions become monotonically repulsive with the interparticle distance.

The above change in the character of interparticle potentials can be rationalized from the understanding of the polymer adsorption characteristics on a single particle. We first consider the case of dilute polymer concentrations. In such regimes, the entropic contributions arising from the excluded volume interactions between the monomers are relatively weak. Secondly, as discussed in section 4.2, for low ϕ_{bulk} the surface concentration (ϕ_{s}) is also significantly lower than that of the surface saturation value, ϕ_{m}. Whence the entropic losses arising from the saturation constraint are also comparatively weak. Consequently, when two particles are brought closer, the polymers are free to adsorb, form more interparticle bridges and gain energetically without incurring the concomitant entropic costs. Together, the strong energetic gain and the weak entropic costs lead to a strong, monotonic attraction between particles at low ϕ_{bulk}.

Upon increasing the bulk polymer concentration, three effects come into play: (i) The one particle results demonstrate that increasing ϕ_{bulk} increases the number of tail segments while the number of loop monomers remains almost unchanged. The latter would increase the propensity to form bridges at a given interparticle distance. (ii) A second effect is the increase in polymer concentration between the particles. This leads to an entropic loss contribution arising from the osmotic confinement effects; (iii) Finally, the increase in the number of bridging segments due to either decreasing interparticle distance or increasing ϕ_{bulk} drives the surface concentration closer to the surface saturation. The latter manifests as an additional entropic loss due to the approach towards the saturation of the surfaces. At higher ϕ_{bulk}, this interplay between bridging-induced attraction, the repulsions induced by confinement and surface saturation determines the pair interactions.

At large interparticle separations, the surfaces are still unsaturated, the polymer confinement effects are weak, and hence the polymer bridging mechanism dominates and results in an effective attraction between the particles. With a decrease in the interparticle distance, when the surface concentration approaches the surface saturation ϕ_{m}, the energetic gain arising from the formation of interparticle bridges also becomes saturated. In such regimes, the confinement and the saturation entropy costs become comparable to bridging resulting in the minimum manifested in the interaction potentials. A further decrease in the interparticle distance results in entropic losses due to confinement and saturation leading to a weakening of interparticle attraction and at small distances, results in a crossover to entropy dominated repulsion. Finally, at very high bulk polymer concentrations, the equilibrium surface concentration, ϕ_{s} becomes comparable to the surface saturation ϕ_{m}. In such cases, the surface is already saturated with the polymer, leading to purely repulsive pair interaction potentials.

Next, we consider the influence of the size of the particle on characteristics of the pair interaction potentials. In Figs. 4.6a and b, we display the pair interaction potentials for two more particle sizes ($R/R_g = 0.5, 0.25$) for again the situation where the surface saturation is fixed and the bulk polymer concentrations are varied. As a function of ϕ_{bulk} it is observed that for all the sizes the interactions are attractive at dilute concentrations followed by a non-monotonic behavior at higher concentrations and finally turns into a repulsive behavior at the highest concentrations. However, the values of minimum in the interaction potentials are observed to decrease monotonically with decrease in the size of the particles. This can be rationalized by recalling from the above discussion that the magnitude of the minimum in interaction is determined by the number of bridging segments between the particles. A smaller particle has smaller surface area leading to the formation of lesser number of bridges. The decrease in bridging leads to an overall weaker attraction between the particles.

Secondly, we observe that the effect of entropic repulsions is less pronounced for smaller particles. To demonstrate this, in Fig. 4.7a we display an effective hard sphere diameter computed using the Barker-Henderson ex-

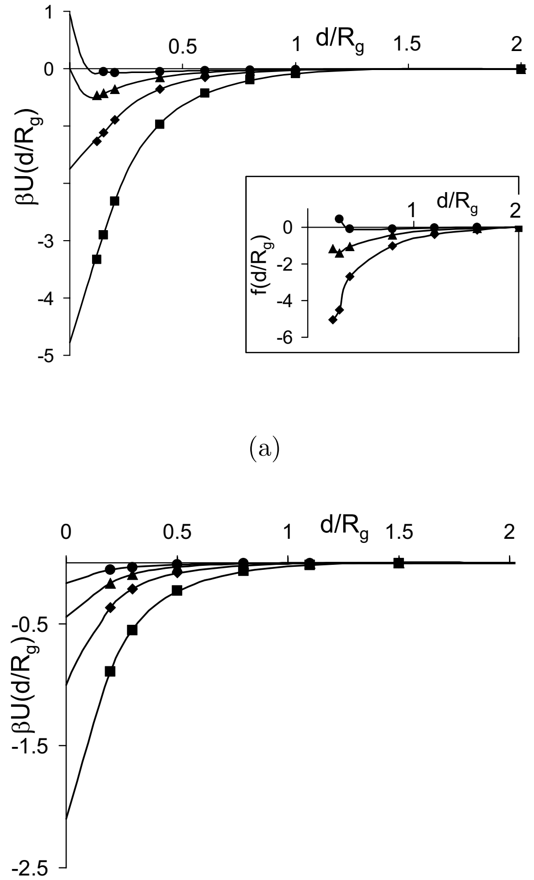

(a)

(b)

Figure 4.6: (a) Pair interaction potentials as a function of interparticle distance d (normalized by polymer radius of gyration R_{g}) for polymer-to-particle size ratios $R/R_{\mathrm{g}} = 0.5$. Bulk concentrations are $\phi_{\mathrm{bulk}} = 1.29\,\text{(squares)}, 2.58\,\text{(diamonds)}, 3.87\,\text{(triangles)}, 5.16\,\text{(circles)}$ and surface saturation $\phi_{\mathrm{m}} = 20.0$. The inset shows corresponding interparticle forces as a function of interparticle distance d/R_{g} for $\phi_{\mathrm{bulk}} = 1.29, 2.58$ and 3.87. (b) Pair interaction potentials for $R/R_{\mathrm{g}} = 0.25$.

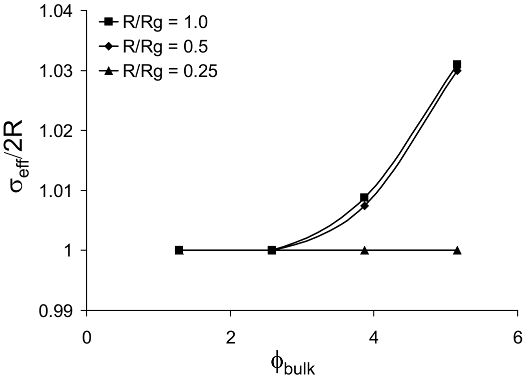

(a)

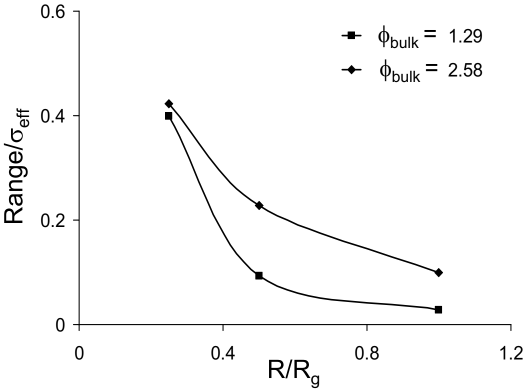

(b)

Figure 4.7: (a) Equivalent hard sphere diameter, σ_{eff} (normalized by particle diameter, $2R$) as a function of bulk polymer concentration, ϕ_{bulk}, for $R/R_{\text{g}} = 1.0, 0.5, 0.25$. (b) Range of attractive interactions (normalized by HS diameter, σ_{eff}) as a function of particle size (R/R_{g}) for bulk polymer concentrations $\phi_{\text{bulk}} = 1.29$ and 2.58.

pression [123]. As can be seen the equivalent HS diameter is much lower for smaller particles and the increase in σ_{eff} for smaller particles requires much higher bulk concentrations as compared to larger particles. This effect can be rationalized by recalling that the repulsive interactions arise due to the entropic confinement and saturation losses. In section 4.2, it is shown that for smaller particles, adsorption mainly happens in the form of tails leading to delayed surface saturation (see Fig. 4.3). Whence for a given bulk concentration, bringing two smaller particles closer results in lower surface concentrations and consequent entropic losses. The latter delays the onset of and decreases the strength of the repulsive interactions.

Finally, the range of the attractive interactions relative to the size of the particle increases with a decrease in particle sizes. To demonstrate this, we compute the range of an equivalent square well potential, denoted λ, by following the extended corresponding state approach proposed by Noro and Frenkel [83]. In Fig. 4.7b we display λ as a function of the particle size for different bulk polymer concentrations. We observe that for dilute polymer concentrations, the range of attraction for smaller particles is much larger than that for larger particles. Explicitly, we observe that for the smallest particle size studied in this work, the range of attraction is $\simeq R$ whereas for $R/R_g = 1.0$ the range is $\sim 0.1R$. These trends can be rationalized by noting that the range is determined by the extent of bridging interactions. As mentioned in section 4.2, even for small particles ($R < R_g$), the tails extend to a distance of $\sim 2R_g$ from the surface of the particles (see Fig. 4.3b). Whence the range of interactions is also correspondingly higher for the smaller particles.

Generically, the above results suggest that for smaller particles there exists a weak, albeit long range attraction that persists up to higher concentrations. In contrast, for larger particles, the interactions are stronger, short ranged and transform into a repulsive behavior at even moderate bulk polymer concentrations. It should be noted that this model, albeit assumes a "reversible equilibrium" adsorption, predicts that the effective interparticle interactions become repulsive at higher polymer concentrations. This feature arises from the surface saturation constraint incorporated in the present model. In previous "reversible adsorption" studies, the intersurface interactions were predicted to be always attractive over the entire range of polymer concentrations [4, 96]. Also for a given set of polymer-to-particle size ratio R/R_{g}, bulk polymer concentration ϕ_{bulk} and adsorption strength λ, the attractive interactions are always found to be weaker for the case of saturable adsorption (finite ϕ_{m}) as compared to the reversible adsorption ($\phi_{\mathrm{m}} \gg \phi_{\mathrm{bulk}}$). The broad picture that emerges from these results is that the interplay between surface saturation, the bulk polymer concentration and the polymer to particle size ratio plays a crucial role in determining the pair interactions between the nanoparticles. In the following section, this microscopic information is used to probe the macroscopic consequences such as stability and percolation characteristics of the mixture.

Recently both computer simulations [121] and liquid state theories [124] have been used to probe the potential of mean field between nanoparticles in solutions of adsorbing polymers. For a model of Lennard Jones bead-spring polymer, the Monte Carlo simulations of Marla and Meredith [121] predict a weakening of the interparticle interactions with decrease in the size of the nanoparticles. For more denser polymer-particle mixtures, integral equation theory of Hooper and Schweizer [124] shows the strength of the interparticle interactions to become proportional to the particle size (and hence decreases with a decrease in the particle size). Though a detailed comparison with these approaches is not possible due to the differences in the models used, the underlying approximations and the range of system parameters studied, these features are in qualitative agreement with the results presented in this section.

4.4 Implications for Percolation and Phase Behavior

In the nanoparticle limit, many experiments have suggested that dramatic changes can result in the stability and viscoelastic properties upon changing the concentration of the bulk polymer [27, 29]. These observations have been qualitatively rationalized by invoking the formation of gels and/or the miscibility characteristics of the polymer-nanoparticle mixtures [25, 28]. The framework developed in this study proves ideal to examine the above issues at a more quantitative level. On the one hand, the pair potentials provide the necessary information to examine the complete phase behavior. Secondly, the field-theoretic approach used here allows access to all the conformational characteristics of the polymer which can be used to compute the thresholds for forming a percolated cluster, a necessary but not sufficient condition for forming a gel. Presumably, a drawback relates to the equilibrium character of the present calculations when compared to the predominant nonequilibrium effects that manifest in experiments. Nonetheless, a knowledge of the equilibrium characteristics is still useful in that it allows one to predict the expected outcomes and identify phenomena attributable to the non-equilibrium effects.

Here, we use simple analytical theories and results from the literature to provide a semi-quantitative picture of the stability and structure of the polymer-nanoparticle mixtures. We focus mainly on the size and polymer concentration effects on two aspects of polymer-particle mixtures: (i) The formation of a percolated cluster of particles resulting from polymer bridges; (ii) The stability and the phase behavior of the polymer particle mixtures. Initially, we consider these features distinct from one another and elucidate the physics governing their trends. Subsequently, we combine these results and comment on their consistency with experimental observations.

4.4.1 Mapping ϕ_{b} to ϕ_{o}

The discussion so far pertained to the case of infinite dilution of one/two particles immersed in a polymer solution whose ambient concentration is ϕ_{b}. However, when a finite concentration of particles η_c is involved, the concentration ϕ_{b} is to be interpreted as the effective far field concentration of the polymer [1, 21, 35]. Experimentally, the measurable quantity is the number of polymers in the solution (or in the different phases) per unit volume, denoted as ϕ_{o}. Whence, to translate the above microscopic, two-particle information into a more macroscopic picture we need to also map ϕ_b to the actual or the overall polymer concentration ϕ_o.

Two effects determine the mapping between ϕ_b and ϕ_o. The adsorption of the polymer increases the polymer concentrations in the vicinity of the particles. Whence, the ϕ_o are expected to be much higher than far field or the ϕ_b. Secondly, at a finite volume fraction of particles, the polymers can only occupy the free space unoccupied by the particles. The latter effect would lead to a lower ϕ_o (measured on a total volume basis) compared to ϕ_b (which corresponds to the free volume). To account for these effects, an approximate mapping is proposed which uses the one particle results in a cell-model approach to yield:

$$\frac{\phi_\mathrm{overall}}{\phi_\mathrm{bulk}} = 1 - \eta_c + \frac{\eta_c}{4\pi R^3/3} \int_R^\infty \left(\frac{\phi(\mathbf{r})}{\phi_\mathrm{bulk}} - 1 \right) d\mathbf{r}, \tag{4.12}$$

where $\phi(\mathbf{r})$ represents the polymer concentration profile around a single nanoparticle (with the far field concentration maintained at ϕ_b). The second term in the above equation accounts for the reduction in volume at finite η_c arising from the space occupied by the particles. The last term captures the adsorption-induced increase in the polymer concentration in the vicinity of the particles. We note that since ϕ_overall is approximated at one particle level, the above approximation is expected to be accurate only for low volume fractions of particles. Nevertheless, in the following we use the approximate mapping to discuss the percolation thresholds and the phase-behavior in the $\phi_\mathrm{o} - \eta_c$ plane.

4.4.2 Bridging-Induced Percolation

We first characterize the particle volume fraction thresholds for forming a polymer bridge induced percolated network. We define the threshold for the latter as one wherein the polymer conformations are such that instantaneously it is possible to find an infinite cluster of particles connected through polymer bridges. This percolation threshold is motivated by experimental results which have suggested the presence of such structures in modifying the rheology of polymer-particle mixtures [25, 27–29]. These clusters are viewed as a result of the transient immobilization of the polymer monomers (due to attractive interactions) near the particles [125]. The model proposed below implements this view while ignoring the dynamical aspects of bridging (which are expected to be important for rheological phenomena, but cannot be accessed in the framework of this work) and instead computes at an equilibrium level the concentration of particles at which a connected structure *formed* by bridges can result.

To characterize the percolation thresholds, we use a heuristic measure, wherein we consider the system percolated when any given particle is connected by bridges on an average to at least two other particles. We approximate the "connectedness" between the particles in a mean field manner and assume it to be proportional to the probability of forming at least one bridge between the particles. At a specified interparticle distance d, the *average* number of bridging chains is given by, $N_{\mathrm{br}}(d) = 1/N \int_0^\infty \phi_{\mathrm{br}}(\mathbf{r}) d\mathbf{r}$ where $\phi_{\mathrm{br}}(\mathbf{r})$ represents the volume fraction profile for bridging segments when the particles are a distance

d apart and N represents the chain length of the polymer. The probability $P_k(d)$ of forming actually k bridges between the particles at the distance d (when the average is $N_{\rm br}$) is assumed to follow a Poisson distribution [126, 127]:

$$P_k(d) = \frac{[N_{\rm br}(d)]^k}{k!} \exp[-N_{\rm br}(d)]. \tag{4.13}$$

Whence, the probability that the particle is connected by at least one bridge to another particle at a distance d is given by: $P_{\rm br}(d) = 1 - \exp[-N_{\rm br}(d)]$. We then define the percolation threshold as the lowest particle density at which the given particle is connected by bridges to at least two other particles. We determine this critical particle density ρ_c as,

$$\rho_c \int d^3\mathbf{r}\, P_{\rm br}(\mathbf{r}) g(\mathbf{r}) \gtrsim 2.0, \tag{4.14}$$

where $g(\mathbf{r})$ is the radial distribution function for the particles and $\rho_c g(\mathbf{r}) d^3\mathbf{r}$ gives the number of particles in a volume $d^3\mathbf{r}$ at the distance $\mathbf{r}$ from the central particle [87]. Finally, we approximate $g(\mathbf{r})$ by its low density approximation as $g(\mathbf{r}) \propto \exp(-\beta U(\mathbf{r}))$, where $U(\mathbf{r})$ represents the polymer-mediated effective interaction potential between the particles [87].

It should be noted that the above measure is more a semi-quantitative hypothesis rather than a rigorous prediction. Indeed, the probability of bridging is not expected to be a true Poisson distribution, nor are the two particle bridging probabilities expected to be applicable when three or more particles are present. Further, while the above measure accounts for the effects of both the number of bridging segments as well as the effective interaction potentials,

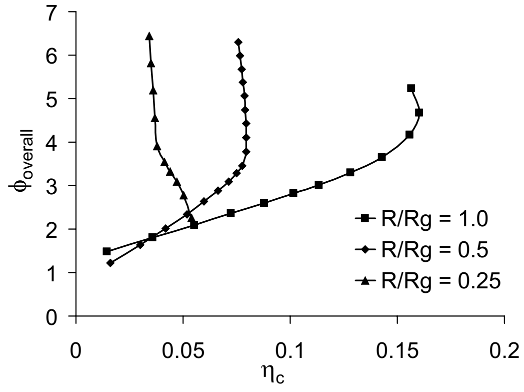

Figure 4.8: Percolation volume fraction (η_c) as a function of overall polymer concentration. The particle sizes are $R/R_\mathrm{g} = 1.0, 0.5$ and 0.25 and surface saturation is fixed at $\phi_\mathrm{m} = 20.0$.

it does not however account for the time-scales that need to be satisfied to form an active network. Nevertheless, the above measure provides a simple means to analyze the effects of size and the polymer concentrations on the formation of a bridged, connected cluster.

Figure 4.8 displays the percolation thresholds obtained using this model. For low ϕ_o (also corresponding to low ϕ_b), the number of interparticle bridges is minimal, but the effective pair interactions are characterized by strong attractions and hence the average interparticle distances are extremely small. Consequently, bridging percolation can occur even at dilute concentration of the particles. Increasing ϕ_o (and ϕ_b), on the one hand leads to an increase in the number of interparticle bridges, thereby increasing the probability of forming a percolated cluster. On the other hand, the interparticle attractions are concomitantly weakened and eventually become repulsive, thereby increasing the average interparticle distances. The repulsive interactions manifest at short distances whereas the increase in the bridging probability occurs at distances comparable to the size of the polymer. In larger particles, these competing effects lead to an initial increase in the percolation threshold (when the weakening of the interactions dominate) followed by a decrease in the percolation threshold (when the increase in the bridging dominates). In contrast, for smaller particles the interaction effects are much weaker, and hence the percolation thresholds are seen to monotonically decrease with an increase in ϕ_o.

In summary, we predict that due to the propensity to form bridges, the bridging-induced percolation thresholds are at extremely dilute volume fractions of the particles and decrease even further with a decrease in the size of the particle. The structural characteristics of the percolated phases (such as necklace-like structures vs three dimensional gels) will also depend on both the size of the particles and the bulk polymer concentration. To elaborate this, one would need further quantitative information on the number and the size distribution of the bridges, the results for which will be presented in Chapter 5. However, the observation/lack thereof of such networked phases depends on the interrelationship between the percolation lines and the miscibility behavior of the mixture and is addressed in the following section.

4.4.3 Phase Behavior and Relationship to Experimental Observations

To determine the phase behavior of the nanoparticle-polymer mixtures, we use a simplistic equation of state invoking the second virial coefficient B_2^* values obtained from pair interaction potentials. The nondimensionalized second virial coefficient is extracted from numerical integration of the interaction potentials as [87],

$$B_2^* = 1 - \frac{3}{8R^3} \int_R^\infty dr\, r^2 \left[\exp(-\beta U(r)) - 1\right], \tag{4.15}$$

In the above $B_2^* = B_2/B_2^{\mathrm{HS}}$, with $B_2^{\mathrm{HS}} = 16\pi R^3/3$ representing the virial coefficient of hard spheres of radius R. In the semi-grand canonical formalism used to compute the pair potentials, the polymers are at a fixed chemical potential. Thus, the equilibrium of the polymer component between the different phases is implicitly ensured. To ensure the equality of the chemical potential and the osmotic pressure of the particle phase, we use an approximate equation of state for the particle phase based on virial expansion:

$$\beta A_{ex} = \frac{\eta_c(4 - 3\eta_c)}{(1 - \eta_c)^2} + 4[B_2^* - 1]\eta_c^2 \tag{4.16}$$

where A_{ex} denotes the excess Helmholtz free energy of the particle phase. The hard sphere free energy for the particles is approximated using the Carnahan-Starling(CS) [86] form and is given by the first term in the above expression. The polymer-mediated interactions to the Helmholtz free energy of the system is approximated at second virial level and is given by the second term in Eq. 4.16. More information on the details and approximations involved in this model are also discussed in the previous chapter 3. To delineate the phase diagrams in $\eta_c - \phi_{\rm o}$ plane, B_2^* corresponding to a fixed $\phi_{\rm b}$ is obtained by using the mean-field based pair-interactions. The packing fractions in the coexisting phases η_c^1 and η_c^2 are then determined by performing common tangent construction on the A_{ex} (Eq. 4.16). Finally, using the coexisting η_c's we determine the coexisting $\phi_{\rm o}$ using Eq. (4.12).

In Fig. 4.9, we display the fluid-fluid coexistence curves (and the percolation thresholds computed in the previous section) for three particle sizes $R/R_{\rm g} = 1.0, 0.5$ and 0.25. It should be noted that the coexistence curves shown here are for polymer concentrations mostly in the semidilute regime. At extremely dilute polymer concentrations ($\phi_{\rm bulk} \rightarrow 0$), one expects a weakening of the effective attractions due to the absence of sufficient polymers to cause bridging interactions. However, the mean-field model in this study is not expected to be directly applicable to this lower region of polymer concentration, and so the lower boundary is indicated schematically to acknowledge its existence, and the features of phase diagram are discussed mainly in terms of the upper phase boundary for the two-phase region.

For all the particle sizes, generically a fluid phase is observed at low polymer concentrations (below the schematic lower boundaries), followed by a bridging-induced phase-separation at higher polymer concentrations and subsequently a stable mixture regime at even higher polymer concentrations. The latter stabilization arises as a consequence of the saturation of the adsorption and the repulsive effective interactions at the higher polymer concentrations.

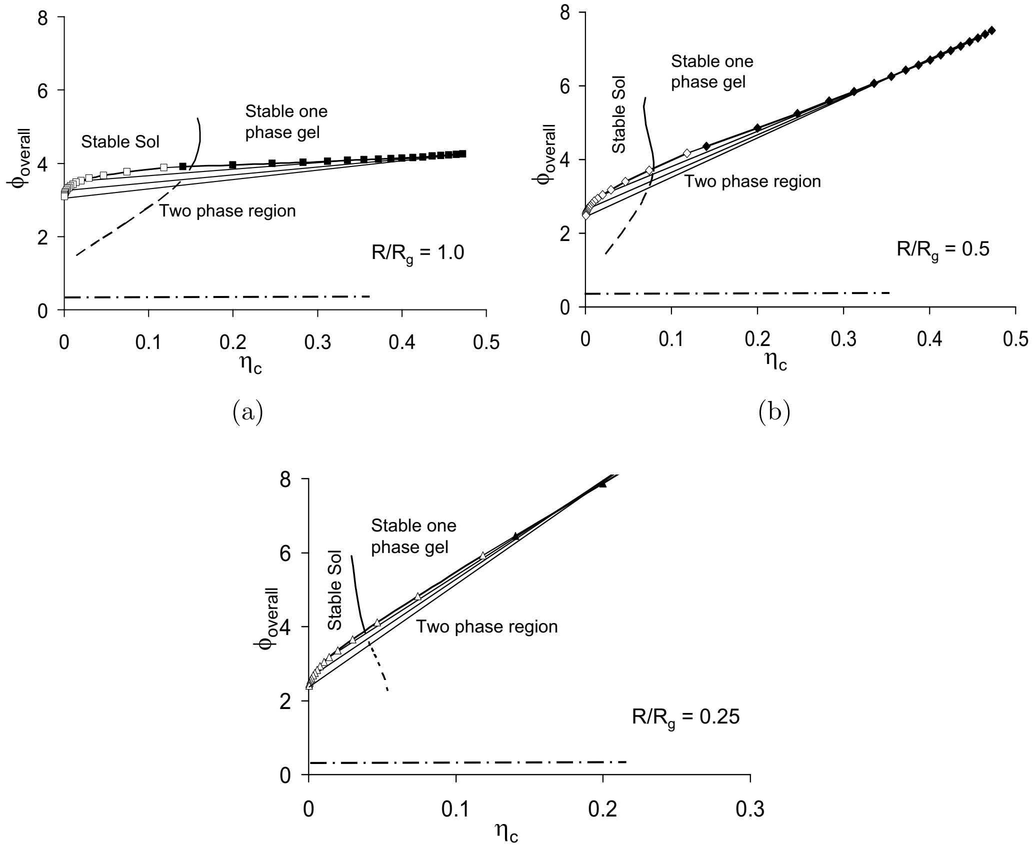

(a)

(b)

(c)

Figure 4.9: Fluid fluid co-existence curve (open and filled symbols) and percolation line (solid line continued as a dotted line into the region of coexistence) in the $\phi_{\text{overall}} - \eta_c$ plane. The area above the co-existence curve shows the one phase region and that below each curve represents the two phase region. The compositions of the coexisting phases are shown by tie lines joining the "floc" (filled symbols) and supernatant (open symbols) compositions. The lower boundary for the two phase region is displayed schematically by dash-dot line. Area to the left of percolation line shows fluid phase and that to the right represents percolated phase: (a) $R/R_{\text{g}} = 1.0$; b) $R/R_{\text{g}} = 0.5$; (c) $R/R_{\text{g}} = 0.25$.

These predictions are qualitatively in agreement with experimental observations in the context of silica/PEO and Laponite/PEO mixtures, where increasing the polymer concentrations have been shown to lead to a transition from macroscopic flocculation to a sterically stabilized dispersion [26, 48]. As discussed earlier, these trends arise from the second virial coefficients B_2^* values which transform from attractive characteristics to repulsive behavior with an increase in the polymer concentrations. The predictions of Fig. 4.9 are also in qualitative agreement with the results in the context of PEG-Lysozyme mixtures (where weak adsorption interactions are expected to prevail) in which a repulsive upturn in B_2^* values were observed with an increase in the polymer concentrations [18].

It is evident from Figs. 4.9 that the relative polymer-particle sizes play an important role in influencing the structure and phase behaviors. At dilute particle concentrations, it is observed that a lowering of the R/R_{g} ratio shifts the upper boundary of the two phase region to lower polymer concentrations. The latter suggests that polymer-nanoparticle mixtures involving smaller particles at dilute particle concentrations tend to become miscible at much lower polymer concentrations compared to the larger particles. This is again consistent with experimental phase behavior for PEO/silica particles [114], where at high pH and low ionic strength, corresponding to conditions that promote reversible adsorption, experiments have reported an increase in miscibility of the mixtures with a decrease in the size of the particle.

A second particle size effect is observed in the compositions of the coexisting phases denoted through the tie lines (shown by the lighter lines). For larger particles, the concentrations of polymer in the two coexisting phases are observed to be more or less the same. The latter suggests that the phase separation in such systems occurs into a particle-rich and particle-depleted phase, both however rich in polymers. On the other hand, for smaller particles, the phase separation is into a supernatant phase that is dilute in both the polymer and the particles, whereas the "floc" phase is rich in both the polymer and particles. The latter trends are consistent with the phenomena of "complex coacervation" commonly observed in the context of protein-polysaccharide mixtures [9] and arise due to the significant adsorbance (cf. Fig. 4.1) of the small particles compared to the larger ones.

The percolation thresholds and the occurrence of a stable one-phase gel are also found to be highly dependent on the size of the particles, which contrasts with the expectations from random percolation theories where the critical volume fractions are independent of the size of the particles [128]. The particle volume fraction for the formation of a one-phase gel are observed to actually shift to very dilute ranges ($\eta_c \simeq 0.05$) for small particles. The latter is in qualitative agreement with many experiments which have observed (indirectly through rheological signatures) the formation of networked structures at extremely low volume fractions for small particles [25]. Interestingly, it is observed that dilution of the single-phase gels for small particles can lead to the formation of a homogeneous (sol) phase, whereas in the case of larger particles it leads to a flocculation-induced phase separation. The latter predictions are

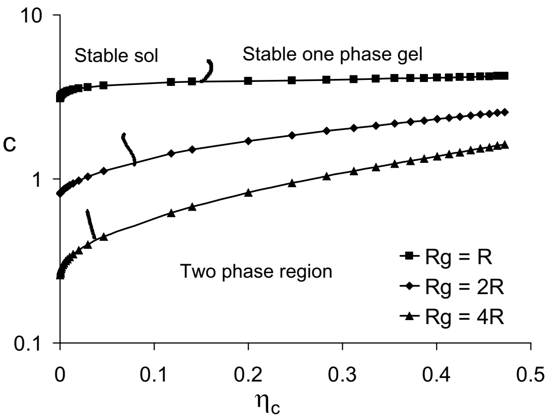

Figure 4.10: Fluid fluid co-existence curves (symbols) and percolation lines (solid lines) in the $c - \eta_c$ plane for $R_{\mathrm{g}} = R, 2R$ and $4R$.

qualitatively similar to the size effects noted during the dilution experiments of Cabane *et al.* [129]

While the results displayed in Fig. 4.9 present an intuitive picture for experiments where the size of the polymer is kept a constant while the particle sizes are varied, an alternate experimental protocol is one where the particle sizes are kept constant while the polymer molecular weights (MW) are varied [29]. Increase in MW decreases the crossover density ρ_p^* for the polymer, resulting in an increase in the normalized bulk polymer concentration, $\phi_{\mathrm{bulk}} = \rho_p/\rho_p^*$. The phase diagrams for such a scenario can be straightforwardly obtained from the results of Fig. 4.9 and are displayed in Fig. 4.10 with "c" now denoting the polymer monomer concentrations expressed in units of particle volume. It is evident that the differences in the phase and percolation behavior of the different sized particles become pronounced in this representation. For instance, for large polymers, the majority of the phase plane is occupied by the region of single-phase gels. However, for smaller polymers such regions do not manifest until much larger particle concentrations. Secondly, it is observed that the region of immiscibility for larger polymers occurs only at very dilute polymer concentrations. On the other hand, for smaller polymers, the region of flocculation-immiscibility occupies the majority of the phase space.

In summary, the effective attractions induced by the polymers are observed to lead to immiscibility of polymer-particle mixtures. The latter is expected to lead to a closed loop miscibility of the polymer-particle mixtures. The results suggest that the size of particles plays an important role in controlling both the quantitative features of the stability and the percolation behavior of the mixtures. It should be noted that this analysis uses equilibrium bridging characteristics and thus, may not capture the non-equilibrium effects which manifest in many experiments [130]. Secondly, many experimental situations involve an interplay between polymer physisorption and electrostatic interactions which are neglected in the present models [131]. Despite these limitations, the qualitative agreement with many experimental observations suggests that the results of this chapter provide a useful framework to understand the stability characteristics of polymer-nanoparticles mixtures.

4.5 Conclusion

In this chapter, the structure, pair interactions and phase behavior of nanoparticle-polymer mixtures where the polymers can adsorb onto the particles are examined. A "saturable adsorption" model is proposed to account for the surface saturation effects observed in adsorption of polymer onto a solid surface. Using polymer self consistent field theory, the effect of particle size, bulk concentrations and the surface saturation on the above characteristics is investigated. The results indicate profound size effects upon the adsorption and pair interaction characteristics. For a single particle, the curvature of the particle is found to significantly enhance the total adsorbed amount, but however most of the adsorbed polymer were found to be present in the form of long tails that extended to a distance of $\simeq 2R_{\mathrm{g}}$ from the particle surface. In the case of pair interactions, the curvature effects interplay with adsorption, saturation and excluded volume interactions to determine the resulting features. Generically it is observed that for lower polymer concentration, the interactions between adsorbed layers are attractive. Whereas, for intermediate polymer concentrations, the interactions are attractive at large distances and become repulsive as the surfaces are brought closer. The strength and the range of pair interactions also depends critically on the particle-to-polymer size ratio R/R_g.

We also analyzed the phase behavior and structure of polymer-nanoparticle mixtures in terms of critical percolation densities and second virial coefficients. For low polymer concentrations, our results suggested that the bridging attraction leads to flocculation and phase separation of polymer nanoparticle mixtures. In contrast, at higher polymer concentrations the interparticle repulsions induced by the polymer excluded volume interactions stabilize the mixture. Our mean field models also predict a significant decrease in the percolation thresholds and an enhancement in the stability of the mixtures upon a decrease in the size of the particles. These results were found to be in qualitative agreement with the related experimental observations.

In the present chapter, we have displayed a set of representative results to describe the effect of surface saturation, polymer concentration and size of the particle on the interparticle potentials. These results are obtained at a fixed segment-surface interaction parameter which, as mentioned earlier, corresponds to the situation of weak to intermediate adsorption strength. Although the actual magnitude of the adsorption interaction parameter will affect the quantitative features of adsorption characteristics, we expect the qualitative features to remain unchanged within the weak adsorption regime. For instance, an increase in the strength of segment-surface interaction is expected to enhance the adsorbance, and hence the strengths of pair interactions will be correspondingly higher. Further, at higher adsorption strength, we expect the surfaces to be saturated at a much lower bulk polymer concentrations. The latter is expected to shift repulsive interactions to lower bulk concentrations. These changes will also affect, albeit in a predictable manner, the resulting phase behavior of the system.

The above framework presents many generalizations which are pursued in the subsequent chapters. In the subsequent chapter, the effective interactions and the conformational characteristics determined in this chapter are supplemented with more detailed information regarding the bridging chains to develop models for the rheological characteristics of the system.

Chapter 5

Gelation in Mixtures of Polymers and Particles

Recently, the properties of polymer-nanoparticle mixtures (also referred to as polymer nanocomposites) have attracted a significant attention in many contexts. Many experiments have shown that the addition of even small loadings of nanoparticles to the polymer matrix can result in order of magnitude property enhancements over that of the neat polymer [25, 28, 29]. These observations have sparked interest in the potential of such materials to serve as lightweight, high strength materials with desirable barrier properties. While the role of microscopic interactions between the polymer and particle component in determining such properties is well-agreed, the fundamental parameters governing such interactions and their explicit relationship to the macroscopic properties themselves are still not well understood. As a consequence, tuning the properties of such materials and designing new materials with desired properties remain a challenging task.

The focus of this chapter is towards the rheological properties of polymer nanocomposites and their dependence on the various microscopic parameters. Many experiments on the rheology of nanoparticle-polymer suspensions have reported dramatic enhancements in the low frequency elasticity (storage modulus) at very low loadings of the particles [25, 28, 31]. At least two proposals have been advanced to explain these observations. The first mechanism implicates the direct particle-particle agglomeration resulting from depletion and van der Waals interactions. For instance, experiments by Weitz and coworkers [132] studied the clustering of PMMA particles induced by depletion of polystyrene and have shown that (in the colloid limit, where the particle sizes R are larger than the size of polymers R_{g}) such particle agglomerated gels can form at low volume fractions of particles. Similarly, Zhu *et. al.* [133] examined the viscoelastic characteristics of Silica filled polymer melts and also presented evidence for the role of "direct" or nonpolymeric filler-filler networks in controlling the reinforcement of such filled polymeric systems.

The alternative mechanism implicates polymer-bridging induced gelation of particles as responsible for the enhancements in the elastic moduli of the composite. Several experimental results supporting this mechanism are available. For instance, in many experiments, the effects on the mechanical properties manifest at particle loadings far below that expected/required for particle gelation. For instance, for systems of PEO containing silica nanoparticles, Zhang and Archer have observed a transition to solid-like viscoelastic response at silica loadings as low as 2 % [25]. More pertinently, they observed that systems involving bare silica particles where the polymer-particle interactions are strongest also induce the strongest reinforcement. Similar results were also observed by Macosko *et al* in the context of Silica particles mixed with PDMS matrix [32].

Broadly, one can expect that in cases where the polymer is incompatible with the particles, the particles will experience strong polymer-mediated attractions leading to a non-equilibrium gelation either through diffusion limited (DLCA) or by a reaction limited (RLCA) cluster aggregation mechanism. Gels resulting from such process have been well-characterized, and the fractal dimension d_f of such gels have been suggested to be around $d_f = 1.8$ for DLCA and $d_f = 2.1$ for RLCA. The scaling dependence of elastic moduli on the volume fraction of particles, η, is of the form $G' \propto (\eta - \eta_c)^{\nu_\eta}$ where the exponent $\nu_\eta \approx 3.4$ and η_c represents the percolation threshold [132, 134]. In contrast, one can expect that a polymer-bridged gel will form when the polymer is compatible with the particles (so that it adsorbs and wets the particle surfaces). However, in contrast to the preceding case, very little information is available on the characteristics of the networks formed by such processes. The unresolved questions include, "What is the percolation/gelation threshold for such polymer bridged gels ?" "How does the percolation volume fraction depend on the size of the polymer relative to the size of particles ?" "How does the elasticity of the networks formed depend on the volume fraction of polymers, polymer concentration, adsorption strength, surface coverage of adsorbable groups ?" "Is there a universality for the elastic behavior of polymer-bridged gels ?" Resolution of these issues is expected to prove important in both understanding the origin of properties of nanoparticle systems and in allowing one to tune the macroscopic properties of such systems.

In the previous chapter, we introduced a 'saturable' adsorption model to mimic the adsorption of polymers onto nanoparticles with a specified maximum adsorption capacity. Explicitly, our study predicted that polymer adsorption on small particles is characterized by the dominance of long tail-like structures extending to a distance of about the radius of gyration R_{g} of the polymers. Secondly, our results also suggested that the polymer-mediated interparticle interactions tend to weaken with a decrease in the size of particles and/or an increase in the concentration of polymers. We used simple analytical models to suggest that the above features lead to a significant increase in the miscibility of the polymer-particle mixtures upon a decrease in the size of the particles. Specifically, in the nanoparticle regime where the size of particles R becomes comparable to or smaller than the radius of gyration of polymer R_{g}, the phase diagrams were predicted to display a large region of stable single phase regime where polymer-bridged gels could form. In the present chapter, we use a novel simulation approach which combines the framework of the previous chapter with Monte Carlo simulations of the many particle system to study the formation, structural characteristics (such as percolation threshold, fractal dimension) and the elastic moduli of polymer-bridging induced gels. It should be emphasized that the present framework is an equilibrium approach and does not account for the time scales involved in the formation of polymer-networked gels. Explicitly, the gelation of particles is quantified through the equilibrium probability of interparticle bridging at a given distance. A cluster is then identified as a series of interconnected particles. In the present approach first the mean field formalism is extended to quantify the conformational characteristics of polymer chains in presence of particles. The latter includes quantities such as the number and probability distributions (as a function of interparticle distance) of interparticle bridges. Subsequently, these microscopic features are used in a Monte Carlo simulation framework to analyze the clustering characteristics, percolation thresholds, structure and the elasticity of the structures. Explicitly, we probe the role of the size asymmetry between the polymer and particle components, the affinity of the polymer to the particle surface (i.e. the adsorption strength), the concentration of the polymer and the adsorption capacity of the surface in influencing the structural characteristics of gels.

Other prior theoretical approaches have focused on the structure, rheology of polymer-mediated gels in colloid/nanoparticles suspensions. However, most of these studies pertain to depletion-induced gels, where the particle clustering is induced by the polymer-mediated attractive interactions between the particles arising from the depletion of polymers in the vicinity of the particles [132, 134–138]. The present work differs from these prior researches in that the focus is upon the gels and clustering arising primarily from the polymer bridging between the particles. In broad terms, most of the previous researches focus on the ‘attractive’ glass gels which result at higher volume fractions of particles ($\eta \sim 0.4$). In contrast, as we will demonstrate later, the bridging-induced gelation occurs at much lower volume fractions of particles ($\eta \sim 0.02$).

The rest of the chapter is arranged as follows: In section 5.1, we detail the Monte Carlo simulation approach with the methodology used for characterizing the cluster statistics and the percolation thresholds. In Section 5.2 we present results elucidating the effects of polymer concentration, relative sizes of the polymer and the particles, the adsorption strength and surface saturation on the size, number and probability distributions of polymer bridges. In section 5.3, we present our results for the cluster statistics, percolation threshold and structural characteristics obtained from the simulations. We relate the bridging statistics obtained from the simulations to the elasticity of the network and discuss the effects of different parameters on the latter. We conclude with a discussion of our results.

5.1 Structure and Elasticity of Polymer-Particle Mixtures

In order to determine the structural features, clustering behavior and connectivity in the polymer-particle mixtures, we propose a hybrid simulation scheme, which combines the thermodynamic interactions with the microscopic structural characteristics. To perform the connectivity simulations detailed later we need the probability that two particles at a given distance are connected. For this we assume that the probability to form interparticle bridges between k neighboring particles to follow a Poisson distribution $M_{\mathrm{br}}(r)^k/k! \exp(-M_{\mathrm{br}}(r))$. Here, $M_{\mathrm{br}}(r)$ represents the average number of bridging chains between the particles at an interparticle distance r and is obtained using eq. 2.47. The probability of formation of at least n interparticle bridges at an interparticle distance r between the particles (or equivalently, the probability that the particles are connected to each other through n bridges) then follows as [126, 127],

$$P_{\mathrm{br}}^{n}(r) = 1 - \sum_{k=0}^{n-1} \frac{M_{\mathrm{br}}^{k}}{k!} \exp[-M_{\mathrm{br}}(r)]. \tag{5.1}$$

Simulation Methodology

The simulation methodology consists of two parts. We use Monte Carlo simulations of a system of particles interacting with the effective pair interaction potentials discussed in the preceding section. The simulations employ a semi-grand canonical framework where the number of particles N_c and the polymer activity coefficient Z are fixed. The grand canonical implementation of SCFT used in the McMillan-Mayer framework allows us to utilize the polymer structural characteristics (discussed in section 2.3) and interparticle interaction potentials (discussed in Section 2.1) in the Monte Carlo simulations. We use a Metropolis algorithm to generate the equilibrium configurations of particles for a given interparticle potential.

In principle, at a given activity coefficient Z of the polymer, the concentration of polymer at infinite dilutions of particles and the overall polymer concentration at finite particle volume fraction can be quite different (cf. Section 4.4). However, for the dilute particle concentration limits of the mixture considered in this chapter (since percolation/gelation is observed to occur in dilute limits), the polymer concentrations at finite particle concentration are expected to be close to the values at infinite dilution of particles. Hence we ignore this distinction between the polymer concentrations and report our simulation results based on the 'infinite dilution' polymer concentrations.

The second aspect of the simulation framework deals with generating and sampling of the particle clusters. The statistical distributions of particle clusters are analyzed using the connectivity matrix algorithm proposed by Sevick *et. al.* [139] We define a cluster as a set of particles which are connected to each other directly or indirectly (through other particles) through polymer bridges. Whether a particle is directly connected is determined based on the bridging probability $P_{\mathrm{br}}(r)$ (cf. Eq. 5.1) and is achieved by randomly generating bonds between the particles. Subsequently, the bonds are accepted based on the bridging probabilities at a given distance r. Continuing this procedure for all pairs of particles results in a symmetric direct connectivity matrix C^D, where $C^D_{ij} = 1$ if the particles i and j are connected and $C^D_{ij} = 0$ otherwise. We then follow the method outlined by Sevick *et. al.* to obtain the complete connectivity matrix corresponding to this direct connectivity matrix. From direct and complete connectivity matrices, different aspects of cluster statistics are extracted: (i) The cluster size distribution, $m(n)$, representing the number of clusters of size n; (ii) The average size of the clusters, $\bar{n}$ defined as [140],

$$\bar{n} = \frac{\sum_n n^2\ m(n)}{\sum_n n\ m(n)}; \tag{5.2}$$

(iii) The average number of clusters, $\int_1^N m(n)\ dn$; (iv) The mean coordination number of the particles in a cluster z, which represents the number of particles directly connected to a given particle. The latter is obtained from the number of non-zero elements in a column of direct connectivity matrix as,

$$z = \frac{1}{N}\sum_{i=1}^{N}\sum_{j=1}^{N} C_{ij}^{D} - 1.0. \tag{5.3}$$

Subtraction of 1.0 in the above equation ensures that the diagonal elements are not included in the calculation of coordination number; (v) The radius of gyration R_{gc} of a cluster of size n, defined as [141],

$$R_{gc}(n) = \frac{1}{n}\sum_{i}^{n}(\mathbf{r}_i - \mathbf{r}_{CM})^2, \tag{5.4}$$

where $\mathbf{r}_{CM} = 1/n\sum_i^n \mathbf{r}_i$ is the center of mass of the cluster. The fractal dimension d_f for clusters is defined through,

$$R_{gc} \propto n^{1/d_f}. \tag{5.5}$$

In determining d_f, we exclude clusters consisting of only a small number of particles; and (vi) The percolation volume fraction η_c is determined by searching for a cluster where a particle is connected to its replica in the neighboring simulation boxes. In principle, this requires replicating the simulation box into 26 copies and generating polymer bonds between the particles in different boxes [140]. However, this process proves computationally expensive and we circumvent this by replicating only such particles that are within a bridging cut off distance, $r_{\text{cut}}^{\text{br}}$ (the interparticle distance where the probability of formation of bridges goes to zero) from the simulation box and then generating the polymer bonds for only these particles. For the systems studied in this work,

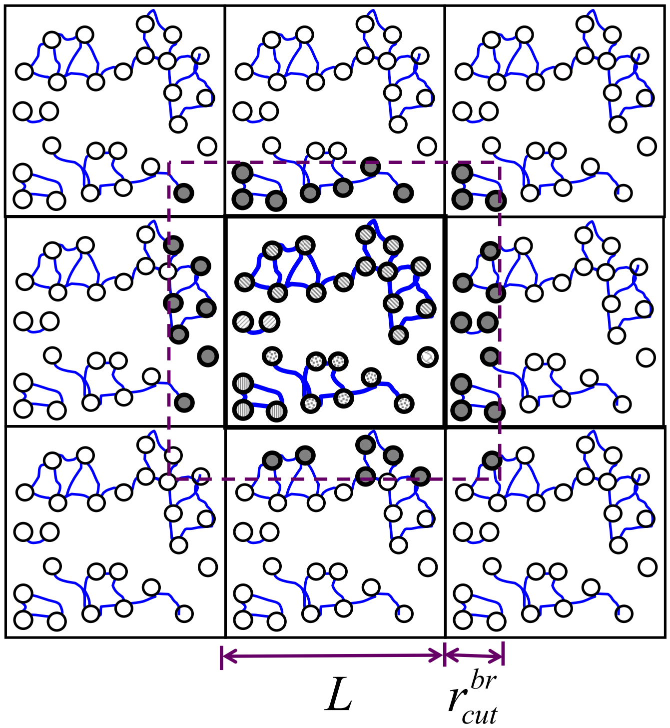

Figure 5.1: Schematic showing determination of 'self connected' cluster. In order to identify a percolated structure, it is necessary to replicate the simulation box 26 times for a 3-D simulation. In this work, the percolated structure is determined by searching for a self connected particle within a 'bridging cut-off' distance $r_{\text{cut}}^{\text{br}}$ for the simulation box and only a part of simulation box is replicated, shown here schematically by dotted lines.

$r_{\mathrm{cut}}^{\mathrm{br}}$ is around $.05 - 0.2$ times the box length and implementing this procedure results in a considerable reduction in the computational time. The percolation probability P is then defined as the fraction of the total number of equilibrium configurations where such a cluster containing 'self-connected' particles is found. We define the percolation threshold, η_c as the volume fraction where this percolation probability reaches 50 % representing the clusters being connected to themselves. We note that though this choice of 50% self-connected configurations is arbitrary, a number of simulation studies have shown that it shows the least finite size effects and is reported to give reliable estimates of percolation thresholds and critical exponents [142–144].

Simulation Details

The initial configuration for the particles was chosen to be a face centered cubic lattice. The Monte Carlo simulations were then carried out in a cubic box with periodic boundary conditions imposed in all three directions. Each simulation consisted of 10000-15000 MC moves with 1000 equilibration moves which are not counted in averaging the cluster statistics. Each MC step involved on an average one displacement move per particle. The cluster statistics was sampled at every fifth MC iteration after equilibration of the system. Despite enforcing the periodic boundary conditions, simulation results for percolation thresholds can be very sensitive to the size of the system. To probe the effect of finite system size in our simulations, we performed the simulations for different system sizes containing $N = 256, 400, 500, 600, 864$ particles. For these system sizes, the mean coordination numbers, the percolation thresholds, and the fractal dimensions were found to be unaffected by the size of the system. The simulation results reported in the rest of the chapter correspond to systems of 864 particles. The analysis of results suggests that the statistical errors arising from the finite system size are within 10% for all the data reported here.

Parameters

The objective in this chapter is to study the role of parameters such as polymer-to-particle size ratio, polymer concentration and adsorption strength in determining the onset and structure of the gel phase. Focusing on the nanoparticle regime (where particle size is comparable to/or smaller than the size of the polymer), the particle-to-polymer size ratios (equivalent to changing the polymer molecular weight) are varied from $R/R_{\mathrm{g}} = 2.0$ to $R/R_{\mathrm{g}} = 0.5$. We primarily consider polymer concentrations in semi-dilute regimes under "good solvent" conditions for the polymer. The non-dimensional excluded volume parameter $B = vN^2/R_{\mathrm{g}}^d$ is chosen to be 10. In the following, all polymer concentrations are normalized by the overlap concentration, ρ^* as $\phi = \rho/\rho*$. The presented results correspond to $\phi > 1.0$ indicating the semidilute concentration regime. In addition, the case of polymer melt is also considered, where the excluded volume interactions between the polymer chains are assumed to be screened. For illustrative purposes, the bulk polymer concentrations are selected such that for the particle sizes considered in this chapter, the polymer-particle mixtures correspond to the stable one phase region of the phase diagram (cf. Fig. 4.9). The nondimensional adsorption strength, $\lambda = \lambda' \ N/R_{\mathrm{g}}$ is varied from 10 to 20. These adsorption strength values correspond to moderate to high affinity between polymer segments and the particle surface. The effect of change in the surface capacity for adsorption is studied by varying the surface saturation concentration from $\phi_{\mathrm{m}} = 8.0$ to 12.0.

5.2 Microscopic Conformational Characteristics

The gelation characteristics of polymer-particle mixtures are expected to be determined by two microscopic features, viz., (i) The interaction potentials which control the average interparticle distances and structure of gels; and (ii) The probability of formation of polymer bridges between the particles at a given interparticle distance. As discussed in the previous chapter, the pair interaction potentials are strongly influenced by parameters such as particle size, polymer concentration, adsorption strength and surface saturation. Fig. 5.2 displays a summary plot of the interaction potentials as a function of interparticle distance (normalized by radius of particle, R) for various physical parameters considered in this chapter. Generically, a decrease in the size of the particles is observed to result in weaker pair interaction potentials. Moreover, at lower polymer concentrations, the overall interactions were dominated by the interparticle bridging and displays a monotonic attraction with decrease in the interparticle distance. However, an increase in the polymer concentration increases the conformational entropy losses for the adsorbed polymer

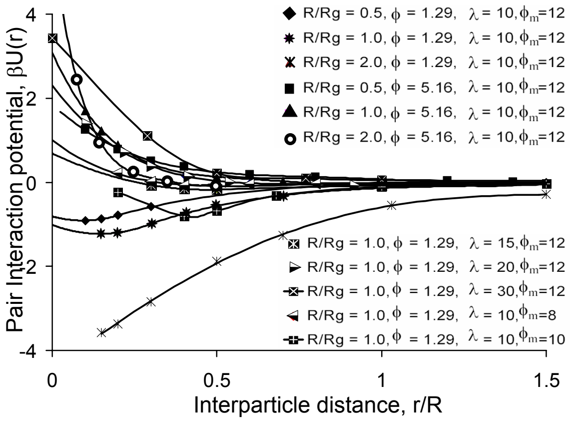

Figure 5.2: Interaction potentials $\beta U(r)$ as a function of interparticle distance, d/R, for different parametric conditions considered in this chapter.

and renders the interactions nonmonotonic — attractive at large interparticle distances and repulsive at smaller distances. At even higher polymer concentrations, the interparticle interactions are seen to become purely repulsive due to the increased entropic repulsions. The above listed effects with an increase in the polymer concentration also correspond to the changes occurring during an increase in the adsorption strength λ and/or a decrease in the surface saturation ϕ_m.

While the formulation outlined in Section 2.3 can be adapted to extract detailed microscopic polymer conformational features in the polymer-nanoparticle system, in the present chapter attention is restricted to two quantities which are pertinent to gelation and the elastic properties of polymer-nanoparticle mixtures. The first is the probability that at a given interparticle

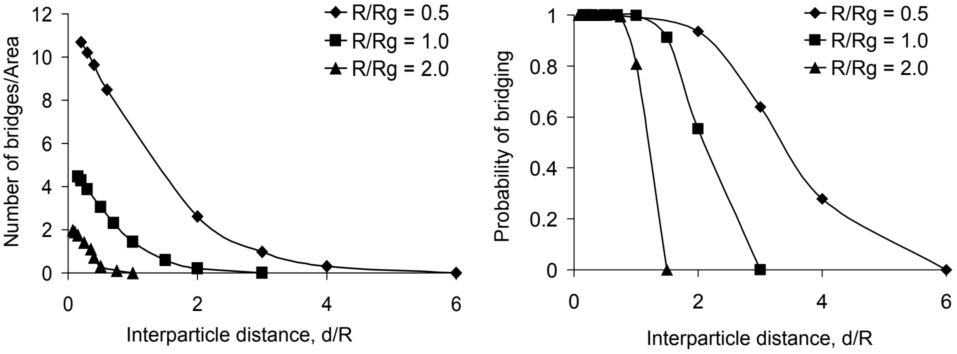

(a) (b)

Figure 5.3: (a) Average number of bridges per unit particle surface area, $N_{\mathrm{br}}/\mathrm{Area}$, as a function of interparticle distance, d/R, for different particle-to-polymer size ratios, $R/R_g = 2.0, 1.0, 0.5$. (b) Probability distribution of bridges, P_{br}, as a function of interparticle distance, d/R, for different particle-to-polymer size ratios, $R/R_g = 2.0, 1.0, 0.5$. The polymer concentration is fixed at 5.16.

distance, d, the two particles are connected, $P_{\mathrm{br}}(d)$. This bridging probability serves as the “gelation potential” in the present model and will determine the formation and the statistics of the clusters. The second quantity is the average number of bridges M_{br} formed between two particles at a given distance d. As will be discussed later, the latter controls the elasticity of the resulting polymer-bridged network. In this section, the dependence of these quantities upon different physical parameters is considered.

In Figs. 5.3a and b, we display the results for the average number of interparticle bridges (normalized by the particle surface area) and probability of bridging as a function of interparticle distance. Since it can be intuitively expected that the number of bridges between two particles will be correlated to their surface areas, it is normalized by surface area to render it a more explicit measure of the size characteristics. It should however be noted that the probability of bridging (Eq. 5.1) is dictated by the number of bridges per particle. It is observed that with a decrease in the size of the particles, there is a significant increase in the number of bridges per unit area. The latter can be rationalized based on the results for adsorption characteristics of the polymers on a single particle, which suggested that with a decrease in the size of the particle, the fraction of segments in tail-like configurations increases. Since the number of bridge-like configurations is expected to be directly related to the number of tail-like configurations, the latter is expected to lead to an increase in the number of interparticle bridges. Another feature observed from Fig. 5.3b is that the probability of the bridging for smaller particles is non-zero even for distances much larger than the size of the particles themselves, reflecting the fact that it is the polymer size which influences the interparticle bridging (we note that the extension of bridges is comparable with R_{g} for all particle sizes).

Figures 5.4a and b illustrate the effects of the polymer concentration ϕ, the surface saturation ϕ_{m} and adsorption strength λ on the number of bridges per unit area and the bridging probabilities. Both the M_{br} and the P_{br} at a given interparticle distance are observed to increase with an increase in either ϕ, ϕ_{m} or λ. As reported in the previous chapter, increase in these parameters leads to an increase in the amount of adsorbed polymer. The increase in the adsorbance results in a concomitant increase in the number of tail-like

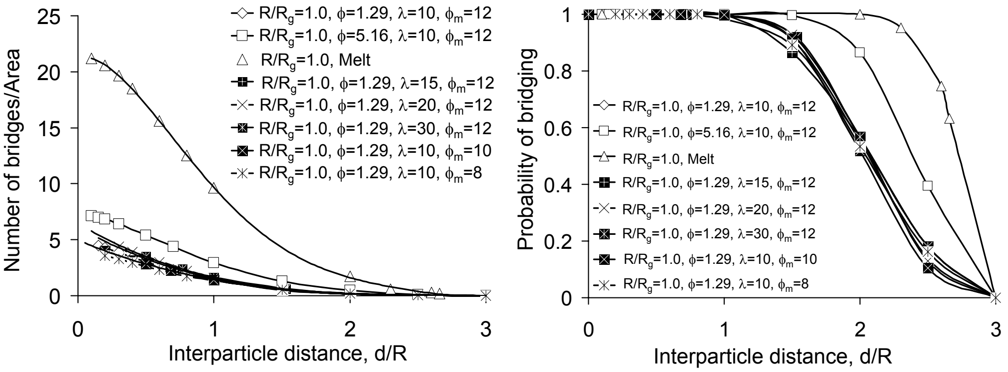

(a) (b)

Figure 5.4: (a) Average number of bridges per unit surface area, $N_{\mathrm{br}}/\mathrm{Area}$, as a function of interparticle distance, d/R, for surface saturations $\phi_{\mathrm{m}} = 12$ and 8 and for $\lambda = 20$ and 10,the bulk polymer concentration $\phi = 1.29$. The size of particle is fixed at $R/R_g = 1.0$. (b) Probability distribution of bridges for the same parameters as in (a).

configurations and interparticle bridges as reflected in Fig 5.4.

To summarize, a decrease in the size of the particles is shown to lead to three distinct effects: (i) It weakens the interparticle interactions which dictate the average interparticle distances; (ii) It increases the probability of bridging at a given interparticle distance d/R and its range relative to the size of the particle; and (iii) It also increases the number of bridges per unit area. Analogous effects are also noted with increase in either the polymer concentration ϕ, the surface saturation ϕ_{m} or the adsorption strength λ. An interplay between such parameters and the resulting competition between the interparticle interactions and interparticle bridging can be expected to determine the onset of percolation, cluster statistics and the elastic moduli of the systems.

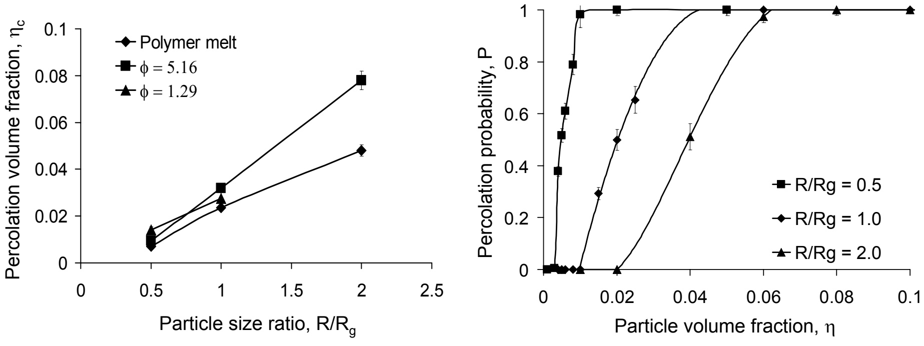

(a) (b)

Figure 5.5: (a) Percolation volume fractions (particle volume fraction at which percolation probability becomes larger than 0.5) as a function of particle size ratio R/R_{g} for polymer concentrations, $\phi = 1.29, 5.16$ and for polymer melt. For $R/R_{\mathrm{g}} = 1$ and $\phi = 1.29$, the attractive interaction potentials induce macroscopic phase separation and are not included in the analysis. (b) Percolation probability (P) as a function of particle volume fraction, η, for different particle-to-polymer size ratios, $R/R_g = 2.0, 1.0, 0.5$ for polymer melt.

5.3 Structure and Elasticity of Polymer Bridged Gels

In this section, we discuss the results of our Monte Carlo simulations for the percolation thresholds, the structural features and the elasticity of the polymer bridging-induced gels and their dependence on the different physical parameters.

Percolation Thresholds

In Fig. 5.5a, we display the percolation thresholds for different particle sizes and polymer concentrations (including polymer melt). We observe that independent of the polymer concentrations, the percolation thresholds decrease substantially with a reduction in the size of the particles. On the other hand for a fixed particle size, lowering ϕ is observed to increase the percolation thresholds for the case of $R/R_g = 0.5$ while for $R/R_g = 1$, percolation thresholds initially increases upon lowering ϕ, and decreases upon further dilution of the polymers. For $R/R_{\mathrm{g}} = 2.0$, the percolation thresholds also increase upon lowering ϕ, but eventually undergoes macrophase separation for $\phi = 1.29$, and hence is not included in this analysis.

To understand the above results, in Figs. 5.5b, we display the probabilities of finding a percolated cluster as a function of particle volume fraction for the case of polymer melt where the particles interact through purely hard sphere interaction potentials. In such cases, the particle clustering is governed solely by the polymer-bridging and thereby explicitly illustrates the effect of particle sizes on the bridging-induced aggregation. For such a situation, the decrease in the percolation thresholds can be attributed to the more pronounced tendency to form interparticle bridges with a decrease in the size of the particles. Indeed for the hard sphere interaction, at a fixed particle volume fraction η, the average interparticle distance d/R is identical for all the particle sizes. However, as seen from Fig. 5.3, for smaller particles, the probability of bridging $P_{\mathrm{br}}(d/R)$ is much higher and is non-zero upto larger distances as compared to that for the larger particles.

To understand the effect of polymer concentration, it is noted from Fig. 5.4a that with a decrease in the polymer concentrations, the number of bridges per unit area decreases. However, the two polymer concentrations considered in Fig. 5.5a also correspond to qualitatively different interparticle interactions (cf. Fig 5.2): (i) For the polymer concentration $\phi = 5.16$ the pair interactions are purely repulsive, with the overall strength of repulsion increasing with an increase in the size of the particles. (ii) At $\phi = 1.29$ the interparticle interactions show a non-monotonic behavior with attractions at large interparticle distances followed by repulsions at smaller distances, with the strength of the attractions increasing with the size of the particles. For the case of $\phi = 5.16$, the observations can be rationalized in terms of the combined effect of the decrease in the number of bridges as well as the influence of the polymer-induced repulsions which serve to increase the average interparticle distances relative to the case of polymer melt. Based on the earlier discussion the dependence of these features upon the size of the particles, it is also intuitive that the percolation thresholds are higher for the larger particles. At polymer concentration $\phi = 1.29$, for $R/R_{\mathrm{g}} = 0.5$, the probability of finding particles at closer distances increases due to the polymer-mediated attractive interactions. For $R/R_{\mathrm{g}} = 0.5$ the induced interparticle attractions are weak and the resulting decrease in the interparticle distances is not sufficient to overcome the lower probability of formation of polymer bridges (at an interparticle distance), whence an increase in the percolation threshold is observed. In contrast, for larger particles, the interparticle attractions are much stronger and compensate the decrease in bridging probabilities resulting in an apparent decrease of the percolation threshold with polymer concentration.

The above results correspond to fixed adsorption strength and surface

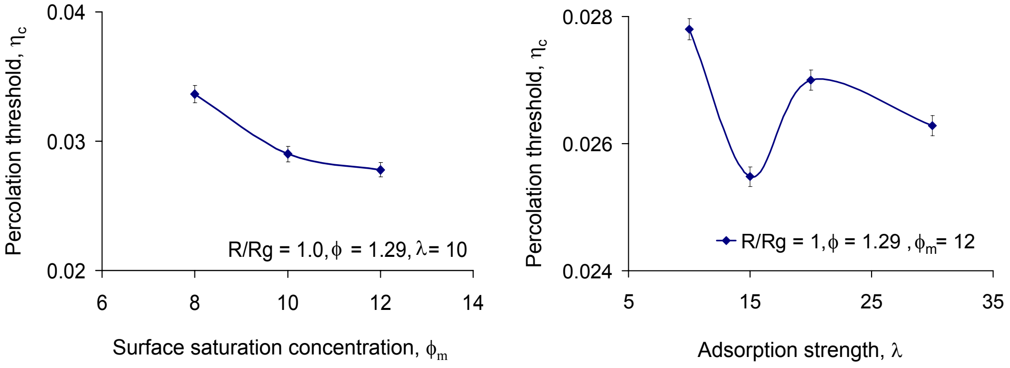

(a) (b)

Figure 5.6: (a) Percolation volume fraction η_c as a function of surface saturation concentration, $\phi_{\rm m}$, for particle-to-polymer size ratios, $R/R_g = 1.0$, $\phi = 1.29$ and $\lambda = 10$. (b) Percolation volume fraction η_c as a function of adsorption strength, λ, for particle-to-polymer size ratios, $R/R_g = 1.0$, $\phi = 1.29$ and $\phi_{\rm m} = 12$.

saturation capacity. In Fig. 5.6a and b, the influence of $\phi_{\rm m}$ and λ on percolation thresholds is analyzed. The percolation thresholds are observed to decrease with an increase in the surface saturation concentrations. This trend can be easily understood from the effect of $\phi_{\rm m}$ on the bridging statistics (cf. Fig. 5.4) and interparticle interactions (cf. Fig. 5.2). An increase in the surface saturation results in an increase in the probability of interparticle bridging at a given interparticle distance and also makes the interparticle interactions attractive. The combined effect of these features manifest in the lowered values of percolation thresholds.

As seen from Fig 5.6b, change in λ results in non-trivial effects on percolation thresholds. With an increase in λ, the percolation thresholds are observed to first decrease followed by an increase at higher λ. This can be understood from the effect of λ on interparticle interactions and on the bridging probability. Increase in λ (at fixed polymer concentration, ϕ and surface saturation ϕ_{m}) induces and strengthens interparticle *repulsions* (cf. Fig. 5.2), thus increasing the interparticle separations, however, it also results in an increase in the probability of bridging at a fixed interparticle distance. For smaller values of λ, the probability of bridging at a fixed interparticle distance is small leading to higher percolation thresholds. With an increase in λ, the enhancement in the probability of bridging counterbalances the increase in the interparticle distances arising due to repulsive interparticle interactions, and the percolation thresholds are observed to decrease. However, a further increase in the adsorption strength increases the interparticle distance further, without an appreciable enhancement in the bridging probability (at a fixed interparticle distance) thus leading to a higher percolation threshold. For large values of λ, the particle surface becomes saturated, beyond which the adsorption strength does not have any significant effect on both the interparticle interactions as well as the bridging probabilities and the percolation thresholds remain fairly unchanged with further increase in λ.

We note that the percolation thresholds for the formation of polymer-bridged gels are in general very low ($\eta_c < 0.1$). These values of η_c are substantially different than that suggested for the case of attractive gels observed in mixtures of non-adsorbing polymer-particle mixtures. In such cases, introduction of short range attraction due to polymer depletion mechanism results in an arrested state termed as ‘attractive glass’ and the fluid to solid transition is predicted to depend on both the strength of attraction and the volume fraction of particles. For purely repulsive interactions between the particles, the transition volume fractions correspond to hard sphere glass transition $\eta_c \approx 0.58$ whereas for the weakly attractive interactions ($U \approx 0 - 1.3$) considered in this study, the predicted transition volume fractions (cf. Eq. 1 in Ref. [134]) for such depletion induced gelation are much higher $\eta_c \geq 0.3$.

Fractal Dimensions

Fractal analysis of network structure near gelation provides an useful tool to understand the morphology of network structures, and establishes an experimental signature to distinguish between different kinds of gels. For the different parameters considered in this chapter, we observed that close to the percolation transition $P \approx 0.5$, the size of the clusters (defined as the number of particles in a cluster) followed a power law dependence with the radius of gyration of the clusters (obtained using Eq. 5.4). We also observed that such power law dependencies were absent for particle volume fractions much lower/higher than the percolation volume fractions. In Fig. 5.7a we display the size of the clusters n as a function of radius of gyration of the clusters R_{gc} for the case of polymer melt and for different particle size ratios at percolation transition. With increase in the size of the particles, we observe that for a fixed size of the clusters, the radius of gyration of the clusters decreases. The latter behavior arises due to higher percolation volume fractions for larger par-

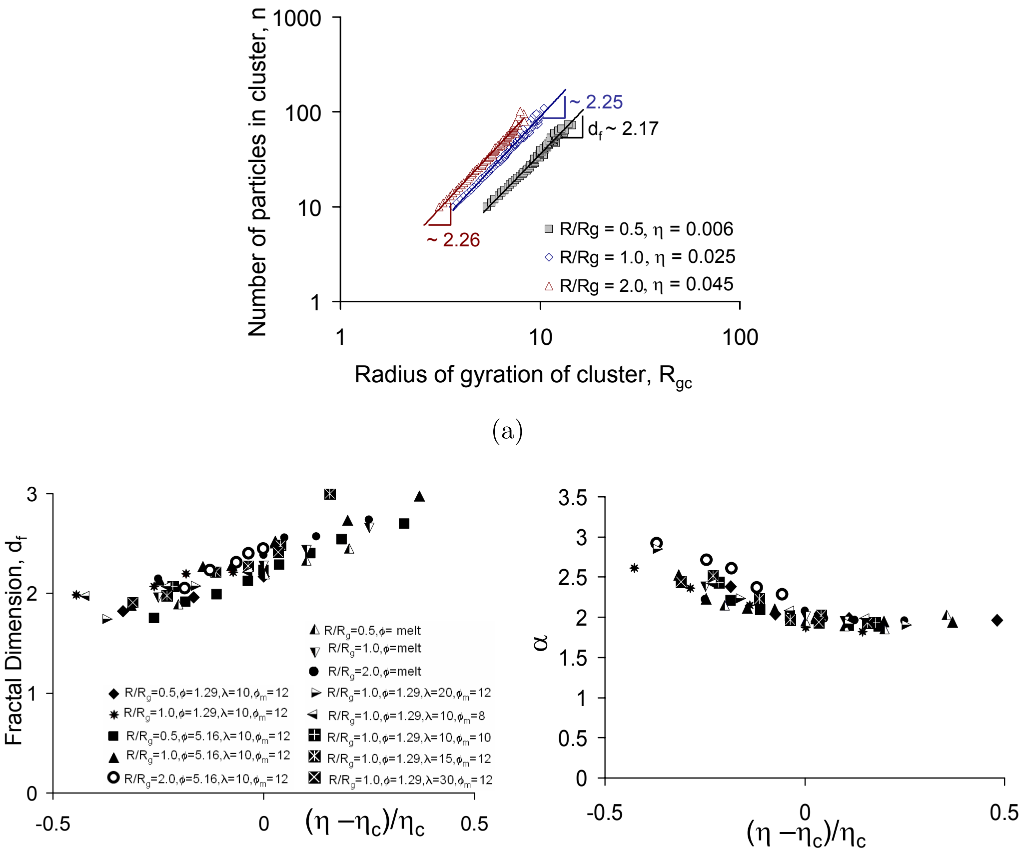

(a)

(b)

(c)

Figure 5.7: (a) Size of the clusters n as a function of radius of gyration of clusters R_{gc}, for particle-to-polymer size ratios, $R/R_{\mathrm{g}} = 2.0, 1.0, 0.5$ for polymer melt. The volume fractions η correspond to percolation thresholds. (b) Fractal dimension as a function of particle volume fraction expressed as $(\eta - \eta_c)/\eta_c$, for particle-to-polymer size ratios, $R/R_{\mathrm{g}} = 2.0, 1.0, 0.5$ for various parametric conditions. (c) The cluster size distribution scaling exponent α $[m(n) \propto n^{-\alpha}]$, as a function of particle volume fraction expressed as $(\eta - \eta_c)/\eta_c$, for particle-to-polymer size ratios, $R/R_{\mathrm{g}} = 2.0, 1.0, 0.5$ for various parametric conditions. The legend of the symbols is same as in Fig. 5.7b.

ticles as compared to the smaller particles. More interestingly, we note that the power law exponents shown in Fig. 5.7a which correspond to the fractal dimensions are insensitive to the size of the particles. To probe this effect further, in Figure 5.7b we present the fractal dimensions (eq. (5.5)) as a function of particle volume fractions expressed as $(\eta - \eta_c)/\eta_c$ for different physical parameters. We observe that close to the percolation transition, the fractal dimensions show a nearly constant value of ≈ 2.2 to 2.4 for the entire range of parameters studied in this chapter. A remarkable feature of this behavior is that the fractal dimension is independent of the nature of interparticle interactions, the size of particles, polymer concentration, surface saturation and the adsorption strength, suggesting that the process of bridging induced aggregation of spherical particles does follow a universal trend. A similar universality is also observed in the cluster size distribution, where the exponent α in the scaling of the number of clusters of size $n, m(n) \propto n^{-\alpha}$ is displayed in Fig. 5.7c. As evident, at the onset of percolation, again the value of α is approximately $2.0 \sim 2.2$ and is universal for the various system parameters.

Similar universalities in fractal dimensions and cluster size distributions have been predicted for attractive colloidal gels and fractal structure resulting in other situations. For particle aggregation induced by short range depletion attractions, Brownian dynamics simulations by Ball *et. al.* [144] predict the cluster size distribution to follow a power law with an exponent $\alpha \sim 2.05$. The corresponding fractal dimensions were reported to be close to 2.5. It should be noted that the values of α and d_f for both the bridging induced gelation and

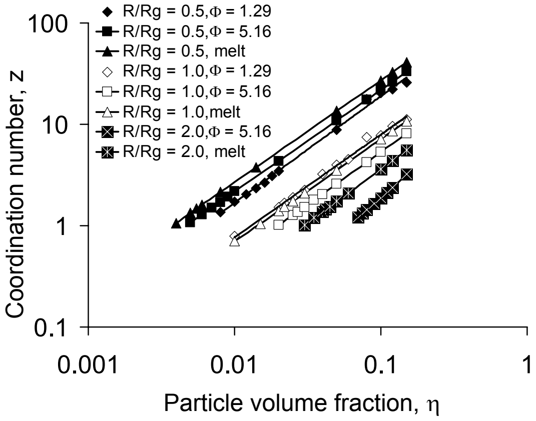

Figure 5.8: Mean coordination number (z), as a function of particle volume fraction, η, for particle-to-polymer size ratios, $R/R_{\mathrm{g}} = 2.0, 1.0, 0.5$ for bulk polymer concentration $\phi = 1.29, 5.16$ and for polymer melt. The error bars are smaller than the sizes of the symbols.

depletion induced flocculation are close to that predicted for the case of random percolation. The cluster distribution statistics and the fractal dimensions can be estimated from the static and dynamic light scattering measurements using the dependence of scattering intensity on the cluster size n and scattering vector q. At high scattering vector $qR_g(n)$, the scattering intensity follows a power law dependence $I(q) \sim q^{-d_f}$ and thus can be used to resolve the structure of fractal aggregates [145]. In this respect, experimental studies can provide a critical test for the universality of the scaling exponents and may prove useful in determining the similarity/differences in the aggregation behavior for the bridging induced gels and depletion induced flocculation.

The degree of connectedness between the particles (quantified by the coordination number, z, eq. (5.3)) characterizes the topological structure of the gel phase and can prove useful in understanding the dynamical phenomena in the polymer-nanoparticle gels. In Fig. 5.8, we display z as a function of particle volume fraction for different particle sizes and polymer concentrations. We observe that for a fixed particle volume fraction, the mean coordination numbers become larger with either a decrease in the particle size and/or with an increase in the polymer concentrations. This trend can be understood in terms of the enhancements in the average number of bridges at an interparticle distance with a decrease in the size of the particle and/or with an increase in the polymer concentrations (cf. Figs. 5.3b and 5.4b). However, the interplay between interparticle attractions and bridging probabilities discussed earlier for $R/R_{\mathrm{g}} = 1.0$ at $\phi = 1.29$ is also evident in the coordination numbers of the gels. For such cases, the strong attractive interactions result in closer interparticle separations, leading to higher coordination numbers than that for the case of $\phi = 5.16$. Broadly, the above behavior suggests a structure which involves highly interconnected gels for smaller particles and loosely connected clusters for larger particles, though polymer concentration can have a non-trivial influence on the particle connectivity.

Elastic Modulus

We use the number distribution of bridges obtained from our simulations to quantify the elastic properties of polymer-nanoparticle mixtures in the post-gel regime. Similar to classical network theories, it is assumed that

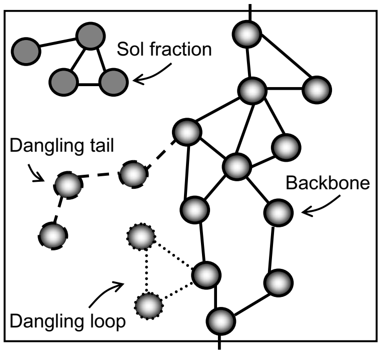

Figure 5.9: Schematic for backbone of a percolated network. The dashed lines and dotted lines indicate dangling end and loop respectively. The solid lines indicate the backbone of the percolated network. The 'sol' fraction is indicated by hashed spheres.

the only contribution to the elastic response of the system comes from the backbone of the percolated network and that the "sol" fraction and the dangling ends of the network do not impart any elasticity to the system. We define the backbone of percolated network as the percolated cluster excluding the dangling tails and dangling loops (see Fig. 5.9) and is identified as the largest biconnected component of a percolated cluster [146]. Since for the present case of bridging-induced percolation, the interparticle bridges serve as the stress bearing bonds between the particles, *the enhancement in the elastic modulus* arising from polymer bridging is assumed to be proportional to the number of such bridges at a given volume fraction of particles and calculate the elastic modulus $\beta G^{'}$ as,

$$D^3 \ \beta G^{'} \approx 4\pi\eta \frac{N_{perc}}{N} \ R_{\mathrm{g}}^3 \ \langle M_{\mathrm{br}} \rangle \tag{5.6}$$

where $D = 2R$ represents the diameter of particle, and $\langle M_{\mathrm{br}} \rangle$ is the average number of bridges per particle in a percolated cluster and is extracted from the Monte Carlo simulations. The factor N_{perc}/N gives the fraction of the particles that belong to the backbone of the percolated clusters and hence contribute to the elastic modulus. This formulation ensures that the polymer bridges that belong to the percolated cluster only participate in the elastic response of the system and correctly yields a zero enhancement in the elastic modulus for non-percolated systems. The above approach is analogous to affine network model for *unentangled* polymer gels [147] where the entanglements between the bridging polymer chains are ignored. For the low volume fractions of particles considered in this study, the fraction of polymer chains in the bridge-like configurations is small relative to the free chains and thus interbridge/interloop entanglements are expected to lead to a negligible contribution to elasticity.

Figures 5.10a and b display the elastic moduli values for gels as a function of particle volume fractions for different particle sizes and polymer concentrations. An increase in the particle volume fractions is observed to result in a monotonic enhancement in the values of G'. The latter is expected since increasing the volume fractions decreases the average interparticle distances and enhances the formation of interparticle bridges. More interestingly, a significant increase in the $G^{'}$ (at a given η) is observed as the particle size decreases from $R/R_{\mathrm{g}} > 1.0$ to $R/R_{\mathrm{g}} < 1.0$. Finally, increase in the bulk polymer concentration is also observed to increase the magnitude of the $G^{'}$. This trend in the $\beta G^{'}$ can be understood from the increase in the surface area resulting

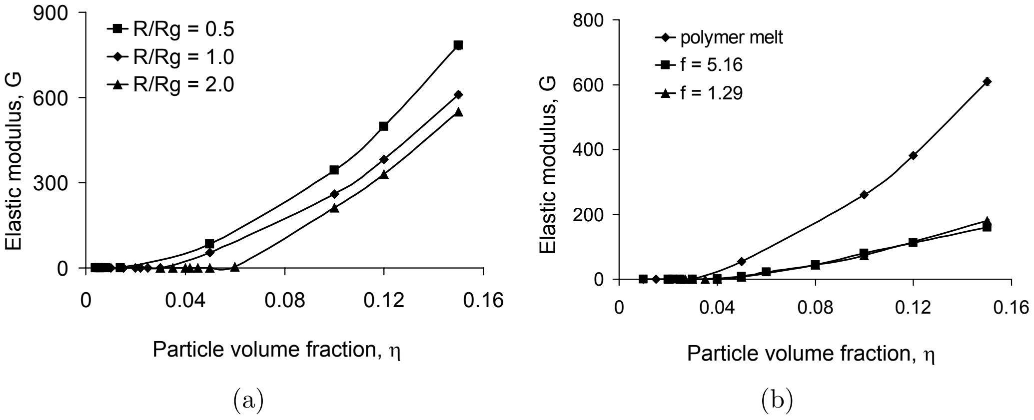

(a) (b)

Figure 5.10: (a) Elastic modulus (G'), as a function of particle volume fraction, η, for particle-to-polymer size ratios, $R/R_\mathrm{g} = 2.0, 1.0, 0.5$ for polymer melt. (b) Same as (a) for particle size $R/R_\mathrm{g} = 1.0$ and for polymer concentrations as indicated. The error bars are smaller than the sizes of the symbols.

at a given η with a decrease in the size of the particles. Increase in the surface area increases the number of interparticle bridges leading to the reinforcement displayed in the $G^{'}$.

Many theoretical as well as experimental studies have suggested that the formation of gel-like structures leads to a power law dependence of the elastic moduli on the particle volume fraction. In Fig. 5.11a, we display the elastic moduli scaled by a constant factor, as a function of particle volume fraction, expressed as $\eta - \eta_c$. As observed from the figure, the elastic moduli follows a universal power law scaling $G \propto (\eta - \eta_c)^{\nu_\eta}$ with $\nu_\eta \approx 1.79$.

The above universal behavior of the elastic moduli exponent is an important outcome of this analysis. The value of this exponent is in good agree-

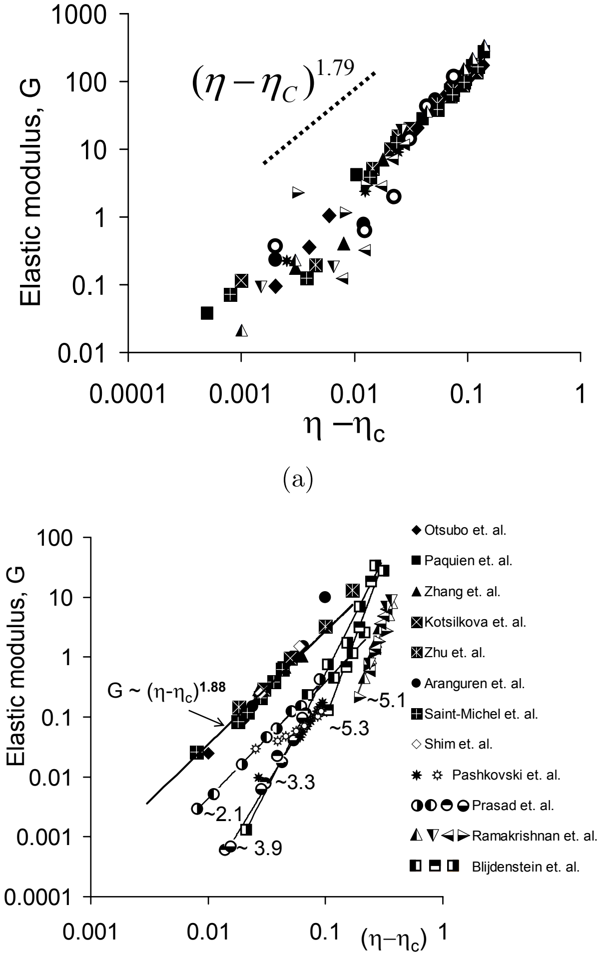

(a)

(b)

Figure 5.11: (a) Master curve for scaled elastic modulus (G') obtained from simulations, as a function of particle volume fraction, $\eta - \eta_c$. The legend of the symbols is same as in Fig. 5.7a. (b) Scaled elastic modulus (G') for experimental polymer-particle systems. The sources of experimental data are listed in Ref. [32, 132, 133, 148–155]

ment with the theoretical predictions for the case of polymer gel while the fractal dimensions observed in this work are also quite close to that obtained for incipient gel for a polymer ($d_f = 2.5$). Thus the simulations predict that while the percolation thresholds for polymer-bridged gels strongly depend on the physical parameters and are governed by subtle interplay between interparticle interactions and polymer bridging, *the overall structural features of the gels resemble that of the entropic gels where the dominating contribution to the elasticity of systems comes from the stretching entropy.* This differs from the energetic gels observed for the case of short range depletion attractions where the strong attractions between the particles contribute to *energetic bending elasticity.* In such cases, the addition of energetic contribution to elasticity results in much higher elastic exponents, ranging from $\nu_\eta \approx 2.1$ to 3.8 depending on the relative influence of stretching entropy and bending energy [156, 157]. The existence of such different scaling exponents provides an approach whereby by examining the volume fraction dependence of elastic moduli, the mechanism of gelation in experimental situations can be distinguished.

5.4 Summary of Results and Relation to Experiments

To summarize, both the polymer-particle size asymmetry and the concentration of the polymer and particle components were observed to have non-trivial effects on the formation, structure and elastic properties of the polymer-particle mixtures. With a decrease in the size of the particles, a significant enhancement in the number of bridges per unit area is predicted. Also for smaller particles, the range of bridging relative to the particle size is much larger than that for the larger particles. These effects result in a substantial decrease in the percolation volume fractions and an early onset of solid-like behavior for such mixtures. Specifically, for the case of semi-dilute solutions and polymer melts, the polymer induced bridging results in a formation of space spanning particle clusters at particle volume fractions as low as 0.5 to 2 %. These predictions are consistent with the experimental values reported for PEO-silica system where in the nanoparticle regime, the percolation thresholds are found to be less than 1-2 % [25]. Also, the smaller particles were found to form highly interconnected gels where as for larger particles the gel structure is much more loosely connected. The latter observation can rationalize the observed enhancement in the elastic moduli and the increased viscosities for silica suspensions in PAAm solutions reported in good solvent with a decrease in the size of the particles [31]. However, it is noted that the authors report a size independent critical floc concentration of 30% which differs substantially from the predictions of this study.

Our results also characterize the effect of the surface properties of the particles. With a decrease in the surface saturation concentration, we predict a decrease in the formation of interparticle bridges, a decrease in the particle clustering and a concomitant increase in the percolation thresholds. Our results provide a quantitative justification for the qualitative model proposed by Macosko *et. al.* to rationalize the differences in rheological responses of bare and surface modified silica [32]. A similar behavior was also reported by

Zhang and Archer where no formation of filler structure was observed for the surface modified silica and the weak polymer-particle interactions were found to exhibit almost no enhancement in the viscoelastic properties [25].

Finally, we compare our results for the elastic moduli with the experimental plateau moduli data for polymer-particle systems which are speculated to form networks via polymer bridging. We note that our study treats the polymeric bridges to be completely reversible and does not account for the non-equilibrium effects that may be important in the experimental situations. Hence, we expect our analysis to be more representative of weak adsorption where the affinity between the particle surface and polymer segments is low to moderate. For such equilibrium bridging induced networks, our results suggest fractal structures with a nearly constant fractal dimension of $d_f = 2.2$ and predict a universal elasticity exponent of ≈ 1.79. In Fig. 5.11b, we display master curves for elastic moduli as a function of the volume fraction, constructed for experimental data reported for a variety of colloidal suspensions in polymer solutions [32, 133, 148–152]. The data correspond to polymer induced aggregation for spherical particles of various sizes and under different conditions of polymer concentration, polymer MWs, surface chemistry and adsorption strengths. Each set of data is scaled on the elastic moduli axis by a single parameter such that different sets of data can be displayed on a single plot. For the cases where the percolation thresholds were not explicitly reported in the experimental studies, the percolation thresholds are approximated such that G' vs. $\eta - \eta_c$ follows a power law and the η_c values thus obtained were found to be within 10% of that suggested by the experiments. It is observed that these experimental data indeed follow power law scalings as shown by the slopes of the curves. More importantly, the data for experimental systems where formation of polymer bridging induced gels is speculated yield a critical exponent of $\nu_\eta \approx 1.88$. On the other hand, the experimental systems with depletion induced energetic interactions [132, 153–155] display significantly higher elastic exponents. There is a striking similarity between the upper experimental master curve and the one obtained from the simulations, both of which yield a critical exponent of ~ 1.79 to 1.88. This agreement suggests that indeed a part of experimental observations on gelation and elasticity can be rationalized through a particle network formed through polymer bridges.

5.5 Conclusions

In this chapter, the structural characteristics of polymer induced gelation in mixture of nanoparticles are investigated. The model system considered here is comprised of spherical particles immersed in semi-dilute solutions of adsorbing polymer. Using the polymer mean field theory, the structural conformations of the polymer at the surface of the particles are examined. This analysis highlights key differences in the bridging characteristics and their influence on the cluster statistics and the percolation thresholds η_c for polymer-particle mixtures, as the size of the particles is changed. The agreement between the experimental observations and simulation predictions suggests that the similarity between the bridging induced gelation and the classical elastic percolation can provide useful insights into the mechanism of gelation in the polymer-nanoparticle mixtures. It is to be noted that the present study considers “equilibrium gelation” in polymer-particle mixtures where the polymer induced bridging is assumed to be completely reversible. Thus, the time scales governing the formation and stability of such polymer bridged networks viz., the life-time of polymer bridges and the time scale for the diffusive encounters between the particles are not accounted.

Chapter 6

Nanorods in Polymeric Solutions

So far, the work presented in this dissertation primarily focused on the polymer-particle systems characterized by isotropy in the shape of particles. However, a number of technologically important applications consist of anisotropic particles such as clay particles, carbon nanotubes, nanofibers etc. In the case of dispersions of such anisotropic particles the aspect ratio becomes an important consideration in determining the phase behavior. Early theoretical works of Onsager [158] and Flory [159, 160] clarified the concentration driven isotropic-nematic transition in thermotropic hard rod dispersions. Onsager's theory [158] truncates a virial expansion for the free energy at the second virial level and finds the equilibrium state of the system by a functional minimization of free energy with respect to angular distribution of rods. In contrast, Flory theory [159, 160] derives the equilibrium distribution of rods such that the combinatorial partition function (equivalent to the entropy of the orientational distribution) of the rods is maximized. The predictions of these theories have been found in approximate agreement with experiments on synthetic as well as naturally occurring rodlike polymers [161–164]. Most developments which have followed later have incorporated additional interactions into the original Onsager's and Flory's theories to predict the occurrence of other orientationally and/or translationally ordered phases [165–168].

Despite the above theoretical progress, the effects of an added polymer on the interactions between anisotropic particles and their resultant phase behaviors are comparatively unexplored. The case of polymer-induced depletion attractions and their effect on the stability of dispersions of rodlike particles have recently been studied by using a second virial approximation [169], scaled particle theories [167] and Monte Carlo simulations [170] etc. However, recent surge in the applications for anisotropic particles such as carbon nanotubes, nanofibers, clay particles etc. has drawn much attention to the role of an added, *adsorbing* polymer in controlling the stability of dispersions of anisotropic particles [171]. Generally, many such systems are characterized by strong van der Waals attractions between the pristine nanofillers which lead to the formation of aggregates and bundles of the filler particles [172–174]. The latter diminishes the dimensional advantage of nanosized fillers, and currently proves to be a big hurdle in realizing the predicted theoretical limits for property enhancements in many cases. To counter this, a variety of different approaches such as surfactant adsorption [172, 175], covalent modification [176–178], block copolymer grafting [179, 180] etc. have been developed to induce short range repulsions between the filler particles so as to prevent their aggregation. An equally attractive strategy that has emerged in this context is the addition of non-specific, albeit adsorbing, polymers to facilitate the isolation and dispersion of the individual filler particles [172]. In such cases, the induced repulsions due to polymer adsorption are speculated to prevent aggregation arising from the strong short range van der Waals attractions [180]. Instances of this strategy have been reported in experiments where the addition of adsorbing polymers such as PMMA, PVP, DNA etc. facilitates a dispersion of carbon nanotubes [172, 181–184]. However, only limited theoretical work exists on the phase behavior of rodlike particles in presence of adsorbing polymers and the effects of polymer-rod preferential interactions on these characteristics.

In many of above applications, beyond achieving a stable dispersion, obtaining a stable ‘percolated’ network of the fillers proves equally important [173, 174, 185, 186]. For instance, dispersing anisotropic filler particles in a polymeric matrix transforms the linear viscoelastic properties of composites from liquid-like characteristics to a solid-like behavior at very low filler loadings [187]. These changes in the rheological properties have been attributed to formation of percolated filler networks in the polymeric matrix. Similar effects have been observed in the context of electrical conductivity of polymer-CNT composites, where beyond a threshold volume fraction of fillers the electrical conductivity of the composites increases by several orders of magnitude [188]. This abrupt change in the conductivity is again attributed to formation of percolated structures of filler particles. Finally, recent experiments by Kashiwagi *et al.* [189] have demonstrated a close relationship between fire retarding properties of nanocomposites and the formation of percolated structures of filler particles. There has again been only limited theoretical work [190] characterizing the role and impact of polymer matrix upon the percolation thresholds.

In this chapter, we present results on the effects of polymer-particle interactions, the concentration of polymer, the radius of rods and the aspect ratio of rods on the adsorption characteristics, the phase behavior and percolation thresholds for nanorods dispersed in polymer solutions. As model for the pristine system, we consider both the cases of simple hard rods as well as rods characterized by strong van der Waals interactions (the latter serving as a model for nanotubes) and limit ourselves to the isotropic-nematic transition in such systems. We use the framework of self consistent field theory for polymers to derive the pair interaction potentials between flat surfaces in polymer solutions [118]. These are then used in a modified Derjaguin approximation [191, 192] to deduce the interactions between cylindrical rods. This approximation does introduce some inaccuracies when the size of the rods in smaller than the range of the interactions, however, the qualitative results obtained within this framework are expected to be accurate. We then follow an approach similar to that proposed by Flory [165, 166] to predict the isotropic-nematic transition for the rodlike particles, now interacting through these "polymer mediated effective interaction potentials." At finite volume fractions of rods, the multibody effects can result in considerable change in the overall concentration of polymer and can be accounted through a method discussed in the Section 4.4. However, for dilute particle concentrations, such effects are expected to be small and we examine the phase behavior based on pair interactions potentials computed at the infinite dilution of rods. Further, we use a simple analytical approach to also predict the percolation thresholds for the rods in the presence of such polymer-induced interactions.

Our results predict that the addition of moderately and strongly adsorbing polymers can result in a stabilization of the dispersions of both hard rods and rods interacting by van der Waals interactions. In this context, an increase in either the polymer concentration and/or the strength of adsorption is shown to favor the formation of stable isotropic phases. Similar conditions are also shown to favor the formation of stable percolated structures. In contrast, at lower adsorption strengths and/or lower polymer concentrations, the percolation transitions are observed to occur within phase separated region. The topology of phase diagrams and the location of percolation lines are also shown to be strongly dependent on the radius of the rods (relative to the polymer size) and the aspect ratio of rods.

The rest of the chapter is arranged as follows: Section 6.1 provides details of the approach used to derive the polymer mediated effective interactions between rodlike particles, and the corresponding extension of Flory theory for isotropic-nematic transition to incorporate such interactions. We also explain the idea behind the model used to study percolation transitions in a system of interacting rodlike particles. In section 6.2, we discuss the adsorption characteristics of polymers on rodlike particles. Section 6.3 presents the phase diagrams for the mixtures of polymer and nanorods with emphasis on the roles of polymer-particle interaction strength, polymer concentrations, the radius of rods and aspect ratio of rods. We also present our results on the influence of van der Waals interactions on the stability of rods in presence of adsorbing polymer. In section 6.4, we analyze the effect of above parameters on the percolation transition of rods. In section 6.5, we discuss our results in the context of the experimental observations for nanorod-polymer mixtures. We conclude with a brief summary and outlook in section 6.6.

6.1 Modeling Framework

6.1.1 Pair Interactions for Rodlike Particles

We first outline the approach followed to obtain the polymer-mediated pair interaction potentials between nanorods dispersed in polymer solutions. The framework consists of three steps: (i) Use of self consistent field theory to derive the polymer-mediated pair interaction potentials between flat surfaces; (ii) Use of Derjaguin approximation to obtain the interactions between parallelly oriented rodlike particles; (iii) A geometrical approximation to obtain the orientational dependence of the interactions.

To effect (i) above, the mean field theoretic approach detailed in chapter 2 is implemented for a system consisting of flat surfaces immersed in a polymer solution. The polymer is modeled as Gaussian chains with the solvent-mediated excluded volume interactions between the monomers accounted in terms of an excluded volume parameter denoted as v. The specific interactions between the polymer segments and the surface of particles are expressed in terms of inverse adsorption length $\lambda^{'}$, which can be mapped onto a square well interaction potential between the polymer and the particle as discussed in Chapter 4. Most nanofillers are also typically characterized by a finite ad-

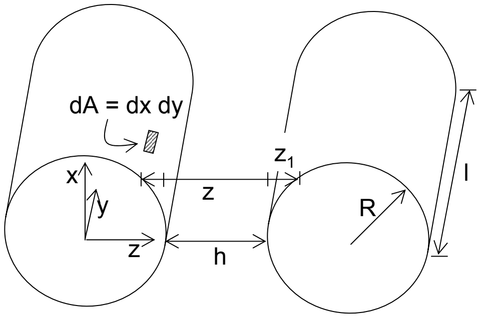

Figure 6.1: Geometry for Derjaguin integration for parallelly oriented cylinders.

sorption capacity which is accounted in our model as an additional entropic cost manifesting when the concentration of adsorbed polymer at the surface approaches a specified surface saturation concentration denoted as ϕ_m [193].

The McMillan-Mayer framework [92] is used to map the two component system of polymers and particles onto a one component system by integrating out the polymer degrees of freedom. As detailed in Chapter 2, this approach allows us to deduce the polymer mediated effective interactions between the flat surfaces in terms of the grand-canonical partition functions of the polymer component with appropriate boundary conditions [51, 193]. The latter are computed by implementing polymer-self consistent field theory in a 1-D Cartesian coordinate system.

To effect (ii), the above-derived 'effective' interaction potentials are used within a Derjaguin approximation to evaluate the interaction potential

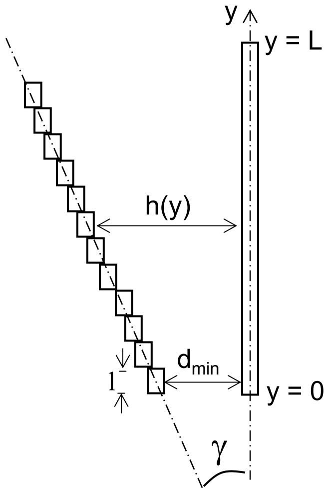

Figure 6.2: Geometrical construction for Derjaguin approximation for rods oriented at an angle γ to each other.

between two rods in parallel configuration. Consider two parallelly oriented cylindrical rods with radius R and length l at a distance h apart as shown in Fig. 6.1. The interaction potential between differential surface element $dA(= dx\ dy)$ on the first surface and a similar differential element on the second cylinder surface can be written as $E_{fp}(z)\ dx\ dy$, where $z \approx h + x^2/R$ and $E_{fp}(z)$ denotes the effective interaction between two flat surfaces at a distance z apart. The total interaction energy can then be expressed as,

$$E_{||}(h) = l\sqrt{R} \int_{h}^{h+2R} \frac{E_{\mathrm{fp}}(z)}{\sqrt{z-h}}\ dz. \tag{6.1}$$

To identify the *orientation dependence* of the interaction potentials (step (iii)), a geometrical construct shown schematically in Fig. 6.2 is used. One of the rods is assumed to be fixed at the origin along the y axis and the other rod inclined at an angle γ with respect to the first rod is represented as a series of subsegments each parallel to the axis of the first rod and arranged along the orientation angle γ. The local inter-rod distance $h(y,\gamma)$ can be expressed in terms of the minimum distance between the rods d_{min} as,

$$h(y,\gamma) = d_{\mathrm{min}} + y \tan\gamma. \tag{6.2}$$

The orientation dependent interaction $E_{\mathrm{orient}}(L, d_{\mathrm{min}}, \gamma)$ is then approximated as a sum of the interactions of all parallel subsegments as,

$$E_{\mathrm{orient}}(L, d_{\mathrm{min}}, \gamma) = \sum_{y=0}^{L} E_{||}[h(y,\gamma)]. \tag{6.3}$$

Averaging over all translational configurations yields the average orientation dependent interaction potential between two rods of length L as,

$$\bar{E}_{\mathrm{orient}}(L, d_{\mathrm{min}}, \gamma) = 1/2L \int_{-L}^{L} E_{\mathrm{orient}}(L'(y'), d'_{\mathrm{min}}(y'), \gamma)\ dy', \tag{6.4}$$

where $L'(y')$ is the length of overlap between two rods when one of the rods is displaced by a distance y' along the y axis and is given by $L - |y'|$, while the minimum distance between the rods $d'_{\mathrm{min}}(y')$ can be obtained as,

$$d'_{\mathrm{min}}(y') = \begin{cases} d_{\mathrm{min}} & \text{if } y' \leq 0; \\ d_{\mathrm{min}} + y' \tan\gamma & \text{if } y' > 0. \end{cases}$$

The orientation dependent second virial coefficient $B_2(\gamma)$ is then obtained as [92],

$$B_2(\gamma) = \int_{2R}^{\infty} (\exp^{-\bar{E}_{\mathrm{orient}}(L, d_{\mathrm{min}}, \gamma)} - 1)\ r^2 dr; \quad r = 2R + d_{\mathrm{min}}. \tag{6.5}$$

6.1.2 Phase Behavior: Flory Theory for Anisotropic Interactions

We extend the Flory theory for isotropic-nematic phase transition [160] to include the above derived polymer mediated effective interactions. For this, we first expand the orientation dependent second virial coefficient $B_2(\gamma)$ (Eq. 6.5) in terms of Legendre polynomials,

$$B_2(\gamma) = \sum_{n \geq 0} C_{2n} P_{2n}(\cos\gamma) \tag{6.6}$$

where P_{2n} denotes the Legendre polynomial of order $2n$. Note that by the symmetry considerations only the even coefficients C_{2n} are non-zero. The angle γ between the cylindrical axes of two rods is related to the respective angles θ_1 and θ_2 between these axes and the space fixed axis, and the respective azimuthal angles ϕ_1 and ϕ_2 as,

$$\cos\gamma = \sin\theta_1 \sin\theta_2 \cos(\phi_1 - \phi_2) + \cos\theta_1 \cos\theta_2. \tag{6.7}$$

Fixing the orientation of rod 1 and averaging over the orientation of rod 2 enables one to write,

$$\langle P_{2n}(\cos\gamma)\rangle = P_{2n}(\cos\theta_1)\langle P_{2n}(\cos\theta)\rangle \tag{6.8}$$

where $\langle \ldots \rangle$ denotes the average over the distribution of orientations. The subscript 2 is dropped on the assumption that the orientations θ_1 and θ_2 are uncorrelated. Substituting Eq. 6.8 in Eq. 6.6, the orientation-dependent polymer induced interaction that a rod segment (oriented at an angle θ_1 with the fixed axis) experiences can be written as,

$$\epsilon(\theta_1) = \sum_{n \geq 0} C_{2n} P_{2n}(\cos\theta_1)\langle P_{2n}(\cos\theta)\rangle \tag{6.9}$$

The subscript 1 can be omitted if the $\epsilon(\theta_1)$ is interpreted as the *mean* polymer-induced interaction for a rod segment. The total orientation dependent contribution to the free energy for the system is then obtained by summing over all $an_xv_x/2$ pairs of rod segments as,

$$H_{\text{orient}}(\theta) = -\frac{an_xv_x}{2}\sum_{n\geq 0} C_{2n}P_{2n}(\cos\theta)\langle P_{2n}(\cos\theta)\rangle \tag{6.10}$$

where a is the aspect ratio of the rods, defined as $a = L/2R$, v_x is the volume fraction of rods defined as, $an_x/(an_x + n_1)$ where n_1 and n_x represent the number of solvent and solute (rod) molecules respectively. The total free energy of the system can then be expressed as,

$$\begin{aligned} H &= n_1v_1 + n_{\text{x}}\log(\frac{v_{\text{x}}}{a}) - (n_1 + \bar{y}n_x)\log[1 - v_{\text{x}}(1 - \frac{\bar{y}}{a})] - n_{\text{x}}(\bar{y} - 1) \\ &- \sum_{\theta} n_{\text{x}\theta}\log(\frac{n_{\text{x}}}{n_{\text{x}\theta}}\sin\theta) + \sum_{\theta} H_{\text{orient}}(\theta), \end{aligned} \tag{6.11}$$

where $n_{\text{x}\theta}$ represents the number of rods that assume orientation θ with respect to the preferred axis of orientation. The first four terms in Eq. 6.11 correspond to the entropic contributions arising from hard rod excluded volume interactions whereas the fifth and sixth terms represent the orientational entropic contribution. These terms are identical to that in the original Flory theory for hard rods [159, 160]. The last term in the Eq. 6.11 corresponds to the effective inter-rod interactions arising from the presence of and interactions with the polymer. The equilibrium orientation distribution function, $n_{\text{x}\theta}/n_{\text{x}}$ which minimizes the above free energy can be obtained as,

$$\frac{n_{\text{x}\theta}}{n_{\text{x}}} = f_1^{-1}\sin\theta\exp[-\alpha\sin\theta - H_{\text{orient}}(\theta)], \tag{6.12}$$

where

$$f_1 = \int_0^{\pi/2} \sin\theta \ \exp[-\alpha \ \sin\theta - H_{\text{orient}}(\theta)]d\theta, \tag{6.13}$$

and

$$\alpha = -\frac{4}{\pi} a \log[1 - v_{\text{x}}(1 - \bar{y}/a)], \tag{6.14}$$

with $\bar{y}$ representing physically the equilibrium disorder in the distribution of rods with respect to the preferred axis of orientation:

$$\bar{y} = \int_0^{\pi/2} (\ \frac{4}{\pi} a \sin\theta \ ) \ \frac{n_{\text{x}\theta}}{n_{\text{x}}} d\theta. \tag{6.15}$$

The averages $\langle P_{2n}(\cos\theta)\rangle$ can then be expressed in terms of the above distribution function as,

$$\langle P_{2n}(\cos\theta)\rangle = f_1^{-1} \int_0^{\pi/2} P_{2n}(\cos\theta) \sin\theta \ \exp[-\alpha \ \sin\theta - H_{\text{orient}}(\theta)]d\theta. \tag{6.16}$$

To determine the phase behavior of the system, the chemical potentials of the rods (denoted as $\mu_{x\text{an}}$)and solvent (denoted as $\mu_{1\text{an}}$) components are required. For the anisotropic phase, these are obtained from Eq. 6.11 as,

$$\mu_{x\text{an}} = \frac{\partial H}{\partial n_{\text{x}}} = \log(v_{\text{x}}/af_1) + v_{\text{x}}(\bar{y} - 1) + av_{\text{x}}^2/2 \sum_{n\geq 0} C_{2n} \langle P_{2n}(\cos\theta)\rangle^2, \tag{6.17a}$$

and

$$\mu_{1\text{an}} = \frac{\partial H}{\partial n_1} = \log(v_1) - \log[1 - v_{\text{x}}(1 - \frac{\bar{y}}{a})] + v_{\text{x}}^2/2 \sum_{n\geq 0} C_{2n} \langle P_{2n}(\cos\theta)\rangle^2. \tag{6.17b}$$

For the isotropic phase, $f_1 = 1.0$, $\bar{y} = a$ and $P_{2n} = 0$ for $n \geq 1$ and the chemical potentials can be identified as,

$$\mu_{x\text{i}} = \log(v_{\text{x}i}/a) + v_{\text{x}i}(a - 1) + av_{\text{x}i}^2 C_0/2 \ , \tag{6.18a}$$

and

$$\mu_{1\mathrm{i}} = \log(v_{1i}) + v_{\mathrm{x}i}^{2} C_0/2 \ . \tag{6.18b}$$

The volume fractions in the coexisting phases are then obtained by equating chemical potentials for individual components (solvent and rod) in the different phases and by a numerical solution of the resulting equations. It should be noted that a semigrand canonical formalism (canonical for the particles and grand canonical for the polymer) [35] is implemented to compute the pair potentials within the McMillan Mayer framework. Thus, equilibrium of the polymer component between the different phases is automatically ensured by using the pair potentials computed at a fixed activity coefficient of polymer. Characterization of the anisotropic phase in terms of the equilibrium disorder parameter $\bar{y}$ requires the simultaneous solution of Eqs. 6.13, 6.15 and 6.16 for a fixed volume fraction of rods, which is then utilized to determine the phase coexistence from Eqs. 6.17 and 6.18. To effect the solution of above equations, the expansion of second virial coefficient $B_2(\gamma)$ (cf. Eq. 6.6) is truncated at $n = 10$ which was found to lead to an excellent convergence of the volume fractions of rods in coexisting phases (for hard rods, $n = 3$ was found to be sufficient for accurate results [194]).

6.1.3 Percolation Thresholds

To analyze the onset of percolation of the rods, a simple connectivity criterion is used. A 'phantom' shell of thickness δ is constructed around the impenetrable rod [195] and the connectivity between the rods is defined in terms of the overlap probabilities of shells of thickness δ for different rods [196]. Physically, the shell thickness δ can be envisioned as the range over which an external perturbation (such as stress, electron transport) gets transferred from a particle to another. In many previous instances [196, 197], a 'permeable' particle model has been used to delineate percolation thresholds. However, for rodlike particles such as carbon nanotubes and nanofibers, the particles are expected to have a hard core and hence the 'core-shell' model of connectivity is expected to be more appropriate than the permeable rod models of percolation. Moreover, such an approach also corresponds to the methodology typically used in the computer simulations to deduce connectivity percolation [198, 199].

Warren [169] has derived an analytical expression for overlap volume $v_{\rm ov}$ between shells enclosing long rodlike particles. Using his result (cf. Eq. A1, Appendix in Ref. [169]), the probability of intersection between two rods is expressed as,

$$\bar{P} \propto V_{\rm ov}/V \approx \frac{2L^2 \sin\gamma}{V} \int_{2R}^{2(R+\delta)} \frac{f(z)}{\sin\gamma}\, g(z) dz; \tag{6.19}$$

where V denotes the volume of the system and $f(z)/\sin\gamma$ represents the overlap shell volume for two infinitely long cylinders oriented at angle γ with each other and a distance z apart. The latter can be expressed as,

$$\frac{f(z)}{\sin\gamma} = \frac{1}{\sin\gamma} \int_{-(R+\delta)+z/2}^{(R+\delta)-z/2} 4[(R+\delta)^2 - (z/2+p)^2)]^{1/2}\, [(R+\delta)^2 - (z/2-p)^2)]^{1/2}\, dp\,. \tag{6.20}$$

In the above, $g(z)$ represents the radial distribution function for the rods, for which we use its low density approximation [87] as $g(z) =$

$1/2\pi \int_0^{2\pi} \exp[-\beta \bar{E}_{\mathrm{orient}}(L,z,\gamma)]d\gamma$ with $\beta \bar{E}_{\mathrm{orient}}(L,z,\gamma)$ denoting the polymer induced effective interaction potential between the two rods (cf. Eq. 6.4). For a finite volume fraction v_{x} of particles, the probability of intersection of a rod with *at least* i other rods can be expressed in terms of $\bar{P}$ as [200],

$$P_{i,N} = 1 - \sum_{k=0}^{i-1} \binom{N}{k} \bar{P}^k (1-\bar{P})^{N-k} \tag{6.21}$$

where N is the total number of rods in the volume V. From Eq. 6.21,the probability of a rod being connected with at least two rods is obtained as,

$$\begin{aligned} P_{2,N} &= 1 - (1-\bar{P})^N - N\bar{P}(1-\bar{P})^{N-1} \\ &\approx 1 - \exp[-v_{\mathrm{x}} V_{\mathrm{ov}}/\pi R^2 L](1 + v_{\mathrm{x}} V_{\mathrm{ov}}/\pi R^2 L). \end{aligned} \tag{6.22}$$

The percolation threshold v_{perc} is then (somewhat arbitrarily) assigned as the volume fraction of rods at which $P_{2,N} = 0.5$, equivalent to the situation of sufficient likelihood for a rod being connected to at least two other rods.

6.1.4 Parameters

The objective in this study is to analyze the role of parameters such as polymer-particle interaction strengths and polymer concentrations upon the stability and equilibrium phases of rodlike particles. Two particle-to-polymer size ratios of $R/R_{\mathrm{g}} = 0.25$ and 0.5 are studied, both of which fall in the "nanoparticle" regime where radius of particle is comparable to/or smaller than the radius of gyration of the polymer. The aspect ratio of rods is varied from $a = L/D = 15$ to 100, and the attention is limited to identification of the isotropic and nematic phases in such systems. Primarily polymer concentrations falling in the semidilute regimes and under 'good solvent' conditions are considered. Correspondingly, the non-dimensional excluded volume parameter $B = vN^2/R_\mathrm{g}^d$ is chosen to be 10. In the following, all polymer concentrations are normalized by the overlap concentration, ρ^* as $\phi = \rho/\rho^*$ and the results presented here correspond to $\phi > 1.0$ (indicating the semidilute concentration regime). In this chapter, the normalized inverse adsorption length $\lambda = \lambda' N/R_\mathrm{g}$ is varied from $\lambda = -15$ to 25. These adsorption strength values span the situations of very low to high affinity between polymer segments and the particle surface (cf. Eq. 4.1). The surface capacity for adsorption is fixed by setting the surface saturation concentration ϕ_m to 20. In determining the percolation thresholds, the thickness of overlap shell for the particles (cf. Eq. 6.19) is assumed to be $\delta = 0.4R$. The implications of this choice are briefly discussed later.

6.2 Adsorption on Rodlike Particles

In order to study the polymer adsorption characteristics on rodlike particles, the diffusion equation for polymer configurations (cf. Eq. 2.27) is solved in a 1-D cylindrical coordinate system and obtain the volume fractions of adsorbed segments ϕ_ads using eq. 2.28. Fig. 6.3 compares the volume fractions of adsorbed polymer segments ϕ_ads as a function of distance from the surface (normalized by R_g) for cylinders and spheres with different radii (Fig. 6.3a) and in polymers with different adsorption strengths (Fig. 6.3b). For $R/R_\mathrm{g} \gg 1$,

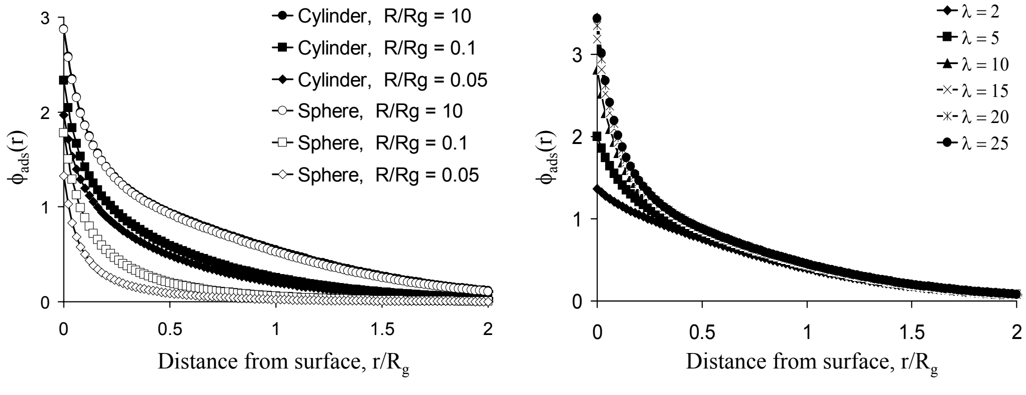

(a) (b)

Figure 6.3: Adsorbed segment volume fractions ϕ_{ads} as a function of distance from surface r (normalized by R_{g}) for (a) cylinders (solid symbols) and spheres (empty symbols) with different radii. $\lambda = 10$ and $\phi = 5.16$. (b) cylinders with $R = R_{\text{g}}$, $\phi = 5.16$ and for adsorption strengths λ as indicated in legend.

both cylindrical and spherical particles are observed to show similar polymer volume fraction profiles, which correspond to that around a flat surface. The latter is expected, since in the limit of $R \gg R_{\text{g}}$, the particles essentially behave as flat surfaces and curvature of the particles does not have any appreciable effect on the adsorption characteristics. However, in the nanoparticle regime ($R \lesssim R_{\text{g}}$), for a cylindrical particle, we observe significantly higher polymer segment volume fractions as compared to that for a sphere for same set of parameters ($R/R_{\text{g}}, \lambda$ and ϕ). The latter implies a stronger adsorption of polymers on the rodlike particles as compared to spherical particles (for the same adsorption length). A second effect is observed in terms of adsorption strength. For a rodlike particle, an increase in the adsorption strength of polymer results in considerably higher volume fractions at and close to the surface of the particles whereas the volume fractions further away from the surface are nearly unchanged. This enhancement in the polymer volume fractions on/near the surface suggests a more tight wrapping of polymers around the rodlike particle at higher λ values. O'Connell *et al.* [172] have discussed such tight wrapping of polymers on the nanotube surfaces. Recent experiments have exploited the latter to control the dispersability of carbon nanotubes by changing solvent conditions which reduces the thermodynamic driving force for wrapping (corresponding to a decrease in λ value) [201]. However, contrary to the observations of adsorption in the form of helical monolayers of polymers by O'Connell *et al.* [172], the above results indicate a substantial amount of adsorbed polymer dangling in the solution in the form of loops and tails of the polymers. Presence of such dangling adsorbed polymers has been indicated using SEM and TEM imaging by Baskaran *et al.* [184]

6.3 Phase Behavior of Hard Rods in Presence of Polymer

In this section, we present results for the interactions and phase behavior of hard rods in polymer solutions and discuss the effects of different physical parameters such as adsorption strengths, polymer concentrations, radius of rods and aspect ratios of rods.

6.3.1 Effect of Adsorption Length λ

Fig. 6.4a presents the 'phase diagram' (in the plane of adsorption length λ vs rod volume fraction) for a dispersion of monodisperse rods of radius $R = 0.25R_g$ and aspect ratio $L/D = 15$ in a polymer solution of concentration $\phi = 1.29$. The dotted lines represent the corresponding coexistence volume fractions for a solution of hard rods (i.e. in the absence of polymer) with the identical aspect ratio. It is seen that the addition of interacting polymers significantly affects the topology of the phase diagram. Addition of non-adsorbing/weakly adsorbing polymer ($\lambda < 0$) leads to a distinct widening of the coexistence region which shifts the isotropic-nematic transitions to very dilute particle volume fractions. With an increase in the polymer-particle adsorption strength, a narrowing of the co-existence region is observed. The latter leads to a decrease in the volume fraction of the nematic phase and an increase in the volume fraction of isotropic phase. $\lambda = 0$ (corresponding to $u_0 = u_c$, cf. Eq. 4.1) represents the condition of critical adsorption strength, for which the effective rod-rod interactions are identical to that of original hard rod mixture. Consequently, the coexistence volume fractions equal that for a dispersion of hard rods of the same aspect ratio. For stronger adsorbing polymers ($\lambda > 0$), first a widening of phase coexistence region leading to a complete immiscibility of the rods is observed at moderate adsorption strengths. However, further increase in adsorption strength is seen to result in a gradual narrowing of the demixed region and a stabilization of rods at higher adsorption strengths. At the highest adsorption strengths, the coexistence volume

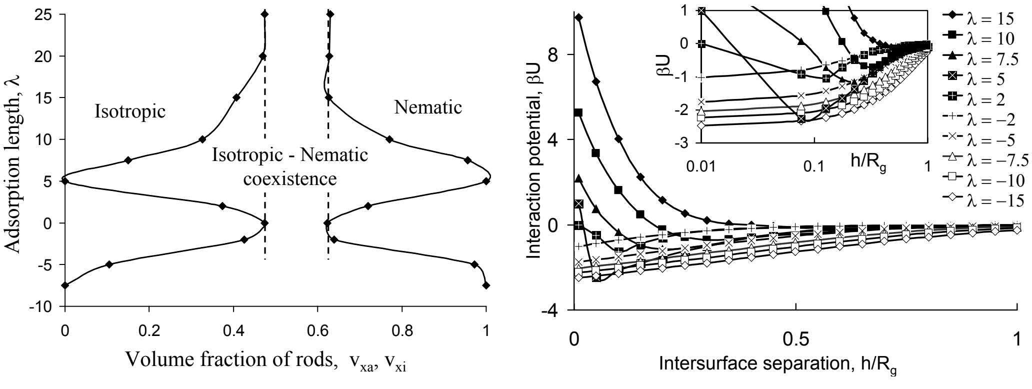

(a) (b)

Figure 6.4: (a) Phase diagram in inverse adsorption length λ vs. volume fraction of rods plane for $R/R_{\mathrm{g}} = 0.25$, $L/D = 15$ and $\phi = 2.58$. The dotted lines show the phase diagram for hard rods with same aspect ratio; (b) Pair interaction potential βU as a function of intersurface distance (normalized by R_{g}) h/R_{g} for polymer concentration $\phi = 2.58$ and $\lambda = \pm 15, \pm 10, \pm 7.5, \pm 5$ and ± 2. The inset displays the attractive part of the interaction potentials on a semi-log scale.

fractions are observed to correspond to that for the hard rods.

The above trends in the phase diagram can be rationalized based on the effect of λ on the effective interaction between surfaces. In Fig. 6.4b the polymer-induced effective interaction potentials βU ($\beta = 1/k_{\mathrm{B}}T$) are displayed as a function of intersurface separation h/R_{g}. The inset depicts the attractive part of the interaction potentials on a magnified, semi-logarithmic scale. For the case of depleting polymers ($\lambda < 0$), the interactions are seen to be purely attractive, with an increase in the attraction strength as the intersurface distance is decreased. It is also evident from the inset to Fig. 6.4b that an increase in λ leads to a corresponding decrease in the strength of attractive interactions. These trends can be understood by noting that for the case of negative λ, the polymer is depleted from the vicinity of the surface, the resultant osmotic imbalance for the polymer induces an effective attraction between the surfaces. With an increase in the λ, the depletion effect and correspondingly entropic loss for the polymer diminishes, resulting in a weakening of the induced attractions. The result is, at low (negative) λ values, the strong depletion induced effective attraction between the rods results in a highly negative second virial coefficient, and hence, the rods are nearly insoluble and we observe a wide region of immiscibility at low values of λ. On the other hand, with an increase in the adsorption strength, the weakening of depletion induced attractions results in the narrowing of the two phase region.

The presence of stronger adsorbing polymer ($\lambda > 0$) is seen to result in non-trivial interaction potentials. Generically, the adsorbing polymer is observed to induce repulsive interactions at shorter distances followed by an attractive minimum at larger separations between the surfaces. With an increase in the λ values, the strength of short distance repulsion is observed to increase, while the depth of attractive minimum first increases from zero at $\lambda = 0$ to a maximum value followed by a decrease at higher λ values. As detailed in Chapter 4, the intersurface interactions in presence of adsorbing polymers are governed by an interplay between three factors: (i) The polymer attempts to increase the number of surface contacts by forming bridges between the surfaces, thus resulting in an enthalpic gain; (ii) Upon confinement, the adsorbed polymer experiences an entropic cost arising from the monomeric excluded volume interactions; (iii) As the surface concentration of adsorbed polymer approaches the maximum adsorption capacity of the surface, the entropic cost arising from the surface saturation constraint starts to manifest. At large intersurface distances, entropic repulsions arising from both the confinement as well as the surface saturation are negligible, and the resulting intersurface interactions are due to the enthalpic gain arising due to the adsorption. With a decrease in the intersurface distance, the confinement and the surface saturation entropy costs become comparable to enthalpic gain, resulting in the minimum manifested in the interaction potentials. At even smaller distances, the confinement and saturation entropy losses dominate the enthalpic gain arising from bridging rendering the intersurface interactions repulsive. For small but positive values of λ, the polymer adsorption is weak and thus the enthalpic gain is also small, resulting in weak interactions. An increase in λ facilitates adsorption of polymer, and the resulting enthalpic gain induces strong attractions at intermediate intersurface distances. For very high values of λ, the individual surfaces are saturated and bringing them closer results in purely repulsive interactions between the surfaces. These nonmonotonic interactions for adsorbing polymers result in the observed phase topology where the two phase region first widens corresponding to increasing (bridging) attractions between the rods, and then with increase in λ narrows down due to weakening of attractive interactions and strengthening of repulsions (steric stabilization).

The above results suggest a novel 'reentrant' phase behavior where at a fixed volume fraction of rods and polymers, the dispersion is immiscible

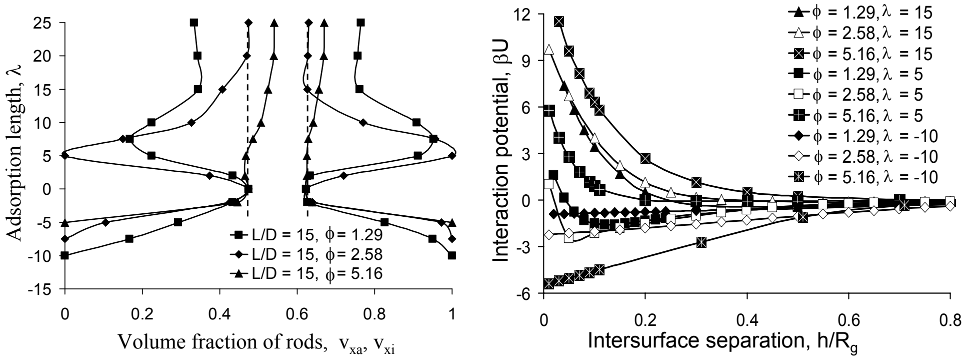

Figure 6.5: (a) Phase diagram in inverse adsorption length λ vs. volume fraction of rods plane for $R = 0.25R_{\mathrm{g}}$, $L/D = 15.$ and $\phi = 1, 29, 2.58$ and 5.16. The dotted lines show the phase diagram for hard rods with same aspect ratio. (b) Pair interaction potential βU as a function of intersurface distance (normalized by R_{g}) h/R_{g} for polymer concentrations $\phi = 1.29, 2.58, 5.16$ and $\lambda = 15, 5$ and -10.

at weak interactions (depletion), then becomes stable and again immiscible as strength of polymer-particle interaction is increased and then finally again stable for the highest attractions. A similar reentrant miscibility has been predicted for spherical particles by Hooper and Schweizer [7]. In a nutshell, the above results suggest two optimal conditions for creating stable dispersions for a hard rod system: addition of either (i) weakly adsorbing ($\lambda \simeq 0$) or (ii) extremely strongly adsorbing ($\lambda \gg 0$) polymers. These results may have implications in choosing appropriate polymeric solvent for stabilization or separation of rodlike particles.

6.3.2 Effect of Polymer Concentration

In Fig. 6.5a, we display the effect of the polymer solution concentration on the phase behavioral characteristics. For non-adsorbing/weakly adsorbing polymers ($\lambda < 0$), the phase diagrams are seen to follow a qualitatively similar behavior for all concentrations, with a monotonic expansion of the coexistence region with an increase in the polymer concentrations for such systems. As evident from Fig. 6.5b, which displays the pair interaction potentials βU as a function of intersurface distance h/R_{g} for different polymer concentrations, the strength of depletion attraction increases with an increase in the concentration of polymers which rationalizes this widening of the region of coexistence.

In contrast, for the case of stronger adsorbing polymers ($\lambda > 0$), the phase topology reflects a sensitive interplay between the polymer concentrations and the adsorption strength. For small positive λ, with an increase in ϕ, the region of immiscibility is observed to first widen and then shrink to isotropic-nematic coexistence similar to hard rod behavior at higher ϕ values. The above trends can be explained by the fact that for moderate adsorption strengths, an increase in the polymer concentration initially leads to an increase in the bridging rendering the induced effective interactions strongly attractive (cf. Fig. 6.5b). This leads to a wider region of immiscibility. However, further increase in polymer concentrations results in a saturation of the surfaces and an increase in the confinement induced entropic costs, resulting in both a strengthening of the short-distance repulsions and a weakening of the attractions. This leads to a narrowing of the coexistence regions. At higher

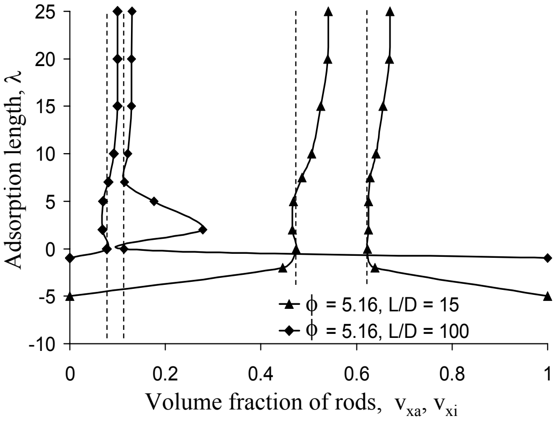

Figure 6.6: Phase diagram in inverse adsorption length λ vs. volume fraction of rods plane for $R = 0.25R_\text{g}$, $\phi = 5.16$ for $L/D = 15$ and 100. The dashed lines show the phase diagram for hard rods with the same aspect ratios.

λ values, the entropic repulsions dominate, resulting in a narrowing of two phase region monotonically with increase in the polymer concentrations. For the highest ϕ values, the purely repulsive interactions lead to a phase behavior which resembles that of the hard rods, and corresponds physically to the phase coexistence of polymer coated rods.

6.3.3 Effect of Aspect Ratio

In Fig. 6.6, we display the effect of the aspect ratio of rods on the phase diagrams. The radius of the rods is fixed at $R = 0.25R_\text{g}$ and the polymer concentration is $\phi = 5.16$. The dotted lines represent corresponding coexistence curves for hard rods with the same aspect ratios. For longer rods, addition of depleting or weakly adsorbing polymers is observed to induce immiscibility at nearly all negative values of λ. This situation can be contrasted for shorter rods where stable regions were found for weakly depleting polymers. For the case of adsorbing polymer ($\lambda \geq 0$), an increase in the aspect ratio of rods is observed to shift the region of coexistence to much lower volume fractions. For larger rods, increase in the adsorption strength results in widening of coexistence region, followed by a narrowing to hard rod coexistence behavior at higher adsorption strengths. In contrast, the smaller rods are observed to follow a hard rod coexistence behavior at all positive adsorption strengths. At higher adsorption strengths, the coexistence volume fractions are observed to shift towards higher values for all aspect ratios.

The above differences in the phase behavior can be understood by noting that the strength of the interrod interactions is proportional to the length of the rods. For negative adsorption lengths, increasing the aspect ratio results in very strong depletion attractions, which induces stronger immiscibility for the case of longer rods. For moderate adsorption strengths, the polymer induced interactions are characterized by short distance repulsions followed by long distance attractions (cf. Fig. 6.4b). An increase in the aspect ratio again results in strengthening of these interactions whose interplay results in a widening of the coexistence region. For higher adsorption strengths, the polymer induces purely repulsive interactions which rationalizes the observed trends as equivalent to the phase behavior of polymer coated rods with renormalized radii determined by the strength of the repulsions.

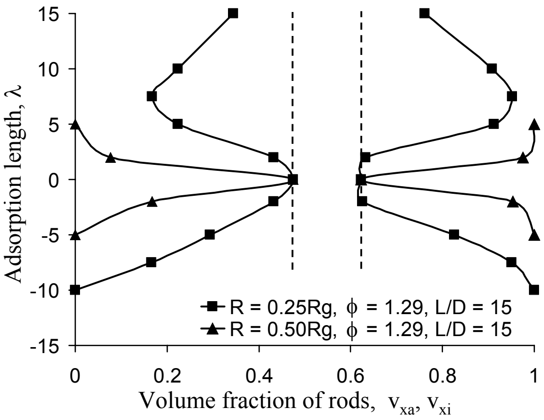

Figure 6.7: Phase diagram in inverse adsorption length λ vs. volume fraction of rods plane for $R = 0.25R_\text{g}$ and $0.5R_\text{g}$, $\phi = 1.29$ and $L/D = 15$. The dotted lines show corresponding phase diagram for hard rods with same aspect ratio.

6.3.4 Effect of Radius of Rods

In Fig. 6.7 we analyze the effect of the radius of the rods (relative to the size of the polymer which is assumed to be fixed) on the topology of the phase diagram for fixed aspect ratio $L/D = 15$ and polymer concentration $\phi = 1.29$. An increase in the radius of the rods is observed to result in a significant broadening of the two phase region for both adsorbing as well as non-adsorbing polymers. The above effects are rationalized in terms of increase in the strength of attractive interactions with increase in the radius of the rods. In case of depleting polymers $\lambda < 0$, increasing the rod size correspondingly increases the depleted volume for the polymer making the inter-rod attractions stronger for thicker rods. Whereas for adsorbing polymers, the increase in the adsorbing surface area enhances polymer induced bridging and correspondingly increases the depth of the inter-rod attractive minimum. Even at higher λ values where the induced short distance repulsions are stronger, the strong long range attractive interactions dominate the phase behavior, leading to complete insolubility of thicker rods.

6.3.5 Effect of van der Waals Attractions

As discussed in the introduction, many nanoscale filler particles used in applications exhibit a strong tendency to aggregate due to strong interparticle van der Waals interactions [179, 180, 202]. While the previous sections focused on the case of rods with just hard body interactions, in this section we analyze the effect of polymers on the overall interactions and stability behavior of rodlike particles characterized by strong van der Waals attractions. For illustrative purposes, we have assumed a van der Waals interaction similar to that reported for the carbon nanotubes [202] with a depth of attraction of $\sim -25k_{\mathrm{B}}T$ per unit length of surface and a range of $\sim 0.4R$. Within this framework, Fig. 6.8a displays the resulting overall interactions (obtained by summing the van der Waals attraction and polymer mediated effective interactions) between flat surfaces. It is seen that at larger intersurface distances the polymer-induced long range repulsions dominate the overall interactions, whereas at small intersurface distances the van der Waals attractions dominate. The main effect resulting from addition of a strongly adsorbing polymer is seen to be the occurrence of a significant repulsive barrier in the overall interactions, with the strength of repulsions increasing with an increase in λ.

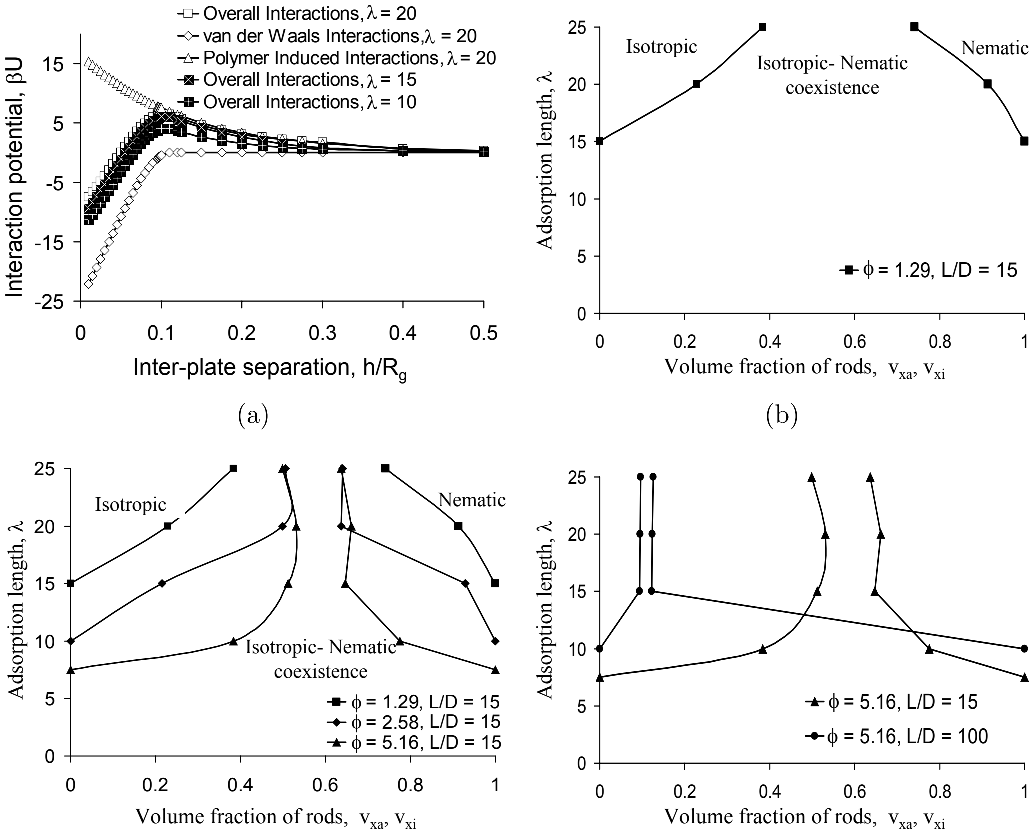

(a) (b)

(c) (d)

Figure 6.8: (a) Overall interactions between the flat plates βU as a function of intersurface separation, h/R_{g}. The overall interactions (squares) are obtained as sum of the van der Waals interactions (diamonds) and the polymer induced 'effective' interactions (triangles); (b) Phase diagram in inverse adsorption length λ vs. volume fraction of rods plane in presence of van der Waals interactions between the rods. $R = 0.25R_{\mathrm{g}}$, $L/D = 15$ and $\phi = 1.29$; (c) Same as (b) for $\phi = 1.29, 2.58, 5.16$; (d) Same as (b) for $L/D = 15$ and 100 and $\phi = 5.16$.

In Fig. 6.8b, we present the resulting phase diagrams illustrating the effect of addition of polymers on the stability of particles characterized by strong van der Waals interactions. We note that in the absence of the added polymer, such strong van der Waals attractions induce phase separations at even very small volume fractions of the rods rendering a delineation of the phase coexistence numerically intractable. This trend persists even during the addition of non-adsorbing/weakly adsorbing polymers ($\lambda \lesssim 5$) where an almost complete immiscibility of the rods is observed. As discussed earlier, in such cases, the polymer-mediated interactions are also attractive and thus enhance the van der Waals induced immiscibility of the rods. However, at higher adsorption strengths, the particle dispersions are seen to become increasingly miscible, with an isotropic-nematic transition and coexistence regions appearing at intermediate volume fractions. The latter trends are consistent with the earlier discussions, where with increasing λ, the polymer-induced repulsions become stronger leading to a repulsive barrier in the overall interactions (cf. Fig. 6.8) which prevents the van der Waals induced aggregation.

The topology of phase diagram is seen to depend on the concentrations of polymer and the aspect ratio of the rods in a manner similar to the earlier discussions in sections 6.3.2 and 6.3.3. Higher concentrations of polymer require much lower adsorption strengths for achieving a stable mixture compared to the lower concentrations of polymer. For a fixed polymer concentration, the stabilization of longer rods is observed to occur at much higher adsorption strengths compared to that for shorter rods. These observations can be rationalized in a manner similar to the behavior exhibited by hard rods.

6.4 Percolation Thresholds

In this section, we consider the percolation thresholds v_{perc} (defined by Eq. 6.22) and their locations relative to the phase coexistence. Shown in Fig. 6.9 are the lines of percolation thresholds in the adsorption strength vs. volume fraction plane for hard rods (Figs. 6.9a and b) and for rods characterized by van der Waals attractions (Fig. 6.9c). The dashed lines in Fig. 6.9 correspond to the phase coexistence curves for the same parameters. For the specific choice of overlap shell thickness δ adopted in this study($\delta = 0.4R$), the overall topology of the percolation lines is observed to follow the respective isotropic branch of the phase coexistence curves. This can be understood by noting that the onset of percolation corresponds physically to the point where the rods are connected and hence are also crowded and would rather order into a nematic phase. More interesting is the influence of polymers on the relative locations of the percolation lines and the coexistence curves. For cases where the polymer-mediated interactions are strongly attractive, phase coexistence is predicted to preempt the percolation. Such situations occur in the context of strongly depleting polymers ($\lambda \ll 0$) and/ polymers with moderate attractive interactions with the particles ($\lambda > 0$, but λ is not too large)(Fig 6.9a). Furthermore, at a given λ, lower polymer concentration is seen to promote the tendency to aggregate (Fig. 6.9b). In such cases, while the attractive interactions bring the particles together (and hence promote percolation, as evident

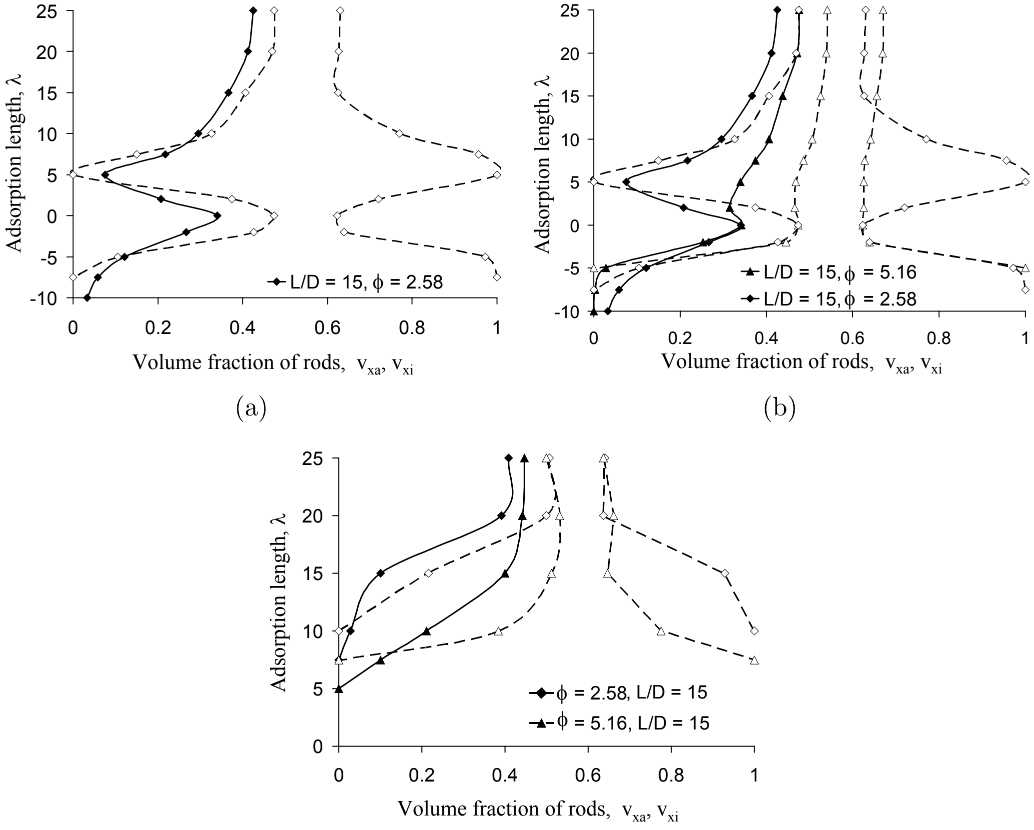

(a)

(b)

(c)

Figure 6.9: Percolation lines (solid lines) and phase coexistence curves (dashed lines) in inverse adsorption length λ vs. volume fraction of rods plane for $R = 0.25R_\mathrm{g}$ for (a) Hard rods with $L/D = 15$ and polymer concentration $\phi = 2.58$. (b) Hard rods with $L/D = 15$ and polymer concentration $\phi = 2.58$ and 5.16. (c) Rods with van der Waals interactions for $L/D = 15$ and $\phi = 2.58, 5.16$.

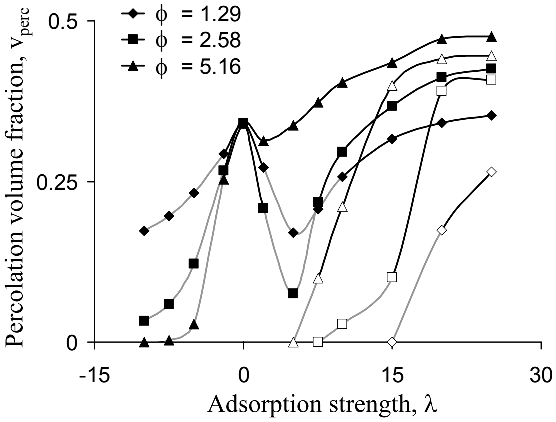

Figure 6.10: Percolation thresholds plotted as a function of inverse adsorption strength λ, for rods with $R = 0.25R_{\rm g}$ for different polymer concentrations. The solid symbols denote hard rods and empty symbols denote rods with van der Waals interactions. The dark lines correspond to the stable isotropic dispersions and light lines show the two phase region.

in the shift of percolation lines to lower volume fractions), the tendency to aggregate overwhelms the percolation characteristics (Fig 6.9b). In contrast, for cases where the interactions are weakly attractive and/or repulsive the percolation lines fall outside the phase coexistence lines. Such conditions result for weakly ($\lambda \gtrsim 0$ but small) and strongly adsorbing ($\lambda \gg 0$) polymers for hard rods and for moderate-to-strongly adsorbing ($\lambda \gg 0$) polymers for rods with vdW interactions (Fig 6.9c). Moreover, at a given λ, higher polymer concentrations are seen to promote such a behavior.

Figure 6.10 summarizes the effect of polymer concentration on the stability and percolation thresholds for hard rods (solid symbols) and rods with van der Waals interactions (empty symbols). The dark lines correspond to

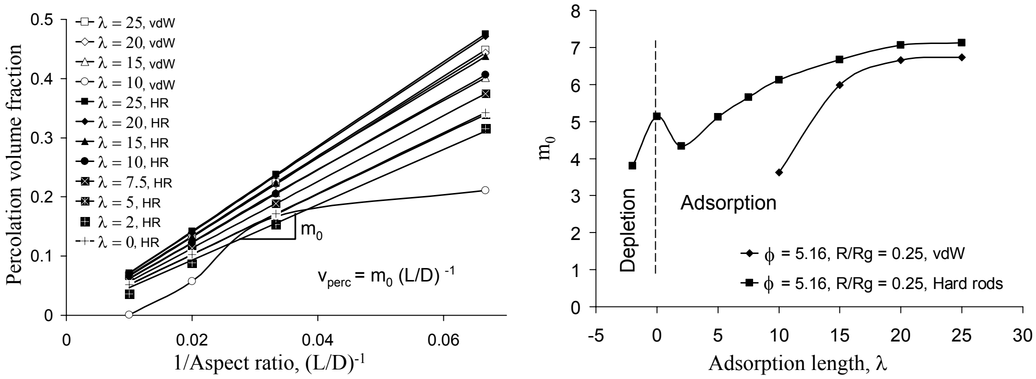

(a) (b)

Figure 6.11: (a) Percolation thresholds v_{perc} plotted as a function of inverse aspect ratio $(L/D)^{-1}$, for rods with $R = 0.25R_{\text{g}}$ and $\phi = 5.16$ for different adsorption strengths. HR denotes hard rods and vdW denotes rods with van der Waals interactions; (b) Slope m_0 of linear fits for percolation thresholds ($v_{\text{x}} = m_0(L/D)^{-1}$) plotted as a function of λ for hard rods and rods with van der Waals interactions.

stable isotropic regions whereas light lines indicate that the percolation falls within the two phase coexistence region. For the case of hard rods, addition of polymers with weakly depletion tendency or weakly adsorbing characteristics can be used to lower the percolation thresholds and still maintain the volume fraction in the stable isotropic region. On the other hand, for the case of van der Waals attractions, stable percolated dispersions can be obtained only by addition of polymers with moderate to high attractive interactions with the particles. However, addition of strongly adsorbing polymer results in a significant increase in the percolation thresholds, and hence moderately adsorbing polymers appear to be an optimal choice to promote percolation.

In many instances, the percolation thresholds have been shown to have a strong relationships with the aspect ratio of the rods and simple linear scaling have been proposed to relate the thresholds to the particle anisotropy [203]. Fig. 6.11 analyzes whether such dependencies also hold when the polymer-mediated interactions are included. In Fig. 6.11a the percolation thresholds are displayed for the cases where percolation of rods occurs in the stable isotropic region. Incredibly, in almost all cases, it is observed that the linear dependence of v_{perc} on the inverse aspect ratio of rods still holds, with however, a slope which depends on the adsorption strength and bare interactions. The slope of such fits (displayed in Fig. 6.11b) exhibits trends consistent with the above discussions. Explicitly, both weakly depleting and weakly adsorbing polymers lower the slopes, and can decrease the percolation thresholds compared to that observed for hard rods. On the other hand, moderate and strong attractions increase the slopes and the corresponding percolation thresholds.

It is noted that the above predictions are by and large consistent with recent observations reported in the context carbon nanotubes [186] where an introduction of a weak depletion attraction was shown to decrease the percolation thresholds significantly. It should however be noted that the above analysis of percolation transitions does depend on the choice of connectivity shell thickness δ. Broadly speaking, a lower (higher) value of δ shifts the percolation lines to higher (lower) volume fractions of rodlike particles. However, the qualitative effects arising from varying the strength of adsorption of polymers, the polymer concentrations and aspect ratio of rods are still expected to remain similar to that portrayed in Figs. 6.9, 6.10, 6.11. The implications of these findings on the optimal conditions for stable and percolated dispersions of rods will be discussed in more detail in the following section.

6.5 Discussion

The results presented in this chapter suggest that the topology of the phase diagram of mixture of polymer and rods is highly dependent on the anisotropy of the rods, relative sizes of the rods and polymers, concentration of the polymer and the strength of adsorption. For the case of non-adsorbing polymer, the polymer depletion-induced attractive interactions are found to result in a large two phase region which widens with an increase in the polymer concentration. A number of previous theoretical [167] and experimental studies [204] report a similar trend in the phase behavior of rodlike particles such as bohemite rods, tobacco mosaic virus etc. in presence of non-adsorbing polymers. Addition of adsorbing polymers is observed to lead to a richer phase behavior where at high polymer concentrations, the polymer induced repulsive interactions result in steric stabilization of the rodlike particles and the isotropic-nematic transition closely resembles to that for hard rods. This 'stabilizing' behavior has also been exploited in many experimental studies, where reversibly associating polymers such as Polyvinyl Pyrolidone, Polystyrene Sulfonate, single stranded DNA are used to solubilize bundles of carbon nanotubes into stable dispersions of individual CNTs [172, 183]. A similar control of dispersion behavior is also reported for carbon nanotubes in presence of pH sensitive polymers such as Poly(acrylic) acid [201, 205]. In such cases, variation of pH of solution provides a means to modify the strength of interaction between the polymer segments and the nanotube surface and can be used to reversibly change the suspension behavior from aggregated (at low pH which corresponds to weak interaction) to well-foliated (at high pH which corresponds to strong interaction) mixtures [201]. The present results also suggest a more tight wrapping of polymer around the rodlike particles as the strength of the polymer-particle interactions is increased.

An interesting outcome of this study is the 'reentrant' behavior of the phase diagram with change in the adsorption strength. At lower adsorption strengths, the depletion induced attractions widen the two phase region, which narrows to hard rod isotropic-nematic transition as the adsorption strength becomes zero. At positive adsorption strength, for certain range of polymer concentration, a distinct broadening of the two phase region is predicted which subsequently narrows to hard rod transition at higher adsorption strengths. Thus at certain volume fractions of rods, the system goes from (coexisting isotropic-nematic) - stable isotropic/nematic -(coexisting isotropic-nematic)-stable isotropic/nematic phases as the surface affinity of the polymers is modified.

It is noted that the topology of the phase diagrams for mixtures of polymer and rodlike particles is influenced not only by the aspect ratio (size anisotropy) of rods but also by the relative sizes of the rods and the polymeric component (cf. section 6.3.4). The latter dependence arises from the polymer-induced interactions which are dependent on the sizes of both the polymer and the particles. These results may have implications in the context of purification/separation applications where adsorbing polymers are added to pristine nanotubes in order to achieve selective dispersions of individual nanotubes and to separate the individual nanotubes from carbonaceous impurities/bundles of tubes [181]. By adding appropriate quantities of polymer with favorable physical properties (λ, molecular weight etc.), it might be possible to achieve conditions that will favor stability of individual nanorods while facilitating separation/aggregations of the impurities/bundles of rods.

This work also studied the effectiveness of adsorbing polymers in increasing dispersability of rods characterized by strong van der Waals interactions. It is observed that for the case of moderate to strongly adsorbing polymer, the polymer induced long range repulsions between nanotubes can reduce the effect of short range van der Waals attractions and can prevent aggregation of nanotubes. Such an approach has already been used in a number of experimental investigations where selective adsorption of polymers leads to exfoliation and stabilization of dispersions of the tubes [180, 206].

Also the percolation thresholds and their relative location to the isotropic-nematic transition for hard rods and for rods characterized by van der Waals interactions are examined. For the latter, a large region of percolated stable isotropic phase is predicted for rods dispersed in solutions of moderate-to-strong attractive polymers. An increase in the polymer concentration and/or adsorption strength is observed to enhance the stability of rods.

However, increase in adsorption strength also shifts the percolation transition to higher volume fractions. Thus, concentrated solutions of moderately adsorbing polymers appear to be an optimal choice for maximizing the properties (such as elastic modulus, electrical conductivity which are dependent on achieving a stable percolated phase at low volume fractions of rods).

6.6 Conclusion

In this chapter, the effect of polymer adsorption strength, polymer concentration, the relative sizes of rods and polymer and aspect ratio of rods on the isotropic-nematic phase separation and percolation transitions in dispersions of rodlike particles in polymer solutions is studied. Within the polymer field theoretic framework, the polymer mediated ‘effective’ interactions between rodlike particles are deduced. The above derived polymer induced effective interactions are incorporated into an adaptation of the Flory theory for anisotropic interactions to investigate the effect of polymer on the phase behavior and percolation transitions of rods. Our study delimits the physical parameters that affect the solubility, phase diagrams and percolation thresholds of rodlike particles in presence of polymers and indicates under what conditions percolated stable dispersions (or easier separations) of rods may be achieved. The change in the polymer concentration and strength of adsorption provides an attractive means to tune the interactions between the rods and to prevent van der Waals induced bundling of nanotubes. The latter may help experimentalists in devising experiments which will result in better dispersions of technologically important rodlike systems such as nanotubes, carbon fibers, fullerenes etc.

It should be noted that the present study considers equilibrium or reversible adsorption of polymer on the surface of the particles and thus does not concern with the non-equilibrium aspects of the polymer adsorption/desorption process. Further, the present framework is also inadequate to account for the kinetic gelation effects that are reported to be important at high volume fractions of rods or for the case of strong depletion attractions [204, 207]. The latter has been speculated to occur during quenches inside the phase coexistence region, when the percolation lines also fall within the coexistence region [208]. While we cannot comment on these effects the relative locations of the percolation lines and phase coexistence curves provide a guideline for the occurrence of such phenomena. Another limitation of the study concerns the accuracy of Derjaguin approximation. The latter is accurate in the limit where the radii of the curved surfaces are significantly larger than the intersurface separation. For the case of polymer induced interactions, the range of interactions is relatively large and in the present study the inter-rod distances where the interactions become negligible are comparable to the radius of the rods. The latter introduces inaccuracies in the quantitative description of interaction potentials. However, the qualitative trends predicted in this work are expected to be accurate.

Chapter 7

Adsorption of Model Proteins on Polymer Grafted Surfaces

Grafting polymer chains on the surface of particles has been widely used as an efficient means to achieve steric stabilization in applications ranging from colloidal stabilization to design of biocompatible surfaces. Grafted polymer chains result in long range repulsive forces between the particles and thus inhibit the particles from reaching short distances where van der Waals forces can lead to particle aggregation. Grafted polymers such as PEO are also found to be highly successful in preventing protein adsorption on the surfaces. A protein that encounters a bare surface experiences purely attractive interactions due to van der Waals interactions and consequently gets adsorbed on the surfaces. Such adsorption of proteins on the foreign materials can result in surface-induced thrombosis [209]. In such contexts, a terminally grafted polymer brush on the surface can induce net long range repulsion in the surface-protein interactions and enhance the biocompatibility of materials used in bioengineering applications.

To date, most theoretical studies have focused on polymer brushes on flat surfaces. For the planar geometry, the density profiles for the polymer are found to follow an approximate parabolic shape and in such cases, the resultant interactions between the surfaces are well understood. Systems of practical interest such as polymeric micelles and polymers grafted on nanoparticles involve polymer brushes on curved particles, for which the curvature of the particle can be expected to lead to significant changes in the structure of a brush. Such cases of grafted polymer brushes on curved particles have been primarily studied in the limit where the particle is much smaller than the polymer chains. Such brushes are described as star polymers and have been studied extensively using scaling theories, MC and MD simulations. In such cases, the density profiles for polymer are found to follow a power law decay away from the core of the star polymer. However, the transition region between flat geometries and star polymers is relatively less explored.

In this chapter, we focus on the effect of curvature of the surface on the structure of a polymer brush and attempt to bridge the gap between the two asymptotic limits viz, flat brush and star polymer. We further analyze the efficacy of such a polymer brush in preventing adsorption of spherical particles (mimicking globular proteins) on the curved surfaces of different sizes. Specifically, some of the issues that we are interested in are (i) how does the curvature of surface affect the structure of the brush? (ii) What is the effect of the size of the protein on the adsorption characteristics? (iii) how do the molecular weight and grafting density of the polymer affect the effectiveness of a brush in preventing the protein adsorption? To address these issues, we implement a numerical self consistent field theory to derive the density profiles of a brush in presence of a protein, idealized as a rigid, structureless spherical particle. The free energies of insertion of protein particles in vicinity of surfaces carrying grafted polymer brush are deduced within the field theoretic framework. In this chapter, we present results on the effect of surface curvature, protein size and grafting density of polymer chains on the structural features of brush and insertion free energies of proteins. We note that the results presented in this chapter are preliminary and primarily qualitative in nature. In a subsequent publication, we plan to present a rigorous scaling analysis of these results.

The rest of the chapter is arranged as follows: In section 7.1, we present an adaptation of polymer self consistent field theory used in this work to describe a polymer brush. In section 7.2, we discuss the effect of surface curvature and grafting density on the structure of a polymer brush. Section 7.3 presents the effect of various physical parameters on the insertion free energies for proteins. The chapter concludes with a discussion on implications of above results on optimum design parameters for biocompatible surfaces in section 7.4.

7.1 Self Consistent Field Theory for Grafted Polymers

We consider a model polymer brush where each of the polymer chains is *irreversibly* attached to the particle surface by one end. We further assume that the grafting points are distributed uniformly on the particle surface. We consider a canonical ensemble of n_{g} Gaussian polymer chains end tethered to a surface at $\mathbf{r} = D$ where D denotes the radius of the surface. The polymer is assumed to be surrounded by an implicit solvent which acts as a good solvent for the polymer resulting in a positive excluded volume parameter v for the polymer.

By following the field theory steps described in chapter 2, the effective Hamiltonian for this model system can written as,

$$\beta F[w(\mathbf{r})] = \frac{v}{2}\int d\mathbf{r}\rho^2(\mathbf{r}) - \int d\mathbf{r}w(\mathbf{r})\rho(\mathbf{r}) - n_{\mathrm{g}}\ln Q(\mathbf{r}_\perp;[w(\mathbf{r})]) \tag{7.1}$$

where $Q(\mathbf{r}_\perp;[w(\mathbf{r})])$ represents a normalized partition function for a polymer chain whose one end is grafted at the surface $\mathbf{r} = D$ with the chain subjected to a self consistent potential field $w(\mathbf{r})$. $Q(\mathbf{r}_\perp;[w(\mathbf{r})])$ can be computed from the propagator for the grafted polymer chain as,

$$Q(\mathbf{r}_\perp;[w(\mathbf{r})]) = \int d\mathbf{r}\ q_{\mathbf{r}_\perp}(\mathbf{r}, s=1;[w(\mathbf{r})]) \tag{7.2}$$

where $q_{\mathbf{r}_\perp}(\mathbf{r}, s;[w])$ represents a propagator for a polymer chain that originates at the grafting surface, $\mathbf{r} = D$ and has its free end at position $\mathbf{r}$. This propagator satisfies a diffusion-like equation:

$$\frac{\partial q(\mathbf{r}, s)}{\partial s} = \frac{Nb^2}{6}\nabla^2 q(\mathbf{r}, s) - w(\mathbf{r})q(\mathbf{r}, s), \tag{7.3}$$

with initial condition given as:

$$q_{\mathbf{r}_\perp}(\mathbf{r}, s=0;[w(\mathbf{r})]) = \delta(\mathbf{r} - D). \tag{7.4}$$

Now we perform a saddle point approximation for Eq. 7.1. Differentiation with respect to $\rho(\mathbf{r})$ results in the self consistency condition for the potential field, $w(\mathbf{r}) = v\rho(\mathbf{r})$. The corresponding density field $\rho(\mathbf{r})$ is obtained by differentiation with respect to $w(\mathbf{r})$ as,

$$\begin{aligned}\rho(\mathbf{r}, w[\mathbf{r}]) &= \int_{\mathbf{r}=D} d\mathbf{r}\ n_{\mathrm{g}} \frac{\partial \ln Q(\mathbf{r}_\perp; [w(\mathbf{r})])}{\partial w[\mathbf{r}]} \\ &= \int_{\mathbf{r}=D} d\mathbf{r} \frac{n_{\mathrm{g}}}{Q(\mathbf{r}_\perp; [w])} \int_0^1 ds\ q_{\mathbf{r}_\perp}(\mathbf{r}, s) q(\mathbf{r}, 1-s) \qquad (7.5)\end{aligned}$$

where $q(\mathbf{r}, s)$ is a complementary propagator that describes a polymer chain that begins at the free end of the grafted polymer chain. $q(\mathbf{r}, s)$ satisfies the diffusion equation (cf. eq. 7.3) with initial condition $q(\mathbf{r}, s = 0) = 1$. Equation 7.1 can then be rewritten as,

$$\beta F[w(\mathbf{r})] = -\frac{1}{2B} \int d\mathbf{r} w^2(\mathbf{r}) - \sigma \ln Q(\mathbf{r}_\perp; [w(\mathbf{r})]) \qquad (7.6)$$

where all lengths are non-dimensionalized by R_{g} and $B = vN^2/R_g^3$. σ denotes the grafting density in terms of number of grafted chains per unit area (in R_{g}^2 units).

As shown by Müller [210] the density operator in eq. 7.5 can be rewritten as:

$$\rho(\mathbf{r}, w[\mathbf{r}]) = \int_0^1 ds\ q_{\mathrm{c}}(\mathbf{r}, s) q(\mathbf{r}, 1-s) \qquad (7.7)$$

where q_c is new complementary propagator defined by :

$$q_{\mathrm{c}}(\mathbf{r}, s; [w]) = \int_{\mathbf{r}=D} d\mathbf{r} \frac{\sigma}{Q(\mathbf{r}_\perp; [w])}\ q_{\mathbf{r}_\perp}(\mathbf{r}, s) \qquad (7.8)$$

As q_{c} is linearly related to $q_{\mathbf{r}_\perp}$, it also satisfies the diffusion equation 7.3, with however, the initial condition,

$$q_{\mathrm{c}}(\mathbf{r}, s = 0; [w(\mathbf{r})]) = \frac{\sigma \delta(\mathbf{r} - D)}{q(\mathbf{r} = D; s = 1; [w(\mathbf{r})])} \qquad (7.9)$$

Additionally, the partition function $Q(\mathbf{r}_\perp)$ for a single chain can also be factorized as:

$$Q(\mathbf{r}_\perp; w[\mathbf{r}]) = \int d\mathbf{r}\ q_{\mathbf{r}_\perp}(\mathbf{r}, s) q(\mathbf{r}, 1-s) \tag{7.10}$$

for all $s \in [0,1]$. Setting $s = 0$ reduces equation 7.10 to,

$$Q(\mathbf{r}_\perp; w[\mathbf{r}]) = q(\mathbf{r}_\perp, 1; [w]) \tag{7.11}$$

Using eq. 7.11, the free energy of the system given by eq. 7.6 can now be rewritten as:

$$\beta F[w(\mathbf{r})] = -\frac{1}{2B}\int d\mathbf{r} w^2(\mathbf{r}) - \sigma \ln q(\mathbf{r}_\perp, 1; [w(\mathbf{r})]) \tag{7.12}$$

Thus evaluation of polymer density operator for a brush requires two solutions of equation 7.3. First solution is effected for $q(\mathbf{r}, s)$ which is required for both the initial condition of q_c (cf. eq. 7.9), and for determining of segment density profile (cf. eq. 7.7). The second solution of eq. 7.3 for q_c with the initial condition given by eq. 7.9 completes the evaluation of densities.

We use above field theory to compute the change in the free energy as an impenetrable protein approaches a polymer brush. We define insertion free energy for a protein molecule at a surface-to-surface distance r as the difference in the free energy for a polymer brush in presence of a protein at r and that for a polymer brush in absence of protein. Thus, the free energy is computed as,

$$\beta \Delta F(r) = \beta F_{\text{Brush + Protein at r}} - \beta F_{\text{Brush}} \tag{7.13}$$

For the case of impenetrable surface of protein, the polymer chains are neither attracted nor repelled by the surface and the appropriate boundary condition in such case is given as $q(\mathbf{r}, s)|_{\mathbf{r}=R} = 0$ where R denotes the radius of protein. For the case of grafted particle, for numerical convenience we assume a weak attractive interaction between the particle surface and polymer chains and treat this interaction using the critical (or reflection) boundary condition,

$$\left.\frac{\partial q}{\partial \mathbf{r}}\right|_{\mathbf{r}=D} = 0. \tag{7.14}$$

However, it should be noted that the use of the reflection boundary (in place of adsorption boundary $q(\mathbf{r}, s)|_{\mathbf{r}=D} = 0$) does not have any appreciable variation in the structure of the brush except at very short distances from the surface [211]. In the subsequent sections, we present preliminary results for the structure of a polymer brush and free energy of insertion for a protein for various physical parameters such as the size of the protein, molecular weight and grafting density of the polymer brush and curvature of the grafted particle.

7.2 Structure of a Polymer Brush

In this section, we analyze the effect of surface curvature and grafting density on the structure and extension of brush. The findings of this section will be utilized later in section 7.3 to rationalize the change in the insertion free energies for a protein as it approaches a brush coated surface.

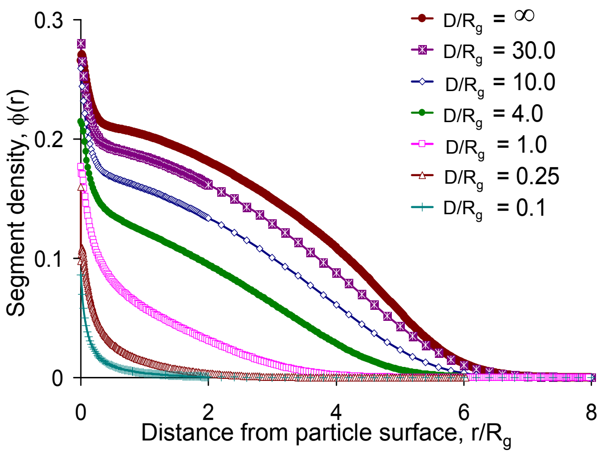

(a)

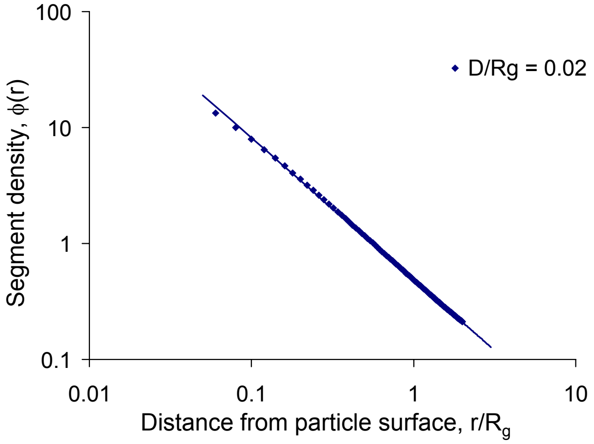

(b)

Figure 7.1: (a) Segment volume fraction profiles for grafted polymer chains $\phi(r)$ as a function of distance from the particle surfaces for spherical particles of different radii. The flat surface volume fraction profile is indicated by $R/R_{\rm g} = \infty$. Grafting density is fixed at $\sigma R_{\rm g}^2 = 1.667$. (b) Segment volume fraction profiles for grafted polymer chains $\phi(r)$ as a function of distance from the particle surfaces for particle radius $D/R_{\rm g} = 0.02$ on log-log scale. Grafting density is fixed at $\sigma R_{\rm g}^2 = 16670$.

7.2.1 Effect of Surface Curvature on the Structure of a Brush

In Fig. 7.1a we display segment volume fractions for grafted polymer brushes as a function of distance from the particle surface for different sized particles. For large radius of curvature, we observe that the brush volume fractions follow a parabolic profile except at very close distance from the surface and at the outer end of brush. For particle radii $D/R_{\mathrm{g}} \gtrsim 10$, we observe a good resemblance in the brush profile on a curved surface and that for a flat surface. As the curvature of the particle is increased (smaller particles), the shape of brush volume fraction profiles becomes more and more concave. As shown in Fig. 7.1b, for very small particles the volume fraction profiles follow a power law dependence on the distance from the surface. We also observe that the extension of brushes shows a significant decrease with decrease in the size of the particles. We quantify the extension of brushes in terms of brush height, H_{brush}. The latter is defined in similar manner as Ref. [212]:

$$H_{\mathrm{brush}} = \left(\frac{\int \phi(r) r^2 (r+D)^2 dr}{\int \phi(r)(r+D)^2 dr} \right)^{1/2} \tag{7.15}$$

Figure 7.2a shows the brush height as a function of radius of grafted surface for different grafting densities. For all grafting densities, we observe that the brush height follows a sigmoidal shape as the particle size is varied. For larger particles $D/R_{\mathrm{g}} \gg 1.0$, the brush height is observed to asymptote to that for planar brushes whereas with decrease in the particle size the brush height decreases rapidly. For larger particles where volume fractions follow a

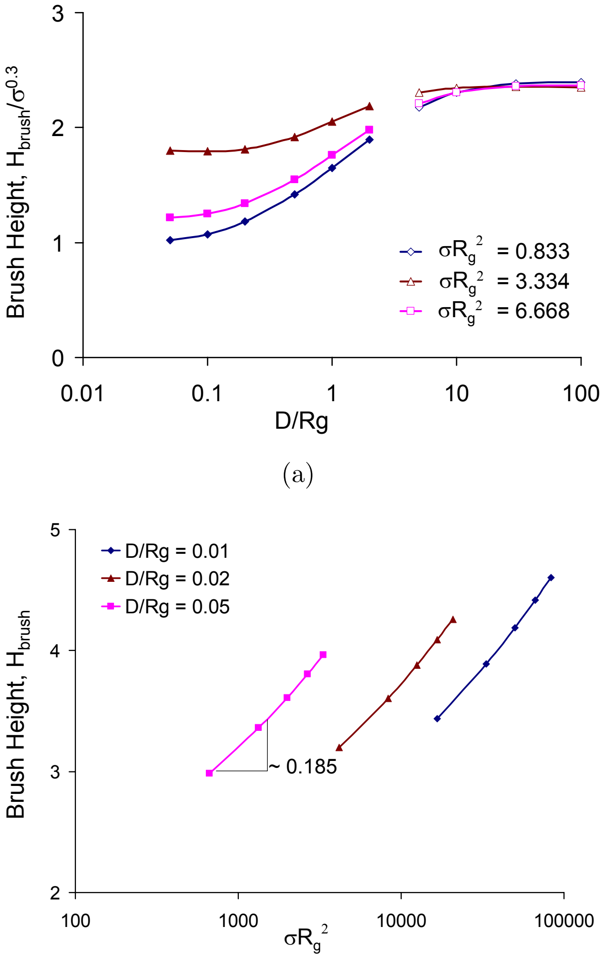

(a)

(b)

Figure 7.2: (a) Brush height (scaled by $(\sigma R_{\mathrm{g}}^2)^{-0.3}$) as a function radius of curvature of surface D/R_{g}. (b) Brush height for small particles ($D/R_{\mathrm{g}} \ll 1.0$) as a function of σR_{g}^2.

parabolic profile, we note that the brush height scales as:

$$H_{\text{brush}}[D] \propto \sigma^{0.3} \tag{7.16}$$

We note that the above scaling exponent for large particles is close to the classical scaling for planar brush where $H \propto \sigma^{0.33}$. On the other hand, as seen from Fig. 7.2b, for the case of small particles ($D/R_{\text{g}} \ll 1.0$), the brush height scales as $H_{\text{brush}} \propto \sigma^{0.185}$. The latter exponent closely corresponds to that for a star polymer where H_{brush} is predicted to scale as $\sigma^{1/5}$ [213].

7.2.2 Effect of Grafting Density on the Structure of a Brush

In Fig. 7.3a we display segment volume fractions for grafted polymer brushes as a function of distance from the particle surface for different grafting densities (defined as number of grafted chains per unit area). The radius of the grafted surface is fixed at $D/R_{\text{g}} = 1.0$. With an increase in the grafting density we observe an increase in both the volume fractions as well as the extension of the brush. In Fig. 7.3b we display the brush height as a function of the grafting density σR_{g}^2 for a particle size $D/R_{\text{g}} = 1.0$. We observe that with increase in the σ, the brush height first increases and eventually levels off to a constant value at higher σ values. As the grafting density increases, the polymer chains start overlapping and assume more extended configurations resulting in larger brush heights. For higher grafting densities the polymer chains are more or less completely extended, and further increase in grafting density does not result in appreciable changes in the brush height.

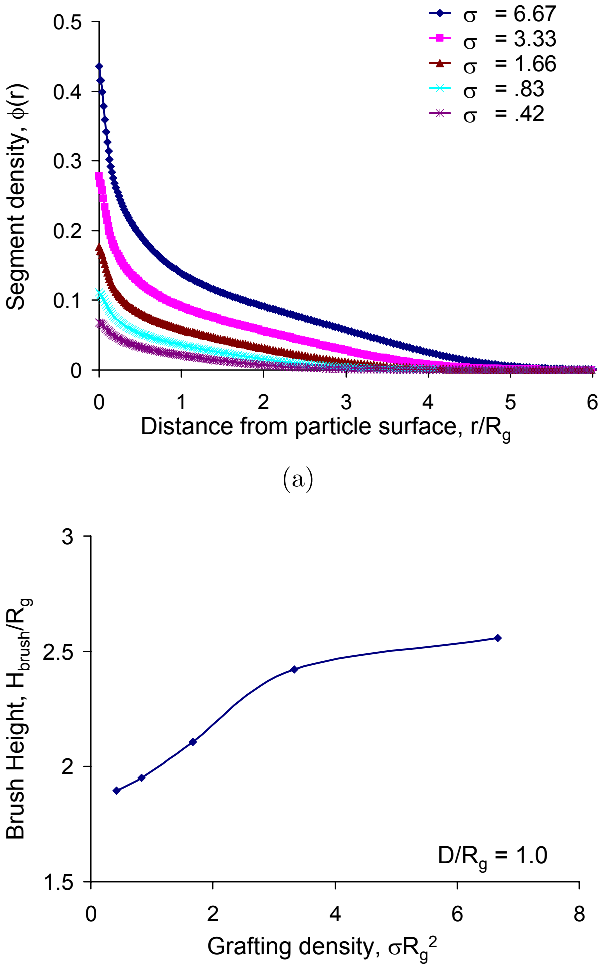

(a)

(b)

Figure 7.3: (a) Segment volume fraction profiles for grafted polymer chains $\phi(r)$ as a function of distance from the particle surfaces for spherical particles of different radii. (b) Brush height as a function of grafting density σR_{g}^2 for $D/R_{\mathrm{g}} = 1.0$.

An increase in the brush height and the polymer volume fractions is expected to result in a longer ranged and stronger steric barrier opposing the inherent attractive van der Waals forces between external objects such as particles and proteins. These preliminary results suggest that higher grafting density will provide better resistance against the protein adsorption. Secondly, for smaller particles, the brush configurations are less extended and may require higher grafting densities as compared to that for larger particles in order to provide the same resistance to protein adsorption.

7.3 Free Energy of Insertion of a Protein onto a Grafted Surface

Many experimental studies suggest that an interplay between parameters such as protein size and polymer grafting density, polymer molecular weight governs the efficiency of inhibition of protein adsorption on grafted surfaces. In this section, we first quantify the effect of each of these physical parameters on the free energy of insertion (defined by eq. 7.13) for a bare protein molecule as it approaches a spherical particle carrying grafted polymer brush. In subsequent sections, we combine these results to develop a general understanding of optimum design parameters for protein resistant surfaces.

7.3.1 Effect of Protein Size

A number of experimental studies have discussed the size of protein molecule as an important factor affecting the protein rejection ability of grafted polymers. For instance, a larger protein can approach a grafted surface only by compressing the brush, which is expected to result in higher steric resistance against adsorption. On the other hand, a smaller sized protein can penetrate a brush without much change in the brush densities, and consequently with a small free energy resisting protein adsorption. In order to analyze the effect of the size of the protein on the insertion free energy, we fix the size of the polymer grafted particle to $D/R_{\mathrm{g}} = 1.0$ and compute the $\beta\Delta F(r)$ for proteins of different sizes.

In Fig. 7.4a, we display the insertion free energy $\beta\Delta F(r)$ as a function of surface to surface distance r between grafted particle and protein (normalized by R_{g}). As the protein molecule approaches the grafted surface, we observe a monotonic increase in the repulsions which corresponds to compression of the grafted polymer chains. The resultant loss in the conformational entropy for grafted polymer chains renders the insertion free energy positive. For all protein sizes, the free energy of insertion is found to be always positive, indicating protein repulsion by the grafted surface. However, with decrease in the size of the proteins, we observe a rapid decrease in the strength of repulsions. In Fig. 7.4b we display the insertion free energy at $r = 0$ (which corresponds to change in the free energy at the closest approach between the grafted surface and the protein) as a function of size of a protein at fixed $\sigma {R_{\mathrm{g}}}^2$ for $D/R_{\mathrm{g}} = 1$. With decrease in the size of the proteins, we first observe a gradual decrease in $\Delta F(0)$ for $R/R_{\mathrm{g}} \gg 1.0$ which becomes steeper for smaller proteins. The latter implies that smaller proteins will adsorb more readily

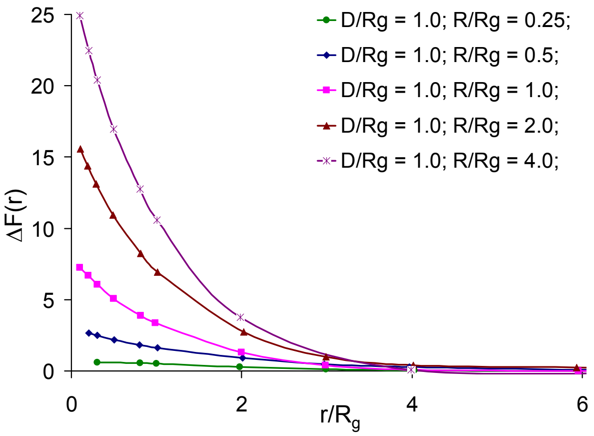

(a)

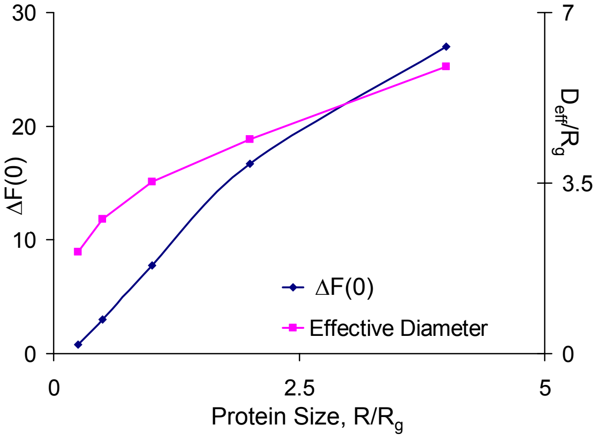

(b)

Figure 7.4: (a) Free energy of insertion $\beta\Delta F(r)$ for a protein with radius R approaching a brush coated surface with radius D for different D/R values. (b) Free energy of insertion at closest approach between grafted surface and protein, $\beta\Delta F(0)$ and D_{eff} as a function of protein size R/R_{g} for $\sigma R_{\text{g}}^2 = 1.667$ and $D/R_{\text{g}} = 1$.

on the grafted surfaces under the influence of van der Waals interactions and thus, will require stronger steric barrier to prevent their adsorption.

We characterize the range of free energy change in terms of an equivalent hard sphere diameter for the grafted surface using Barker-Henderson expression [83, 123]:

$$D_{\text{eff}} = \int_0^\infty (1 - \exp[-\Delta F(r)])\, dr \tag{7.17}$$

Fig. 7.4b displays the effective hard sphere diameter $D_{\text{eff}}/R_{\text{g}}$ as a function of protein size R/R_{g}. It can be noted that D_{eff} shows qualitatively similar behavior as that for $\Delta F(0)$: with decrease in the size of the protein molecule the effective hard sphere diameter decreases. Overall, the above trends suggest that with a decrease in the protein size, the resistance of grafting surface for protein adsorption decreases. $\Delta F(0)$ gives a good measure of strength of repulsions induced by the grafted polymer where as D_{eff} can serve as convenient parameter accounting for the range of such repulsions. With decrease in size of the protein, we observe a decrease in both the range and strength of the induced repulsions, which implies that smaller proteins experience lesser resistance by the grafted surface layers and can penetrate much further in the grafted polymer layers as compared to larger particles.

7.3.2 Effect of Grafting Density

In Fig. 7.5a we display the free energy of insertion as a function of intersurface distance for different values of surface densities σR_{g}^2. As expected, we observe that at any interparticle distance, the free energy of insertion increases as the grafting density is increased, with the increase in free energy being more prominent closer to the surface of the particle. As discussed in previous section, higher grafting densities result in an overall increase in the volume fraction of the polymer, which results in stronger repulsions between the grafted polymer chains. In Fig. 7.5b, we display the free energy of insertion at the closest approach as a function of σR_{g}^2. With increase in the σR_{g}^2 there is a sharp increase in the $\Delta F(0)$ at lower σ values followed by a gradual change at higher grafting densities. Moreover, at higher grafting densities, the distance at which $\Delta F(r) \rightarrow 0$ also increases. The latter indicates that at higher grafting densities, the perturbation in the brush caused by the presence of protein extends to much larger distances and is a manifestation of larger brush height for denser brushes. In Fig. 7.5b, we present the range of free energy in terms of an equivalent hard sphere diameter obtained using eq. 7.17. With increase in the grafting densities, we observe first a sharp increase in D_{eff} at lower grafting densities and relatively less steep increase at higher σ values. The above behavior of D_{eff} and $\Delta F(0)$ suggests that an increase in σ increases both the range and strength of the induced repulsions. The latter implies that denser polymer brushes will provide better resistance against protein adsorption.

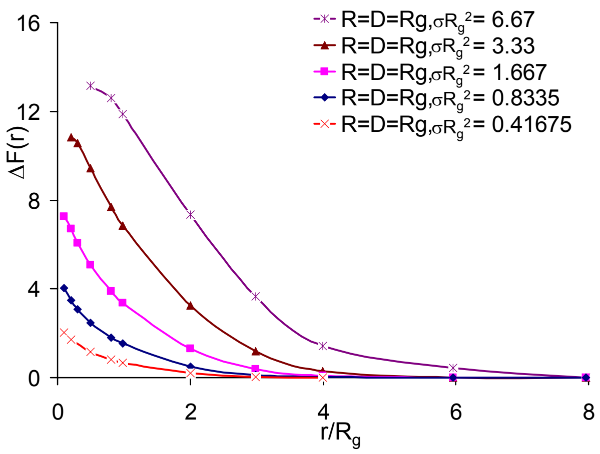

(a)

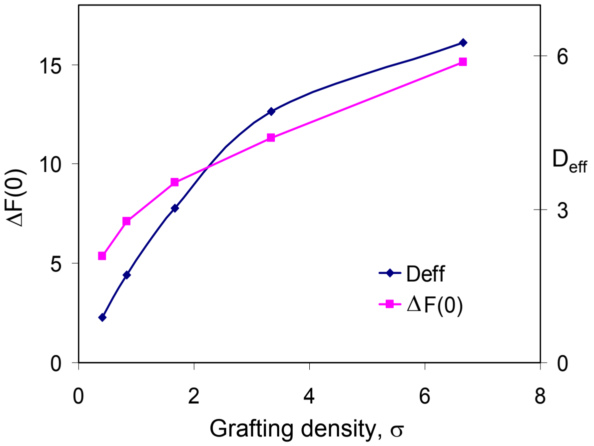

(b)

Figure 7.5: (a) Free energy of insertion $\beta \Delta F(r)$ for a protein with radius $R/R_{\mathrm{g}} = 1$ approaching a brush coated surface with radius $D/R_{\mathrm{g}} = 1$ for different grafting densities. (b) Free energy of insertion at closest approach between grafted surface and protein, $\beta \Delta F(0)$ and the effective diameter D_{eff} as a function of grafting density σR_{g}^2. $D/R_{\mathrm{g}} = R/R_{\mathrm{g}} = 1.0$

7.3.3 Effect of van der Waals Interactions

In the previous sections, we had ignored the van der Waals attractions between the particles surface and the protein molecules and discussed the changes in the free energies for idealized hard sphere surfaces, albeit in presence of grafted polymer layer on the particle surface. In this section, we introduce van der Waals interactions between the grafted surface and the protein molecule and study their effect on the overall interactions. We approximate the van der Waals attraction using the DLVO theory [214]:

$$\beta U_{\text{vdW}}(r) = \begin{cases} \infty, & r < D + R + \epsilon \\ -\frac{A}{6}\left[\left(\frac{(R+D)^2}{2(r^2-(R+D)^2}\right) + \left(\frac{(D+R)^2}{2r^2}\right) \right. & \\ \left. + \ln\left[\frac{r^2-(D+R)^2}{r^2}\right]\right], & r \geq D + R + \epsilon \end{cases} \tag{7.18}$$

where D and R represent the radii of the grafted particle and protein respectively. A denotes Hamaker constant and ϵ is the distance of closest approach between the protein and the particles and is introduced to ensure that U_{vdW} does not diverge at contact. In the following analysis, we set Hamaker constant to $5kT$ and $\epsilon = 0.05$. These parameters are found to well describe globular proteins like lysozyme for a wide range of ionic strengths [215].

Next, we define the overall interactions between the polymer grafted surface and protein as the sum of (i) the free energy change $\beta\Delta F(r)$ of the system as the protein molecule approaches the particle (discussed in previous sections) and (ii) the van der Waals interaction between the particle and protein obtained using eq. 7.18. In Fig. 7.6a, we display the overall interactions for various sizes of proteins for fixed grafting density $\sigma R_{\text{g}}^2 = 1.667$ and $D/R_{\text{g}} = 1$.

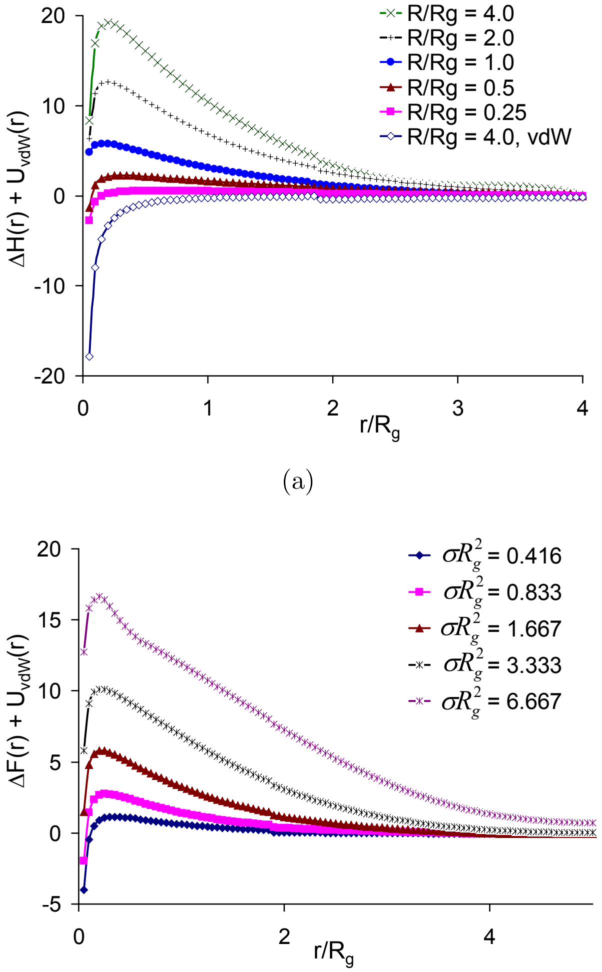

(a)

(b)

Figure 7.6: (a) Overall interaction experienced by a protein approaching a brush coated surface for different protein sizes for $D/R_\mathrm{g} = 1$ and $\sigma R_\mathrm{g}^2 = 1.667$. (b) Overall interaction experienced by a protein approaching a brush coated surface for different grafting densities for $R/R_\mathrm{g} = D/R_\mathrm{g} = 1$.

The bottommost curve shows van der Waals attraction between a bare particle (without polymer grafting) and a protein of size R/Rg = 4.0. The remaining curves from bottom-to-top correspond to overall interactions for protein sizes $R/R_\mathrm{g} = 0.25, 0.5, 1.0, 2.0, 4.0$ respectively. The overall interactions are observed to be a non-monotonic function of distance between the surface and the protein molecule. The interactions are found to be weakly repulsive at larger distances. The strength of repulsion increases at intermediate distances whereas at smaller distances the repulsive interactions weaken, and for smaller particles the interactions are observed to become attractive at shorter distances. The above trends in overall interactions can be understood from the relative strength of polymer induced interactions and van der Waals attractions. At larger distances the long range polymer induced repulsions dominate, where as at smaller distances the short range vdW attractions dominate the overall interactions. We further observe that the strength of the repulsive barrier in the overall interactions critically depends on the size of the protein molecule and decreases as the size of the protein is decreased. These results suggest that at a fixed grafting density, the grafted surfaces will more efficiently prevent the adsorption of larger proteins as compared to that of smaller proteins. In Fig 7.6b, we display the overall interactions between a grafted particle and a protein molecule as a function of interparticle distance for different grafting densities. We observe that indeed the higher grafting densities introduce higher repulsive barrier, implying better resistance against aggregation.

7.4 Summary and Discussion

In summary, we have analyzed the structure of grafted polymer brush and their effect on the adsorption of protein on curved surfaces. For larger particles, the brush volume fractions show classical parabolic profile [212]. The height of such brushes is observed to be independent of surface curvature and follows a power law dependence on grafting density: $H \propto \sigma^{\nu}$. For this case of brushes on large particles, our results show a scaling exponent of $\nu = 0.3$. The latter is close to the classical scaling exponent for flat brushes $\nu = 0.33$ for moderately dense brushes in good solvent [212, 213]. For smaller particles ($R/Rg < 1.0$), the brush height is observed to show a more intricate dependence on the size of the particle and grafting density.

We also analyzed the effect of polymer grafting on the insertion free energy of spherical proteins. Our results suggest that at fixed grafting density, the resistance of the grafted polymer to protein adsorption diminishes with decrease in the size of the protein molecules. Secondly, we observed that increase in the surface grafting provides stronger steric hindrance to protein adsorption. The above results are consistent with previous experimental [216]and simulation works [217] where higher grafting densities are predicted to provide better barrier against adsorption of proteins. Furthermore, our study suggest that smaller protein molecules are more easily adsorbed and thus to prevent such an adsorption of smaller proteins one would require higher grafting densities. Malmsten et. al. [216] have made a similar observation in context of adsorption of serum proteins on PEG coated surfaces where larger proteins are observed to be more efficiently rejected by the PEG coated surface.

It should be noted that during the adsorption process the protein can undergo denaturation, which may have significant effect on the adsorption process. This study ignores the such structural changes in protein molecule and idealizes it as a spherical particle. Secondly, we model the polymer as a self avoiding Gaussian polymer. Water soluble polymer such as PEG show some distinctive traits that are not accounted in such a model. For instance, experimental data on aqueous PEO solutions [218] reveals concentration dependent excluded volume effect, i.e. $v = v(\rho(r))$. Though the self consistent field model detailed in section 7.1 can be easily extended to incorporate this effect, the results presented in this chapter are for the case of uniform v. Nonetheless, the above results provide a qualitative understanding of the role of different physical parameters, such as curvature of brush, grafting density and protein size in preventing the adsorption of proteins on curved surfaces.

Chapter 8

Summary and Outlook

In this chapter, we first present a summary of the research work detailed in this dissertation, followed by recommendations for future work for understanding the phase behavior, structural characteristics and rheological properties of polymer-particle systems.

8.1 Summary of Research

An important contribution of this work to the field of multicomponent polymer-particle systems is the development of a generic unified multiscale approach which successfully addresses the disparity in the length scales encountered in such systems and allows simultaneous identification of phase behavior, percolation/gelation transitions and structural and rheological properties of the systems under consideration. The subsequent applications of this approach to the case of non-adsorbing, adsorbing and grafted polymer chains in presence of nanoparticles have led to a predictive understanding of the influence of 'microscopic' parameters that characterize such binary systems on the macroscopic thermodynamics, phase behavior, structure and rheology of these mixtures.

Specifically, our research effort was focused on understanding the effect of polymer on the interparticle interactions, resultant phase behavior and structural features of polymer-particle mixtures. The size and length scale asymmetries in such systems render both the particle-based simulations as well as coarse grained field theoretic approaches unsuitable. To address these challenges, we implemented a multiscale approach which allows for coarse graining of polymeric component in the system and maps the two component system in terms of an effective one component system consisting of just particles. The resultant one component system is characterized by *polymer mediated effective interactions*. To extract the latter, we adapted a mean field approach and implemented a numerical version of polymer self consistent field theory in bispherical coordinates. The latter allowed us to access a wide range of polymer and particle sizes, while simultaneously eliminating the artifacts arising from geometrical discretizations. In the subsequent studies, we adapted the above developed framework : (i) to incorporate multibody effects in the nanoparticle regime (ii) to examine the phase behavior and percolation characteristics (iii) to probe the polymer bridging induced gelation phenomena and (iv) to predict the structure and elastic properties of particulate gels.

Our implementation of above approach for the case of nanoparticles in non-adsorbing polymers highlighted several surprising features that distinguished the nano-sized particles from the particles in colloidal size range. In nanoparticle regime, we showed that the volume of the polymer depletion layers far exceeds the particle size itself and leads to significant multibody interaction effects. The latter were approximated through a novel free volume approach to demonstrate that the multibody effects can lead to significant strengthening of the attractive depletion interactions and can result in demixing in the protein-polymer mixtures.

Next, we studied the phase behavior, percolation transitions and structural characteristics of nanoparticles in adsorbing polymeric solutions. We proposed a ‘saturable adsorption model’ which accounts for the finite adsorption capacity of nano-sized particles. Our results demonstrated that an interplay between surface saturation, polymer concentration and polymer-to-particle size ratio governs the interactions between the particles. The latter are observed to result in a rich phase behavior ranging from bridging flocculation to steric stabilization.

Our studies on the conformational characteristics allowed a direct comparison between the structure of polymer layers on flat surfaces and that on highly curved nanoparticles. Our results demonstrate that adsorption on large particles/flat surfaces is primarily in the form of loop-like structures where as the adsorption on smaller particles is characterized by prominence of tail-like structures. The latter significantly enhances the probability of formation of polymeric bridges in the nanoparticle regime. These microscopic structural features were incorporated into a hybrid simulation approach which in conjunction with graph theory led to direct identification of polymer induced clustering of particles. Our results suggest significant lowering of gelation volume fractions in the nanoparticle regime and show an excellent agreement with the published experimental observations. An important outcome of this study is the identification of universality in the structural characteristics and elastic properties of polymer-bridged gels of particles. The predicted universal scalings for structure and elastic moduli show an excellent agreement with the experimental data for a number of polymer-particle systems and can provide a quantitative approach to delineate the mechanisms of gelation in polymer-nanoparticle systems.

We also studied the adsorption characteristics, the effective pair-interaction potentials and the resulting phase behavior, percolation transitions of rod-like nanoparticles dispersed in solutions of adsorbing polymers. By using polymer self-consistent field theory in conjunction with a Derjaguin approximation we computed the polymer-mediated orientation-dependent pair interaction potentials between cylindrical nanorods. A modified Flory theory and a simple analytical model is then used to delineate the different equilibrium phases and the onset of percolation for nanorods in polymer solutions. We analyzed the influence of polymer-surface affinity, the polymer concentrations, the radius of rods, and the aspect ratio of rods, on the topology of equilibrium phases and percolation regimes. As a model mimicking nanotube-polymer mixtures, we also considered the influence of strong rod-rod van der Waals interactions on the above equilibrium characteristics.

Finally, we studied the effect of grafted polymer chains on protein adsorption for different sizes of protein molecules and various grafting densities. We model polymer grafting on a particle surface within the self-consistent field framework and idealize the protein as a spherical particle. We analyze the effect of surface curvature on the structure of polymer brush and examine the free energy change as the protein approaches a grafted polymer layer under different physical conditions. Our analysis delimits the optimum design parameters for the prevention of van der Waals induced adsorption of proteins on a particle surface.

8.2 Recommendations for Future Work

The approach developed in this dissertation presents many generalizations which can lead to a more comprehensive understanding of the manner in which the microscopic properties of constituents influence macroscopic interactions, phase behavior and rheology of polymer-particle systems. In the following we suggest possible directions for future research that will help us better understand the physics of nanoparticle-polymer mixtures and how it differs from colloid-polymer mixtures.

8.2.1 Complexation and Phase behavior in Polyelctrolyte-Particle Mixtures

Systems involving particles in presence of charged polymers such as polyelectrolytes, polyampholytes etc. are commonly encountered in a variety of industrial applications such as colloidal stabilization, food and dairy formulations, protein separations [219, 220]. Also, many biophysical processes such as DNA-histone complexation are governed by electrostatic interactions between the components [221].

A number of physical parameters determine the electrostatics of polyelectrolyte solutions. These include the charge distribution along the polymer chain, the concentration of counterions (which are attracted to polyelectrolyte via a long-ranged Coulombic attraction), pH, salt concentration and solvent quality. The presence of particles adds further to these complexities making the theoretical studies of polyelectrolyte-particle systems far more difficult than their neutral counterparts. Moreover, bending of a charged polymer molecule around a curved surface is governed by the intra-chain repulsions and chain interactions with the counterions cloud surrounding the chain and results in a significant amount of electrostatic energy [219]. Hence curvature of the particle is expected to lead to a marked effect on adsorption of a polyelectrolyte as compared to adsorption of neutral polymer on spherical particles. Though polyelectrolyte adsorption on spherical geometries is of particular interest in most colloidal science applications and bio-cellular processes, most earlier analytical and/or scaling studies of these systems are limited to flat geometries.

The simultaneous presence of both, short-range (excluded volume) and long-range (Coulombic) interactions in polyelectrolyte solutions gives rise to many complex features in context of polyelectrolyte-particle interactions. Some of the interesting issues in this context are:

1. Depending on salt concentration, pH, polymer concentration, polyelectrolyte molecular weight etc, polyelectrolyte-micelles and

polyelectrolyte-protein systems exhibit a rich phase behavior including liquid-liquid, liquid-solid phase transitions [222]. The physics behind these phase transitions is poorly understood.

2. In polyelectrolyte-micelle and polyelectrolyte-protein systems, conformations of polyelectrolytes on the particle surface, particularly, polymer bridging between the particles have been speculated to play an important role in the phase behavior [223]. Theoretical understanding of these polyelectrolyte conformations is quite limited.

The hybrid framework developed in this research which combines the polymer field theory with particle based simulations is especially well suited for studying the thermodynamics and phase behavior in PE-particle systems. At a mean field level, the PE mediated interactions between the particles can be discerned by simultaneous solutions of polymer field theory equations and Poisson Boltzman equation. Further, the conformational characteristics of PE chains near the particle surface can be straightforwardly extracted by implementing the two point propagator approach described in Section 2.3 and can be incorporated into particle based approaches to gain insights into the complexation and self assembly in such systems.

8.2.2 Phase Behavior, Structure and Rheology in Mixtures of Copolymer/Polymer Blends and Nanoparticles

In this research, our focus was limited to the effect of homopolymers on the interactions, phase behavior and structural features of particulate suspensions. However, a substantial number of the practical situations comprise of nanoparticles in presence of copolymers or blends of different homopolymers. Such mixtures are being actively investigated for their potential to yield complex, highly ordered composites for next generation catalysts, selective membranes, and photonic band gap materials. The specific morphology and hence the applicability of these materials critically depends on the polymer architecture and on parameters such as the size and volume fraction of the particles, size asymmetry between different polymeric components/blocks and their relative affinities for the particle surfaces etc. Though polymer self consistent field theories have shown remarkable success in modeling thermodynamics of pure polymers and copolymers, not much theoretical work exists on the effect of copolymers/blends on the phase behavior and self assembly characteristics in inhomogeneous systems containing particles. The framework developed in this research can be easily generalized for the case of polymer blends as well as copolymers and can help understand the morphology and thermodynamic behavior of copolymer-particle mixtures.

8.2.3 Dynamics and Flow Behavior of Nanoparticles in Polymeric Media

Experimental studies on polymer-nanoparticle systems show a variety of interesting effects regarding the dynamics and flow behavior of polymer-nanocomposites. For instance, studies of dynamical behavior of polymers near surfaces have observed significant changes in polymer mobility, slippage under shear etc. These observations have been speculated to be correlated to the interactions between the particles and polymers. The equilibrium studies presented in this dissertation have highlighted profound differences in the equilibrium interactions and structural characteristics in the nanoparticle regime in comparison with that for larger particles. These results can be combined in hybrid molecular dynamic approaches to clarify the role of interactions, polymer structural features (such as interparticle bridging) and rheology in influencing the dynamics and flow behavior of polymer-nanoparticle mixtures. Interesting connections between interaction potential and rheology have been suggested in studies on associating polymers and mode coupling theories. Exploring such connections between the equilibrium characteristics and dynamics of polymer-nanocomposites can have significant practical implications.

Bibliography

[1] Asakura S. and F. Oosawa. Interaction between particles suspended in solutions of macromolecules. *Journal Of Polymer Science*, 33:183–192, 1958.

[2] Vrij A. Polymers at interfaces and the interactions in colloidal dispersions. *Pure And Applied Chemistry*, 48:471–483, 1976.

[3] W. Poon. Colloids as big atoms. *Science*, 304:830–831, 2004.

[4] J. M. H. M. Scheutjens and G. J. Fleer. Interaction between 2 adsorbed polymer layers. *Macromolecules*, 18:1882–1900, 1985.

[5] G. Rossi and P. A. Pincus. Interactions between unsaturated-polymer adsorbed surfaces. *Europhysics Letters*, 5:641–646, 1988.

[6] A. Johner, J. F. Joanny, S. D. Orrite, and J. B. Avalos. Gelation and phase separation in colloid-polymer mixtures. *Europhysics Letters*, 56:549–555, 2001.

[7] J. B. Hooper and K. S. Schweizer. Theory of phase separation in polymer nanocomposites. *Macromolecules*, 39:5133–5142, 2006.

[8] C. Singh, G. T. Pickett, E. Zhulina, and A. C. Balazs. Modeling the inter-

actions between polymer-coated surfaces. *Journal Of Physical Chemistry B*, 101:10614–10624, 1997.

[9] C. Schmitt, C. Sanchez, S. Desobry-Banon, and J. Hardy. Structure and technofunctional properties of protein-polysaccharide complexes: A review. *Critical Reviews In Food Science And Nutrition*, 38:689–753, 1998.

[10] R. Piazza. Interactions and phase transitions in protein solutions. *Current Opinion In Colloid & Interface Science*, 5:38–43, 2000.

[11] S. M. Illet, A. Orrock, W. C. K. Poon, and P. S. Pusey. Phase behavior of a model colloid-polymer mixture. *Physical Review E*, 51:1344–1352, 1995.

[12] D. G. A. L. Aarts, R. Tuinier, and H. N. W. Lekkerkerker. Phase behaviour of mixtures of colloidal spheres and excluded-volume polymer chains. *Journal Of Physics-Condensed Matter*, 14:7551–7561, 2002.

[13] O. Spalla. Nanoparticle interactions with polymers and polyelectrolytes. *Current Opinion In Colloid & Interface Science*, 7:179–185, 2002.

[14] S. S. Ray and M. Okamoto. Polymer/layered silicate nanocomposites: a review from preparation to processing. *Progress In Polymer Science*, 28:1539–1641, 2003.

[15] P. C. LeBaron, Z. Wang, and T. J. Pinnavaia. Polymer-layered silicate nanocomposites: an overview. *Applied Clay Science*, 15:11–29, 1999.

[16] B. Cabane. Structure of some polymer detergent aggregates in water. *Journal Of Physical Chemistry*, 81:1639–1645, 1977.

[17] A. McPherson. Crystallization of macromolecules - general-principles. *Methods In Enzymology*, 114:112–120, 1985.

[18] A. M. Kulkarni, A. P. Chatterjee, K. S. Schweizer, and C. F. Zukoski. Effects of polyethylene glycol on protein interactions. *Journal Of Chemical Physics*, 113:9863–9873, 2000.

[19] O. Galkin and P. G. Vekilov. Control of protein crystal nucleation around the metastable liquid-liquid phase boundary. *Proceedings Of The National Academy Of Sciences Of The United States Of America*, 97:6277–6281, 2000.

[20] A. P. Chatterjee and K. S. Schweizer. Microscopic theory of polymer-mediated interactions between spherical particles. *Journal Of Chemical Physics*, 109:10464–10476, 1998.

[21] H. N. W. Lekkerkerker, W. C. K. Poon, P. N. Pusey, A. Stroobants, and P. B. Warren. Phase-behavior of colloid plus polymer mixtures. *Europhysics Letters*, 20:559–564, 1992.

[22] R. Tuinier, D. G. A. L. Aarts, H. H. Wensink, and H. N. W. Lekkerkerker. Pair interaction and phase separation in mixtures of colloids and excluded volume polymers. *Physical Chemistry and Chemical Physics*, 5:3707 – 3715, 2003.

[23] P. G. Bolhuis, E. J. Meijer, and A. A. Louis. Colloid-polymer mixtures in the protein limit. *Physical Review Letters*, 90, 2003.

[24] H. M. Schaink and J. A. M. Smit. Mean field calculation of polymer segment depletion and depletion induced demixing in ternary systems of globular proteins and flexible polymers in a common solvent. *Journal Of Chemical Physics*, 107:1004–1015, 1997.

[25] Q. Zhang and L. A. Archer. Poly(ethylene oxide)/silica nanocomposites: Structure and rheology. *Langmuir*, 18:10435–10442, 2002.

[26] B. Cabane, K. Wong, P. Lindner, and F. Lafuma. Shear induced gelation of colloidal dispersions. *Journal Of Rheology*, 41:531–547, 1997.

[27] D. C. Pozzo and L. M. Walker. Reversible shear gelation of polymer-clay dispersions. *Colloids And Surfaces A-Physicochemical And Engineering Aspects*, 240:187–198, 2004.

[28] J. Zebrowski, V. Prasad, W. Zhang, L. M. Walker, and D. A. Weitz. Shake-gels: shear-induced gelation of laponite-peo mixtures. *Colloids And Surfaces A-Physicochemical And Engineering Aspects*, 213:189–197, 2003.

[29] H. A. Baghdadi, H. Sardinha, and S. R. Bhatia. Rheology and gelation kinetics in laponite dispersions containing poly(ethylene oxide). *Journal Of Polymer Science Part B-Polymer Physics*, 43:233–240, 2005.

[30] M. Aubouy, O. Guiselin, and E. Raphael. Scaling description of polymer interfaces: Flat layers. *Macromolecules*, 29:7261–7268, 1996.

[31] Y. Otsubo and K. Watanabe. Rheological studies on bridging flocculation. *Colloids and Surfaces*, 50:341–352, 1990.

[32] M. I. Aranguren, E. Mora, J. V. Degroot, and C. W. MacOsko. Effect of reinforcing fillers on the rheology of polymer melts. *Journal Of Rheology*, 36:1165–1182, 1992.

[33] H. Ji, D. Hone, P. A. Pincus, and G. Rossi. Polymer bridging between 2 parallel plates. *Macromolecules*, 23:698–707, 1990.

[34] J. B. Avalos and A. Johner. Structure of adsorbed polymer layers. *Faraday Discussions*, pages 111–119, 1994.

[35] M. Dijkstra, R. van Roij, and R. Evans. Phase diagram of highly asymmetric binary hard-sphere mixtures. *Physical Review E*, 59:5744–5771, 1999.

[36] Doi M. and S. F. Edwards. *The Theory of Polymer Dynamics.* Oxford University Press, New York, 1986.

[37] K. Freed. *Renormalization Group Theory of Macromolecules.* Wiley, New York, 1987.

[38] G. H. Fredrickson, V. Ganesan, and F. Drolet. Field-theoretic computer simulation methods for polymers and complex fluids. *Macromolecules*, 35:16–39, 2002.

[39] E. Helfand. Theory of inhomogeneous polymers - fundamentals of gaussian random-walk model. *Journal Of Chemical Physics*, 62:999–1005, 1975.

[40] de Gennes P. G. *Scaling concepts in polymer physics.* Cornell University Press, New York, 1979.

[41] J. F. Joanny, L. Leibler, and P. G. Degennes. Effects of polymer-solutions on colloid stability. *Journal Of Polymer Science Part B-Polymer Physics*, 17:1073–1084, 1979.

[42] J. R. Roan and T. Kawakatsu. Self-consistent-field theory for interacting polymeric assemblies. i. formulation, implementation, and benchmark tests. *Journal Of Chemical Physics*, 116:7283–7294, 2002.

[43] L. Leibler. Theory of microphase separation in block co-polymers. *Macromolecules*, 13:1602–1617, 1980.

[44] T. Odijk. Depletion around a protein sphere interacting with a semidilute polymer solution. *Langmuir*, 13:3579–3581, 1997.

[45] G. J. Fleer, A. M. Skvortsov, and R. Tuinier. Mean-field equation for the depletion thickness. *Macromolecules*, 36:7857–7872, 2003.

[46] W. T. Vetterling H. Press, S. A. Teukolsky and B. P. Flannery. *Numerical Recipes in C.* Cambridge University Press, New York, 1992.

[47] M. Aubouy and E. Raphael. Scaling description of a colloidal particle clothed with polymers. *Macromolecules*, 31:4357–4363, 1998.

[48] J. M. H. M. Scheutjens and G. J. Fleer. Statistical-theory of the adsorption of interacting chain molecules .2. train, loop, and tail size distribution. *Journal Of Physical Chemistry*, 84:178–190, 1980.

[49] A. N. Semenov, J. BonetAvalos, A. Johner, and J. F. Joanny. Adsorption of polymer solutions onto a flat surface. *Macromolecules*, 29:2179–2196, 1996.

[50] J. M. Mendez-Alcaraz, A. Johner, and J. F. Joanny. Density profiles and interaction between irreversibly adsorbed polymer layers. *Macromolecules*, 31:8297–8304, 1998.

[51] J. B. Avalos, A. Johner, and J. F. Joanny. Bridging by adsorbed polymers between 2 surfaces. *Journal Of Chemical Physics*, 101:9181–9194, 1994.

[52] R. Tuinier, J. Rieger, and C. G. de Kruif. Depletion-induced phase separation in colloid-polymer mixtures. *Advances In Colloid And Interface Science*, 103:1–31, 2003.

[53] M. Fuchs and K. S. Schweizer. Structure of colloid-polymer suspensions. *Journal Of Physics-Condensed Matter*, 14:R239–R269, 2002.

[54] P. G. Bolhuis, A. A. Louis, and J. P. Hansen. Influence of polymer-excluded volume on the phase-behavior of colloid-polymer mixtures. *Physical Review Letters*, 89, 2002.

[55] E. J. Meijer and D. Frenkel. Computer-simulation of polymer-induced clustering of colloids. *Physical Review Letters*, 67:1110–1113, 1991.

[56] M. Fuchs and K. S. Schweizer. Structure and thermodynamics of colloid-polymer mixtures: A macromolecular approach. *Europhysics Letters*, 51:621–627, 2000.

[57] M. Fuchs and K. S. Schweizer. Macromolecular theory of solvation and structure in mixtures of colloids and polymers. *Physical Review E*, 6402, 2001.

[58] A. A. Louis, P. G. Bolhuis, E. J. Meijer, and J. P. Hansen. Polymer induced depletion potentials in polymer-colloid mixtures. *Journal Of Chemical Physics*, 117:1893–1907, 2002.

[59] S. Ramakrishnan, M. Fuchs, K. S. Schweizer, and C. F. Zukoski. Concentration fluctuations in a model colloid-polymer suspension: experimental tests of depletion theories. *Langmuir*, 18:1082 – 1090, 2002.

[60] S. Ramakrishnan, M. Fuchs, K. S. Schweizer, and C. F. Zukoski. Entropy driven phase transitions in colloid-polymer suspensions: Tests of depletion theories. *Journal Of Chemical Physics*, 116:2201–2212, 2002.

[61] S. Tanaka and M. Ataka. Protein crystallization induced by polyethylene glycol: A model study using apoferritin. *Journal Of Chemical Physics*, 117:3504–3510, 2002.

[62] N. L. Abbott, D. Blankschtein, and T. A. Hatton. Protein partitioning in 2-phase aqueous polymer systems .1. novel physical pictures and a scaling-thermodynamic formulation. *Macromolecules*, 24:4334–4348, 1991.

[63] O. Annunziata, N. Asherie, A. Lomakin, J. Pande, O. Ogun, and G. B. Benedek. Effect of polyethylene glycol on the liquid-liquid phase transition in aqueous protein solutions. *Proceedings Of The National Academy Of Sciences Of The United States Of America*, 99:14165–14170, 2002.

[64] R. Lindner and G. Ralston. Effects of dextran on the self-association of human spectrin. *Biophysical Chemistry*, 57:15–25, 1995.

[65] P. R. tenWolde and D. Frenkel. Enhancement of protein crystal nucleation by critical density fluctuations. *Science*, 277:1975–1978, 1997.

[66] A. P. Minton. Effect of a concentrated "inert" macromolecular cosolute on the stability of a globular protein with respect to denaturation by heat and by chaotropes: A statistical-thermodynamical model. *Biophysical Journal*, 78:101–109, 2000.

[67] Y. Q. Zhou and C. K. Hall. Solute excluded-volume effects on the sta-

bility of globular proteins: A statistical thermodynamic theory. *Biopolymers*, 38:273–284, 1996.

[68] D. Hall and A. P. Minton. Macromolecular crowding: qualitative and semiquantitative successes, quantitative challenges. *Biochimica Et Biophysica Acta-Proteins And Proteomics*, 1649:127–139, 2003.

[69] P. G. de Gennes. *C. R. Hebd. Seances Acad. Sci., Ser. A B, Sci. Math. Sci. Phys*, 288:351–, 1979.

[70] E. Eisenriegler. Small mesoscopic particles in dilute and semidilute solutions of nonadsorbing polymers. *Journal Of Chemical Physics*, 113:5091–5097, 2000.

[71] T. Odijk. Protein-macromolecule interactions. *Macromolecules*, 29:1842–1843, 1996.

[72] R. P. Sear. Entropy-driven phase separation in mixtures of small colloidal particles and semidilute polymers. *Physical Review E*, 56:4463–4466, 1997.

[73] Y. L. Chen, K. S. Schweizer, and M. Fuchs. Phase separation in suspensions of colloids, polymers and nanoparticles: Role of solvent quality, physical mesh, and nonlocal entropic repulsion. *Journal Of Chemical Physics*, 118:3880–3890, 2003.

[74] P. Paricaud, S. Varga, and G. Jackson. Study of the demixing transition in model athermal mixtures of colloids and flexible self-excluding poly-

mers using the thermodynamic perturbation theory of wertheim. *Journal Of Chemical Physics*, 118:8525–8536, 2003.

[75] des Cloizeaux J. and Jannink G. *Polymers in Solution: Their Modelling and Structure*. sOxford University Press,, New York, 1990.

[76] R. Tuinier and H. N. W. Lekkerkerker. Polymer density around a sphere. *Macromolecules*, 35:3312–3313, 2002.

[77] H. Reiss. Statistical geometry in the study of fluids and porous-media. *Journal Of Physical Chemistry*, 96:4736–4747, 1992.

[78] M. Dijkstra, R. van Roij, and R. Evans. Phase behavior and structure of binary hard-sphere mixtures. *Physical Review Letters*, 81:2268–2271, 1998.

[79] K. Sasahara, P. McPhie, and A. P. Minton. Effect of dextran on protein stability and conformation attributed to macromolecular crowding. *Journal Of Molecular Biology*, 326:1227–1237, 2003.

[80] N. Tokuriki, M. Kinjo, S. Negi, M. Hoshino, Y. Goto, I. Urabe, and T. Yomo. Protein folding by the effects of macromolecular crowding. *Protein Science*, 13:125–133, 2004.

[81] A. Hanke, E. Eisenriegler, and S. Dietrich. Polymer depletion effects near mesoscopic particles. *Physical Review E*, 59:6853–6878, 1999.

[82] R. Tuinier, H. N. W. Lekkerkerker, and D. G. A. L. Aarts. Interaction potential between two spheres mediated by excluded volume polymers. *Phys. Rev. E*, 65:060801, 2002.

[83] M. G. Noro and D. Frenkel. Extended corresponding-states behavior for particles with variable range attractions. *Journal Of Chemical Physics*, 113:2941–2944, 2000.

[84] G. A. Vliegenthart and H. N. W. Lekkerkerker. Predicting the gas-liquid critical point from the second virial coefficient. *Journal Of Chemical Physics*, 112:5364–5369, 2000.

[85] A. A. Louis. Beware of density dependent pair potentials. *Journal Of Physics-Condensed Matter*, 14:9187–9206, 2002.

[86] N. F. Carnahan and K. E. Starling. Intermolecular repulsions and the equation of state for fluids. *Journal Of Chemical Physics*, 51:635, 1969.

[87] J. P. Hansen and I. R. McDonald. *Theory of Simple Liquids*. Academic, New York, 1986.

[88] R. Tuinier. *Private Communication*, 2005.

[89] A. A. Louis. *Private Communication*, 2005.

[90] I. Lynch, S. Cornen, and L. Piculell. Investigation of the segregative phase separation induced by addition of polystyrene to aot oil-continuous microemulsions. *Journal Of Physical Chemistry B*, 108:5443–5452, 2004.

[91] Striolo A., Colina C. M., Gubbins K. E., Elvassore N., and Lue L. The depletion attraction between pairs of colloid particles in polymer solution. *Molecular Simulation*, 30:437–449, 2004.

[92] D. A. McQuarrie. *Statistical Mechanics.* University Science, CA, 2000.

[93] T. Odijk. Many-body depletion interactions among protein spheres in a semidilute polymer solution. *Journal Of Chemical Physics*, 106:3402–3406, 1997.

[94] E. Dickinson. Caseins in emulsions: interfacial properties and interactions. *International Dairy Journal*, 9:305–312, 1999.

[95] P. G. Degennes. Polymer-solutions near an interface .1. adsorption and depletion layers. *Macromolecules*, 14:1637–1644, 1981.

[96] P. G. Degennes. Polymers at an interface .2. interaction between 2 plates carrying adsorbed polymer layers. *Macromolecules*, 15:492–500, 1982.

[97] J. M. H. M. Scheutjens and G. J. Fleer. Statistical-theory of the adsorption of interacting chain molecules .1. partition-function, segment density distribution, and adsorption-isotherms. *Journal Of Physical Chemistry*, 83:1619–1635, 1979.

[98] E. Dickinson. Milk protein interfacial layers and the relationship to emulsion stability and rheology. *Colloids And Surfaces B-Biointerfaces*, 20:197–210, 2001.

[99] O. Guiselin. Irreversible adsorption of a concentrated polymer-solution. *Europhysics Letters*, 17:225–230, 1992.

[100] A. Johner, J. BouetAvalos, C. C. vanderLinden, A. N. Semenov, and J. F. Joanny. Adsorption of neutral polymers: Interpretation of the numerical self-consistent field results. *Macromolecules*, 29:3629–3638, 1996.

[101] A. N. Semenov, J. F. Joanny, A. Johner, and J. BonetAvalos. Interaction between two adsorbing plates: The effect of polymer chain ends. *Macromolecules*, 30:1479–1489, 1997.

[102] S. Q. Zhou and X. Q. Zhang. Microscopic approach for the site distribution and thermodynamic properties of a single-component polymer subjected to an external field. *Physical Review E*, 6401, 2001.

[103] A. Yethiraj and C. E. Woodward. Monte-carlo density-functional theory of nonuniform polymer melts. *Journal Of Chemical Physics*, 102:5499–5505, 1995.

[104] A. Yethiraj and C. K. Hall. Integral-equation theory for the adsorption of chain fluids in slitlike pores. *Journal Of Chemical Physics*, 95:3749–3755, 1991.

[105] A. Yethiraj. Molecular modeling of polymers at surfaces. *Chemical Engineering Journal*, 74:109–115, 1999.

[106] P. A. Pincus, C. J. Sandroff, and T. A. Witten. Polymer adsorption on colloidal particles. *Journal De Physique*, 45:725–729, 1984.

[107] C. M. Marques and J. F. Joanny. Adsorption of semi-dilute polymer-solutions on fractal colloidal grains. *Journal De Physique*, 49:1103–1109, 1988.

[108] S. F. Edwards. The statistical mechanics of polymers with excluded volume. *Proceedings of Physical Society London*, 85:613, 1965.

[109] M. Aubouy, J. M. Dimeglio, and E. Raphael. Irreversible adsorption of a polymer melt on a colloidal particle. *Europhysics Letters*, 24:87–92, 1993.

[110] J. Klein and P. Pincus. Interaction between surfaces with adsorbed polymers - poor solvents. *Macromolecules*, 15:1129–1135, 1982.

[111] J. Klein and P. F. Luckham. Forces between 2 adsorbed poly(ethylene oxide) layers in a good aqueous solvent in the range 0-150 nm. *Macromolecules*, 17:1041–1048, 1984.

[112] E. M. Blokhuis, K. I. Skau, and J. B. Avalos. Free energy formalism for polymer adsorption: Self-consistent field theory for weak adsorption. *Journal Of Chemical Physics*, 119:3483–3494, 2003.

[113] F. Lafuma, K. Wong, and B. Cabane. Bridging of colloidal particles through adsorbed polymers. *Journal Of Colloid And Interface Science*, 143:9–21, 1991.

[114] S. F. Liu, V. Legrand, M. Gourmand, F. Lafuma, and R. Audebert. General phase and rheological behavior of silica/peo/water systems. *Colloids And Surfaces A-Physicochemical And Engineering Aspects*, 111:139–145, 1996.

[115] A. A. Gorbunov and A. M. Skvortsov. Statistical properties of confined macromolecules. *Advances In Colloid And Interface Science*, 62:31–108, 1995.

[116] G. P. Vanderbeek, M. A. C. Stuart, G. J. Fleer, and J. E. Hofman. A chromatographic method for the determination of segmental adsorption energies of polymers - polystyrene on silica. *Langmuir*, 5:1180–1186, 1989.

[117] B. Cabane, R. Duplessix, and T. Zemb. High-resolution neutron-scattering on ionic surfactant micelles - sds in water. *Journal De Physique*, 46:2161–2178, 1985.

[118] M. Surve, V. Pryamitsyn, and V. Ganesan. Depletion and pair interactions of proteins in polymer solutions. *Journal Of Chemical Physics*, 122, 2005.

[119] J. Popov, V. N.and Niederle and L. Hlavat. *Functional Integrals in Quantum Field Theory and Statistical Physics.* Springer, New York, 1986.

[120] V. S. Stenkamp and J. C. Berg. The role of long tails in steric stabilization and hydrodynamic layer thickness. *Langmuir*, 13:3827–3832, 1997.

[121] K. T. Marla and J. C. Meredith. Nanoscale colloids in a freely adsorbing polymer solution: A monte carlo simulation study. *Langmuir*, 20:1501–1510, 2004.

[122] B. O'Shaughnessy and D. Vavylonis. Non-equilibrium in adsorbed polymer layers. *Journal Of Physics-Condensed Matter*, 17:R63–R99, 2005.

[123] J. A. Barker and D. Henderson. What is liquid - understanding states of matter. *Reviews Of Modern Physics*, 48:587–671, 1976.

[124] J. B. Hooper and K. S. Schweizer. Contact aggregation, bridging, and steric stabilization in dense polymer-particle mixtures. *Macromolecules*, 38:8858–8869, 2005.

[125] G. D. Smith, D. Bedrov, and O. Borodin. Structural relaxation and dynamic heterogeneity in a polymer melt at attractive surfaces. *Physical Review Letters*, 90, 2003.

[126] W. Feller. *An Introduction to Probability Theory and Its Applications.* Wiley, New York, 1971.

[127] U. Alon, I. Balberg, and A. Drory. New, heuristic, percolation criterion for continuum-systems. *Physical Review Letters*, 66:2879–2882, 1991.

[128] M. Sahimi. *Applications of Percolation Theory.* Taylor and Francis, Bristol, PA, 1993.

[129] C. Cabane, K. Wong, and R. Duplessix. Macromolecules for control of distances in colloidal dispersions. *Acs Symposium Series*, 384:312–327, 1989.

[130] H. M. Schneider, P. Frantz, and S. Granick. The bimodal energy landscape when polymers adsorb. *Langmuir*, 12:994–996, 1996.

[131] V. Hlady and J. Buijs. Protein adsorption on solid surfaces. *Current Opinion In Biotechnology*, 7:72–77, 1996.

[132] V. Prasad, V. Trappe, A. D. Dinsmore, P. N. Segre, L. Cipelletti, and D. A. Weitz. Universal features of the fluid to solid transition for attractive colloidal particles. *Faraday Discussions*, 123:1–12, 2003.

[133] Z. Y. Zhu, T. Thompson, S. Q. Wang, E. D. von Meerwall, and A. Halasa. Investigating linear and nonlinear viscoelastic behavior using model silica-particle-filled polybutadiene. *Macromolecules*, 38:8816–8824, 2005.

[134] P. N. Segre, V. Prasad, A. B. Schofield, and D. A. Weitz. Glasslike kinetic arrest at the colloidal-gelation transition. *Physical Review Letters*, 86:6042–6045, 2001.

[135] J. Bergenholtz, W. C. K. Poon, and M. Fuchs. Gelation in model colloid-polymer mixtures. *Langmuir*, 19:4493–4503, 2003.

[136] S. A. Shah, Y. L. Chen, S. Ramakrishnan, K. S. Schweizer, and C. F. Zukoski. Microstructure of dense colloid-polymer suspensions and gels. *Journal Of Physics-Condensed Matter*, 15:4751–4778, 2003.

[137] S. A. Shah, Y. L. Chen, K. S. Schweizer, and C. F. Zukoski. Viscoelasticity and rheology of depletion flocculated gels and fluids. *Journal Of Chemical Physics*, 119:8747–8760, 2003.

[138] V. Kobelev and K. S. Schweizer. Nonlinear elasticity and yielding of depletion gels. *Journal Of Chemical Physics*, 123, 2005.

[139] E. M. Sevick, P. A. Monson, and J. M. Ottino. Monte-carlo calculations of cluster statistics in continuum models of composite morphology. *Journal Of Chemical Physics*, 88:1198–1206, 1988.

[140] S. B. Lee and S. Torquato. Pair connectedness and mean cluster size for continuum-percolation models - computer-simulation results. *Journal Of Chemical Physics*, 89:6427–6433, 1988.

[141] M. Lattuada, H. Wu, and M. Morbidelli. Hydrodynamic radius of fractal clusters. *Journal Of Colloid And Interface Science*, 268:96–105, 2003.

[142] D. M. Heyes and J. R. Melrose. Percolation cluster statistics of lennard-jones fluids. *Molecular Physics*, 66:1057–1074, 1989.

[143] N. A. Seaton and E. D. Glandt. Aggregation and percolation in a system of adhesive spheres. *Journal Of Chemical Physics*, 86:4668–4677, 1987.

[144] K. G. Soga, J. R. Melrose, and R. C. Ball. Continuum percolation and depletion flocculation. *Journal Of Chemical Physics*, 108:6026–6032, 1998.

[145] P. Sandkuhler, J. Sefcik, M. Lattuada, H. Wu, and M. Morbidelli. Modeling structure effects on aggregation kinetics in colloidal dispersions. *Aiche Journal*, 49:1542–1555, 2003.

[146] R. Tarjan. Depth-first search and linear graph algorithms. *SIAM Journal on Computing*, 1:146–160, 1972.

[147] M. Rubinstein and R. H. Colby. Elastic-modulus and equilibrium swelling of near-critical gels. *Macromolecules*, 27:3184–3190, 1994.

[148] Y. Otsubo and Y. Nakane. Simulation of bridging flocculation and elastic percolation in suspensions. *Langmuir*, 7:1118–1123, 1991.

[149] J. N. Paquien, J. Galy, J. F. Gerard, and A. Pouchelon. Rheological studies of fumed silica-polydimethylsiloxane suspensions. *Colloids And Surfaces A-Physicochemical And Engineering Aspects*, 260:165–172, 2005.

[150] R. Kotsilkova, D. Fragiadakis, and P. Pissis. Reinforcement effect of carbon nanofillers in an epoxy resin system: Rheology, molecular dynamics, and mechanical studies. *Journal Of Polymer Science Part B-Polymer Physics*, 43:522–533, 2005.

[151] S. E. Shim and A. I. Isayev. Rheology and structure of precipitated silica and poly(dimethyl siloxane) system. *Rheologica Acta*, 43:127–136, 2004.

[152] F. Saint-Michel, F. Pignon, and A. Magnin. Fractal behavior and scaling law of hydrophobic silica in polyol. *Journal Of Colloid And Interface Science*, 267:314–319, 2003.

[153] E. E. Pashkovski, J. G. Masters, and A. Mehreteab. Viscoelastic scaling of colloidal gels in polymer solutions. *Langmuir*, 19:3589–3595, 2003.

[154] S. Ramakrishnan, Y. L. Chen, K. S. Schweizer, and C. F. Zukoski. Elasticity and clustering in concentrated depletion gels. *Physical Review E*, 70, 2004.

[155] T. B. J. Blijdenstein, E. van der Linden, T. van Vliet, and G. A. van Aken. Scaling behavior of delayed demixing, rheology, and microstructure of emulsions flocculated by depletion and bridging. *Langmuir*, 20:11321–11328, 2004.

[156] O. Farago and Y. Kantor. Entropic elasticity at the sol-gel transition. *Europhysics Letters*, 57:458–463, 2002.

[157] S. Arbabi and M. Sahimi. Mechanics of disordered solids .1. percolation on elastic networks with central forces. *Physical Review B*, 47:695–702, 1993.

[158] L. Onsager. The effects of shape on the interaction of colloidal particles. *Ann. N. Y. Acad. Sci.*, 51:621–659, 1949.

[159] P. J. Flory. Phase equilibria in solutions of rod-like particles. *Proceedings of Royal Society of London A*, 234:73–89, 1956.

[160] P. J. Flory and G. Ronca. Theory of systems of rodlike particles .1. athermal systems. *Molecular Crystals And Liquid Crystals*, 54:289–309, 1979.

[161] E. L. Wee and W. G. Miller. Liquid crystal-isotropic phase equilibriums in the system poly(.gamma.-benzyl .alpha.-l-glutamate)-methylformamide. *Journal of Physical Chemistry*, 75:1446–1452, 1971.

[162] P. W. Morgan. Synthesis and properties of aromatic and extended chain polyamides. *Macromolecules*, 10:1381–1390, 1977.

[163] J. P. Straley. *Molecular Crystals and Liquid Crystals*, 22:233, 1977.

[164] P. J. Flory and P. A. Irvine. Liquid-crystalline transitions in homologous para-phenylenes and their mixtures .2. theoretical treatment. *Journal Of The Chemical Society-Faraday Transactions I*, 80:1807–1819, 1984.

[165] P. J. Flory and G. Ronca. Theory of systems of rodlike particles .2. thermotropic systems with orientation-dependent interactions. *Molecular Crystals And Liquid Crystals*, 54:311–330, 1979.

[166] M. Warner and P. J. Flory. The phase-equilibria in thermotropic liquid-crystalline systems. *Journal Of Chemical Physics*, 73:6327–6332, 1980.

[167] H. N. W. Lekkerkerker and A. Stroobants. Phase-behavior of rod-like colloid plus flexible polymer mixtures. *Nuovo Cimento Della Societa Italiana Di Fisica D-Condensed Matter Atomic Molecular And Chemical Physics Fluids Plasmas Biophysics*, 16:949–962, 1994.

[168] G. J. Vroege and H. N. W. Lekkerkerker. Phase-transitions in lyotropic colloidal and polymer liquid-crystals. *Reports On Progress In Physics*, 55:1241–1309, 1992.

[169] P. B. Warren. Depletion effect in a model lyotropic liquid crystal-theory. *Journal De Physique I*, 4:237–244, 1994.

[170] S. V. Savenko and M. Dijkstra. Phase behavior of a suspension of colloidal hard rods and nonadsorbing polymer. *Journal Of Chemical Physics*, 124, 2006.

[171] M. J. O'Connell, P. Boul, L. M. Ericson, C. Huffman, Y. H. Wang, E. Haroz, C. Kuper, J. Tour, K. D. Ausman, and R. E. Smalley. Reversible water-solubilization of single-walled carbon nanotubes by polymer wrapping. *Chemical Physics Letters*, 342:265–271, 2001.

[172] M. J. O'Connell, S. M. Bachilo, C. B. Huffman, V. C. Moore, M. S. Strano, E. H. Haroz, K. L. Rialon, P. J. Boul, W. H. Noon, C. Kittrell, J. P. Ma, R. H. Hauge, R. B. Weisman, and R. E. Smalley. Band gap fluorescence from individual single-walled carbon nanotubes. *Science*, 297:593–596, 2002.

[173] M. Moniruzzaman and K. I. Winey. Polymer nanocomposites containing carbon nanotubes. *Macromolecules*, 39:5194–5205, 2006.

[174] R. H. Baughman, A. A. Zakhidov, and W. A. de Heer. Carbon nanotubes - the route toward applications. *Science*, 297:787–792, 2002.

[175] B. Vigolo, A. Penicaud, C. Coulon, C. Sauder, R. Pailler, C. Journet, P. Bernier, and P. Poulin. Macroscopic fibers and ribbons of oriented carbon nanotubes. *Science*, 290:1331–1334, 2000.

[176] J. Chen, M. A. Hamon, H. Hu, Y. S. Chen, A. M. Rao, P. C. Eklund, and R. C. Haddon. Solution properties of single-walled carbon nanotubes. *Science*, 282:95–98, 1998.

[177] P. J. Boul, J. Liu, E. T. Mickelson, C. B. Huffman, L. M. Ericson, I. W. Chiang, K. A. Smith, D. T. Colbert, R. H. Hauge, J. L. Margrave, and R. E. Smalley. Reversible sidewall functionalization of buckytubes. *Chemical Physics Letters*, 310:367–372, 1999.

[178] K. D. Ausman, R. Piner, O. Lourie, R. S. Ruoff, and M. Korobov. Organic solvent dispersions of single-walled carbon nanotubes: Toward solutions of pristine nanotubes. *Journal Of Physical Chemistry B*, 104:8911–8915, 2000.

[179] R. Shvartzman-Cohen, Y. Levi-Kalisman, E. Nativ-Roth, and R. Yerushalmi-Rozen. Generic approach for dispersing single-walled car-

bon nanotubes: The strength of a weak interaction. *Langmuir*, 20:6085–6088, 2004.

[180] I. Szleifer and R. Yerushalmi-Rozen. Polymers and carbon nanotubes - dimensionality, interactions and nanotechnology. *Polymer*, 46:7803–7818, 2005.

[181] M. Yudasaka, M. Zhang, C. Jabs, and S. Iijima. Effect of an organic polymer in purification and cutting of single-wall carbon nanotubes. *Applied Physics A-Materials Science & Processing*, 71:449–451, 2000.

[182] A. B. Dalton, W. J. Blau, G. Chambers, J. N. Coleman, K. Henderson, S. Lefrant, B. McCarthy, C. Stephan, and H. J. Byrne. A functional conjugated polymer to process, purify and selectively interact with single wall carbon nanotubes. *Synthetic Metals*, 121:1217–1218, 2001.

[183] M. Zheng, A. Jagota, E. D. Semke, B. A. Diner, R. S. Mclean, S. R. Lustig, R. E. Richardson, and N. G. Tassi. Dna-assisted dispersion and separation of carbon nanotubes. *Nature Materials*, 2:338–342, 2003.

[184] D. Baskaran, J. W. Mays, and M. S. Bratcher. Noncovalent and nonspecific molecular interactions of polymers with multiwalled carbon nanotubes. *Chemistry Of Materials*, 17:3389–3397, 2005.

[185] J. K. W. Sandler, J. E. Kirk, I. A. Kinloch, M. S. P. Shaffer, and A. H. Windle. Ultra-low electrical percolation threshold in carbon-nanotube-epoxy composites. *Polymer*, 44:5893–5899, 2003.

[186] B. Vigolo, C. Coulon, M. Maugey, C. Zakri, and P. Poulin. An experimental approach to the percolation of sticky nanotubes. *Science*, 309:920–923, 2005.

[187] F. M. Du, R. C. Scogna, W. Zhou, S. Brand, J. E. Fischer, and K. I. Winey. Nanotube networks in polymer nanocomposites: Rheology and electrical conductivity. *Macromolecules*, 37:9048–9055, 2004.

[188] F. M. Du, J. E. Fischer, and K. I. Winey. Effect of nanotube alignment on percolation conductivity in carbon nanotube/polymer composites. *Physical Review B*, 72, 2005.

[189] T. Kashiwagi, F. M. Du, J. F. Douglas, K. I. Winey, R. H. Harris, and J. R. Shields. Nanoparticle networks reduce the flammability of polymer nanocomposites. *Nature Materials*, 4:928–933, 2005.

[190] X. L. Wang and A. P. Chatterjee. Connectedness percolation in athermal mixtures of flexible and rigid macromolecules: Analytic theory. *Journal Of Chemical Physics*, 118:10787–10793, 2003.

[191] B. V. Derjaguin. *Kolloid Z.*, 69:155–164, 1934.

[192] L. R. White. On the deryaguin approximation for the interaction of macrobodies. *Journal Of Colloid And Interface Science*, 95:286–288, 1983.

[193] M. Surve, V. Pryamitsyn, and V. Ganesan. Nanoparticles in solutions of adsorbing polymers: Pair interactions, percolation, and phase behavior. *Langmuir*, 22:969–981, 2006.

[194] H. N. W. Lekkerkerker, P. Coulon, R. Vanderhaegen, and R. Deblieck. On the isotropic-liquid crystal phase-separation in a solution of rodlike particles of different lengths. *Journal Of Chemical Physics*, 80:3427–3433, 1984.

[195] A. L. R. Bug, S. A. Safran, G. S. Grest, and I. Webman. Do interactions raise or lower a percolation-threshold. *Physical Review Letters*, 55:1896–1899, 1985.

[196] A. L. R. Bug, S. A. Safran, and I. Webman. Continuum percolation of permeable objects. *Physical Review B*, 33:4716–4724, 1986.

[197] M. Foygel, R. D. Morris, D. Anez, S. French, and V. L. Sobolev. Theoretical and computational studies of carbon nanotube composites and suspensions: Electrical and thermal conductivity. *Physical Review B*, 71, 2005.

[198] P. G. Bolhuis, A. Stroobants, D. Frenkel, and H. N. W. Lekkerkerker. Numerical study of the phase behavior of rodlike colloids with attractive interactions. *Journal Of Chemical Physics*, 107:1551–1564, 1997.

[199] M. Grujicic, G. Cao, and W. N. Roy. A computational analysis of the percolation threshold and the electrical conductivity of carbon nanotubes

filled polymeric materials. *Journal Of Materials Science*, 39:4441–4449, 2004.

[200] S. H. Munsonmcgee. Estimation of the critical concentration in an anisotropic percolation network. *Physical Review B*, 43:3331–3336, 1991.

[201] J. C. Grunlan, L. Liu, and Y. S. Kim. Tunable single-walled carbon nanotube microstructure in the liquid and solid states using poly(acrylic acid). *Nano Letters*, 6:911–915, 2006.

[202] L. A. Girifalco, M. Hodak, and R. S. Lee. Carbon nanotubes, buckyballs, ropes, and a universal graphitic potential. *Physical Review B*, 62:13104–13110, 2000.

[203] A. P. Philipse. The random contact equation and its implications for (colloidal) rods in packings, suspensions, and anisotropic powders. *Langmuir*, 12:1127–1133, 1996.

[204] M. P. B. van Bruggen and H. N. W. Lekkerkerker. Tunable attractions directing nonequilibrium states in dispersions of hard rods. *Macromolecules*, 33:5532–5535, 2000.

[205] M. S. Strano. Polymer-wrapped nanotubes. *Nature Materials*, 5:433–434, 2006.

[206] R. Shvartzman-Cohen, E. Nativ-Roth, E. Baskaran, Y. Levi-Kalisman, I. Szleifer, and R. Yerushalmi-Rozen. Selective dispersion of single-walled

carbon nanotubes in the presence of polymers: the role of molecular and colloidal length scales. *Journal Of The American Chemical Society*, 126:14850–14857, 2004.

[207] M. P. B. vanBruggen, F. M. vanderKooij, and H. N. W. Lekkerkerker. Liquid crystal phase transitions in dispersions of rod-like colloidal particles. *Journal Of Physics-Condensed Matter*, 8:9451–9456, 1996.

[208] M. P. B. van Bruggen and H. N. W. Lekkerkerker. Metastability and multistability: Gelation and liquid crystal formation in suspensions of colloidal rods. *Langmuir*, 18:7141–7145, 2002.

[209] A. Halperin. Polymer brushes that resist adsorption of model proteins: Design parameters. *Langmuir*, 15:2525–2533, 1999.

[210] M. Muller. Phase diagram of a mixed polymer brush. *Physical Review E*, 65, 2002.

[211] Fredrickson G. H. *The Equilibrium Theory of Inhomogenous Polymers*. Clarendon Press, Oxford, 2005.

[212] C. M. Wijmans and E. B. Zhulina. Polymer brushes at curved surfaces. *Macromolecules*, 26:7214–7224, 1993.

[213] M. Aubouy, G. H. Fredrickson, P. Pincus, and E. Raphael. End-tethered chains in polymeric matrices. *Macromolecules*, 28:2979–2981, 1995.

[214] E. Verwey and J. Overbeek. *Theory of the Stability of Lyophobic Colloids*. Elsevier, Amsterdam, 1948.

[215] A. Kulkarni and C. Zukoski. Depletion interactions and protein crystallization. *Journal Of Crystal Growth*, 232:156–164, 2001.

[216] M. Malmsten, K. Emoto, and J. M. Van Alstine. Effect of chain density on inhibition of protein adsorption by poly(ethylene glycol) based coatings. *Journal Of Colloid And Interface Science*, 202:507–517, 1998.

[217] M. Jonsson and H. O. Johansson. Effect of surface grafted polymers on the adsorption of different model proteins. *Colloids And Surfaces B-Biointerfaces*, 37:71–81, 2004.

[218] P. Molyneux. *Water-soluble synthetic polymers : properties and behavior*. CRC Press, Boca Raton, Fla., 1984.

[219] R. R. Netz and D. Andelman. Neutral and charged polymers at interfaces. *Physics Reports-Review Section Of Physics Letters*, 380:1–95, 2003.

[220] R. R. Netz and J. F. Joanny. Complexation between a semiflexible polyelectrolyte and an oppositely charged sphere. *Macromolecules*, 32:9026–9040, 1999.

[221] H. Schiessel. The physics of chromatin. *Journal Of Physics-Condensed Matter*, 15:R699–R774, 2003.

[222] A. Shafir, D. Andelman, and R. R. Netz. Adsorption and depletion of polyelectrolytes from charged surfaces. *Journal Of Chemical Physics*, 119:2355–2362, 2003.

[223] R. Podgornik. Polyelectrolyte-mediated bridging interactions. *Journal Of Polymer Science Part B-Polymer Physics*, 42:3539–3556, 2004.

[224] N. Kozer and G. Schreiber. Effect of crowding on protein - protein association rates: Fundamental differences between low and high mass crowding agents. *Journal Of Molecular Biology*, 336:763–774, 2004.

[225] R. Tuinier. Segment-sphere size ratio influence on the stability of a polymer-colloid mixture. *European Physical Journal E*, 10:123–128, 2003.

[226] J. L. Doublier, C. Garnier, D. Renard, and C. Sanchez. Protein-polysaccharide interactions. *Current Opinion In Colloid & Interface Science*, 5:202–214, 2000.

[227] M. W. Matsen. Comment on "attraction between nanoparticles induced by end-grafted homopolymers in good solvent". *Physical Review Letters*, 95, 2005.

[228] K. T. Marla and J. C. Meredith. Simulation of interaction forces between nanoparticles in the presence of lennard-jones polymers: Freely adsorbing homopolymer modifiers. *Langmuir*, 21:487–497, 2005.

[229] S. H. Chen, W. R. Chen, and F. Mallamace. The glass-to-glass transition and its end point in a copolymer micellar system. *Science*, 300:619–622, 2003.

[230] S. Ramakrishnan, M. Fuchs, K. S. Schweizer, and C. F. Zukoski. Concentration fluctuations in a model colloid-polymer suspension: Experimental tests of depletion theories. *Langmuir*, 18:1082–1090, 2002.

[231] G. J. Fleer, J. van MAle, and A. Johner. Analytical approximation to the scheutjens-fleer theory for polymer adsorption from dilute solution. 1. trains, loops, and tails in terms of two parameters: The proximal and distal lengths. *Macromolecules*, 32:825–844, 1999.

[232] F. Sciortino, S. V. Buldyrev, C. De Michele, G. Foffi, N. Ghofraniha, E. La Nave, A. Moreno, S. Mossa, I. Saika-Voivod, P. Tartaglia, and E. Zaccarelli. Routes to colloidal gel formation. *Computer Physics Communications*, 169:166–171, 2005.

[233] M. E. Cates, M. Fuchs, K. Kroy, W. C. K. Poon, and A. M. Puertas. Theory and simulation of gelation, arrest and yielding in attracting colloids. *Journal Of Physics-Condensed Matter*, 16:S4861–S4875, 2004.

[234] K. Yurekli, R. Krishnamoorti, M. F. Tse, K. O. Mcelrath, A. H. Tsou, and H. C. Wang. Structure and dynamics of carbon black-filled elastomers. *Journal Of Polymer Science Part B-Polymer Physics*, 39:256–275, 2001.

[235] M. Plischke, D. C. Vernon, B. Joos, and Z. Zhou. Entropic rigidity of randomly diluted two- and three-dimensional networks. *Physical Review E*, 60:3129–3135, 1999.

[236] E. R. Duering, K. Kremer, and G. S. Grest. Structure and relaxation of end-linked polymer networks. *Journal Of Chemical Physics*, 101:8169–8192, 1994.

[237] M. Sahimi and S. Arbabi. Mechanics of disordered solids .2. percolation on elastic networks with bond-bending forces. *Physical Review B*, 47:703–712, 1993.

[238] G. Rossi and P. A. Pincus. Properties of polymer layers adsorbed on surfaces under nonequilibrium conditions. *Macromolecules*, 22:276–283, 1989.

[239] Y. Otsubo. Effect of polymer adsorption on the rheological behavior of silica suspensions. *Journal Of Colloid And Interface Science*, 112:380–386, 1986.

[240] D. Stauffer, A. Coniglio, and M. Adam. Gelation and critical phenomena. *Advances In Polymer Science*, 44:103–158, 1982.

[241] P. G. Degennes. Scaling theory of polymer adsorption. *Journal De Physique*, 37:1445–1452, 1976.

[242] J. Buitenhuis, L. N. Donselaar, P. A. Buining, A. Stroobants, and H. N. W. Lekkerkerker. Phase-separation of mixtures of colloidal

boehmite rods and flexible polymer. *Journal Of Colloid And Interface Science*, 175:46–56, 1995.

[243] J. S. Vanduijneveldt and H. N. W. Lekkerkerker. Phase-behavior of hard particles. *Journal Of Statistical Physics*, 78:103–116, 1995.

[244] P. A. Irvine, D. C. Wu, and P. J. Flory. Liquid-crystalline transitions in homologous para-phenylenes and their mixtures .1. experimental results. *Journal Of The Chemical Society-Faraday Transactions I*, 80:1795–1806, 1984.

[245] P. A. Irvine and P. J. Flory. Liquid-crystalline transitions in homologous para-phenylenes and their mixtures .3. relation of orientation-dependent interactions to optical anisotropies. *Journal Of The Chemical Society-Faraday Transactions I*, 80:1821–1830, 1984.

[246] M. Aubouy and E. Raphael. Surface-tethered polymers in polymeric matrices. *Journal De Physique Ii*, 3:443–448, 1993.

[247] V. A. Baulin, E. B. Zhulina, and A. Halperin. Self-consistent field theory of brushes of neutral water-soluble polymers. *Journal Of Chemical Physics*, 119:10977–10988, 2003.

Vita

Megha Madhukar Surve was born in Ratnagiri, India on 18 March 1978, the daughter of Madhukar S. Surve and Madhuri M. Surve. She received the Bachelor of Engineering degree in Chemical Engineering from the Shivaji University, India in 1998 and the Master of Technology from the Indian Institute of Technology Bombay, India in 2002. She started her graduate studies at the University of Texas at Austin in August, 2002.

Permanent address: A/P: Pedhambe,
Tal: Sangameshwar,
Dist: Ratnagiri,
MH, India, 415608

This dissertation was typeset with LaTeX[†] by the author.

[†] LaTeX is a document preparation system developed by Leslie Lamport as a special version of Donald Knuth's TeX Program.